NASA CR-134961

Second Annual Report
National Aeronautics and Space Administration
Lewis Research Center
Grant NGR 23-004-068

(NASA-CR-134961) THE OBLIQUE IMPINGEMENT OF AN AXISYMMETRIC JET Annual Report (Michigan State Univ.) 185 p HC $7.50 CSCL 20D

N76-16375

Unclas
G3/34 13392

THE OBLIQUE IMPINGEMENT OF AN AXISYMMETRIC JET

FEB 1976
RECEIVED
NASA STI FACILITY
INPUT BRANCH

Division of Engineering Research
MICHIGAN STATE UNIVERSITY
East Lansing, Michigan 48823
December 21, 1972

Second Annual Report
National Aeronautics and Space Administration
Lewis Research Center
Grant NGR 23-004-068

THE OBLIQUE IMPINGEMENT OF AN AXISYMMETRIC JET

prepared by

John F. Foss
Stanley J. Kleis

Division of Engineering Research
MICHIGAN STATE UNIVERSITY
East Lansing, Michigan 48823
December 21, 1972

ABSTRACT

The mechanics of the oblique impingement of an axisymmetric jet have been investigated. The kinematic constraint of no penetration requires the jet to spread and/or to deflect vertically in order to provide a sufficient cross sectional area for the mass flux. The selection between these two effects is established by the dynamical effects represented in the three-dimensional momentum equation. The velocity field, as expressed by the convective acceleration of the mean flow is primarily balanced by the three-dimensional pressure distribution above the plate and tailored by the Reynolds stress distribution. It is shown that an alternative description of the pertinent phenomena may be constructed by considering the vorticity transport equation. The gradients of the (easily measured) two-dimensional surface pressure field are source terms for the lateral and longitudinal vorticity components and the azimuthal vorticity structure in the approaching jet is reoriented to create a deformation in the isotach pattern which is characteristic of secondary flows.

The jet responds by deflecting vertically for a sufficiently slow approach to the plate; for this, the intersection of the conical free jet isotach with an imaginary reference plane characterizes the interaction. The spreading effect is important for larger angles and/or closer spacings. The stagnation point is located near the upstream edge of the interaction and is physically displaced from the maximum pressure point on the plate.

TABLE OF CONTENTS

	page
ABSTRACT	iii
TABLE OF CONTENTS	v
LIST OF TABLES	vii
LIST OF FIGURES	ix
NOMENCLATURE	xv
1. INTRODUCTION	1
2. EXPERIMENTAL FACILITY	3
3. THE MAJOR PHENOMENA OF THE OBLIQUE IMPINGEMENT OF AN AXISYMMETRIC JET	4
3.1. Problem Statement	4
3.2. Spreading and Curvature Effects in an Obliquely Impinging Jet	5
3.2.1. Jet spreading	5
3.2.2. Curvature of the jet	8
3.3. Vorticity Considerations	12
3.4. The Development of an Analytical Model	17
3.5. Additional Phenomena	18
3.6. Phenomena Identified in the First Annual Report	21
4. THE CENTERLINE PRESSURE DISTRIBUTIONS	22
5. THE STAGNATION POINT	24
5.1. General Considerations	24
5.2. Analytical Considerations	25
5.2.1. The orientation of the stagnation streamline	25
5.2.2. Consequences of stagnation point at or displaced from the maximum surface pressure	28
5.2.3. Relationship between the stagnation and surface pressure gradients near the stagnation streamline	30
5.3. Experimental Investigation of the Stagnation Phenomena	32
5.3.1. Technique and interpretation	32
5.3.2. Experimental results	33
5.3.3. Summary and analysis of the stagnation point investigation	35
6. SUMMARY	35
7. REFERENCES	36
APPENDIX A.	37
APPENDIX B.	73
APPENDIX C.	77
APPENDIX D.	85

PRECEDING PAGE BLANK NOT FILMED

LIST OF TABLES

		page
1.	Radius r as a function of x/d to define the 0.1 isotach (u(x, r)/u(o) = 0.1) for the fully developed and uniform nozzle exit conditions. (The data shown are from those cases for which the measured x-component momentum flux was constant to within ± 3 percent.)	89
2.	Summary of percent widths, distance to maximum pressure and isobar which aligns with free isotach intersection.	90
3.	Ratio of ω_y vorticity flux through the plate to the vorticity flux through a small height at the x location of the maximum pressure. Uniform nozzle exit condition.	20
4.	Data from the stagnation point investigation.	91

PRECEDING PAGE BLANK NOT FILMED

LIST OF FIGURES

		page
1a.	Externally blown flap STOL aircraft configuration	93
1b.	The round-jet/plane-wall flow field, coordinate system and nomenclature.	93
2.	Detail of uniform flow nozzle.	94
3.	Isobar plot values shown are $p(x, y, 0)/\rho\lambda u(0)^2 \sin\alpha \times 10^2$ for the conditions 3, 0.75, u.	95
4.	Isobar plot values shown are $p(x, y, 0)/\rho\lambda u(0)^2 \sin\alpha \times 10^2$ for the conditions 3, 1, u.	96
5.	Isobar plot values shown are $p(x, y, 0)/\rho\lambda u(0)^2 \sin\alpha \times 10^2$ for the conditions 3, 0.5626, fd.	97
6.	Isobar plot values shown are $p(x, y, 0)/\rho\lambda u(0)^2 \sin\alpha \times 10^2$ for the conditions 3, 0.667, fd.	98
7.	Isobar plot values shown are $p(x, y, 0)/\rho\lambda u(0)^2 \sin\alpha \times 10^2$ for the conditions 3, 0.75, fd.	99
8.	Isobar plot values shown are $p(x, y, 0)/\rho\lambda u(0)^2 \sin\alpha \times 10^2$ for the conditions 3, 1, fd.	100
9.	Isobar plot values shown are $p(x, y, 0)/\rho\lambda u(0)^2 \sin\alpha \times 10^2$ for the conditions 6, 0.75, u.	101
10.	Isobar plot values shown are $p(x, y, 0)/\rho\lambda u(0)^2 \sin\alpha \times 10^2$ for the conditions 6, 1, u.	102
11.	Isobar plot values shown are $p(x, y, 0)/\rho\lambda u(0)^2 \sin\alpha \times 10^2$ for the conditions 6, 1.5, u.	103
12.	Isobar plot values shown are $p(x, y, 0)/\rho\lambda u(0)^2 \sin\alpha \times 10^2$ for the conditions 6, 0.75, fd.	104
13.	Isobar plot values shown are $p(x, y, 0)/\rho\lambda u(0)^2 \sin\alpha \times 10^2$ for the conditions 6, 1, fd.	105
14.	Isobar plot values shown are $p(x, y, 0)/\rho\lambda u(0)^2 \sin\alpha \times 10^2$ for the conditions 6, 1.5, fd.	106
15.	Isobar plot values shown are $p(x, y, 0)/\rho\lambda u(0)^2 \sin\alpha \times 10^2$ for the conditions 9, 1, u.	107
16.	Isobar plot values shown are $p(x, y, 0)/\rho\lambda u(0)^2 \sin\alpha \times 10^2$ for the conditions 9, 1.5, u.	108

PRECEDING PAGE BLANK NOT FILMED

		page
17.	Isobar plot values shown are $p(x, y, 0)/\rho \lambda u(0)^2 \sin \alpha \times 10^2$ for the conditions 9, 1, fd.	109
18.	Isobar plot values shown are $p(x, y, 0)/\rho \lambda u(0)^2 \sin \alpha \times 10^2$ for the conditions 9, 1.5, fd.	110
19.	Isobar plot values shown are $p(x, y, 0)/\rho \lambda u(0)^2 \sin \alpha \times 10^2$ for the conditions 9, 2, fd.	111
20.	Isobar plot values shown are $p(x, y, 0)/\rho \lambda u(0)^2 \sin \alpha \times 10^2$ for the conditions 12, 1.5, u.	112
21.	Isobar plot values shown are $p(x, y, 0)/\rho \lambda u(0)^2 \sin \alpha \times 10^2$ for the conditions 12, 1.5, fd.	113
22.	Isobar plot values shown are $p(x, y, 0)/\rho \lambda u(0)^2 \sin \alpha \times 10^2$ for the conditions 12, 2, fd.	114
23.	Isobar plot values shown are $p(x, y, 0)/\rho \lambda u(0)^2 \sin \alpha \times 10^2$ for the conditions 15, 1, u.	115
24.	Isobar plot values shown are $p(x, y, 0)/\rho \lambda u(0)^2 \sin \alpha \times 10^2$ for the conditions 15, 2, fd.	116
25.	Isobar plot values shown are $p(x, y, 0)/\rho \lambda u(0)^2 \sin \alpha \times 10^2$ for the conditions 30, 2, u.	117
26.	Isobar plot values shown are $p(x, y, 0)/\rho \lambda u(0)^2 \sin \alpha \times 10^2$ for the conditions 30, 3, u.	118
27.	Isobar plot values shown are $p(x, y, 0)/\rho \lambda u(0)^2 \sin \alpha \times 10^2$ for the conditions 60, 2, u.	119
28.	Isotach contours $\alpha = 3$, $h/d = 0.75$, uniform.	120
	a. $x/d \approx 0$	120
	b. $x/d = 1$	121
	c. $x/d = 2$	122
	d. $x/d = 3$	123
	e. $x/d = 4$	124
	f. $x/d = 5$	125
29.	Isotach contours $\alpha = 9$, $h/d = 1$, uniform.	126
	a. $x/d \approx 0$	126
	b. $x/d = 1$	127
	c. $x/d = 2$	128
	d. $x/d = 3$	129
	e. $x/d = 4$	130
	f. $x/d = 5$	131
30.	Isotach contours $\alpha = 15$, $h/d=1$, uniform.	132
	a. $x/d \approx 0$	132
	b. $x/d = 1$	133
	c. $x/d = 2$	134

page

d. $x/d = 3$ 135
e. $x/d = 4$ 136
f. $x/d = 5$ 137

31. Control volume for the analysis of the round-jet/plane-wall flow field. 138

32. Normalized centerline pressure $p/\rho \lambda u(0)^2 \sin \alpha$ and the normalized curvature of the jet's momentum flux centerline $Kd/\sin \alpha$. The x/d origin for each h/d value represents the intersection point of the 0.1 free isotach. $\alpha = 3$ degrees, uniform exit condition 139

33. Normalized centerline pressure $p/\rho \lambda u(0)^2 \sin \alpha$ and the normalized curvature of the jet's momentum flux centerline $Kd/\sin \alpha$. The $x/d = 0$ origin for each h/d value represents the intersection point of the 0.1 free isotach. $\alpha = 3$ degrees, fully developed exit condition 140

34. Normalized centerline pressure $p/\rho \lambda u(0)^2 \sin \alpha$ and the normalized curvature of the jet's momentum flux centerline $Kd/\sin \alpha$. The $x/d = 0$ origin for each h/d value represents the intersection point of the 0.1 free isotach. $\alpha = 6$ degrees, uniform exit condition 141

35. Normalized centerline pressure $p/\rho \lambda u(0)^2 \sin \alpha$ and the normalized curvature of the jet's momentum flux centerline $Kd/\sin \alpha$. The $x/d = 0$ origin for each h/d value represents the intersection point of the 0.1 free isotach. $\alpha = 6$ degrees, fully developed exit condition 142

36. Normalized centerline pressure $p/\rho \lambda u(0)^2 \sin \alpha$ and the normalized curvature of the jet's momentum flux centerline $Kd/\sin \alpha$. The $x/d = 0$ origin for each h/d value represents the intersection point of the 0.1 free isotach. $\alpha = 9$ degrees, uniform exit condition 143

37. Normalized centerline pressure $p/\rho \lambda u(0)^2 \sin \alpha$ and the normalized curvature of the jet's momentum flux centerline $Kd/\sin \alpha$. The $x/d = 0$ origin for each h/d value represents the intersection point of the 0.1 free isotach. $\alpha = 9$ degrees, fully developed exit condition 144

38. Normalized centerline pressure $p/\rho \lambda u(0)^2 \sin \alpha$ and the normalized curvature of the jet's momentum flux centerline $Kd/\sin \alpha$ The $x/d = 0$ origin for each h/d value represents the intersection point of the 0.1 free isotach. $\alpha = 12$ degrees, uniform exit condition 145

39. Normalized centerline pressure $p/\rho \lambda u(0)^2 \sin \alpha$ and the normalized curvature of the jet's momentum flux centerline $Kd/\sin \alpha$. The $x/d = 0$ origin for each h/d value represents the intersection point of the 0.1 free isotach. $\alpha = 12$ degrees, fully developed exit condition 146

page

40. Normalized centerline pressure $p/\rho \lambda u(0)^2 \sin \alpha$ and the normalized curvature of the jet's momentum flux centerline $Kd/\sin \alpha$. The $x/d = 0$ origin for each h/d value represents the intersection point of the 0.1 free isotach. $\alpha = 15$ degrees, uniform exit condition 147

41. Normalized centerline pressure $p/\rho \lambda u(0)^2 \sin \alpha$ and the normalized curvature of the jet's momentum flux centerline $Kd/\sin \alpha$. The $x/d = 0$ origin for each h/d value represents the intersection point of the 0.1 free isotach. $\alpha = 15$ degrees, fully developed exit condition 148

42. Normalized centerline pressure $p/\rho \lambda u(0)^2 \sin \alpha$ and the normalized curvature of the jet's momentum flux centerline $Kd/\sin \alpha$. The $x/d = 0$ origin for each h/d value represents the intersection point of the 0.1 free isotach. $\alpha = 30$ degrees, uniform exit condition 149

43. Normalized centerline pressure $p/\rho \lambda u(0)^2 \sin \alpha$ and the normalized curvature of the jet's momentum flux centerline $Kd/\sin \alpha$. The $x/d = 0$ origin for each h/d value represents the intersection point of the 0.1 free isotach. $\alpha = 60$ degrees, uniform exit condition 150

44. $Kd/\sin \alpha$ for the conditions $\alpha = 3$ degrees, uniform, and the indicated h/d values. The abscissa of the separate curves has been shifted such that the intersection of the 0.1 free isotach occurs at the origin. 151

45. $Kd/\sin \alpha$ for the conditions $\alpha = 3$ degrees, fully developed, and the indicated h/d values. The abscissa of the separate curves has been shifted such that the intersection of the 0.1 free isotach occurs at the origin. 152

46. $Kd/\sin \alpha$ for the conditions $\alpha = 3$ degrees, fully developed and the indicated h/d values. The abscissa of the separate curves has been shifted such that the intersection of the 0.1 free isotach occurs at the origin. 153

47. $Kd/\sin \alpha$ for the conditions $\alpha = 6$ degrees, fully developed, and the indicated h/d values. The abscissa of the separate curves has been shifted such that the intersection of the 0.1 free isotach occurs at the origin. 154

48. $Kd/\sin \alpha$ for the conditions $\alpha = 9$ degrees, uniform, and the indicated h/d values. The abscissa of the separate curves has been shifted such that the intersection of the 0.1 free isotach occurs at the origin. 155

49. $Kd/\sin \alpha$ for the conditions $\alpha = 9$ degrees, fully developed, and the indicated h/d values. The abscissa of the separate curves has been shifted such that the intersection of the 0.1 free isotach occurs at the origin. 156

page

50. Kd/sin α for the conditions α = 12 degrees, uniform, and the indicated h/d values. The abscissa of the separate curves has been shifted such that the intersection of the 0.1 free isotach occurs at the origin. 157

51. Kd/sin α for the conditions α = 12 degrees, fully developed and the indicated h/d values. The abscissa of the separate curves has been shifted such that the intersection of the 0.1 free isotach occurs at the origin. 158

52. Kd/sin α for the conditions α = 15 degrees, uniform, and the indicated h/d values. The abscissa of the separate curves has been shifted such that the intersection of the 0.1 free isotach occurs at the origin. 159

53. Kd/sin α for the conditions α = 15 degrees, fully developed, and the indicated h/d values. The abscissa of the separate curves has been shifted such that the intersection of the 0.1 free isotach occurs at the origin. 160

54. Kd/sin α for the conditions α = 30 degrees, uniform, and the indicated h/d values. The abscissa of the separate curves has been shifted such that the intersection of the 0.1 free isotach occurs at the origin. 161

55. Kd/sin α for the conditions α = 60 degrees, uniform, and the indicated h/d values. The abscissa of the separate curves has been shifted such that the intersection of the 0.1 free isotach occurs at the origin. 162

56. Schematic representation of general isotach distribution showing the axisymmetric region in the undisturbed flow, the buffer region and the near wall region. 163

57a. Flux of streamwise vorticity into the flow as a result of the surface pressure distribution, fully developed cases (α degrees, h/d). Note, 15, 1, u is for the uniform exit condition. 164

57b. Flux of streamwise vorticity into the flow as a result of the surface pressure distribution, fully developed cases (α degrees, h/d). 165

58. Vorticity, pressure relationships for normal jet impingement. 166

59. Physical characteristics of oblique jet impingement. 167

60. Experimental technique for the acquisition of the velocity and surface static pressure data. 168

page

61. Measured, v_w, and equivalent stagnation streamline velocities (as inferred from the surface pressure), v_p, to determine the stagnation point for the conditions α = 3 degrees, h/d = 1, uniform. 169

62. Measured, v_w, and equivalent stagnation streamline velocities (as inferred from the surface pressure), v_p, to determine the stagnation point for the conditions α = 9 degrees, h/d = 1, uniform 170

63. Measured, v_w, and equivalent stagnation streamline velocities (as inferred from the surface pressure), v_p, to determine the stagnation point for the conditions α = 15 degrees, h/d = 1, uniform. 171

NOMENCLATURE

C.S.	control surface
C.V.	control volume
d	diameter of nozzle exit
E	energy flux; $\iint \rho u^3 \, dydz$
F	force
$\hat{i}$	x-component unit vector
J	momentum flux; $\iint \rho u^2 dydz$, $J(0)$ = momentum flux from nozzle
J_0	momentum flux based on $Q(0)$, $\rho Q(0)^2 A_o$
$\hat{j}$	y-component unit vector
$\hat{k}$	z-component unit vector
K	radius of curvature of jet, see (5)
M	mass flux, $\iint \rho u \, dydz$
$\hat{n}$	outward drawn unit vector
p	pressure
Q	magnitude of the velocity vector, $Q(0) \equiv Q(0,0,0)$
r	radius for cylindrical coordinates
R_j	radius of the jet (arbitrarily defined)
u	x-component velocity, $\vec{v} \cdot \hat{i}$, $u(0) \equiv u(0,0,0)$
v	y-component velocity; $\vec{v} \cdot \hat{j}$
$\vec{v}, \underset{\sim}{u}$	vector velocity
v_w	velocity recorded by hot-wire in the stagnation point experiment
v_p	"velocity" calculated from the wall pressure tap in the stagnation point analysis, see Figure 61.
V	volume
w	z-component velocity; $\vec{v} \cdot \hat{k}$
x, y, z	coordinates (see Figure 1)
z_c	jet centerline defined by the center of the circular isotach pattern at a given x location
z_m	jet centerline defined by the moment-of-momentum equation (33)

Superscripts

$(\bar{\ })$	time average quantity
$(\ '\ )$	fluctuating quantity

Subscripts

$(\ )_e$	entrainment
$(\ )_j$	pertaining to the jet
$(\ )_o$	condition at the nozzle exit
$(\ )_T$	true value
$(\ )_x$, $(\ )_z$	x and z component values

Greek Symbols

α	inclination angle of the jet
δ	a small increment, used as δz and δn, lengths which are small with respect to d
θ	azimuthal coordinate (r, θ, x)
λ_u, λ_{fd}	momentum flux ratio characterizing the nozzle exit velocity distribution $\lambda = J(0)/J_o$, $\lambda_u = 0.809$, $\lambda_d = 0.676$
ν	kinematic viscosity
ρ	density
ω	vorticity vector

1. INTRODUCTION

The mechanics of the oblique impingement of an axisymmetric jet on a plane surface are examined in detail in this report. Figure 1 shows a schematic drawing of the problem under consideration and the coordinate system used to describe the flow field. The kinematic features of the flow above the plate are examined in the context of the conservation of mass, the vorticity of the jet, and the vorticity introduced by the jet-plate interaction. The dynamic features of the flow are examined in terms of the surface pressure distribution and the cause-effect relationships which exist between the pressure and velocity/vorticity distributions. This report represents the primary results of the second year's activities supported by the NASA grant NGR 23-004-068.

This study was motivated by the externally blown flap (e.b.f.), a configuration under consideration as a means of gaining large lift coefficients for STOL aircraft. For this application problem the airfoil extends no more than five or six jet diameters beyond the jet; hence, the extensive data for the inclination angle α and the height above the plate h/d are restricted to the limited streamwise domain of $0 \leq x/d \leq 6$ for the static pressures. With the exception of the pressure data for $\alpha = 30$, and $\alpha = 60$ degrees, the present investigation is relevant to the flow resulting from the interaction of the propulsion jet with the main airfoil. The information herein is appropriate to an over- or under- wing configuration. A schematic of the latter is shown in Figure 1 The documented flow is an approximation of that which would be presented to the wing-flap juncture. The 30 and 60 degree conditions are representative of the direct interaction of the propulsion jet with the flap.

The data base used to establish the mechanics of jet-plate interaction is comprised of (1) surface static pressures measured at 0.1 inch increments in y at discrete x locations, (2) velocity measurements from 0.1 inch increments in y at discrete z positions and at integer x/d locations from 0 to 5. These data have been used to create quantitative measures of the important phenomena occurring in the flow. Analytical considerations have been used to develop these measures and to infer significant relationships or implications which demonstrate the nature of the phenomena occurring in this flow field.

The data base which serves as the primary resource for this

report was used in the First Annual Report to define measures of the flow field which were relevant to the externally blown flap problem. The measures and analyses of the present report are to define the basic character of the flow. This is considered to be complementary to the information of [1]. The identification of the oblique jet mechanics will contribute to several aspects of the externally blown flap development activity. Since the oblique jet impingement is the simplest form of the e.b.f. flow field, the basic aspects of the two flows will be similar. The mechanics identified in the present study can serve as the basis for the interpretation of the e.b.f. flow field response to the complicating factors of (1) an external streaming flow, (2) the curvature and a finite extent of the impingement plate (the airfoil), and (3) the presence of the deflecting flap. The mechanics identified herein will also allow an inference of the minimum spacing for multiple jets such that their flow fields show no significant interaction. The turbulent motions which are responsible for the acoustic emissions from the impingement region are related to the mean flow field characteristics identified herein. Subsequent studies of the turbulence structure will be guided by these results.

A general review of the literature pertinent to this problem was presented in [1] and no additional studies directly relevant to this problem have been identified. Consequently, a literature review will not be included herein. A brief description of the experimental facility is given in Section 2. Section 3 presents a comprehensive statement of the mechanics of the mean flow in the obliquely impinging axisymmetric jet. Specifically, Section 3.2 identifies the spreading and curvature effects; Section 3.3 considers the vorticity aspects of the motion; Section 3.4 identifies a generalized framework for the development of a computing scheme; Section 3.5 introduces the additional phenomena of the stagnation point and the y-component vorticity considerations; and Section 3.6. reiterates the important characteristics identified in the First Annual Report. Section 4 presents the detailed information which can be extracted from a consideration of the centerline pressure values. Section 5 presents a detailed consideration of the stagnation point: specifically, Section 5.2 presents the analytical considerations which demonstrate the consequences of separate physical locations for the stagnation and the maximum pressure points; Section 5.3, the experimental results; and Section 5.4, the relationship of the isotachs and the stagnation point. The appendices are

used to communicate the pertinent results available in [1].

2. EXPERIMENTAL FACILITY

The large volume of data considered in this report (and in [1]) is essentially made possible by the on-line IBM 1800 digital computer facility. The quantitative evaluation of the several measures of the experimental data, i.e. integrations and the preparation of level curves (isotachs and isobars) is made feasible by the availability of the hot-wire and pressure transducer data on punched cards. This data processing facility and the experimental flow system are described in detail in [1].

Two nozzle configurations were used to examine the influence of the initial conditions of the jet-plate interaction. A fully developed flow was developed in a 2 inch I.D., 12 ft long tube; this is referred to as the fully developed (f.d.) condition. A second nozzle was used to approximate a uniform (u) flow. A nominally flat-top velocity profile was created with this nozzle and these results will be referred to as the uniform (u) condition. Details of this nozzle are given in Figure 2 along with an exit velocity profile.

The velocity data which were used to create the isotach patterns (selected isotachs have been reproduced in Appendix A for reference purposes) were obtained with a single vertical wire (parallel with z). Consequently, these readings are most appropriately referred to as approximately (i.e. discounting pitch effects) the magnitude of the velocity in the x-y plane of the wire. Since the x-component is dominant except at the edge of the jet where $u(x, y, z) << u(x, o, z)$, the reasonable approximation is that the hot-wire reading is the x-component of velocity. This distinction is necessary when the various flux integrals are formed or when the comparison with analytical flux predictions, e.g. the Reichardt model are examined. See Sections 4.3 and 4.4 of [1], respectively, for these processed forms of the velocity data.

A special series of experiments was performed to investigate the stagnation point. These experiments involved the flow, traverse, and data processing systems described in [1]. The appropriate details of the test procedure will be covered along with the presentation of the experiments.

3. THE MAJOR PHENOMENA OF THE OBLIQUE IMPINGEMENT OF AN AXISYMMETRIC JET

3.1. Problem Statement

The purpose of this section is to consider the dominant phenomena which occur in the jet-plate interaction. Subsequent sections will consider appropriate details of the separate phenomena.

A useful conceptualization of the jet-plate interaction is based upon the no-penetration constraint imposed by the plate on the motion of the jet fluid. That is, there is no z component of velocity in the plane of the plate. In its absence, the jet fluid which would have penetrated through the plane of the plate will pass a given x location by spreading laterally along the surface of the plate and by increasing the area available for mass flux by causing the jet to curve upward. In the context of the kinematics of the problem, it is only necessary that the appropriate mass flux occurs across any x = constant location; the relative importance of spreading and curvature is dependent upon the dynamics of the jet-plate interaction. That is, the pressure distribution within the jet determines the curvature and spreading effects. It is not possible to identify a cause and effect relationship based upon the conservation of mass equation since this is not the governing phenomena for the problem.

The above considerations allow a somewhat more precise statement of the desired description of jet-plate interaction mechanics. Specifically, it should identify the magnitude of (1) the jet spreading and (2) the curvature of upward deflection effects; and identify the factors which are responsible for the selection process which results in the balance between these two effects. Clearly, the surface pressure distribution is mechanistically related to these two aspects of the motion in the jet. However, the surface pressure distribution itself is also an important aspect of the interaction process. Somewhat less obvious is the relationship between the surface pressure distribution and the x-component vorticity flux through an x = constant plane. This voriticity component is an important factor in the boundary layer control characteristics provided by the flow which bleeds between the lower surface of the airfoil and the flaps. The relationship between the pressure and the x-component vorticity will be examined in detail. The

curvature and spreading measures will first be examined; a model of the jet-plate interaction will then be presented.

3.2. Spreading and Curvature Effects in an Obliquely Impinging Jet

3.2.1. Jet spreading

From conservation of mass consideration, it is argued in Section 3.1 that the jet will both spread laterally along the surface of the plate, and curve upward. It is the purpose of this section to quantitatively evaluate these two effects.

In order to evaluate the spreading effects, some knowledge or reliable estimate of a reference or intersection contour of the jet on the plate is necessary. Such a reference contour can be established by the intersection of the free (uniform or fully developed) jet with an imaginary plane in the same relative position as the plate. More specifically, if one considers the axisymmetric surface defined by the condition $u(x, r)$ = constant, the intersection of this surface with the plane of the plate defines a contour. From the data of the present study, it is possible to quite accurately determine the functional relationship for the average $r(x)$ values such that $u(r,x)/u(o) = 0.1, 0.3, 0.5, 0.7, 0.9$; the average is based upon the large ensemble of experimental conditions with the following characteristics: (1) different α and h/d values, (2) an undisturbed isotach pattern, and (3) r values which are themselves smoothed over multiple y traverses. The 0.1 isotach ($u/u(o) = 0.1$) was chosen for this purpose since it best describes the outer boundary of the jet. Only the cases which demonstrated conservation of momentum were used to establish the radii of the 0.1 isotach for the five downstream x/d locations. Table 1 presents these $r(x)$ values. The linearly increasing values define a cone. The intersection of a cone with a plane defines an ellipse, parabola, or hyperbola depending upon the relative magnitudes of the cone and the intersection angles. These generated contours are termed free isotach intersections. The isobar and the free isotach intersection contours are shown in Figures 3 to 27. The shape of the two curves is remarkably similar which allows several measures of the interaction to be established. These are discussed below.

The zero isobar is considered to be a significant measure of the outer jet boundary. That is, the zero isobar can be interpreted as the

limiting extent of the dynamic effects in the flow. The small negative pressures beyond this isobar are a result of the entrainment effects. It is reasonable to assume, but it has not been shown, that the zero isobar is related to the stagnation line where the jet fluid, flowing laterally outward along the plate, meets the entrained fluid. The stagnation pressure of the entrained fluid would be approximately (clearly no greater than) the atmospheric value. Since the free isotach intersection characterizes the size of the undisturbed jet in the plane of the plate, the ratio of this contour width to that of the zero isobar can be used to describe the relative jet width. If the isobar family of curves were parametric, then the x location used to measure the relative width would not influence the magnitude of the ratio since the free isotach intersection is defined by a cone and a plane. The isobars, especially the zero isobar, are apparently not members of a single family; therefore, there is some influence of x-location on the relative width measure. The arbitrary decision was made to evaluate the width measurements at the x location of the maximum pressure. Since the zero free isotach grows at a different rate than the 0.1 free isotach, the distance from the appropriate point at the nozzle exit to the maximum pressure location is considered to be pertinent supplementary information. Table 2 presents the percent width and nozzle-to-plate data taken from the isobar contours.

The relatively constant percentage width values in Table 2 for the three to nine or twelve degree cases are considered to be quite significant. Contrary to what might be reasonably expected, it appears that there is very little systematic spreading of the jet with increasing α values. Considering a nominal value of 0.7 for the ratio of these two jet width measures, the majority of the data for both nozzles is within $\pm$ 0.05 or $\approx \pm$ 7 percent. Within this domain of cases, there are some second order systematic and non-systematic variations. The systematic deviations are dependent upon the increasing α values and probably the distance to the maximum pressure location. The scattered or non-systematic variations may be caused by geometric, flow, or measurement condition abnormalities (for example, an improper α value in the experiment or a zero drift in the pressure transducers). The significant deviations from this cluster about 0.7 are considered to be the u: α = 12, h/d = 1.5; α = 15, h/d = 1; α = 30, h/d = 2,3; and α = 60, h/d = 2 cases in which a

pronounced and systematic trend is observed where the width of the jet is considerably larger than the free isotach intersection. These differences in the width ratios are apparently related to the much different interaction phenomena. Specifically, based upon these ratios and based upon the available isotach information, the cases with a nominal width ratio of 0.7 appear to preserve the basic axisymmetric character of the jet and to confine the interaction phenomena to the region below the center of the jet. For the larger angle cases, the axisymmetric character of the jet is destroyed and the lateral flow along the surface of the plate is greatly enhanced as is the region of dynamic importance represented by the isobars.

Table 2 also presents the magnitude of the normalized pressure of the isobar which aligns with the 0.1 free isotach intersection contour. The pattern in which these values are essentially constant from three to twelve degrees is again apparent. A nominal value of 0.27 and second order variations are indicated by the table. The percentage variations between different cases in the magnitude of the isobar which aligns with the free isotach are larger than the percentage variations for the width measures. Also, the variations in the uniform cases are greater than in the fully developed cases and it can be observed that a pattern of larger-pressure for smaller-distance-to-impact is established. These are considered to be mechanistically related to the relatively steep velocity gradient at the edge of the uniform exit condition jet. The tabulated values are considered to be accurate within approximately ± 10 percent; the correspondence of free isotach/isobar contour was not exact and the equivalent isobar value often had to be obtained by interpolation.

Large deviations from the nominal 0.27 value are observed for the uniform cases of α = 15, 30, and 60. The significantly larger pressure magnitudes for these cases and the much smaller percentage width measures noted above both signify qualitatively different interaction phenomena compared to the smaller angles. These differences, then, are to be related to the strength of the interaction. The strong interaction destroys the axisymmetric character of the upper portion of the jet; a weak interaction does not.

A quite significant quantitative aspect of the isobar/free isotach alignment is that the factor of sin α, used to normalize the pressures,

allows the identification of a single nominal value over the range of α = 3 to 15 degrees. This is approximately a five-fold variation in the magnitude of sin α and hence a five-fold variation in the magnitude of the surface pressure. This simple dependence of the pressure on the jet angle would suggest that the z-component of the momentum flux is responsible for the elevated pressure in this region; this is in contrast to the centerline pressures which will show an additional effect associated with the overall jet and the local curvature effects.

The isobars represent a measure of the dynamic width of the jet. The isobar field could not be wider than the jet flow but the converse could occur. That is, the inertia of the lateral motion induced by the pressure gradient within the active region of the jet-plate interaction could move the jet fluid beyond the zero isobar. In this event, the isobar would under-estimate the jet width. Figures 28 to 30 have been prepared to compare the isotach contours with the lateral pressure distribution for the uniform cases: $\alpha = 3$, $h/d = 0.75$; $\alpha = 9$, $h/d = 1$; and $\alpha = 15$, $h/d = 1$. These figures demonstrate that the jet does spread beyond the zero isobar; however, the velocity beyond this boundary is relatively small. The above considerations are therefore restricted to the notion of the dynamic width of the jet.

3.2.2. Curvature of the jet

For the cases of weak jet-plate interaction, there are only minor changes in the spread as a function of α and h/d. Consequently, it is concluded that any significant differences between cases will be manifest in the curvature of the jet. The curvature of the entire jet can be computed from the surface pressure values. The assumptions and analytical considerations which make this possible are identified in the following; the curvature magnitudes will be examined following the analysis.

Special experimental tests and an estimate of the maximum plausible influence of the static pressure was used in [1] to demonstrate that the x-component momentum flux was essentially constant for all cases. As a consequence of this, control volume momentum and moment-of-momentum analyses may be used to define the height above the plate $z_m(x)$ of the center of momentum flux $J_x (\cong J(o) \cos \alpha = \text{constant})$. The quantity $z_m(x)$ can be considered to be the elevation of the jet (as if it were concentrated along a line). The curvature of the jet is given in terms of the curvature of $z_m(x)$ by the relationship

$$K = \frac{d^2 z_m/dx^2}{[1 + (dz_m/dx)^2]^{3/2}} \tag{1}$$

The expression for $z_m(x)$ developed in [1] will be used to evaluate the curvature. The expression from [1] was made incomplete by the exclusion of a term which accounted for an entrainment effect. The corrected analysis is presented in Appendix B and the corrected form is

$$\frac{z_m}{d} = \frac{h}{d} + \frac{x}{d}\frac{F_p}{J(o)\cos\alpha} - \frac{x}{d}\tan\alpha - \frac{1}{J(o)\cos\alpha}\int_{A_{plate}} \frac{x}{d}\, p dA$$

$$-\frac{1}{2} J(o)\cos\alpha \left\{ \int_{A_{entrainment}} \rho Q_e^2 [z\hat{n}\cdot\hat{i} - x\hat{n}\cdot\hat{k}]dA + \int_{A_{entrainment}} \rho Q_e^2 \hat{k}\cdot\hat{n}\, dA \right\} \tag{2}$$

where Q_e is the entrainment velocity at the control surface and the control surface is defined in Figure 31. The bracketed term is shown to be small for $x/d \leq 5$ in Appendix B. The derivatives for the curvature are evaluated as

$$\frac{dz_m}{dx} = \frac{F_p}{J(o)\cos\alpha} + \frac{x}{d}\frac{dF_p/J(o)\cos\alpha}{dx/d} - \tan\alpha - \frac{x}{d}\int_{-\infty}^{\infty} p dy \frac{1}{J(o)\cos\alpha} \tag{3a}$$

but since $dF_p/dx = \int_{-\infty}^{\infty} p dy$,

$$\frac{dz_m}{dx} = \frac{1}{J(o)\cos\alpha} - \tan\alpha \tag{3b}$$

and

$$\frac{d^2 z_m}{dx^2} = \frac{1}{J(o)\cos\alpha}\int_{-\infty}^{\infty} p dy. \tag{4}$$

Consequently

$$K = \frac{\frac{1}{J(o)\cos\alpha}\int_{-\infty}^{\infty} p\,dy}{\left\{\left(\frac{F_p}{J(o)\cos\alpha} - \tan\alpha\right)^2 + 1\right\}^{3/2}} \tag{5}$$

Although the curvature involves the second derivative of z_m, it can be evaluated in terms of quantities which are quite accurately known, as shown by (5).

An approximate relationship involving K is pertinent to the interpretation of the curvature data; specifically, since the maximum magnitude of dz_m/dx is $-\tan\alpha$, the largest coefficient multiplying the numerator of K is $[1+\tan^2\alpha]^{-3/2}$. Since $0.9 \leq (1+\tan^2\alpha)^{-3/2} \leq 1$ for $0 \leq \alpha \leq 15$ degrees, the variation of the denominator is neglected and $[1+\tan^2\alpha]^{3/2} \approx 1$ is considered to represent a satisfactory assumption. Consequently,

$$K \cong d^2z_m/dx^2 \tag{6}$$

The area under the K(x) curve is then

$$\begin{aligned} \text{Area under } K(x) &\cong \int_0^x \frac{d}{dx}\left(\frac{dz_m}{dx}\right) dx \\ &\cong \left.\frac{dz_m}{dx}\right]_x - \left.\frac{dz_m}{dx}\right]_0 \\ &\cong \tan\alpha + \left.\frac{dz_m}{dx}\right]_x \end{aligned} \tag{7}$$

Since $dz_m(\infty)/dx = 0$, the total area under the K(x) curve is approximately $\tan\alpha$. This may be used as a reference condition to compare the K(x) curves for a given α as a function of h/d.

A second general observation may be made concerning the K(x) distributions. Unless the plate influences the jet at the exit of the nozzle, the curvature will vary from zero to a negative value (if the entrainment effect is important) to positive values (for a sufficient duration to allow the area under the K curve to be $\approx \tan\alpha$) and return to zero for large downstream distances. The centerline pressure will have the same general character; however, the pressure may be influenced by the local

effects in the flow whereas the curvature is a measure of the overall behavior of the jet.

The curvature and the centerline pressure are presented together in Figures 32 to 45. The comparison of these two distributions is considered to offer an effective measure of the curvature effects. If the two curves have the same character, it is concluded that the local curvature effects are not very important and that the jet is essentially turned en masse. The extent to which the two curves have a different character is used as an indication of the presence of local curvature or a relatively rapid jet approach to the plate. A shift in the x/d location has been applied to these (and subsequent plots) to align the 0.1 free isotach intersection with the x/d = 0 location. This allows a better visual comparison between cases. The $\Delta x/d$ values to accomplish the shift are presented in Table 2.

The most important characteristic of these data is their slope as a function of the streamwise distance. The slopes were not evaluated since the usual errors associated with differentiation of data would have been encountered; the reader is asked to mentally compare the slopes of the K and p (x, 0, 0) curves. The trend indicated by the uniform, α = 3 degree cases (h/d = 0.75 and 1) is characteristic of all the data. That is, the p(x, 0, 0) distribution reaches a maximum at a smaller x/d than does K(x) and this difference between the two curves is less pronounced as h/d increases. This trend is quite pronounced for the fully developed, α = 3 degree cases. The condition wherein the centerline pressure reaches a maximum value before the curvature, reflects the dependence of p(x, 0, 0) on the local flow condition. As h/d is decreased, the velocity gradients of the flow approaching the plate are increased and the surface pressure required to turn the flow locally is increased. The quantitative character of this observation is demonstrated by the plots.

Figures 44 to 55 present a comparison of the curvatures for various h/d values at a given α. These plots are prepared such that the 0.1 free isotach would be shifted to x = 0. The purpose of this comparison is to demonstrate the accommodation of the curvature to the different geometries. That is, the jet curves more rapidly for smaller h/d values.

3.2.3. Summary of spreading/curvature effect

The original question addressed in this section can now be answered.

It was noted that the constraints imposed by the conservation of mass required that the jet spread laterally along the plate and/or be curved upward because of the no penetration condition imposed by the plate. The relative spreading measures indicate that for the relatively small angles, $\alpha \lesssim 12$ degrees, the lateral spread of the jet is a second order effect. For these same cases, the curvature is a strongly varying function of α and h/d; that is, the jet primarily responds to the presence of the plate by turning upward.

The larger angle cases appear to be qualitatively different. The upper portion of the jet does not retain its axisymmetric character and the relative width of the zero isobar to the 0.1 free isotach is increased with respect to the smaller angle cases. The pressure distributions show a more peaked character with the relatively large maxima apparently accounting for the strong turning of the fluid at the upstream edge of the jet.

3.3. Vorticity Considerations

The upward deflection of the jet can be expressed in terms of the deviation of the z-component velocities in the jet from the equivalent values which would be realized if the plate were not present. Similarly, the spreading of the jet is associated with the excess y-component velocities. The detailed velocity distributions are expected to be governed by the three-dimensional pressure distribution above the plate and tailored by the Reynolds shear stress distribution. The consideration of the jet-plate interaction mechanics based upon these aspects is reasonable in the context of the nature of the flow but such a description is quite difficult to relate to the extant or anticipated experimental data; i.e., there is a lack of p(x, y, z) data. An equivalent, but conceptually quite different approach is to consider the flow in terms of the vorticity processes occurring in the jet-plate interaction. This has the implicit benefit that the important x-component vorticity will be directly involved in the description of the problem. It has the major benefit that the three-dimensional pressure distribution in the jet flow does not enter into the description of the problem; rather, the surface pressure distribution, which is accurately known, enters the description as a source of vorticity. These considerations require the control volume description of the vorticity equations; these relationships are developed below.

The Navier-Stokes equations for an incompressible flow can be operated upon to create the vorticity transport equation; specifically,

$$\nabla \times \left[\frac{D\mathbf{u}}{Dt} = -\frac{1}{\rho} \nabla p + \nu \nabla^2 \mathbf{u} \right] = \left[\frac{D\boldsymbol{\omega}}{Dt} = \boldsymbol{\omega} \cdot \nabla \mathbf{u} + \nu \nabla^2 \boldsymbol{\omega} \right] \tag{8}$$

Performing a volume integral of this differential equation for a motion which is steady in its time mean quantities and applying the Gauss Theorem to transform volume integrals of divergence terms into surface integrals yields (note that $(\overline{\ })$ denotes a time averaged value)

$$\int_{c.s.} \overline{\boldsymbol{\omega}\, \mathbf{u}} \cdot \hat{n}\, dA = \int_{c.v.} \overline{\boldsymbol{\omega} \cdot \nabla \mathbf{u}}\, dV + \int_{c.s.} \nu\, \nabla \overline{\boldsymbol{\omega}} \cdot \hat{n}\, dA. \tag{9}$$

The term on the left is the net flux of the vorticity from the control volume by the convective action of the velocity field, ($\overline{\boldsymbol{\omega}\, \mathbf{u}} \cdot \hat{n} = \overline{\boldsymbol{\omega}}\, \overline{\mathbf{u}} \cdot \hat{n} + \overline{\boldsymbol{\omega}'\, \mathbf{u}'} \cdot \hat{n}$ where $\boldsymbol{\omega}'$ and $\mathbf{u}'$ are the turbulent fluctuations about the mean). The first term on the right hand side of equation 9 is the production of vorticity by the amplification effect of stretching or reorienting vortex filaments. The third term can be expected to be important <u>only</u> at a solid surface where the viscous terms are important in an otherwise turbulent transport dominated flow field. The viscous term may be expressed in terms of the surface pressure gradients; this is developed in the following.

$$\frac{\partial \boldsymbol{\omega}}{\partial n} = i \frac{\partial \omega_x}{\partial z} + j \frac{\omega_y}{\partial y} + k \frac{\partial \omega_z}{\partial z} \tag{10}$$

Since $\omega_x = (\partial x/\partial y - \partial v/\partial z)$ and $\omega_y = (\partial u/\partial z - \partial v/\partial x)$, the vorticity terms at the surface of the plate may be written as

$$\omega_x(x, y, 0) = -\left.\frac{\partial v}{\partial z}\right|_{z=0} \tag{11a}$$

$$\omega_y(x, y, 0) = \left.\frac{\partial u}{\partial z}\right|_{z=0} \tag{11b}$$

These quantities may, in turn, be expressed in terms of the surface pressure distributions as

$$\left.\frac{Dv}{Dt}\right|_{z=0} = 0 = -\frac{1}{\rho} \left.\frac{\partial p}{\partial y}\right|_{z=0} + \nu \left.\frac{\partial^2 v}{\partial z^2}\right|_{z=0}$$

or

$$\frac{1}{\rho}\frac{\partial p}{\partial y}\bigg|_{z=0} = \nu \frac{\partial}{\partial z}\left(\frac{\partial v}{\partial z}\right)\bigg|_{z=0}$$

$$= -\nu \frac{\partial}{\partial z}\,\omega_x\bigg|_{z=0} \tag{12a}$$

and

$$\frac{Du}{Dt}\bigg|_{z=0} = 0 = -\frac{1}{\rho}\frac{\partial p}{\partial x}\bigg|_{z=0} + \nu \frac{\partial^2 u}{\partial z^2}\bigg|_{z=0}$$

or

$$\frac{1}{\rho}\frac{\partial p}{\partial x}\bigg|_{z=0} = \nu \frac{\partial}{\partial z}\left(\frac{\partial u}{\partial z}\right)\bigg|_{z=0}$$

$$= \nu \frac{\partial}{\partial z}\,\omega_y\bigg|_{z=0} \tag{12b}$$

Consequently, using (12a) and (12b) in (9) and noting that a negative sign will precede the last term since $\nabla \mathbf{u} \cdot n < 0$,

$$\int_{c.s.} \overline{\omega \mathbf{u} \cdot \hat{n}}\, dA = \int_{c.v.} \overline{\mathbf{u} \cdot \Delta \mathbf{u}}\, d\forall + \hat{i}\int_{A_{plate}} \left(\frac{1}{\rho}\frac{\partial p}{\partial y}\right) dA$$

$$- \hat{j}\int_{A_{plate}} \left(\frac{1}{\rho}\frac{\partial p}{\partial x}\right) dA - \hat{k}\int_{A_{plate}} \nu \frac{\partial \omega_z}{\partial z}\, dA \tag{13}$$

The mathematical framework for the model of the jet-plate interaction is represented by equation 13. The physical characteristics required of the model can be inferred by an examination of the data already presented. The pertinent features of these data are considered in the following.

In the description of the physical nature of the jet-plate interaction, it will be useful to speak in general terms about a "non-destructive" interaction between the jet and the plate. The term non-destructive is to imply that the upper portion of the jet retains its axisymmetric character and the influence of the plate is confined to a portion of the flow near the plate. The isotachs of Figures 28 to 30, the isotachs of

Appendix A and the photographs of the dusty jet, Figures 3b and c of [1] all demonstrate this effect. This non-destructive case is distinguished from the condition in which the approach to the plate is so abrupt that no portion of the jet retains its axisymmetric form. The influence of these two interaction conditions on the spread/curvature isotach patterns ($\alpha \leq 15$ degrees) reveals that within the x/d range investigated ($x/d \leq 5$) the non-destructive description is applicable to all cases except $\alpha = 15$, $h/d = 1$, $x/d = 4, 5$ and possibly $\alpha = 12$, $h/d = 1$, $x/d = 5$. The projected centerline of the jet passes through the plane of the plate at $x/d = 3.75$ and 4.75 for these two cases respectively. It is not possible to determine whether the non-destructive character is maintained for large x/d values where the projected centerline of the shallower angle cases would penetrate the plane of the plate. However, one could reasonably anticipate that for sufficiently small α and sufficiently large h/d, the curvature of the jet would allow the oblique jet to approach the character of an axisymmetric, parallel flow, wall jet. In this regard, the three-dimensional wall jet studies by Sforza and Herbst [2] are quite instructive. The upper portion of the isotach pattern of a rectangular wall jet does approach an axisymmetric form at sufficiently large downstream distances; hence, the same behavior is reasonable for the shallow angle, obliquely impinging jet.

The conceptual model of the jet-plate interaction is based upon vorticity considerations and will be developed from the observations of the non-destructive interaction cases. The larger angle cases are more complex and additional effects must be included for their description.

For the streamwise domain in which the jet-plate interaction is non-destructive the influence of the plate on the jet is manifest in two rather distinct regions. The phenomena occurring in these regions allow them to be distinguished from each other and from the approaching jet. In the immediate vicinity of the plate $0 \leq z < \delta z$ (where $\delta z/d << 1$) the velocity distribution can apparently be characterized by isotachs which are nearly parallel to the plate and quite closely spaced. Such a condition is inferred from the isotach presentations of [1], see Appendix A, in which the experimental data of the y traverses indicate quite large velocities near the surface of the plate, and it is shown schematically in Figure 56. Since each lower valued isotach must lie between the measured isotach location and the plane of the plate, it can be inferred that a very close

isotach spacing exists in this region of the flow. The region of the flow defined by $0 \leq z \leq \delta z$ will be termed the <u>near wall</u> region. The second region lies between the near wall region and the axisymmetric portion of the flow. The boundary between the upper portion (of the second region) and the axisymmetric jet is diffuse, the two regions rather merge together. For convenience, this will be termed the <u>buffer region</u>.

The conditions leading to the establishment of a near wall region are easily visualized in terms of equation 13 and the recognition that the isobar patterns of Figures 3 to 27 are reasonable manifestations of the jet-plate interaction. That is, with a pressure distribution such that $p(x, 0, 0)$ forms a maximum in the $p(y)$ distribution at a given x location, $\partial p/\partial y$ will be such as to cause a flux of x-component vorticity into the flow. Also, the ω_y vorticity present at the surface, as a result of the jet flow over the plate, will experience a $\partial u/\partial y$ reorientation effect such that the terms $\omega_y \partial u/\partial y$ and $1/\rho \ \partial p/\partial y$ of (7) both cause a flux of ω_x at a given x location. (The signs are $-\omega_x$ for $y > 0$ and $+\omega_x$ for $y < 0$.) It is reasonable to expect that both of these effects will only influence the flow near the plate. The net effect is shown by the particular form of (13) for the spatial region defined by the limits on the integrals

$$\int_0^\infty \int_0^{\delta z} \overline{\omega_x u} \, dzdy \Big|_x = \int_0^{\delta z} \int_0^\infty \int_0^x \overline{\omega_y \partial u/\partial y} \, dxdy + \int_0^\infty \int_0^x \frac{1}{\rho} \frac{\partial p}{\partial y} \, dxdy \quad (14)$$

where the ω_x entering the control volume at $x = 0$ is considered to be zero $\omega_x \partial u/\partial x << \omega_y \partial u/\partial u$, and the signs on the r.h.s. terms indicate that negative ω_x is carried out of the control volume.

One of the contributions of equation (13) and the vorticity considerations is that the localized nature of these effects is easily accepted. That is, the identification of the vorticity transport effects as the controlling phenomenon makes the existence of a near wall region a reasonable result.

Figure 56 also shows the buffer zone; this observed region is similarly compatible with a description of the flow in which vorticity transport effects govern the motion. The ω_θ of the approach flow is essentially converted to ω_y in the near wall region; this, in turn, results in some production of ω_x in the near wall region as noted above. The vorticity in the axisymmetric portion remains essentially unchanged. The

juncture of these two regions, which occurs at δ_z and increasing y values for decreasing isotach magnitudes, results in a large and localized production of ω_x. That is, the ω_x production term $\omega_\theta \, \partial u/\partial \theta$ is clearly large at the location where the isotach makes a sharp bend to pass between the plate and the "undisturbed" jet. This ω_x vorticity is of opposite sign to that produced by the two effects operative in the nearwall region. The upper portion of the buffer region is not sharply defined. The isotachs change gradually from their circular shape in the axisymmetric region. This characteristic supports the implicit feature of the model in which the governing effects are concentrated near the surface. The upper portion of the buffer region is the (passive) effect caused by the vortex reorientation near the plate.

The utilization of the vorticity transport equation has allowed rational explanations for the observed near wall, buffer and axisymmetric regions of the flow field. The same observations could be related to the momentum equations; however, the relationship of the acceleration, pressure gradient and net shear stress to the observed three regions, with their particular spatial extents, would have to be argued in such a manner that the two are simply compatible. It does not seem possible to provide an apriori argument for the qualitative nature of a pressure distribution which would create a maximum y-component velocity quite near the surface and leave the central core of the flow in an axisymmetric form.

3.4. The Development of an Analytical Model

In addition to its use in describing the physical nature of the jet-plate interaction, the model presented in 3.3 is considered to offer an excellent framework for the development of a numerical computation scheme to describe this flow. Lighthill [3] has presented several arguments in favor of a calculation technique based upon the governing equations for vorticity and not velocity. The diffusive nature of the vorticity equations as opposed to the action of a pressure at a distance allows a forward stepping solution to be more easily developed. It is anticipated that such a consideration would be most important for the present problem. As the jet approaches and impacts the plate, a description which allows the interaction to be calculated on the basis of the behavior at the surface and its subsequent influence on the interior

of the flow field is clearly superior to the alternative formulation requiring a construction of the three-dimensional pressure field with its consequent upstream effect. The development of such a numerical computation scheme is simply noted here; there is no immediate activity nor plan to pursue such a development.

3.5. Additional Phenomena

The principal or governing phenomena of the flow field are represented by the discussion in Section 3.3; however, there are additional features of the flow which are considered significant. The location and character of the stagnation point and some quantitative aspects of the flux of ω_y vorticity into the flow are considered in this section.

The vorticity considerations (3.3) tacitly assumed that the vorticity above the plate had a positive ω_y component, i.e., the flow in the jet at $(x, y, \delta z)$ is in the streamwise direction. This is valid for the region downstream of the stagnation point $(x_s, 0, 0)$. The stagnation point will occur at $y=0$ from the symmetry of the problem; the symmetry of the problem also demands that $\bar{u}\ (x_j < x < x_s,\ 0,\ \delta z) < 0$ (where δz is a small z value) and x_j is the upstream boundary of the jet fluid near the plate. This region of reversed flow need not exist instantaneously if the stagnation point moves about laterally but the mean value of u must have this character. The three-dimensional pattern near x_s is not easily visualized since $u > 0$ can be expected at $(x_j < x < x_s,\ \pm\delta y,\ \delta z)$ for relatively small δy. From the isobars, it is clear that this region of reversed flow is relatively extensive if the stagnation point occurs at the maximum pressure location. The stagnation point for an obliquely impinging axisymmetric jet is <u>not</u> at the location of the maximum pressure; it is near the upstream edge of the interaction region defined by the isobar pattern. The support for this observation is given in a later section; its implications for the flow model are of concern here.

The factors which cause the flow to select the location of the stagnation point are apparently the geometric condition that the stagnation streamline be located near the lower edge of the jet and the accommodation of the vorticity in the approach flow to that about the stagnation point. For example, the vorticity at the stagnation point is zero but its x gradient influences the orientation of the stagnation

streamline. Directly upstream of the stagnation point the vorticity is negative and of opposite sign to that of the approach flow. Directly downstream, the vorticity is positive and in the same sense as that of the approach flow. The selection of the stagnation point is clearly a complicated physical process and it would be a difficult thing to predict. It is unclear what difficulties this might pose for the numerical calculation scheme discussed in 3.4 in terms of formulating the forward stepping scheme.

Only the x-component vorticity was considered in Section 3.3 since the qualitative behavior of the flow can be described in terms of this variable. A quantitative description would necessitate an accurate assessment of ω_y as well since this component does contribute to ω_x in the form of $\omega_y \partial u/\partial y$.

The isobar patterns clearly show that the dominant vorticity flux into the flow is ω_x; however, along the centerline only ω_y is introduced through the surface. It is possible to compare the magnitude of the flux through the plate to the flux through a small section of δz height at some x location. The analytical considerations for this are shown below.

The flux per unit width of ω_y through an area of height δz at any x location can be expressed as

$$\int_0^{\delta z} \bar{\omega}_y \, \bar{u} \, dz \cong \int_0^{\delta z} \bar{u} \frac{\partial \bar{u}}{\partial z} dz$$

$$= \int_0^{\delta z} \frac{1}{2} \frac{\partial}{\partial z} \bar{u}^2 \, dz$$

$$= \frac{\bar{u}^2}{2} \tag{15}$$

The flux of ω_y per unit width through the plate surface from x = 0 to x = x is given as (from (9) and (12b))

$$\int_0^x \nu \frac{\partial}{\partial z} \omega_y \, dx = -\int_0^x \frac{1}{\rho} \frac{\partial p}{\partial x} dx = -\frac{1}{\rho} [p(x, 0, 0) - p(0, 0, 0)] \tag{16}$$

These two quantities can be normalized using the centerline velocity at

the exit plane of the jet and their ratio can be formed to demonstrate the relative magnitude of the vorticity flux through the surface as compared with that in the flow field. It should be noted that the two are of opposite sign for $x_s \leq x \leq x$ (max pressure)

$$\frac{\text{vorticity flux through surface from 0 to x}}{\text{vorticity flux through area of height } \delta z \text{ at x}} =$$

$$\frac{2[p(0,0,0) - p(x,0,0)]/\rho u^2(o)}{\bar{u}(x,0,\delta z)^2/u^2(o)} \tag{17}$$

Measurements of $p(x,0,0)$ and $\bar{u}(x,0,\delta z)$ were made to evaluate the location of the stagnation point; the measurements and the conclusions regarding the stagnation point location will be presented in a later section. The pertinent results from this study are cited in Table 3 to evaluate the ratio given by (17).

Table 3. Ratio of ω_y vorticity flux through the plate to the vorticity flux through a small height at the x location of the maximum pressure. Uniform nozzle exit condition

α	h/d	x/d*	$\delta z/d$	$\{\frac{2}{\rho}[p(x,0,0)-p(0,0,0)\}/\{u(x,0,\delta z)^2\}$
3	1	4.08	0.0328	14.54 / 46.2 = 0.315
9	1	2.13	---	27.4 / 49.9 = 0.55
15	1	1.25	---	46.2 / 63.6 = 0.73

These ratios show that a significant amount of $-\omega_y$ is added to the $+\omega_y$ vorticity near the plate for all cases. The vorticity so added increases rather strongly as α increases; this is reasonable based upon the observation of the centerline pressure relationship to the overall and local jet curvature effects. The data shows that the $+\omega_y$ vorticity flux through δz increases in magnitude even as the $-\omega_y$ vorticity flux increases. This result is attributed to the importance of the production term due to stretching $(\omega_y \partial v/\partial y)$. Consequently the production term is quite important in the description of the vorticity processes occurring in the flow. Since

$\partial v/\partial y$ is related to the ω_x distribution, i.e., $v(x, y, \delta z) = [\partial v(x, y, 0)/\partial z]\delta z = -\omega_x \delta z$, an analytical model would have to consider the simultaneous solution of the x and y components of vorticity.

3.6. Phenomena Identified in the First Annual Report

Several important phenomena were identified and presented in [1]. A summary of these phenomena is presented here for completeness.

A control volume as shown in Figure 31, with boundaries extending over the exit plane of the jet and the downstream plane of constant x, the plane of the plate, and the sides of the flow field in the entrainment region will be used for this discussion. A special experiment to evaluate the shear force on the plate and an evaluation of the maximum probable pressure force acting in the negative x direction have been used to show that the x-component momentum flux is essentially constant for the oblique jet impingement problem (see [1]).

The impingement process has the effect of suppressing the entrainment of mass into the jet flow. The constant momentum flux combined with the decreased mass flux cause a decreased rate of energy dissipation. Analytically, this is described as a constant value of $\int u^2\, dA$ and a less-than normal increase in $\int u\, dA$ which results in a less-than-normal decrease in $\int u^3\, dA$, where the integration is over a plane normal to the axis of the jet. Mechanistically, it is inferred that the decreasing energy flux is a measure of the work done by the jet fluid to accelerate the ambient fluid as it is entrained into the jet flow. Since the plate inhibits this entrainment process, the relatively high velocity fluid in the jet is protected from the decelerating effects of the entrainment process and the only energy decrement incurred in this region is that associated with the boundary layer in the near wall region ($0 \le z \le \delta z$). The mass and energy flux values are shown in Appendix C. The data for the uniform and fully developed nozzle conditions are shown separately and the data are segregated with respect to how well the measured x-component momentum flux agrees with the quantity $J(o)\cos\theta$. The data for which the measured momentum flux is within three percent of that at the exit plane is considered to be quantitatively valid. That which differs by more than three percent from the constant value is considered to be qualitatively instructive in that it shows the appropriate trends for

the mass and energy flux values.

An interesting difference between the uniform and fully developed exit plane conditions is the greater rate of entrainment of ambient fluid for the fully developed condition. It is inferred that this greater entrainment rate is related to the large scale motions in the initial region of this flow. The mass rates of flow for the two nozzles of the present study and for several other studies which have been reported are also presented in Appendix C. A comprehensive study of the initial condition effects on the near field of an axisymmetric jet is presently being conducted as a part of the continuing activity under this grant.

The jet-plate interaction can be considered complete in some sense when the total z-component momentum of the initial jet is destroyed. Therefore, the degree of completeness of the interaction is shown in terms of the ratio of the net force on the plate to the initial z-component momentum flux. Curves of $\int_0^x \int_{-\infty}^{\infty} p \, dy \, dx / J_z(o)$ are presented in [1]. Alternatively (and less graphically) the z-component momentum flux, normalized by the initial z-component momentum flux, provides a measure of the degree of completeness of the interaction. The tabular representation of these values taken directly from [1] is presented in Appendix D.

4. THE CENTERLINE PRESSURE DISTRIBUTIONS

From a mechanistic viewpoint, the surface pressure is the agent which causes the spreading and jet curvature imposed upon the jet by the no-penetration condition through the plane of the plate. On this basis, the only apriori constraint on the surface pressures is that the pressure integral over the plate surface is equal to the z-component momentum flux from the jet. One aspect of the total pressure distribution is the pressure along the line (x, 0, 0); that is, the centerline pressure distribution. In Section 3.2 the centerline pressures were compared with the curvature of the jet to demonstrate the local, in addition to the global, effects of the curvature. The essential point is that the centerline pressure distribution is governed by the geometric and, to some degree, the initial flow structure conditions of the jet. In this sense it is an effect, the no-penetration condition is the cause.

A different condition exists for the streamwise vorticity. The centerline pressure can be interpreted as the cause of the amount of x-component vorticity added to the flow by the "flux through the plate surface." Equation 18 provides the basis for this statement; specifically,

$$\omega_x \text{ introduced through the differential area dxdy via the pressure distribution} = \nu \frac{\partial \omega_x}{\partial z} \, dydx = -\frac{1}{\rho} \frac{\partial p}{\partial y} dydx \quad (18)$$

The flux through a given area of the plate cannot be directly related to the flux through a specific y-z area at some x location. The reason for this is that the velocity field near the plate will convect and the velocity gradients will amplify or reorient vorticity which enters the flow field through this mechanism. However, it is possible to identify the total vorticity which enters the flow and to attach some meaning to this measure of the ω_x vorticity flux. Consequently, (18) is integrated over the region from y=0 to + (or -) ∞ and from 0 to x. The resulting value is that total ω_x introduced into the flow via this mechanism; specifically

$$\omega_x \text{ introduced via the pressure distribution} = -\int_0^x \int_0^y \frac{1}{\rho} \frac{\partial p}{\partial y} \, dy \, dx$$

$$= -\int_0^x \frac{1}{\rho} \left[p(x, \infty, 0) - p(x, 0, 0) \right] dx$$

$$= +\int_0^x \frac{p(x, 0, 0)}{\rho} \, dx \quad (19)$$

Equation 19 demonstrates the importance of the centerline pressure distribtuion to the flux of ω_x. These integrated values are presented in a composite form in Figure 57. Only the fully developed cases are shown for $\alpha < 15$ degrees, the uniform ones are essentially the same.

The strong dependence of the vorticity flux upon α, and h/d for a given α, is evident. The strong differences shown for the various α and h/d cases suggest that the flows near the plate surface are strongly dependent upon these two parameters. However, the data of

Table 2 show that the width of the flow field and the pressures in the neighborhood of the 0.1 free isotach intersection are weakly dependent upon these two parameters for the non-destructive interaction cases. Therefore, it is inferred that the differences in the flow structure associated with the flux of ω_x are confined to the central region of the flow field.

5. THE STAGNATION POINT

5.1. General Considerations

An important characteristic of the oblique jet impingement which must be established for a complete description of the flow field is the location of, and local behavior around, the stagnation point. The identification of the stagnation point characteristic is considered to be of particular importance for those characteristics which depend upon the details of the flow field near the surface such as the heat transfer, acoustic noise generation, and the production of streamwise vorticity.

The stagnation streamline is defined as the locus of points everywhere tangent to the velocity field with a terminus on the impact plate. The stagnation point is the location of the terminal point. The possibility of a finite length stagnation line will be suggested by the experimental data and it cannot be excluded by analytical considerations. The possibility of a finite length stagnation line is also suggested by the following considerations. An infinitely long stagnation line exists in a two-dimensional flow and a stagnation point or circular stagnation line exists in an axisymmetric flow. Similarly, an open conduit of any shape placed with its axis parallel to a uniform stream will result in a closed, stagnation line around its upstream circumference.
The three-dimensional flow may be qualitatively different from the axisymmetric or two-dimensional condition. For example, consider the open conduit placed in a uniform stream and consider a sawcut to be made through the surface parallel to the axis. If the only possible stagnation states are a point or a closed line curve, then a single stagnation point would have to exist opposite the sawcut. Since the flow will still pass inside and outside the contour defined by the previously closed body, the symmetry would demand that an azimuthal flow exist

from the stagnation point, around the upstream surface and exhaust down the gap of the sawcut. The alternative is to conceptualize a three-dimensional stagnation line extending part way around the upstream surface. This aside from the oblique jet impingement problem is to demonstrate, by analogy, the possibility of a finite length stagnation line. The oblique jet impingement is a three-dimensional flow. The possibility of a finite length, non-closed, stagnation line would seem to exist.

Another characteristic of the stagnation point is its relationship to the location of the maximum pressure point. For a vertical (α = 90 degrees) jet impingement condition, it is clear that a stagnation point exists at the terminus of the center streamline and at the location of the maximum pressure. The centerline pressure data shown in the previously discussed figures indicate that the maximum plate pressure is not at the projected location of the center streamline; these figures also suggest that the maximum pressure may not be located at the stagnation point. The analytical considerations which can be made for the stagnation point are presented in the next subsection. An experimental technique to evaluate the stagnation condition and the results of this evaluation for three cases are presented in this section.

5.2. Analytical Considerations*

The equations of motion (Navier-Stokes and continuity) can be evaluated in the neighborhood of the stagnation point in order to establish certain characteristics of the stagnation streamline. These analytical considerations are presented in this subsection (5.2).

5.2.1. The orientation of the stagnation streamline

Let (δx, 0, δz) be the coordinates of a position on the stagnation streamline. The stagnation point will be designated (0,0,0) for the purposes of this analysis and the symbol δs will designate an incremental

*The remainder of Section 5 is adapted from the second semi annual report [4]. A portion of the analytical considerations was incomplete although the results were not affected and the experimental data have been more completely analyzed. For these reasons, and because of the limited distribution of the semi annual report, these subsections are repeated herein.

length along the streamline where $\delta s = [\delta x^2 + \delta z^2]^{1/2}$ and $\delta x/d \sim \delta z/d << 1$ is understood. The slope of the stagnation streamline at the stagnation point is given as

$$\text{slope of stagnation streamline at } (0,0,0) = \lim_{\delta s \to 0} \frac{\delta z}{\delta x} \tag{20}$$

and this slope can be expressed in terms of the velocity field as

$$\lim_{\delta s \to 0} \frac{\delta z}{\delta x} = \lim_{\delta s \to 0} \frac{w(\delta x, 0, \delta z)}{u(\delta x, 0, \delta z)} \tag{21}$$

Assuming that the u and w components are analytic functions, the limit of the velocity ratio can be expressed in terms of the Taylor expansion of the velocities. Only the lowest order, non-zero terms of the expansion need be retained in anticipation of taking the limit. All partial derivatives are understood to be evaluated at (0, 0, 0); $\partial u/\partial x = \partial w/\partial x = 0$ because of the no slip condition and $\partial w/\partial z = 0$ by continuity.

$$\lim_{\delta x \to 0} \frac{w(\delta x, 0, \delta z)}{u(\delta x, 0, \delta z)} = \frac{\frac{\delta z^2}{2} \frac{\partial^2 w}{\partial z^2} + \ldots}{\delta z \frac{\partial u}{\partial z} + \frac{\delta z^2}{2} \frac{\partial^2 u}{\partial z^2} + \delta x \delta z \frac{\partial^2 u}{\partial x \partial z} + \ldots} \tag{22}$$

$$= 0 \text{ for } \partial u/\partial z \neq 0 \tag{22a}$$

$$>, <, = \quad 0 \text{ for } \partial u/\partial z = 0 \tag{22b}$$

Condition (22a) shows that if the vorticity at a point is non-zero then the streamline at that point (in the direction perpendicular to the vorticity) lies in the plane of the plate and hence cannot be a stagnation streamline. Equation 22 can be operated upon to provide a more easily interpreted form when (22b) is applicable. Dividing by $\delta x \delta z$ yields

$$\lim_{\delta s \to 0} \frac{\delta z}{\delta x} = \frac{\frac{1}{2} \frac{\delta z}{\delta x} \frac{\partial^2 w}{\partial z^2} + \ldots}{\frac{1}{2} \frac{\delta z}{\delta x} \frac{\partial^2 u}{\partial x^2} + \frac{\partial^2 u}{\partial x \partial z} + \ldots} \tag{23}$$

The second derivative of u with respect to x and z can be expressed in terms of w from the continuity equation as

$$0 = \frac{\partial}{\partial z}\left[\frac{\partial u}{\partial x} + \frac{\partial v}{\partial y} + \frac{\partial w}{\partial z}\right]$$

$$= \frac{\partial^2 u}{\partial x \partial z} + \frac{\partial}{\partial z}\frac{\partial v}{\partial y} + \frac{\partial^2 w}{\partial z^2}$$

and since $\partial^2 v/\partial z \partial y = 0$ by symmetry,

$$\frac{\partial^2 u}{\partial x \partial z} = -\frac{\partial^2 w}{\partial z^2} \tag{24}$$

Consequently (23) can be written as

$$\lim_{\delta s \to 0} \frac{\delta z}{\delta x} = \frac{\frac{1}{2}\frac{\delta z}{\delta x}\frac{\partial^2 w}{\partial z^2}}{-\frac{1}{2}\frac{\delta z}{\delta x}\frac{\partial^2 u}{\partial x^2} + \frac{\partial^2 w}{\partial z^2}} \tag{25}$$

Equation 25 can be examined for the orientation of the stagnation streamline for the condition that (1) the stagnation point occurs at the maximum pressure point and (2) that the stagnation point occurs at a location where the streamwise pressure gradient is positive. The $\partial^2 u/\partial z^2$ derivative can be related to the pressure gradient by the x-component momentum equation evaluated in the plane of the surface; specifically,

$$\frac{\partial p}{\partial x} = \mu \frac{\partial^2 u}{\partial z^2} \quad \text{for } z = 0 \tag{26}$$

Consequently, for the condition $\partial^2 u/\partial z^2]_0 = \partial p/\partial x\,]_0 = 0$, equation 25 becomes

$$\lim_{\substack{\delta x \to 0 \\ \delta z \to 0}} \frac{\delta z}{\delta x} = \frac{1}{2}\frac{\delta z}{\delta x} \qquad \text{for } \left.\frac{\partial p}{\partial x}\right]_0 = 0 \tag{27a}$$

which is only possible if $\lim \delta z/\delta x = 0$ or ∞. A zero value cannot

represent a stagnation point; hence, the stagnation streamline intersects the plate at an angle of $\pi/2$ when the stagnation point occurs at the maximum pressure. This would occur for the $\alpha = \pi/2$ condition.

For $\partial p/\partial x \neq 0$, equation 25 can be expressed as

$$\lim_{\delta s \to 0} \frac{\delta z}{\delta x} = \frac{\frac{\delta z}{\delta x}}{-\frac{\frac{\partial^2 u}{\partial z^2}}{\frac{\partial^2 w}{\partial z^2}} \left(\frac{\delta z}{\delta x}\right) + 2} \tag{27b}$$

and (27b) shows that (note that the denominator must be equal to unity)

$$\frac{\delta z}{\delta x} = \frac{\frac{\partial^2 w}{\partial z^2}}{\frac{\partial^2 u}{\partial z^2}} \tag{28}$$

Using (24) and noting that

$$\frac{\partial^2 w}{\partial z^2} = -\frac{\partial}{\partial x}\left(\frac{\delta u}{\partial z}\right)$$

$$= -\frac{\partial}{\partial x}\,\omega_y \tag{29}$$

The streamline orientation at the stagnation point is

$$\lim_{\delta s \to 0} \frac{\delta z}{\delta x} = \frac{-\nu \frac{\partial \omega_y}{\partial x}}{\frac{1}{\rho}\frac{\partial p}{\partial x}} \tag{30}$$

That is, the orientation of the stagnation streamline can be expressed in terms of the pressure and surface vorticity gradients at the stagnation point.

5.2.2. Consequences of stagnation point at or displaced from the maximum surface pressure

The relationship between the vorticity which is introduced into the flow field by the viscous shear at the wall and the static pressure on

the plate has been presented in Section 3.3, viz.,

$$\frac{1}{\mu}\frac{\partial p}{\partial x}\bigg|_{z=0} = \frac{\partial}{\partial z}\omega_y\bigg|_{z=0} \quad \text{and} \quad \frac{1}{\mu}\frac{\partial p}{\partial y}\bigg|_{z=0} = -\frac{\partial}{\partial z}\omega_x\bigg|_{z=0} \qquad \begin{matrix}(12b)\\(12a)\end{matrix}$$

Since the solenoidal condition on vorticity demands that it appear in closed loops (i.e., $\nabla \cdot \underset{\sim}{\omega} = 0$), it is of interest to note the relationship between the created vorticity and the stagnation point considerations.

Consider the case of vertical jet impingement. In this condition, the stagnation point is centered in the axisymmetric flow field and the stagnation point is clearly at the maximum pressure. That is $\lim \delta z \to 0 \;\; \delta x \to 0 \;\; w/u = -\infty$ and $\partial p/\partial x = 0 = \partial p/\partial y$. A fluid element immediately adjacent to the stagnation streamline will possess vorticity in the sense indicated by Figure 58. The vorticity of such an element must change sign along its trajectory from above the plate to a location in the boundary layer flow along the plate. This vorticity sign change is accomplished by the viscous diffusion term of the vorticity transport equation, viz., from (8)

$$\underset{(1)}{\frac{D\underset{\sim}{\bar{\omega}}}{Dt}} = \underset{(2)}{\underset{\sim}{\bar{\omega}} \cdot \nabla \underset{\sim}{\bar{u}}} + \underset{(3)}{\nu\nabla^2 \underset{\sim}{\bar{\omega}}} + \underset{(4)}{\overline{\underset{\sim}{\omega} \cdot \nabla \underset{\sim}{u}}} - \underset{(5)}{\overline{\underset{\sim}{u} \cdot \nabla \underset{\sim}{\omega}}} \qquad (8)$$

(1) convective transport and local time rate of change of vorticity,

(2) "production" of vorticity by vortex filament stretching and re-orientation,

(3) diffusion of vorticity,

(4) production of vorticity from the fluctuating vorticity-velocity interaction,

(5) vorticity transport by the turbulent motion.

As shown by Figure 58, the flux of vorticity at z=0 is symmetric about the stagnation point, that is, the new vorticity introduced into the flow is created in symmetric loops about the stagnation point. Also, the fluid which originally comprised a vortex loop will remain in the same loop (on the time average) as the sign of the vorticity is changed along the trajectory. This rather straight forward condition provides a useful reference for the considerations of oblique jet impingement.

For an oblique impingement, the center streamline will not, in general, be the stagnation streamline; hence the vorticity structure near the stagnation point will be quite different from the normal impingement case. This is shown schematically in Figure 59. For example, the fluid in the original loop 1-1a is not in a common vortex loop following the impingement; that is, the vorticity of the fluid at 1 changes sign, the vorticity of the fluid at 1a does not. Consequently, the vortex and material lines are different for the oblique jet impingement case. The $\omega = 0$ surface will be non-symmetric and strongly three-dimensional for this flow. It is not obvious what shape this surface will assume away from the centerplane. Smoke flow visualization studies have shown that the entrained flow stagnates and then separates from the surface as shown in the sketch.

It is not clear what geometric configuration is assumed by the closed vortex loop involving the fluid at 1 when it has progressed to a position just upstream of the stagnation point. It seems likely that these loops which are created following the stagnation process on the adjacent streamline are somewhat symmetric about the stagnation point. In this regard, the production of the new vorticity would be similar to the processes occurring in the normal impingement case.

5.2.3. Relationship between the stagnation and surface pressure gradients near the stagnation streamline

An analysis of the surface and stagnation pressure gradients will be necessary for the proper interpretation of the experimental measurements. Specifically, we will show that the surface pressure in the backflow region near the stagnation point is less than the stagnation pressure of the streamline in the neighborhood of and located upstream of the stagnation streamline. Figure 59 shows the terms for the analysis. Point A lies along the stagnation streamline point B is the intersection of the normal at A and the second streamline of interest and point C is at the intersection of the second streamline and the contour which lies along the normal trajectory of the streamlines from $x_s - \delta_x$ to the streamline passing through B.

The pressure at $(x_s - \delta x, 0, 0)$ can be written as

$$p(x_s - \delta x, 0, 0) = p(c) + \int_0^L \frac{\partial p}{\partial n} \, dn \tag{31}$$

where L is the distance from C to $(x_s - \delta x, 0, 0)$. The stagnation pressure and the velocity at C can be used to express p(c) as

$$p(c) = p_s(c) - \frac{\rho Q^2(c)}{2} \tag{32}$$

and the integral along n can be written as

$$\int_0^L \frac{\partial p}{\partial n} \, dn = \int_0^1 \frac{\rho Q^2}{(R/L)} \frac{dn}{L} \tag{33}$$

The maximum modulus theorem can be used to express this integral value as

$$\int_0^1 \frac{\rho Q^2}{(R/L)} \frac{dn}{L} \leq \frac{\rho Q^2)_{max}}{R/L)_{min}} \tag{34}$$

and since $Q_{max} = Q(c)$ equation (26) becomes

$$p(x_s - \delta x, 0, 0) \leq p_s(c) - \frac{\rho Q^2(c)}{2} + \frac{\rho Q^2(c)}{R/L)_{min}} \tag{35a}$$

and

$$p(x_s - \delta x, 0, 0) < p_s(c) \quad \text{if } R/L > 2. \tag{35b}$$

The dimension L is related to the displacement of B with respect to A and consequently can be made as small as desired. Hence, the condition $R > 2L$ is assured, since R is finite as $L \to 0$. (Note, $R \to \infty$ as $L \to 0$.)

It is now necessary to show that this result is general; that is, that it applies for all small δz. For sufficiently small L, the stagnation pressure at C (or B) and the pressure at $(x_s - \delta x, 0, 0)$ can be related to the values at A and $(x_s, 0, 0)$ respectively using a first order Taylor series. Hence the inequality of (28) can be used to express an inequality between these pressure gradients. Specifically, assuming the stagnation pressure changes to be negligible over these small displacements,

$$p_s(B) = p_s(C) = p_s(A) - \frac{\partial p_s}{\partial n}\delta n \tag{36}$$

and

$$p(x_s - \delta x, 0, 0) = p(x_s, 0, 0) - \frac{\partial p}{\partial x}\ \delta x \tag{37}$$

Since $p(x_s, 0, 0) = p_s(A)$ and $p_s(C) > p(x_s - \delta x, 0, 0)$ (38)

$$\frac{\partial p_s}{\partial n}\ \delta n < \frac{\partial p}{\partial x}\ \delta x \tag{39}$$

geometrically, it can be shown as in Figure 59 that $\delta x > \delta n$ for small δx. Consequently $\partial p/\partial x > \partial p_s/\partial n$.

The important result of these considerations is that the surface pressure is always less than the equivalent stagnation pressure except at the stagnation point. This is a necessary result for the proper interpretation of the stagnation point.

5.3. Experimental Investigation of the Stagnation Phenomena

5.3.1. Technique and interpretation

Stagnation phenomena for the oblique jet are difficult to investigate because the phenomena are basically unsteady and hence a suitable averaging process is required. Various schemes to determine the time-mean stagnation streamline by use of its singular characteristic as the only streamline to intersect the plate were unsuccessfully investigated. Holographic interferometry with a dense gas tracer and a heated jet with a platinum resistance temperature sensor (high frequency response ≈ 3khz) were used to attempt this discrimination. The results from the attempts were not decisive. The common and often successful technique of attempting to locate the position of zero shear stress was not attempted because the expected stress magnitudes for these small angles would be quite small and hence difficult to discriminate and because this flow is strongly three-dimensional which would necessitate a measurement over a small length and width compounding the sensitivity requirements. Also, a suitable averaging would have to be inherent in the transducer or in the subsequent

signal processing in order that the time variation would be properly accounted for.

An experimental technique involving simultaneous hot-wire and surface static pressure distributions was developed and successfully employed. For this technique, the hot-wire probe was positioned close to the plate ($z \cong 0.15$ cm, $z/d \cong 0.04$) and the velocity magnitude was recorded as a function of the distance from the jet $v_w(x)$. A pressure survey for the same conditions allowed the calculation of a velocity as if the surface pressure was the stagnation pressure for that streamline, this value was designated v_p. A linear shift δx of the hot-wire velocity data to the z-value of the plate, along the line defined by the wire position z and the jet angle α plus the divergence angle β of the 0.1 isotach, was then used to provide a comparison between v_p and v_w. The equation for this shift is $\Delta x = \Delta z \tan^{-1} (\alpha + \beta)$. The stagnation point is considered to be at the intersection of these two curves. A sketch of this technique is shown in Figure 60.

5.3.2. Experimental results

Three cases were selected for comprehensive evaluation of the stagnation point location, $h/d = 1$ and $\alpha = 3, 6, 9$ degrees for the "uniform nozzle" configuration. The results of the special traverses to determine v_w and v_p are shown in Figures 61 to 63. . In general, two v_w traverses were made at different z/d values. The results from the two traverses were in reasonable agreement for the three different angles; the most complete set (i.e., z/d value) was used for these results. The data themselves are presented in Table 4. The results for these three conditions show that <u>the stagnation point does not occur at the location of the maximum surface pressure.</u> The v_w and v_p data for $\alpha = 3$ degrees, $h/d = 1$, (see Figure 61), did not indicate that a stagnation point existed. However, when the velocity data from the hot-wire probe were shifted an additional distance of 0.57d a stagnation region is evidenced. The required shift is interpreted as an upward deflection of the jet by the increased static pressure on the plate. The location of the jet's center, based upon momentum flux considerations (z_m of the first annual report), does not show a shift above the geometric trajectory for the condition $\alpha = 3$ degrees, $h/d = 1$, uniform; such shifts are indicated for $\alpha = 3$ degrees and $h/d = 0.75$ and 0.5. However, it is reasonable that the low velocity fluid along

the stagnation streamline could be affected by the surface pressure for the $h/d = 1$ case.

The location of the stagnation point is quite difficult to infer from these results. Apparently a more accurate description is to identify a stagnation region in the neighborhood of $x/d \cong 3.8$. The flow field is considered to possess a single stagnation streamline at an instant; however, the inherent unsteadiness of the flow could well produce an apparent stagnation region even though the time mean flow field will also possess, by assumption, a unique stagnation streamline. If viscous effects reduced the stagnation pressure between the velocity measurement location and the surface, then this additional shift would not be as large as is indicated. A shift of $\Delta x/d = 1.5$ for the hot-wire velocity data (v_w) would cause the stagnation and maximum surface pressure locations to be coincident. However, this would result in a condition in which the local surface pressure would exceed the equivalent stagnation pressure; this condition is shown to represent a physically impossible situation in equation 39. It should be noted that a linear shift of the data over a net distance of $\Delta x/d = 1.20$ is too great to allow detailed comparison between the v_p and v_w results.

The data for the case $\alpha = 9$ degrees, $h/d = 1$, u, see Figure 62, appear to be quite straightforward in terms of locating the stagnation point, $x/d \cong 1.9$, and demonstrating that the stagnation point does not occur at the maximum pressure location. The absence of a vertical deflection is compatible with the z_c and z_m results for this case (see Figure 45d, First Annual Report) and represents a reasonable trend as compared with the three degree case since the jet approaches the plate with a less glancing trajectory. A slight negative shift is suggested (but not shown) to provide a tangential condition between the v_p and v_w curves.

The measured v_p and the measured-shifted v_w distributions for $\alpha = 15$ degrees are shown in Figure 63. These results suggest that the jet trajectory is steeper than 19 degrees in the region between the plane of the measured velocities ($z/d = 0.0308$) and the surface; hence, the indicated shift is too great. This observation is based upon equation 39 in which it was shown that the surface pressure should not exceed the equivalent stagnation pressure. The solid line on Figure 63 presents the estimated upstream shift appropriate for this case. The resulting tangent point between v_p and v_w is in the neighborhood of $x/d = 1.3$.

5.3.3. Summary and analysis of the stagnation point investigation

The determination of the stagnation point by the special traverses discussed above allow the relationship between the general velocity field and the stagnation point to be examined. The approximate locations of the stagnation points for the three cases are

uniform, $h/d = 1$,	$\alpha = 3$	$x/d \cong 3.8$
	9	1.9
	15	1.3

A comparison of these results to the isotach plots of Figures 28 to 30 shows that the stagnation point is in the vicinity of the intersection of the jet edge ($u/u(0) = 0.1$ isobar) with the plate.

There are two physical effects which could cause the inferred stagnation point to be in error; they are self-compensating and their magnitudes are difficult to estimate although they are certainly too small to affect the qualitative nature of the above conclusions. Shear effects will degrade the magnitude of the stagnation pressure between the measurement location and the surface of the plate. To the extent that this occurs, the measured velocity represents an excessive stagnation velocity and the v_w magnitudes would be corrected by subtracting a prescribed δv_w value. The physical proximity of the velocity measurement and the surface pressure measurement would cause this to be a relatively small error. If the velocity were measured at a z location where $p > p_{ambient}$, then the stagnation pressure is larger than that indicated by the $\rho v_w^2/2$ value. Hence a correction of adding a separately prescribed δv_w would be required to relate the hot-wire and surface pressure data. It is difficult to estimate reasonable values for δv_w for the static pressure correction; however, it can reasonably be assumed that this correction increases as the wall pressure increases, that is, $d(\delta v_w)/dx > 0$. Consequently, the alignment of the v_w and v_p curves would always occur at a point farther upstream, allowing for this correction, and this reinforces the result that the maximum pressure and the stagnation point are physically displaced.

6. SUMMARY

The kinematic, no penetration constraint requires that the fluid in the jet spread laterally or deflect vertically upward to provide the required cross sectional area for the jet mass flux.

The selection between these two responses is based upon the dynamics of the jet-plate interaction as characterized by the momentum equation.

Analytical and experimental considerations are used to demonstrate that for sufficiently small angles, the primary response of the jet is an upward curvature; however, a complex interaction between curvature and spreading is suggested for angles larger than (nominally) 12 degrees as would be encountered in the interaction between the jet and the deflecting flaps of a STOL configuration.

The description of the jet-plate interaction in terms of vorticity is well motivated by both analytical and experimental considerations. Such a description provides a rational framework to model the three-dimensional character of the flow in which the upper portion retains its axisymmetric structure and the distortion of the jet occurs primarily near the surface. Streamwise vorticity is introduced into the flow field by the lateral surface pressure gradient and the reorientation of the azimuthal vorticity of the approaching jet.

Similarly, there is a surface flux and a production by stretching of the lateral vorticity. Such phenomena account for the localized jet distortion. The streamwise vorticity could be used to provide enhanced boundary layer control if properly accounted for in the flap gap design for an externally blown flap airfoil.

The physical displacement between the stagnation point and the maximum pressure point is examined analytically and demonstrated from the experimental data for incidence angles of 15 degrees and less. The possibility of a finite length stagnation line is demonstrated for a non-analytic velocity distribution and the relationship between the incidence angle at impact and the surface vorticity and pressure gradients is established assuming an analytic velocity field.

7. REFERENCES

1. Foss, J.F. and S.J. Kleis, "A study of the round-jet/plane-wall flow field," First Annual Report, Grant NGR 23-004-068, Michigan State University, October 8, 1971.
2. Sforza, P.M., and G. Herbst, "A study of three-dimensional, incompressible, turbulent wall jets," PIBAL Report No. 1022, Polytechnic Institute of Brooklyn, October 1967.
3. Lighthill, M.J., "II. Introduction. Boundary layer theory," Chapter 1 of Part II of Laminar Boundary Layers, L. Rosenhead, ed., Oxford University Press, 1963.
4. Foss, J.F. and S.J. Kleis, "The multiple round-jet/plane-wall flow field," Second Semi-Annual Report, Grant NGR 23-004-068, Michigan State University, May 5, 1972.

APPENDIX A. Selected Isotachs from the First Annual Report

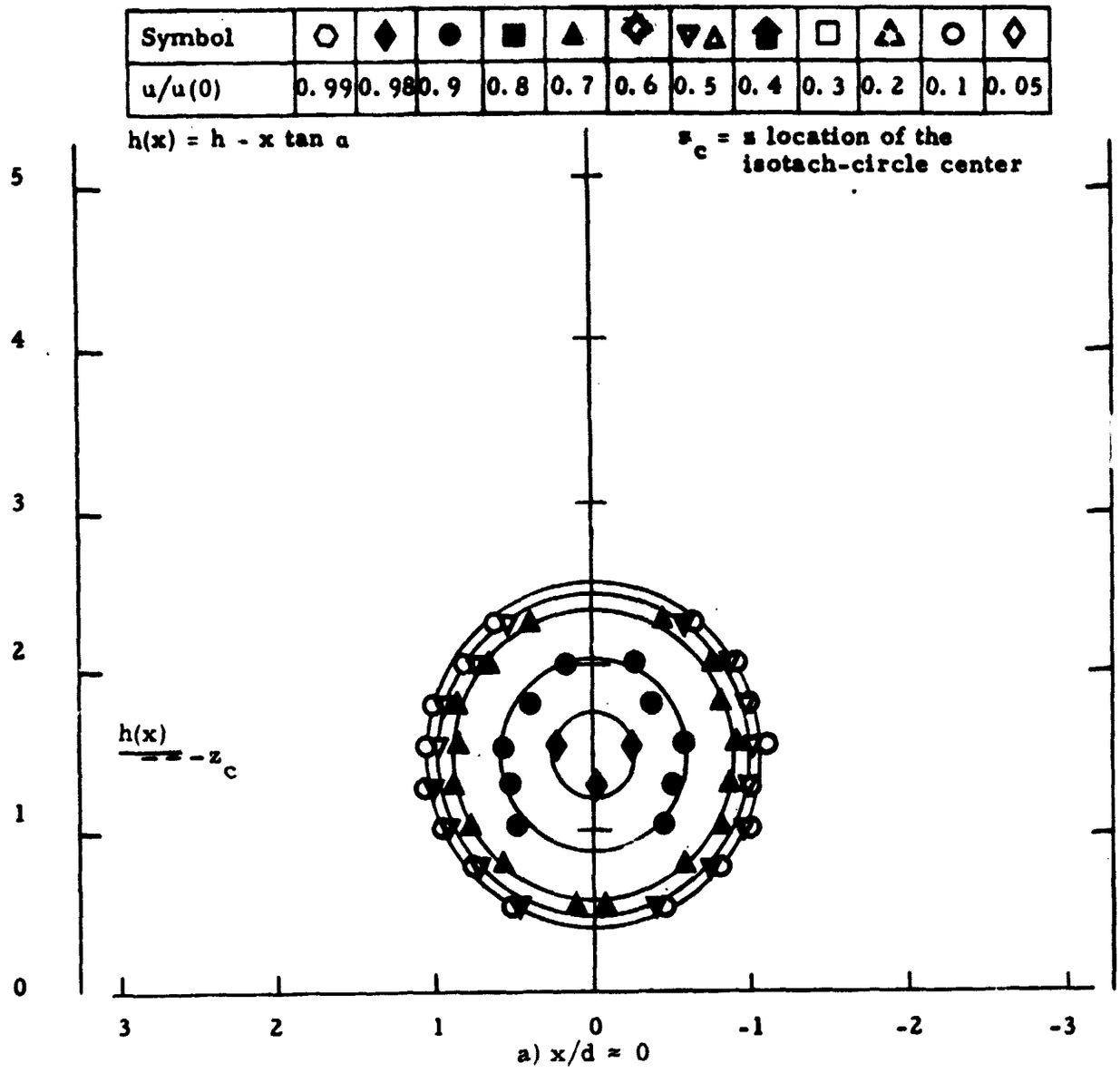

Figure 14. Isotach contours $\alpha = 3$, $h/d = 0.75$, fully developed.

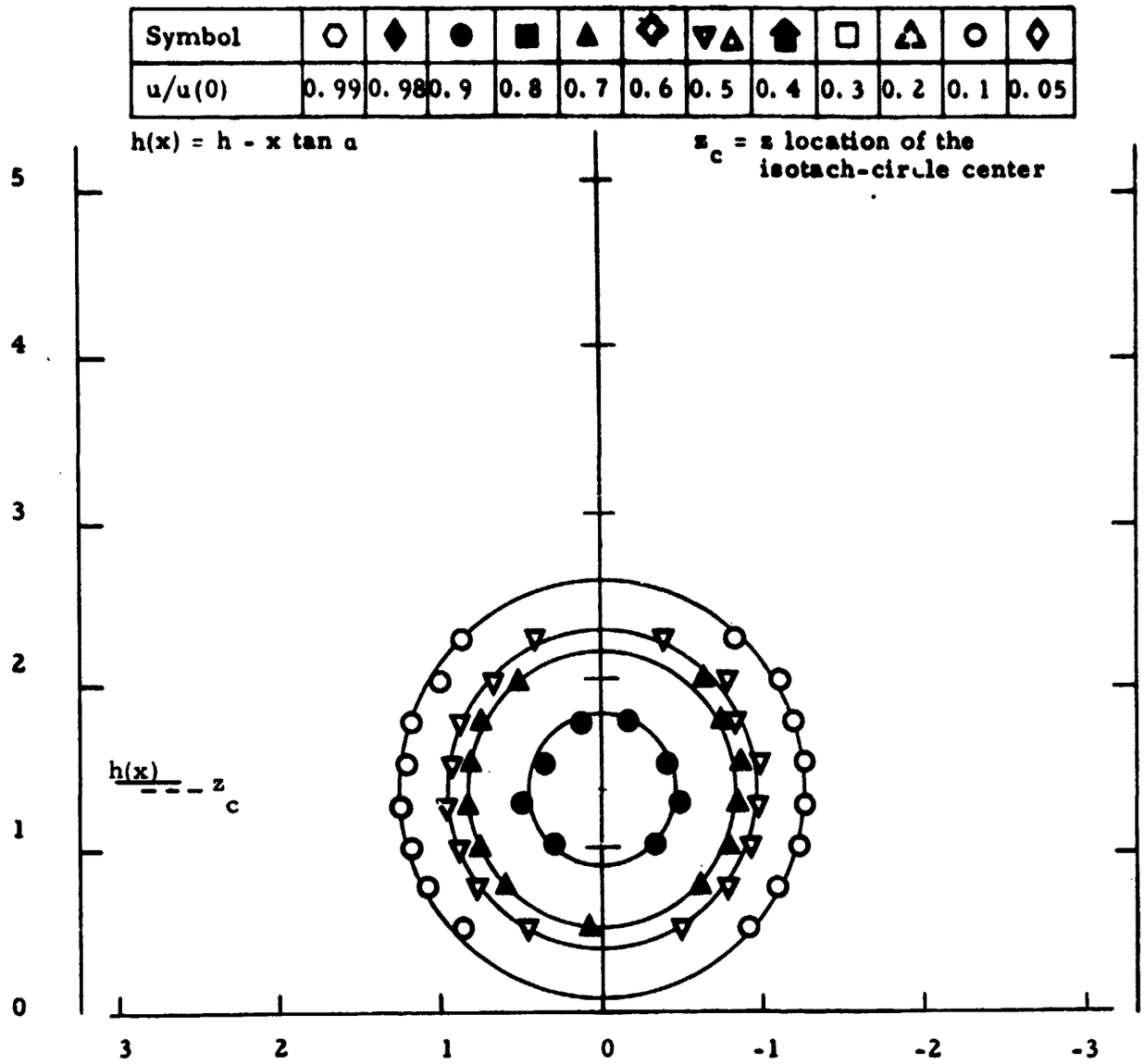
Symbol
u/u(0)
0.99
0.98
0.9
0.8
0.7
0.6
0.5
0.4
0.3
0.2
0.1
0.05
h(x) = h - x tan α
z_c = z location of the isotach-circle center
h(x)
z_c
5
4
3
2
1
0
3
2
1
0
-1
-2
-3

b) x/d = 1

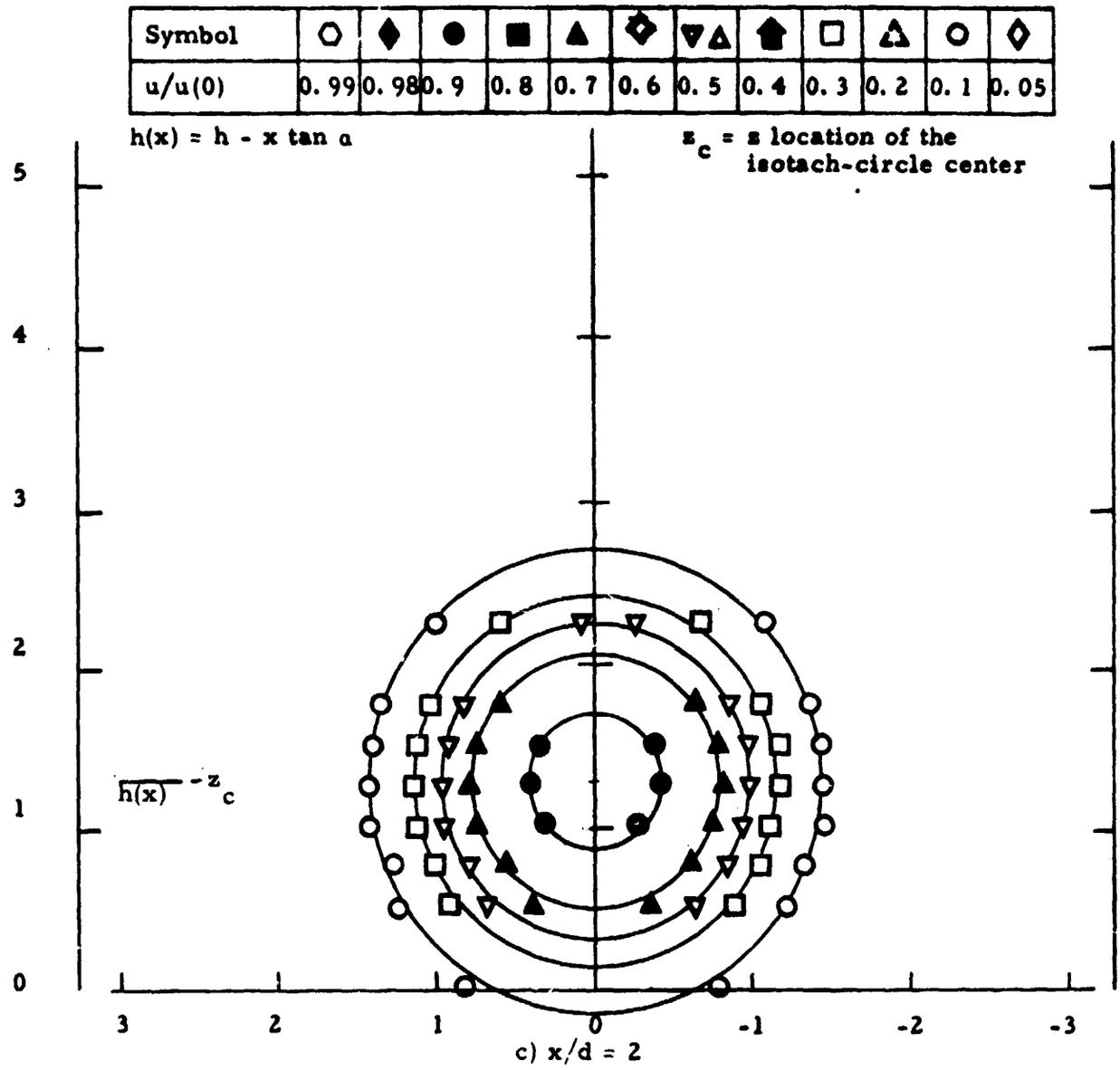
Symbol
u/u(0)
0.99
0.98
0.9
0.8
0.7
0.6
0.5
0.4
0.3
0.2
0.1
0.05
h(x) = h - x tan α
z_c = z location of the isotach-circle center
$\frac{}{h(x)} - z_c$
5
4
3
2
1
0
3
2
1
0
-1
-2
-3

c) x/d = 2

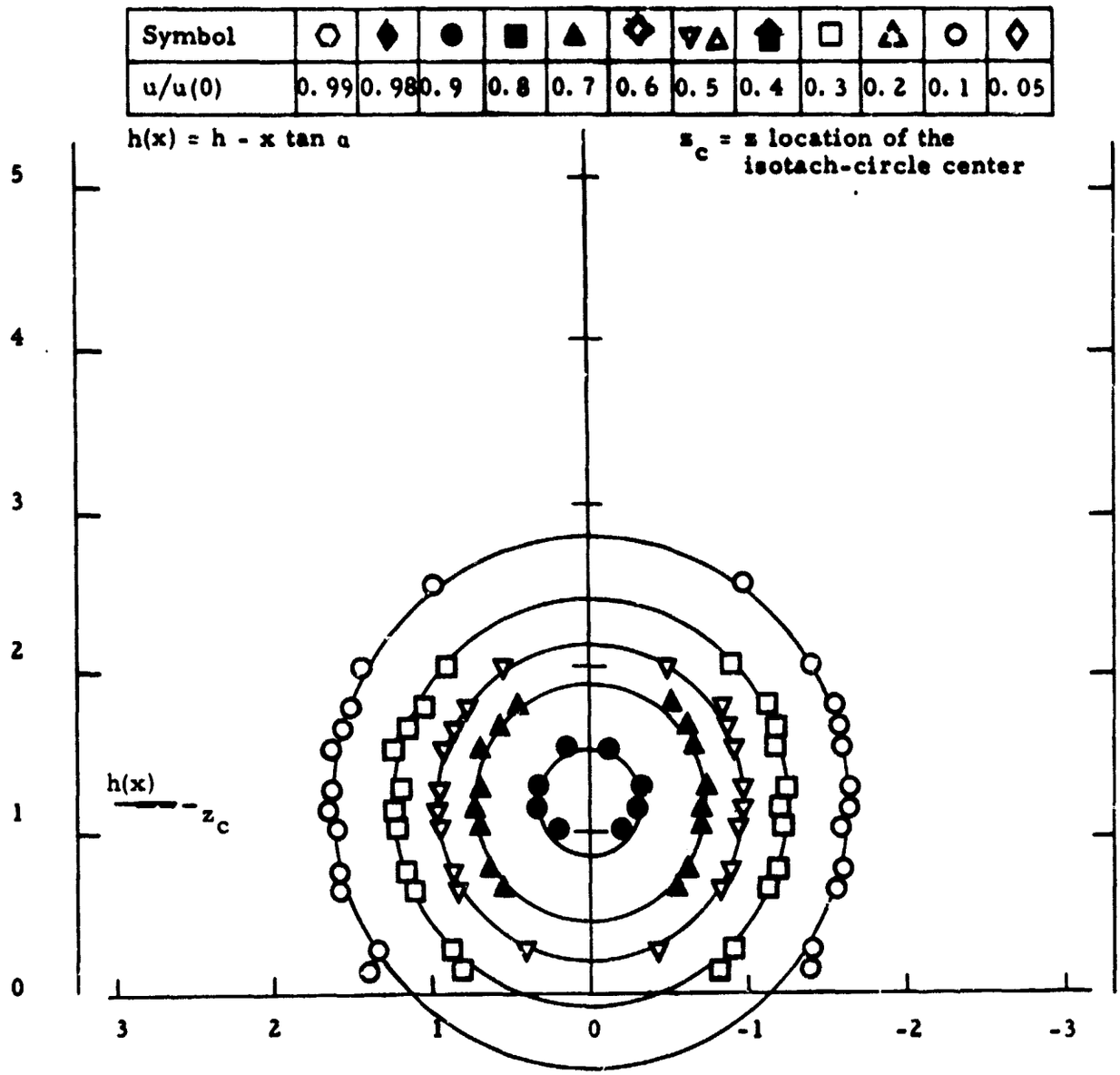
Symbol
u/u(0)
0.99
0.98
0.9
0.8
0.7
0.6
0.5
0.4
0.3
0.2
0.1
0.05
h(x) = h - x tan α
z_c = z location of the isotach-circle center
h(x)
z_c
5
4
3
2
1
0
3
2
1
0
-1
-2
-3

d) x/d = 3

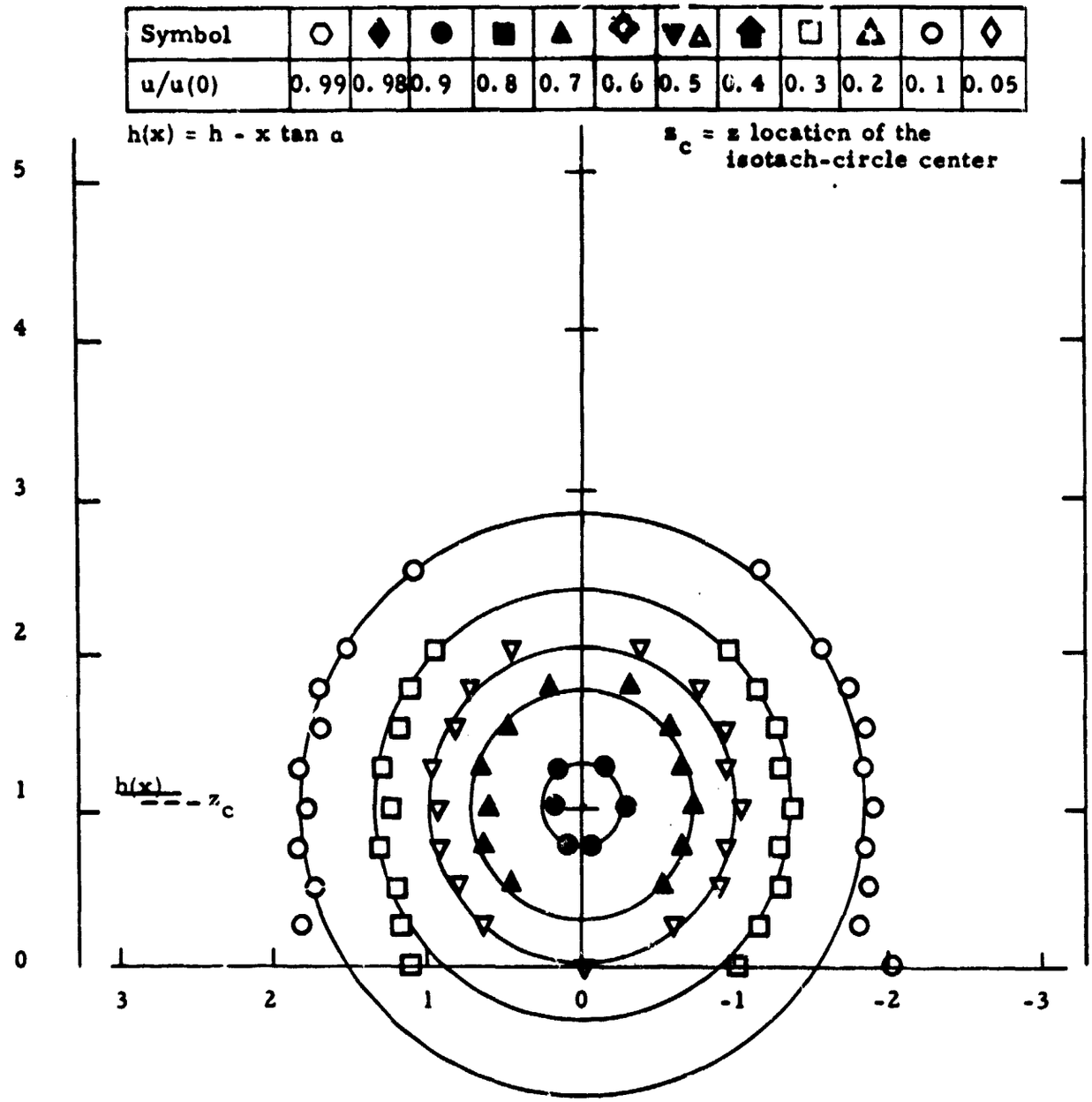
Symbol
u/u(0)
0.99
0.98
0.9
0.8
0.7
0.6
0.5
0.4
0.3
0.2
0.1
0.05
h(x) = h - x tan α
z_c = z location of the isotach-circle center
h(x)
z_c
5
4
3
2
1
0
3
2
1
0
-1
-2
-3

e) x/d = 4

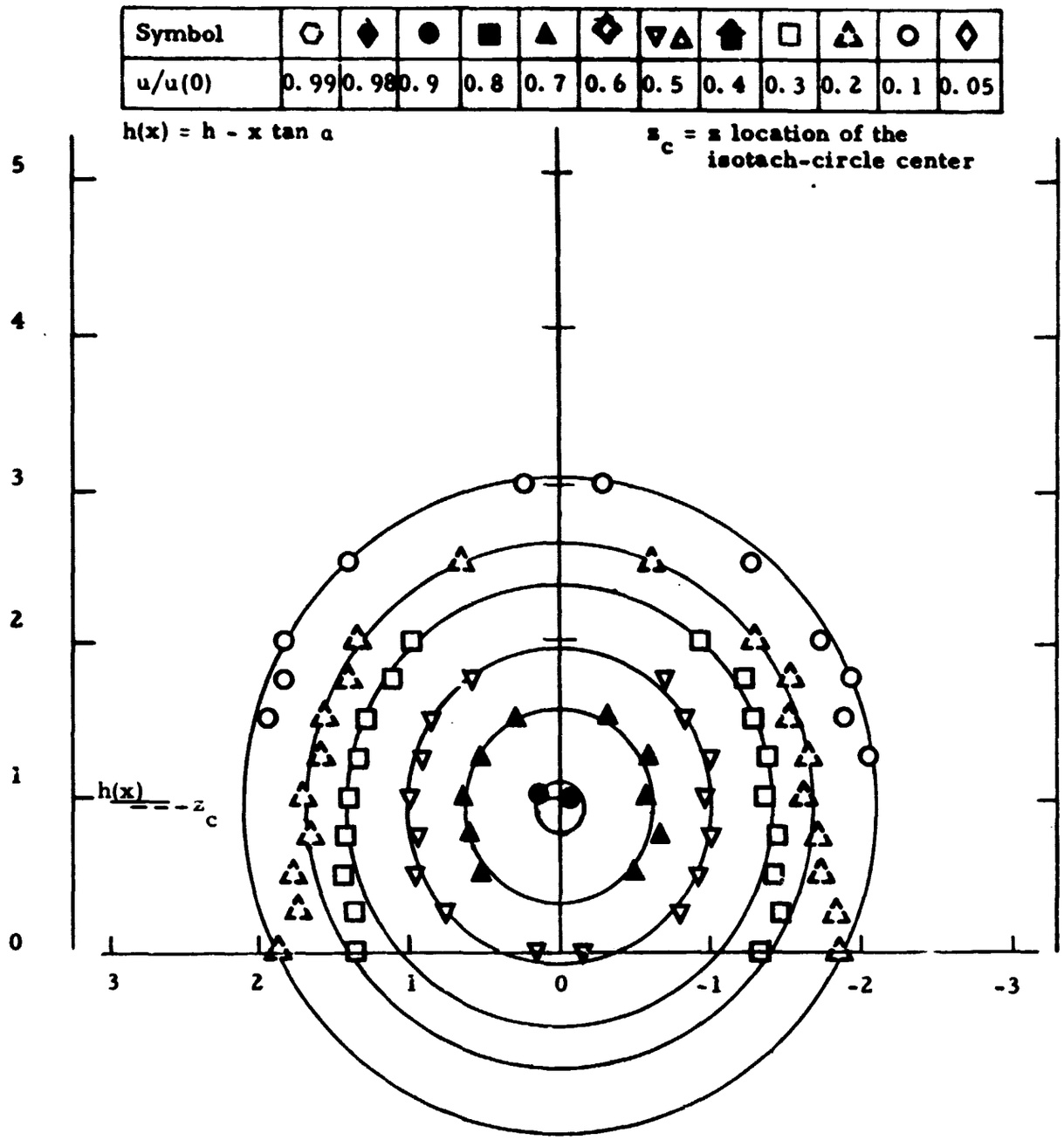
Symbol
u/u(0)
0.99
0.98
0.9
0.8
0.7
0.6
0.5
0.4
0.3
0.2
0.1
0.05
h(x) = h - x tan α
z_c = z location of the isotach-circle center
h(x)
z_c
5
4
3
2
1
0
3
2
1
0
-1
-2
-3

i) x/d = 5

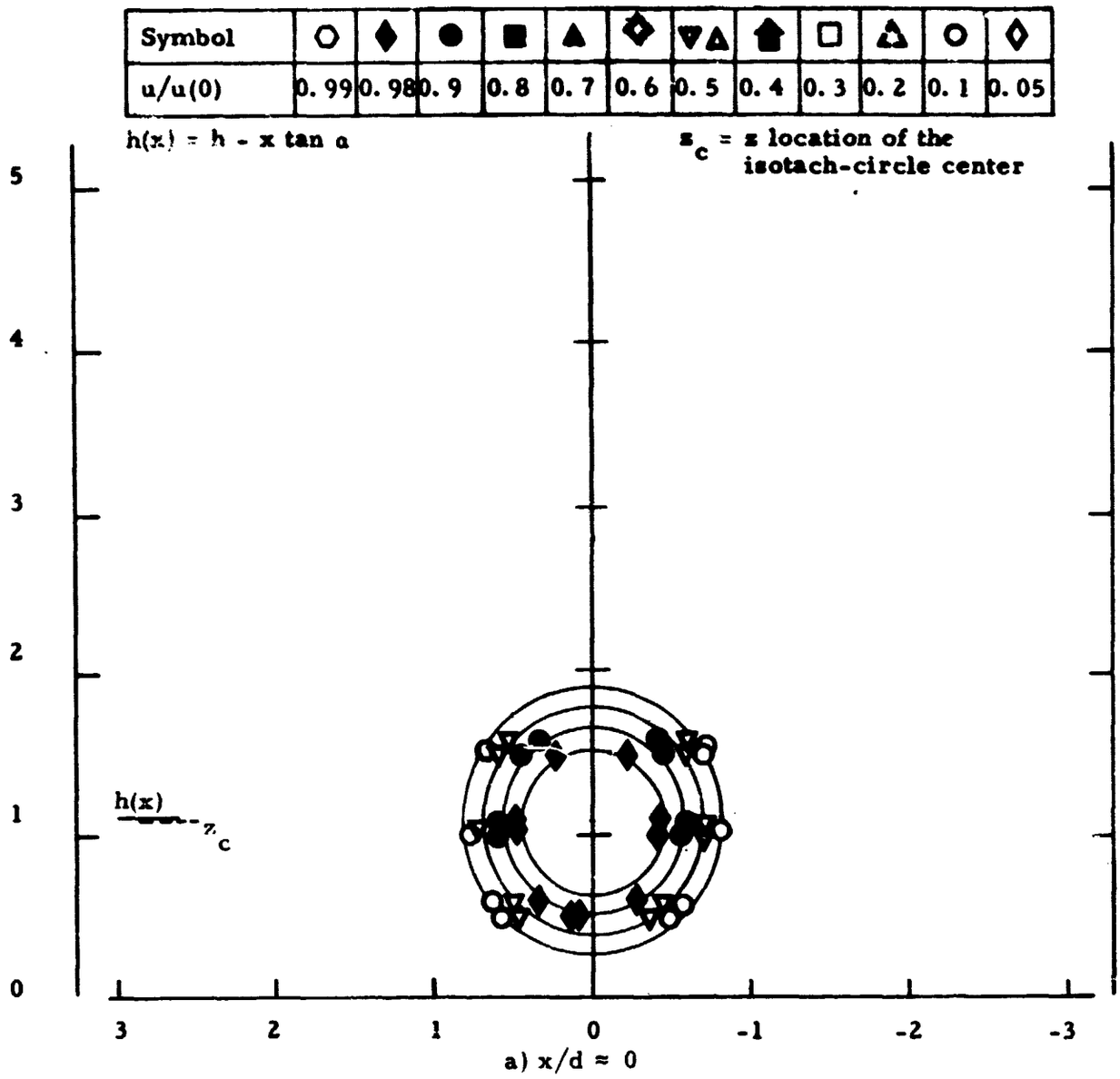

Figure 18. Isotach contours $\alpha = 6$, $h/d = 0.75$, uniform.

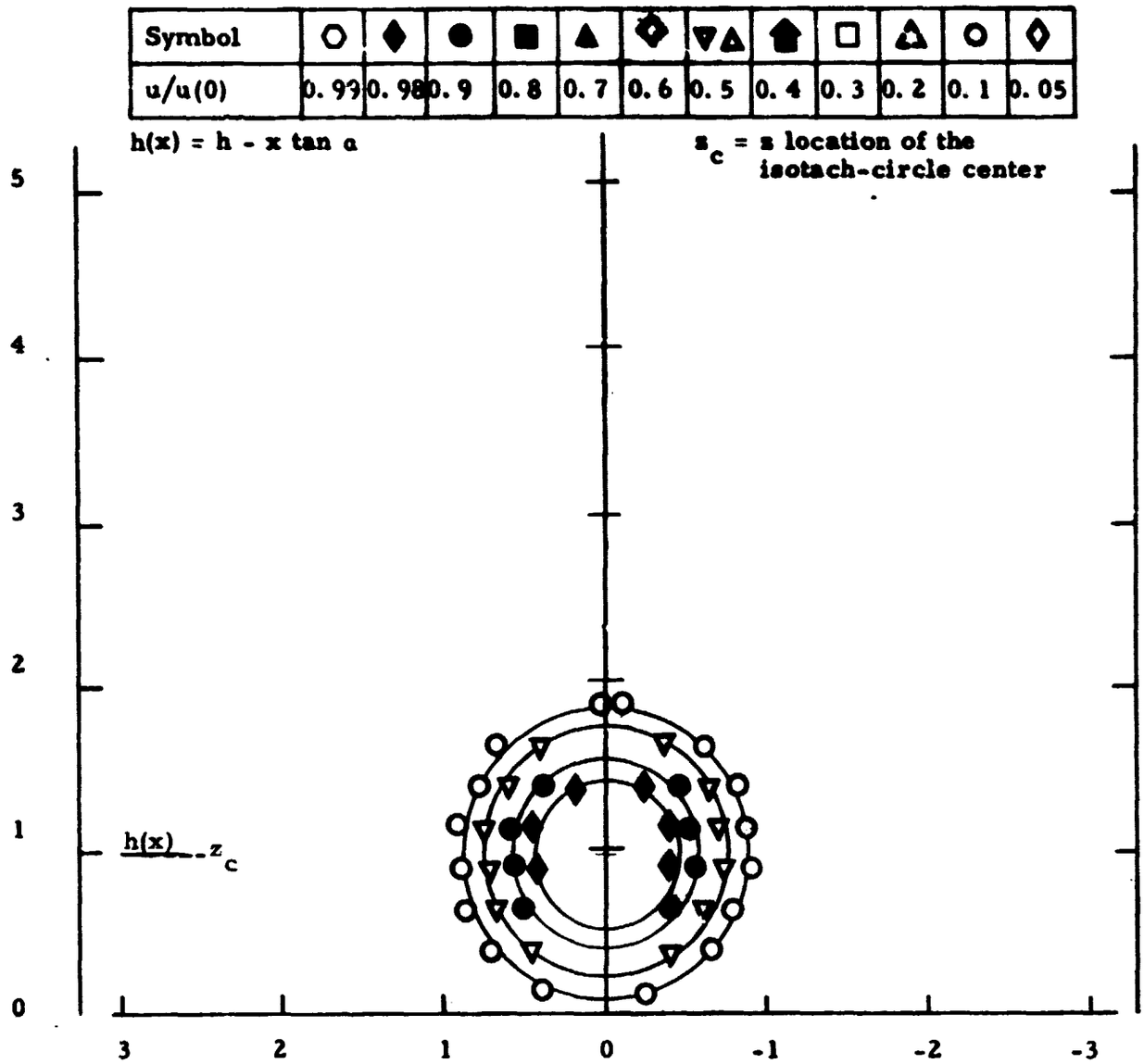
Symbol
u/u(0)
0.99
0.98
0.9
0.8
0.7
0.6
0.5
0.4
0.3
0.2
0.1
0.05
h(x) = h - x tan α
z_c = z location of the isotach-circle center
h(x)
z_c
5
4
3
2
1
0
3
2
1
0
-1
-2
-3

b) x/d = 1

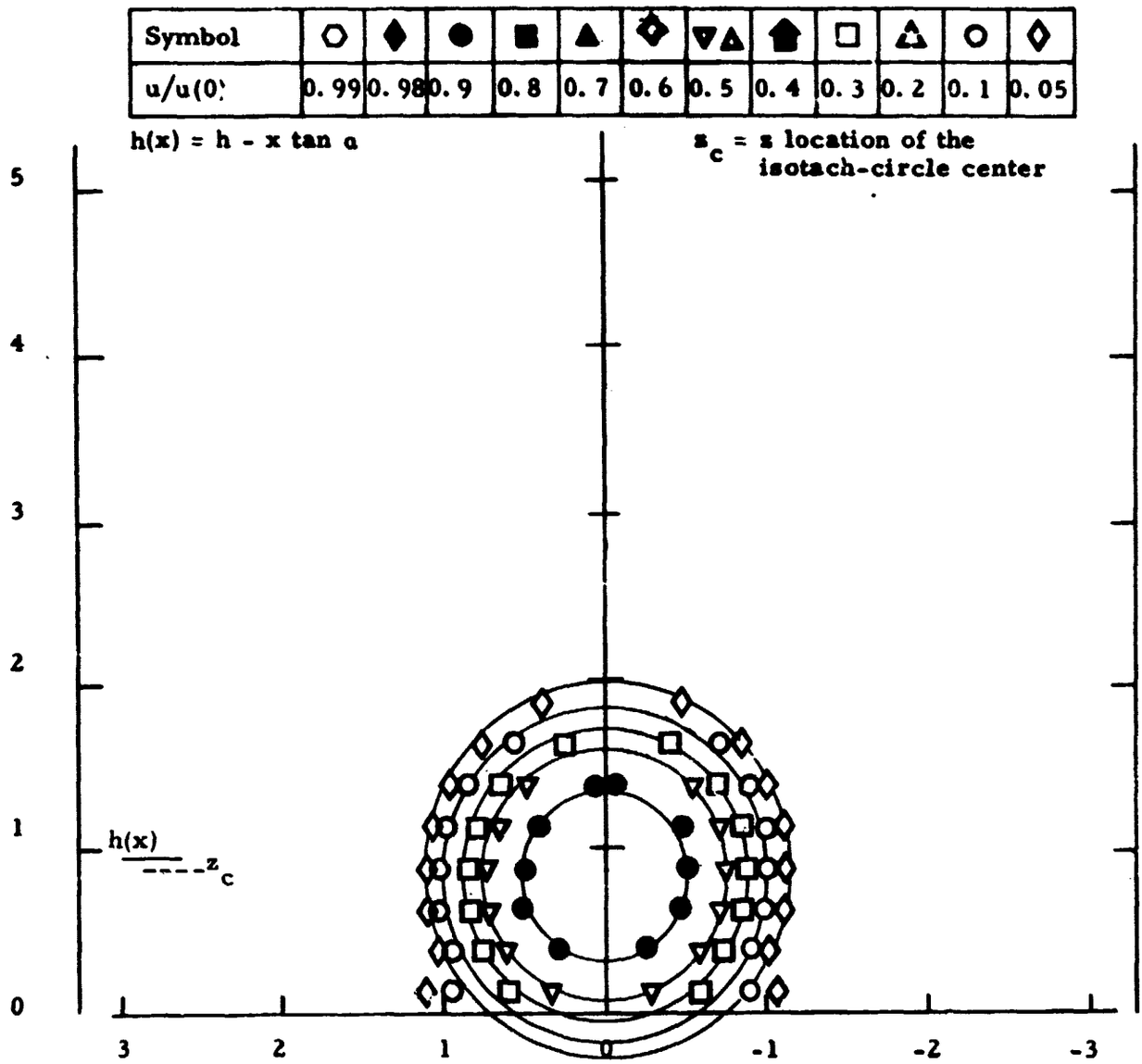
Symbol
u/u(0)
0.99
0.98
0.9
0.8
0.7
0.6
0.5
0.4
0.3
0.2
0.1
0.05
h(x) = h - x tan α
z_c = z location of the isotach-circle center
h(x)
z_c
5
4
3
2
1
0
3
2
1
0
-1
-2
-3

c) x/d = 2

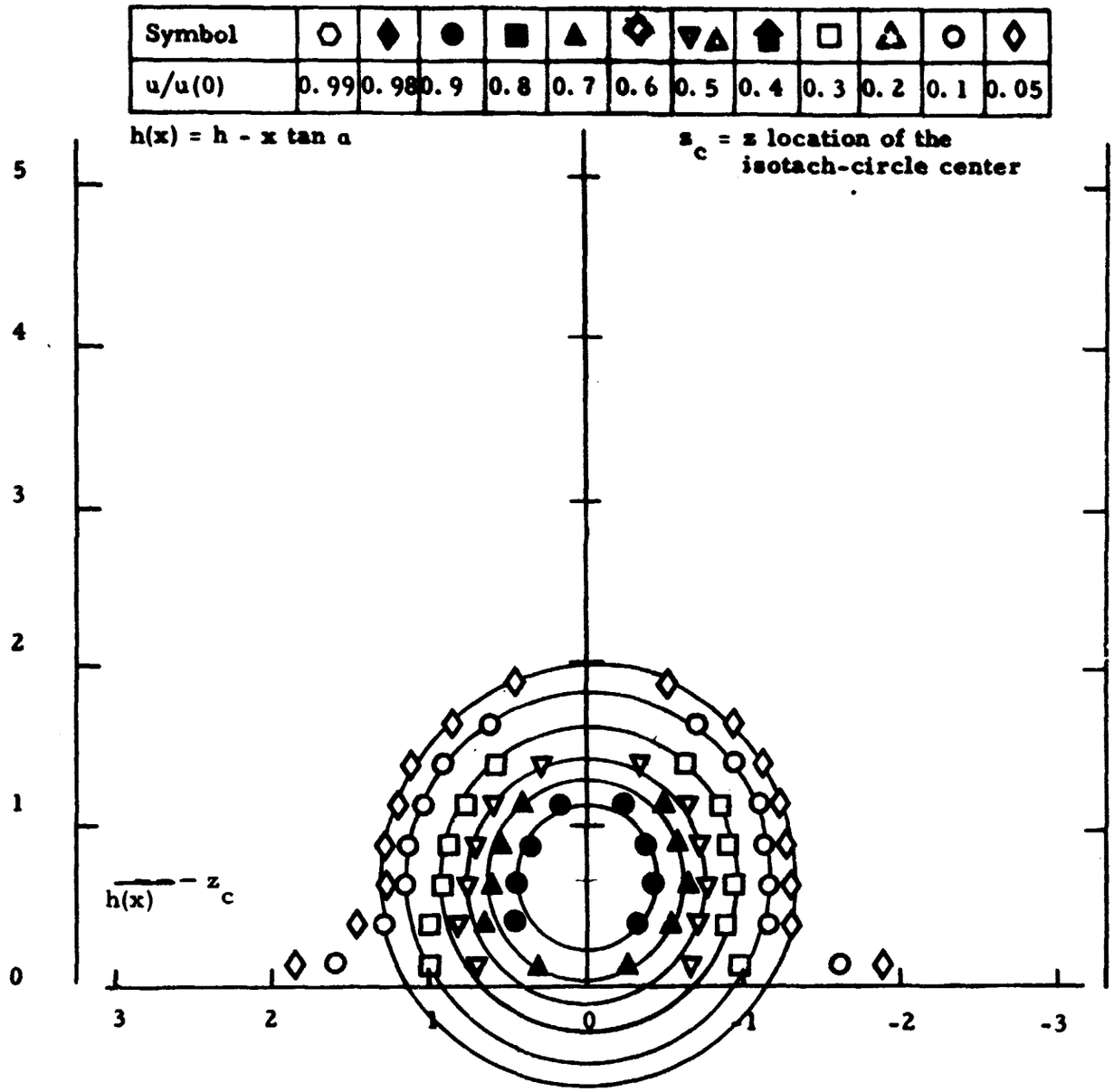
Symbol
u/u(0)
0.99
0.98
0.9
0.8
0.7
0.6
0.5
0.4
0.3
0.2
0.1
0.05
h(x) = h - x tan α
z_c = z location of the isotach-circle center
h(x)
z_c
5
4
3
2
1
0
3
2
1
0
-1
-2
-3

d) x/d = 3

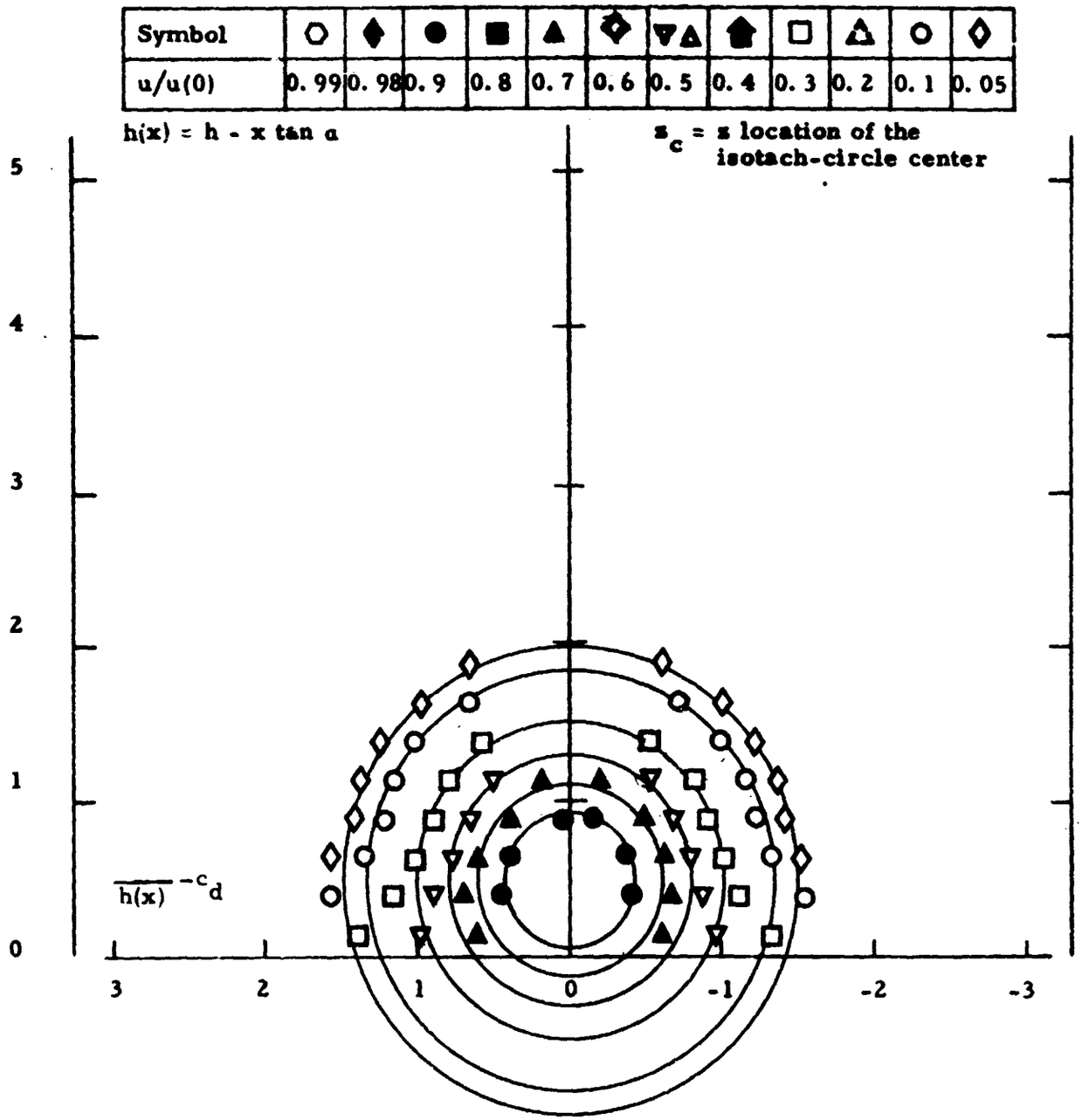
Symbol
u/u(0)
0.99
0.98
0.9
0.8
0.7
0.6
0.5
0.4
0.3
0.2
0.1
0.05
h(x) = h - x tan α
z_c = z location of the isotach-circle center
$\frac{-c_d}{h(x)}$
5
4
3
2
1
0
3
2
1
0
-1
-2
-3

e) x/d = 4

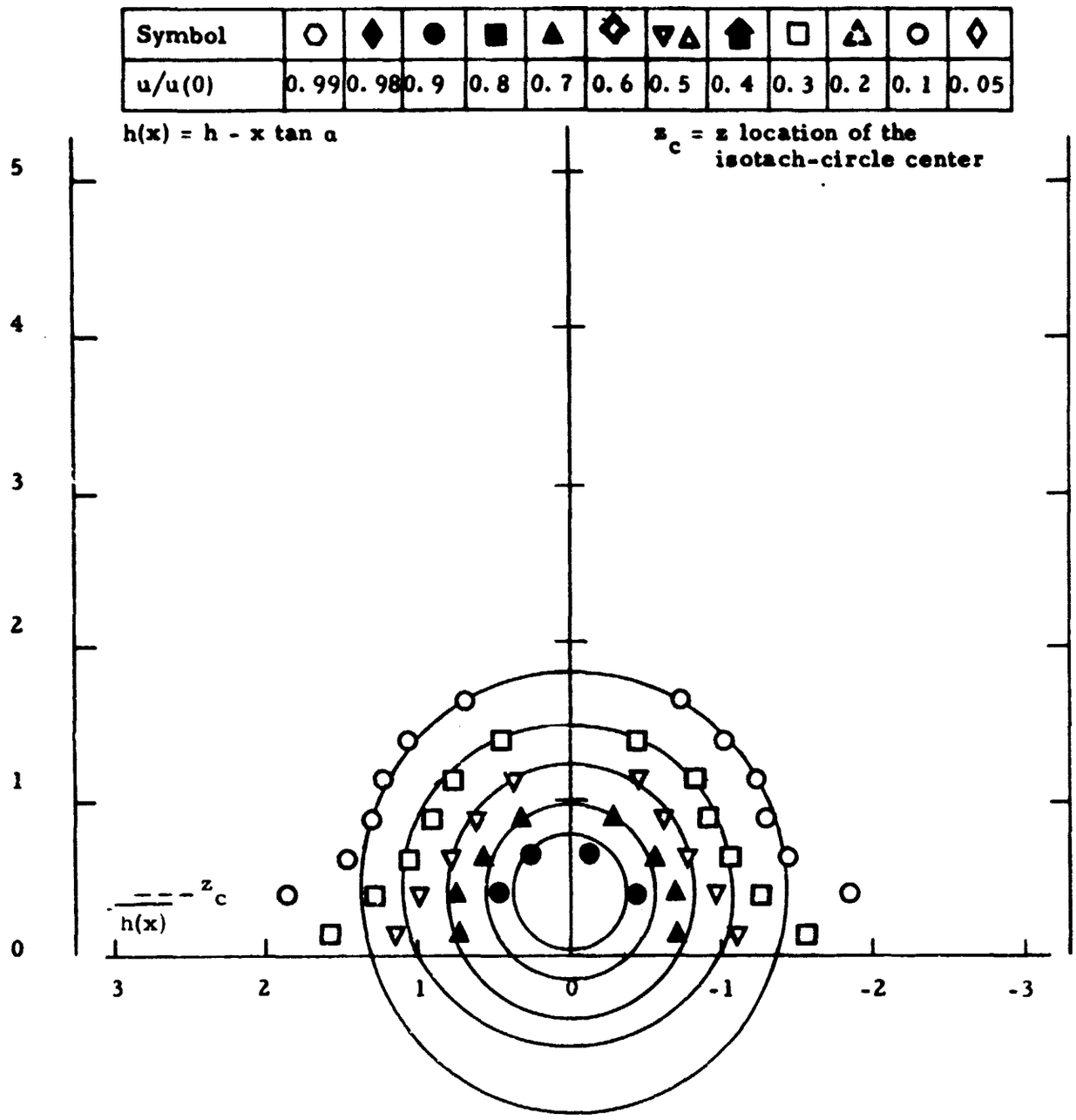
Symbol
u/u(0)
0.99
0.98
0.9
0.8
0.7
0.6
0.5
0.4
0.3
0.2
0.1
0.05
h(x) = h - x tan α
z_c = z location of the isotach-circle center
$\frac{z_c}{h(x)}$
5
4
3
2
1
0
3
2
1
0
-1
-2
-3

f) x/d = 5

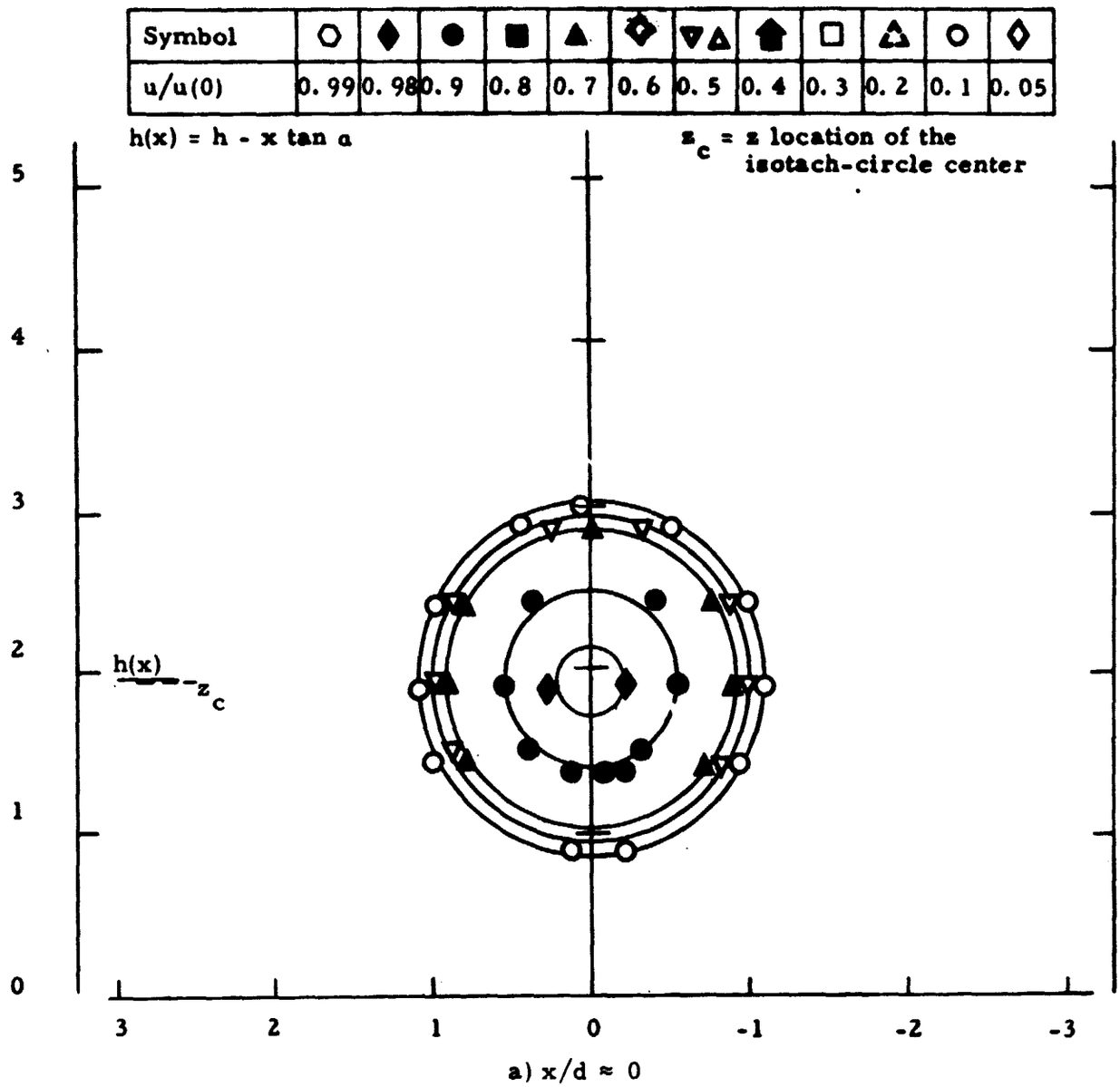

Figure 21. Isotach contours $\alpha = 9$, $h/d = 1$, fully developed.

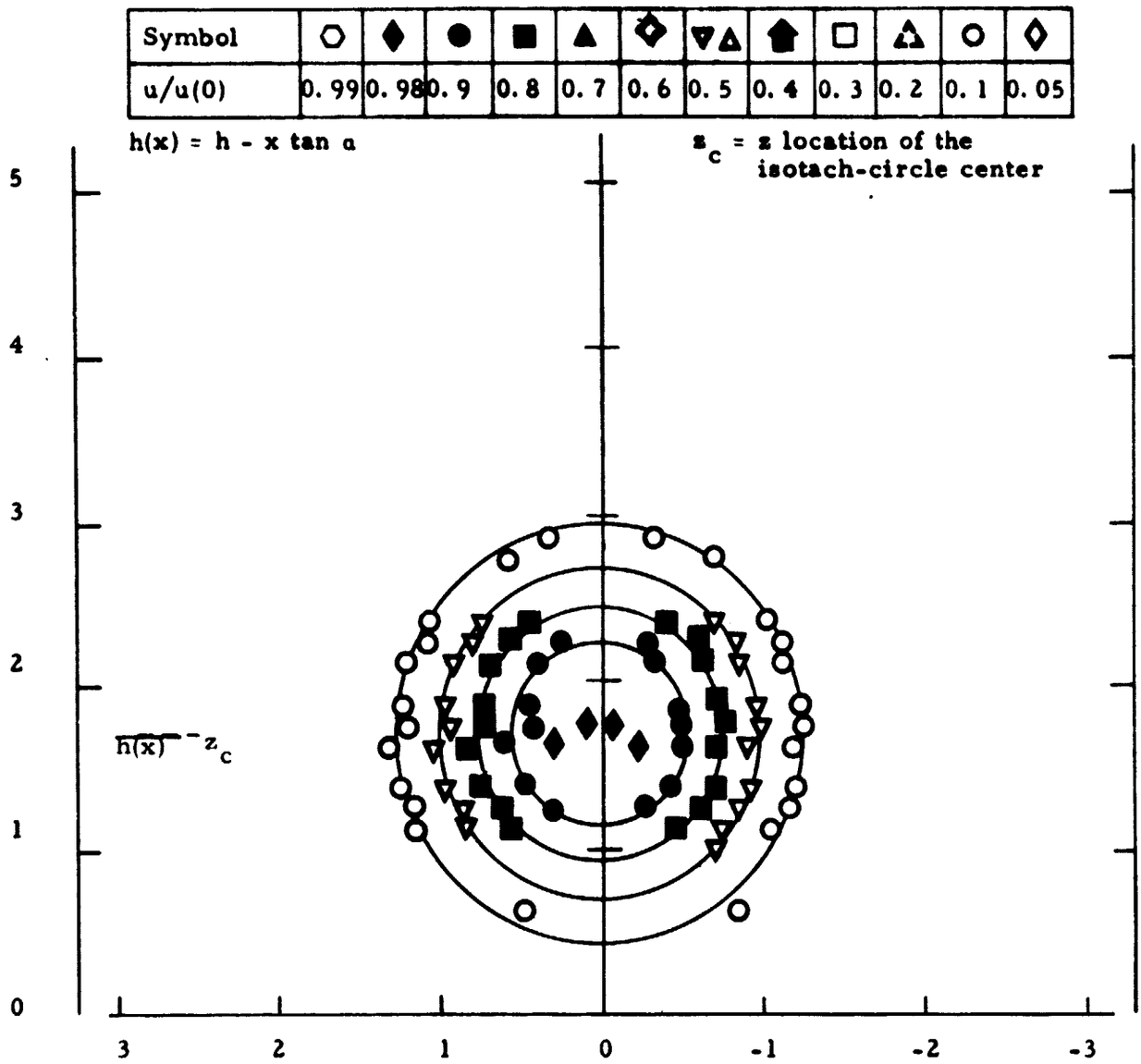
Symbol
u/u(0)
0.99
0.98
0.9
0.8
0.7
0.6
0.5
0.4
0.3
0.2
0.1
0.05
h(x) = h - x tan α
z_c = z location of the isotach-circle center
$\overline{h(x)} - z_c$
5
4
3
2
1
0
3
2
1
0
-1
-2
-3

b) x/d = 1

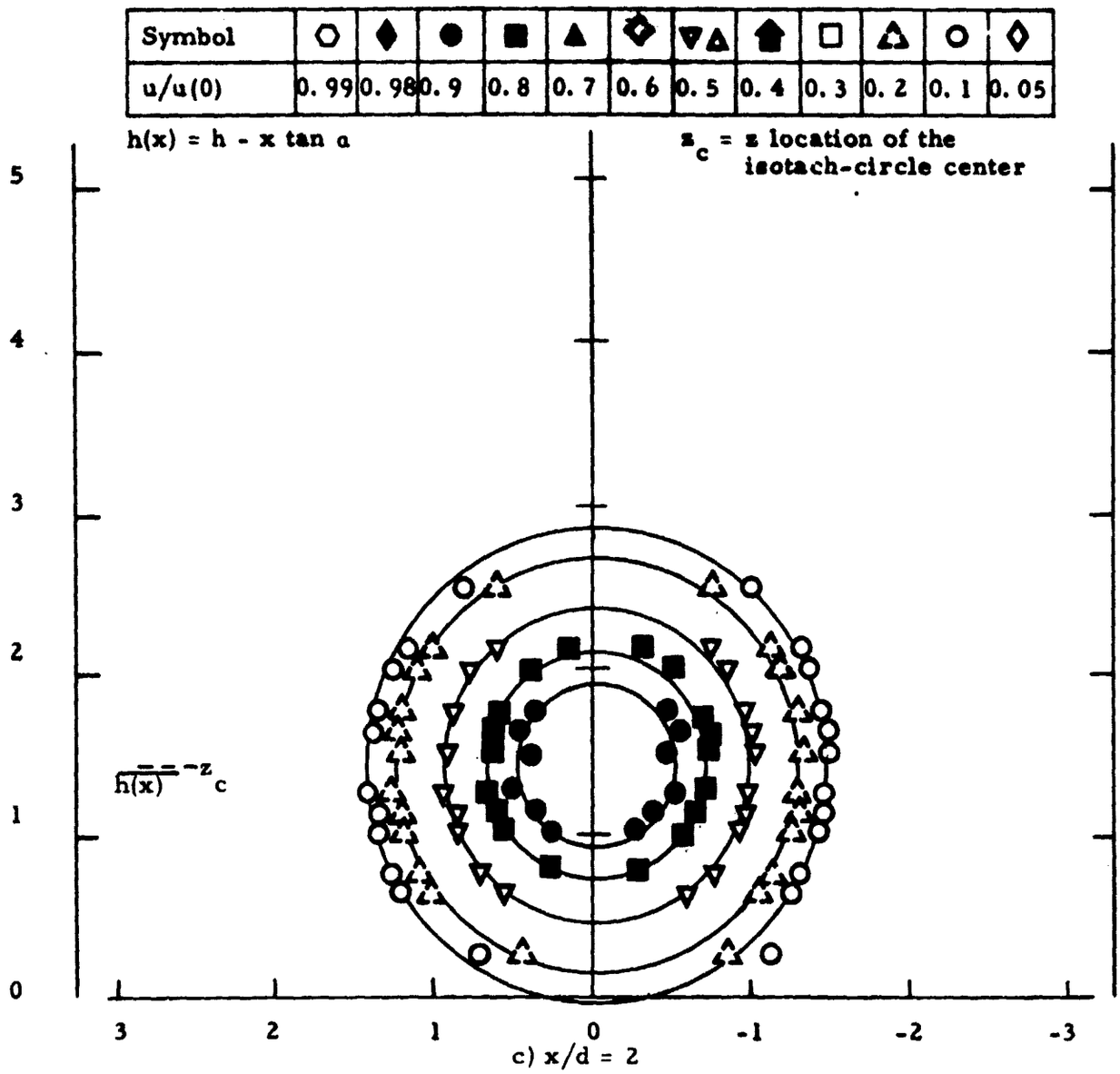
Symbol
u/u(0)
0.99
0.98
0.9
0.8
0.7
0.6
0.5
0.4
0.3
0.2
0.1
0.05
h(x) = h - x tan α
z_c = z location of the isotach-circle center
5
4
3
2
1
0
3
2
1
0
-1
-2
-3

c) x/d = 2

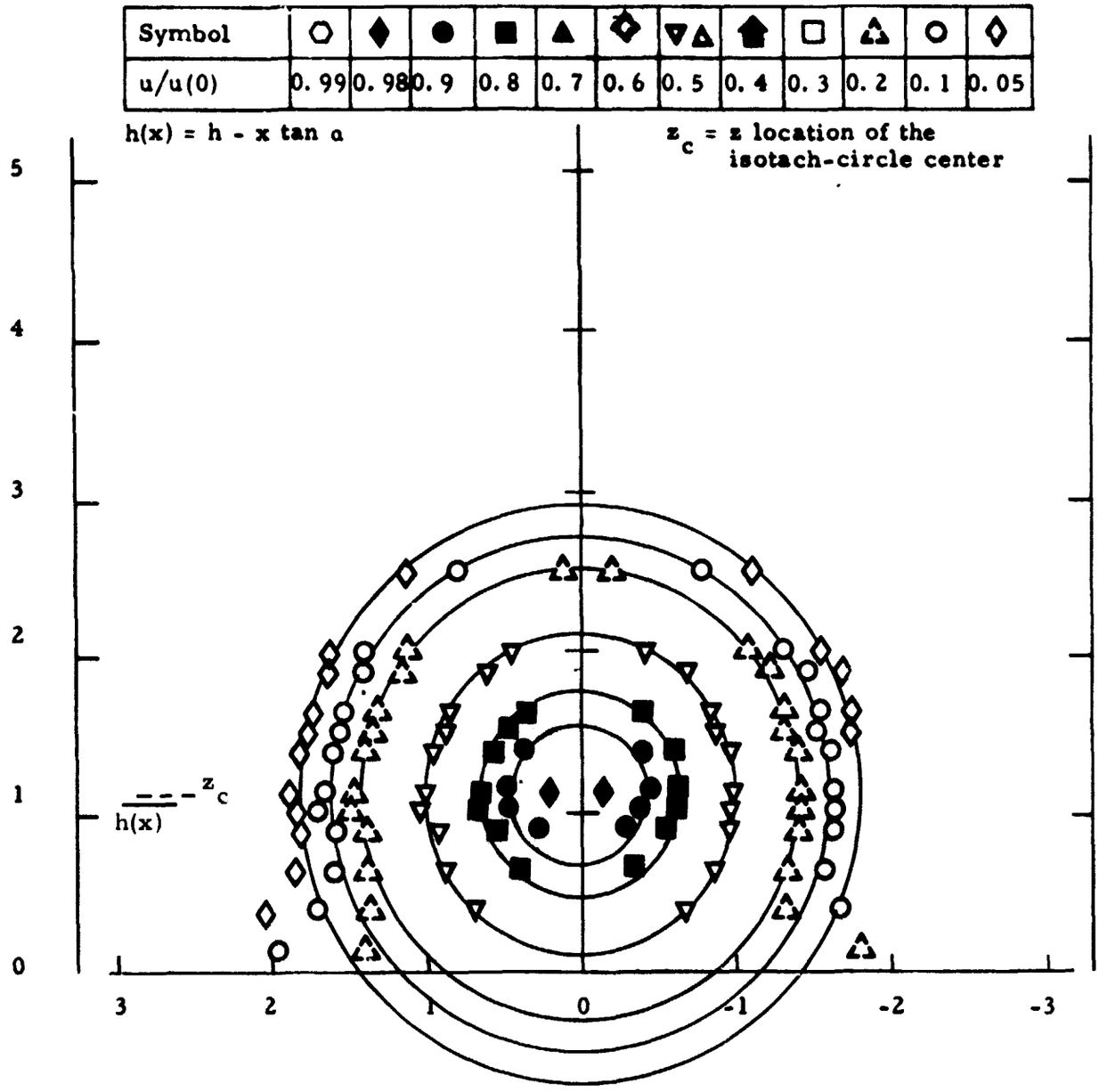
Symbol
u/u(0)
0.99
0.98
0.9
0.8
0.7
0.6
0.5
0.4
0.3
0.2
0.1
0.05
h(x) = h - x tan α
z_c = z location of the isotach-circle center
z_c / h(x)
5
4
3
2
1
0
3
2
1
0
-1
-2
-3

d) x/d = 3

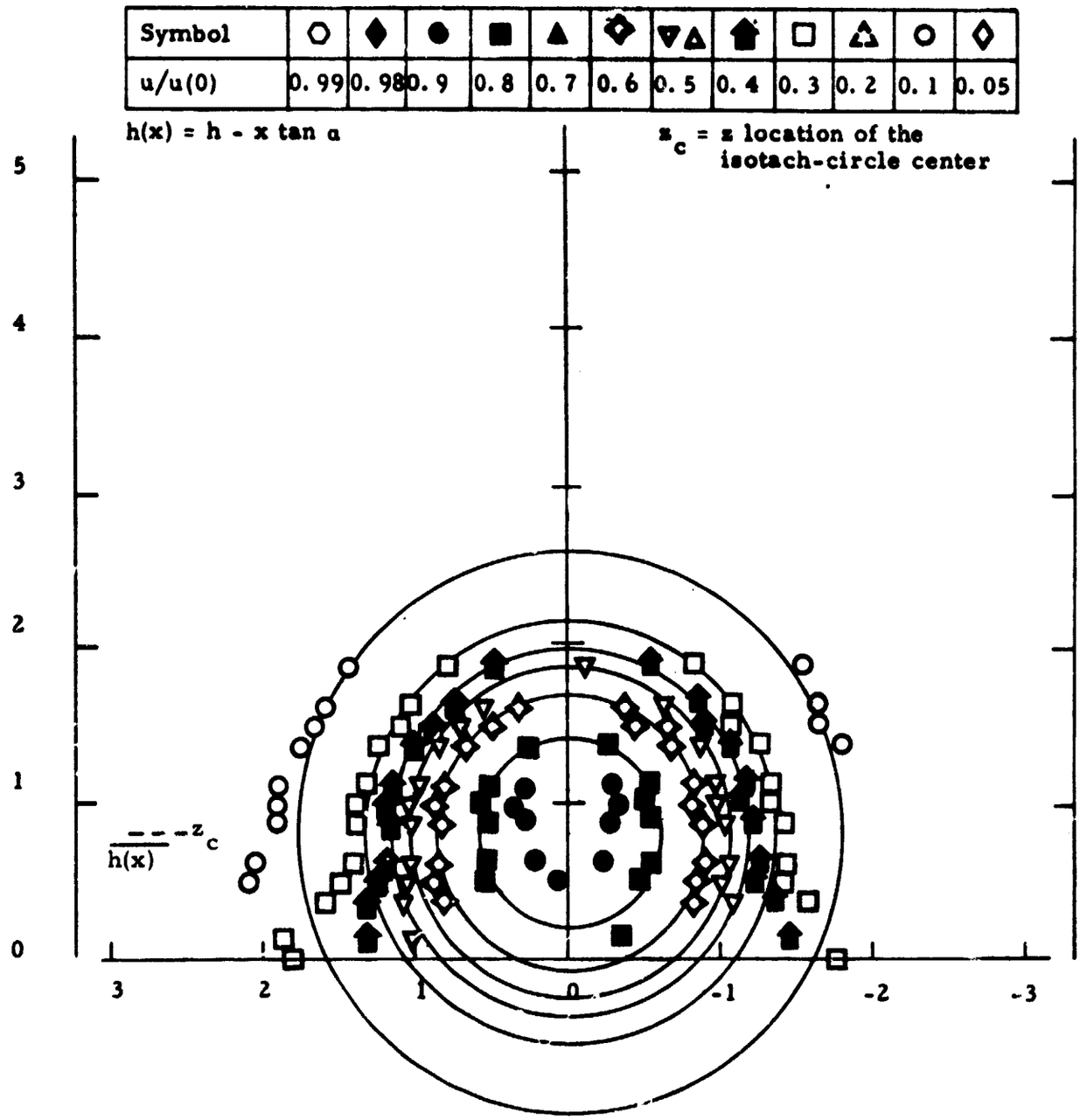
Symbol
u/u(0)
0.99
0.98
0.9
0.8
0.7
0.6
0.5
0.4
0.3
0.2
0.1
0.05
h(x) = h - x tan α
z_c = z location of the isotach-circle center
z_c / h(x)
5
4
3
2
1
0
3
2
1
0
-1
-2
-3

e) x/d = 4

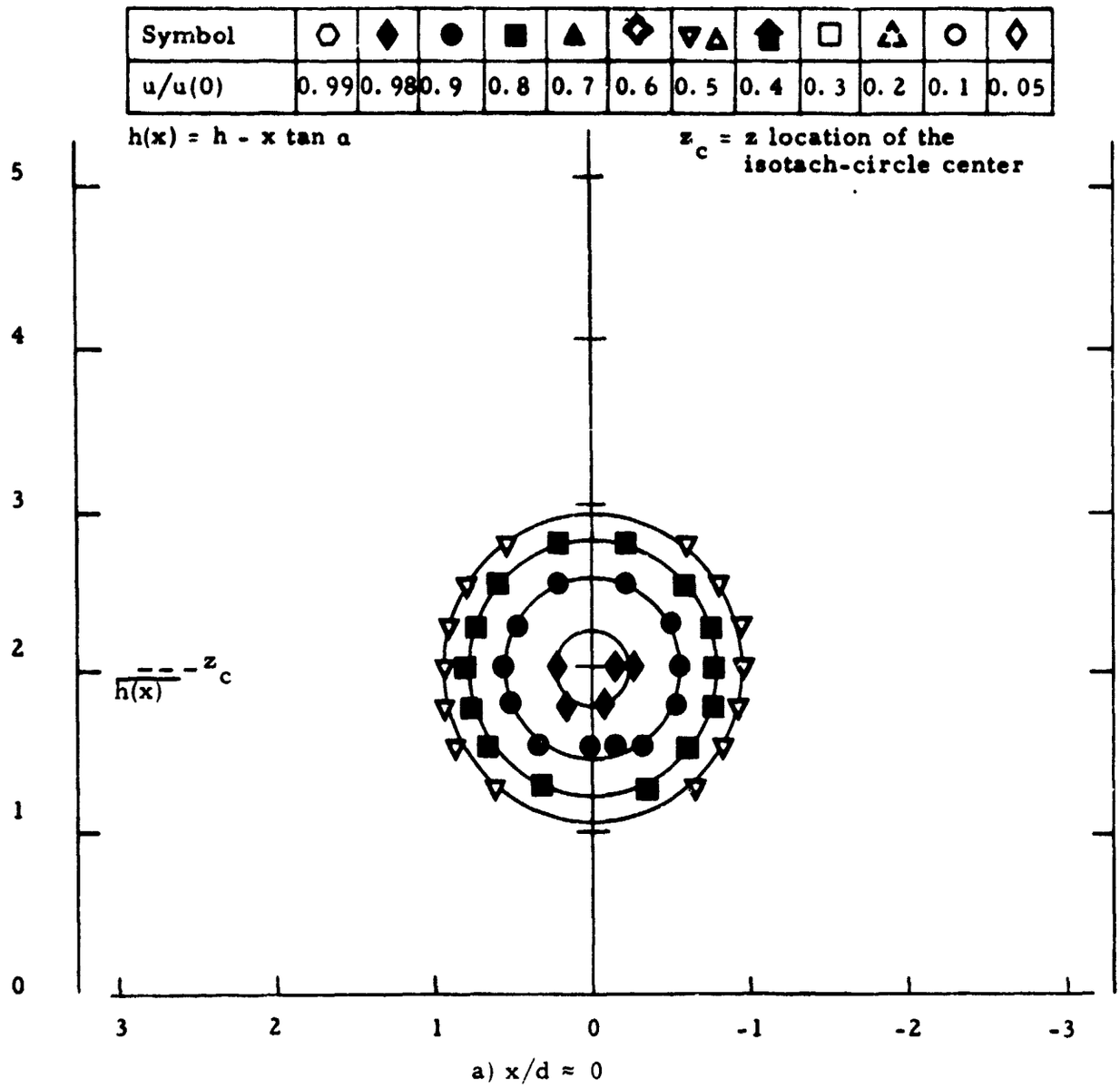

a) x/d ≈ 0

Figure 22. Isotach contours α = 12, h/d = 1, fully developed.

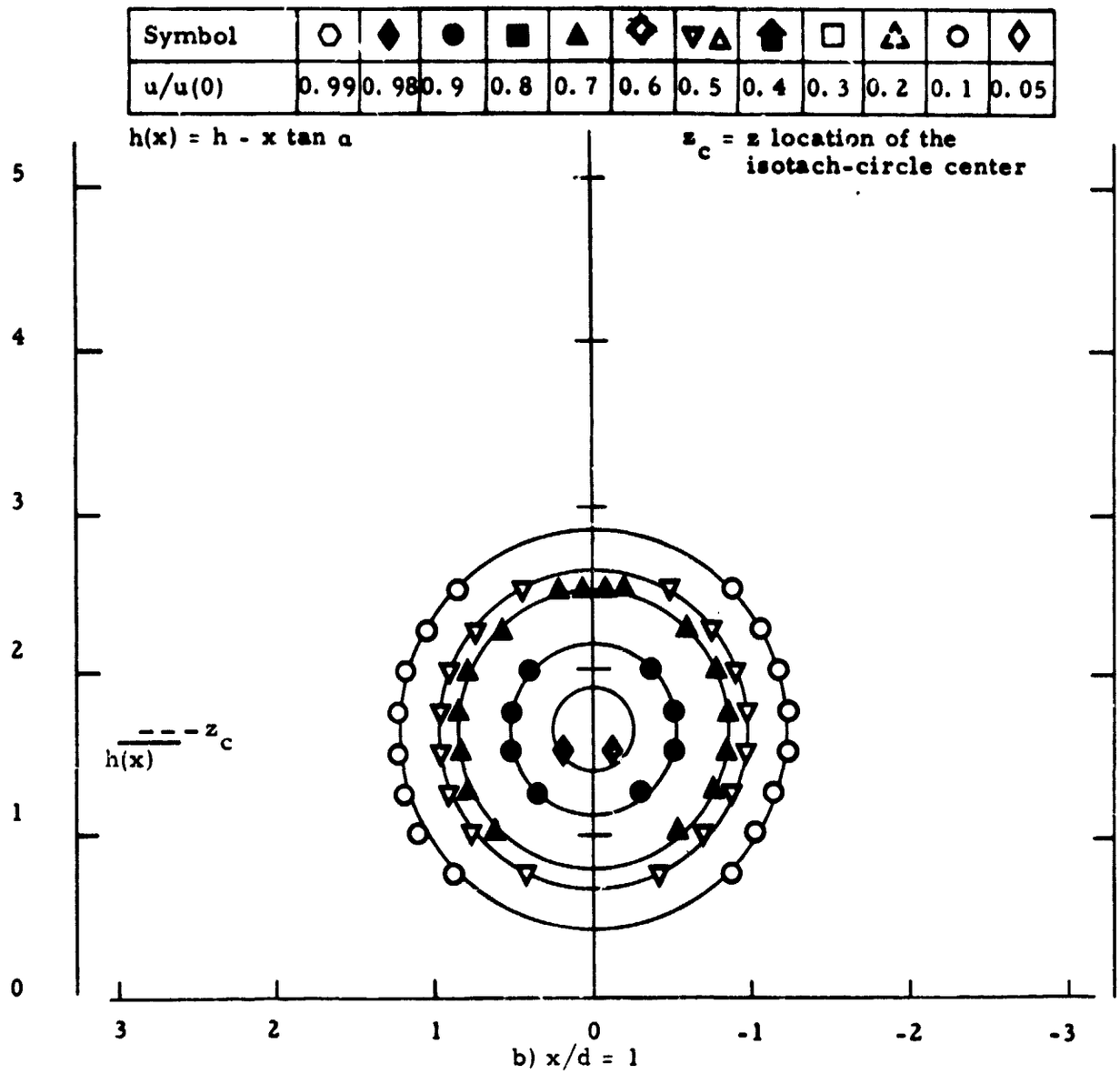
Symbol
u/u(0)
0.99
0.98
0.9
0.8
0.7
0.6
0.5
0.4
0.3
0.2
0.1
0.05
h(x) = h - x tan α
z_c = z location of the isotach-circle center
z_c / h(x)
5
4
3
2
1
0
3
2
1
0
-1
-2
-3

b) x/d = 1

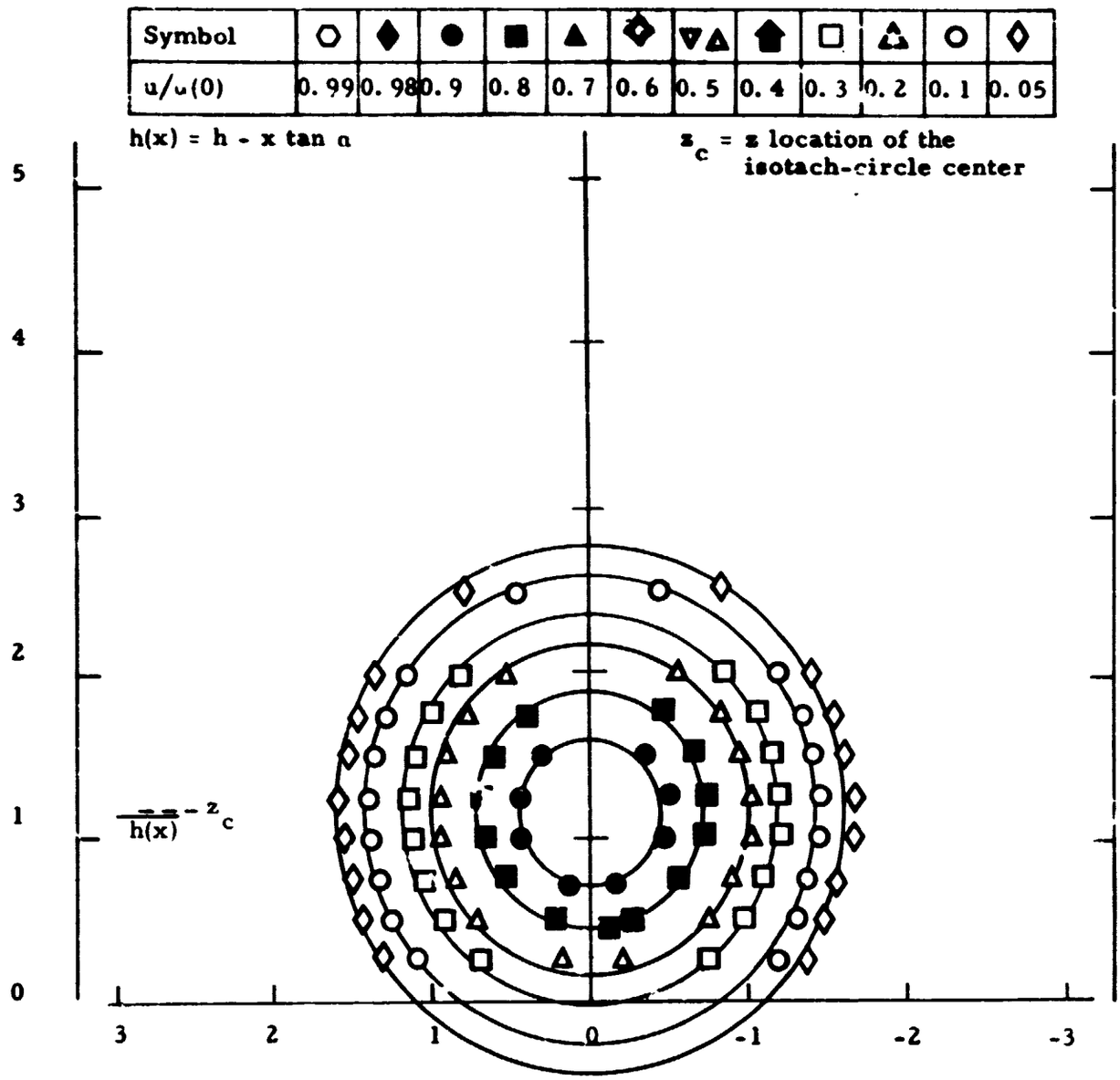
Symbol
u/u(0)
0.99
0.98
0.9
0.8
0.7
0.6
0.5
0.4
0.3
0.2
0.1
0.05
h(x) = h - x tan α
z_c = z location of the isotach-circle center
5
4
3
2
1
0
3
2
1
0
-1
-2
-3

c) x/d = 2

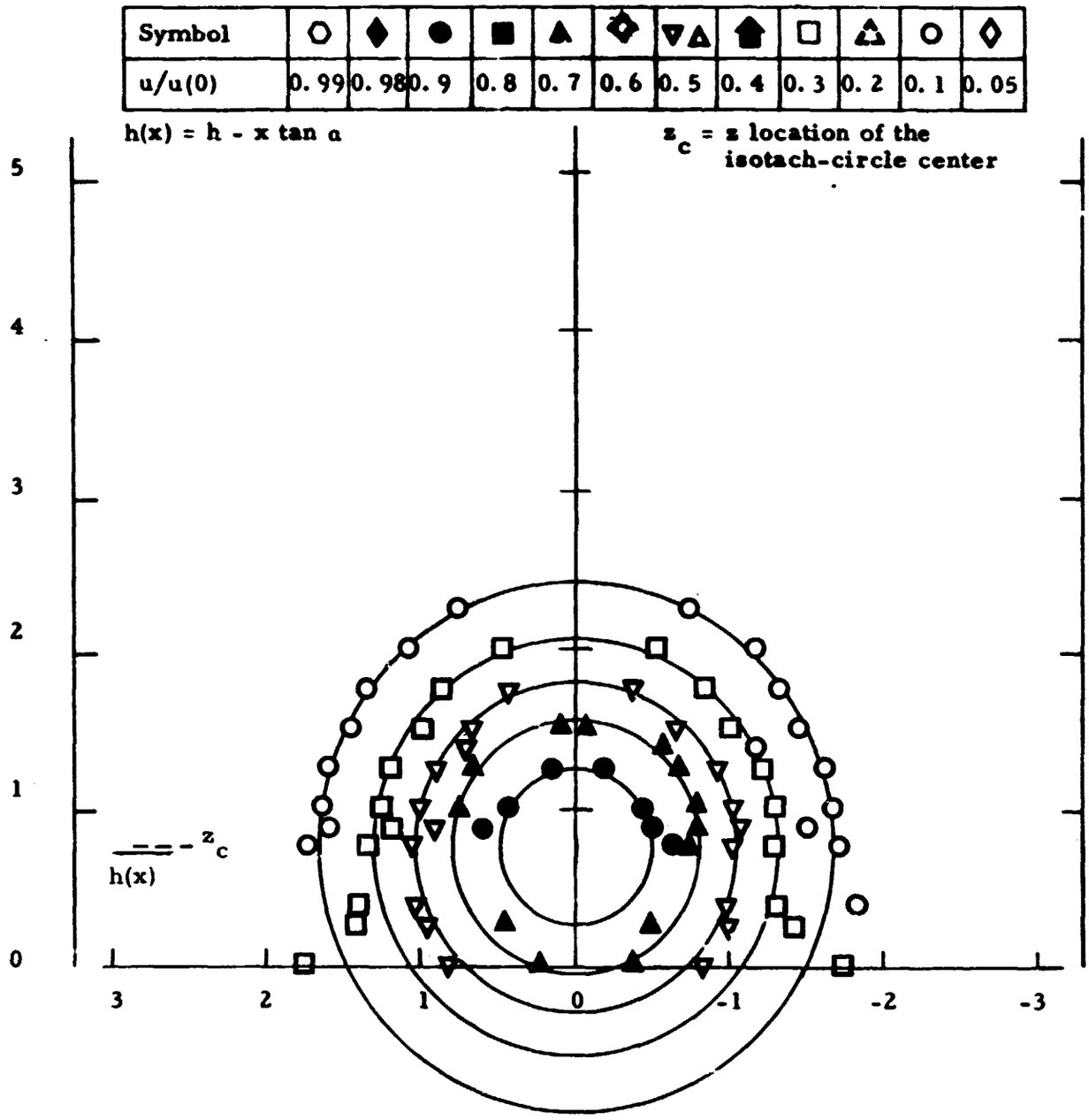
Symbol
u/u(0)
0.99
0.98
0.9
0.8
0.7
0.6
0.5
0.4
0.3
0.2
0.1
0.05
h(x) = h - x tan α
z_c = z location of the isotach-circle center
- z_c / h(x)
5
4
3
2
1
0
3
2
1
0
-1
-2
-3

d) x/d = 3

Symbol	○	◆	●	■	▲	◆	▽▲	⬟	□	△	○	◇
u/u(0)	0.99	0.98	0.9	0.8	0.7	0.6	0.5	0.4	0.3	0.2	0.1	0.05

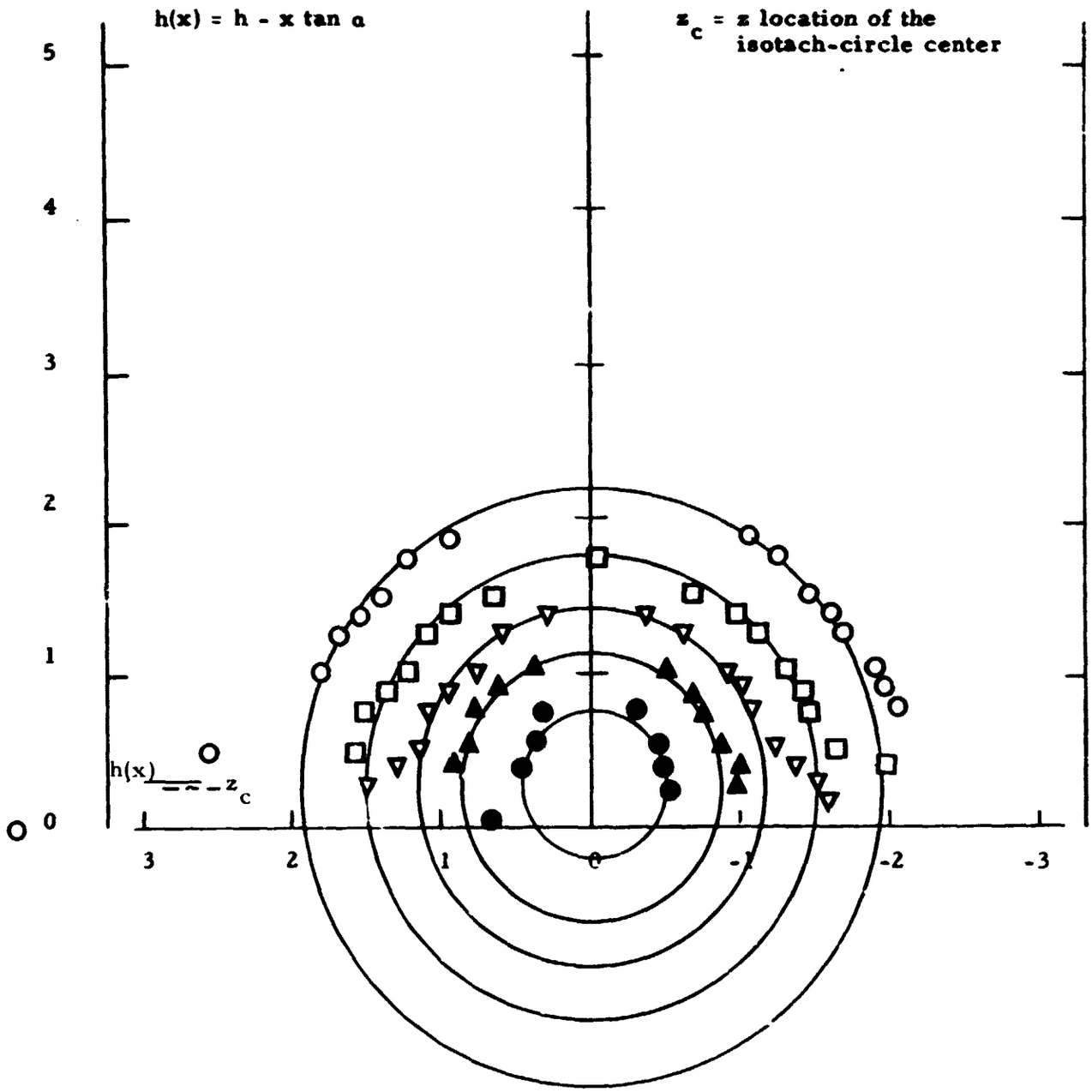

e) x/d = 4

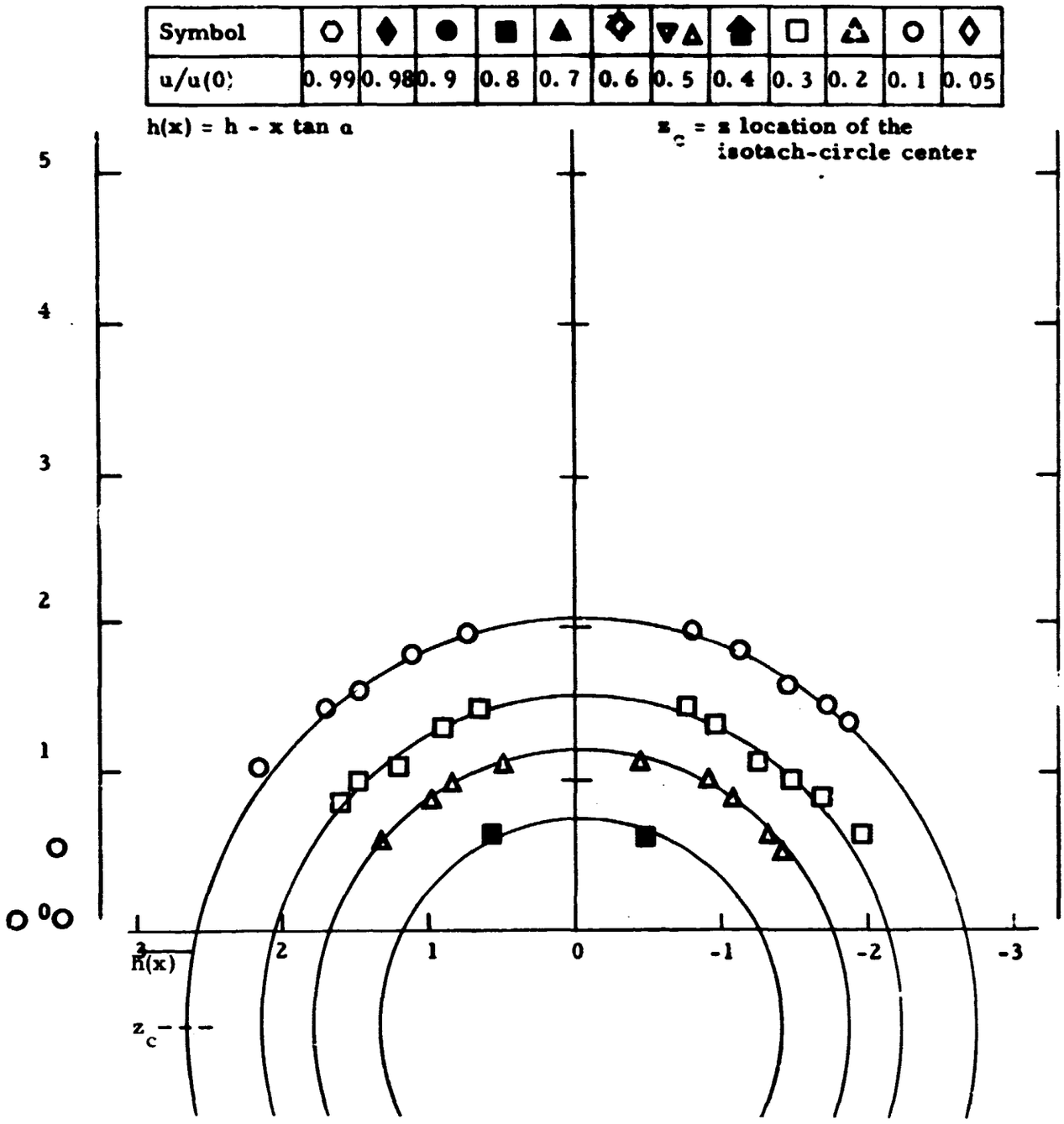
Symbol
u/u(0)
0.99
0.98
0.9
0.8
0.7
0.6
0.5
0.4
0.3
0.2
0.1
0.05
h(x) = h - x tan α
z_c = z location of the isotach-circle center
5
4
3
2
1
0
3
2
1
0
-1
-2
-3
h(x)
z_c

f) x/d = 5

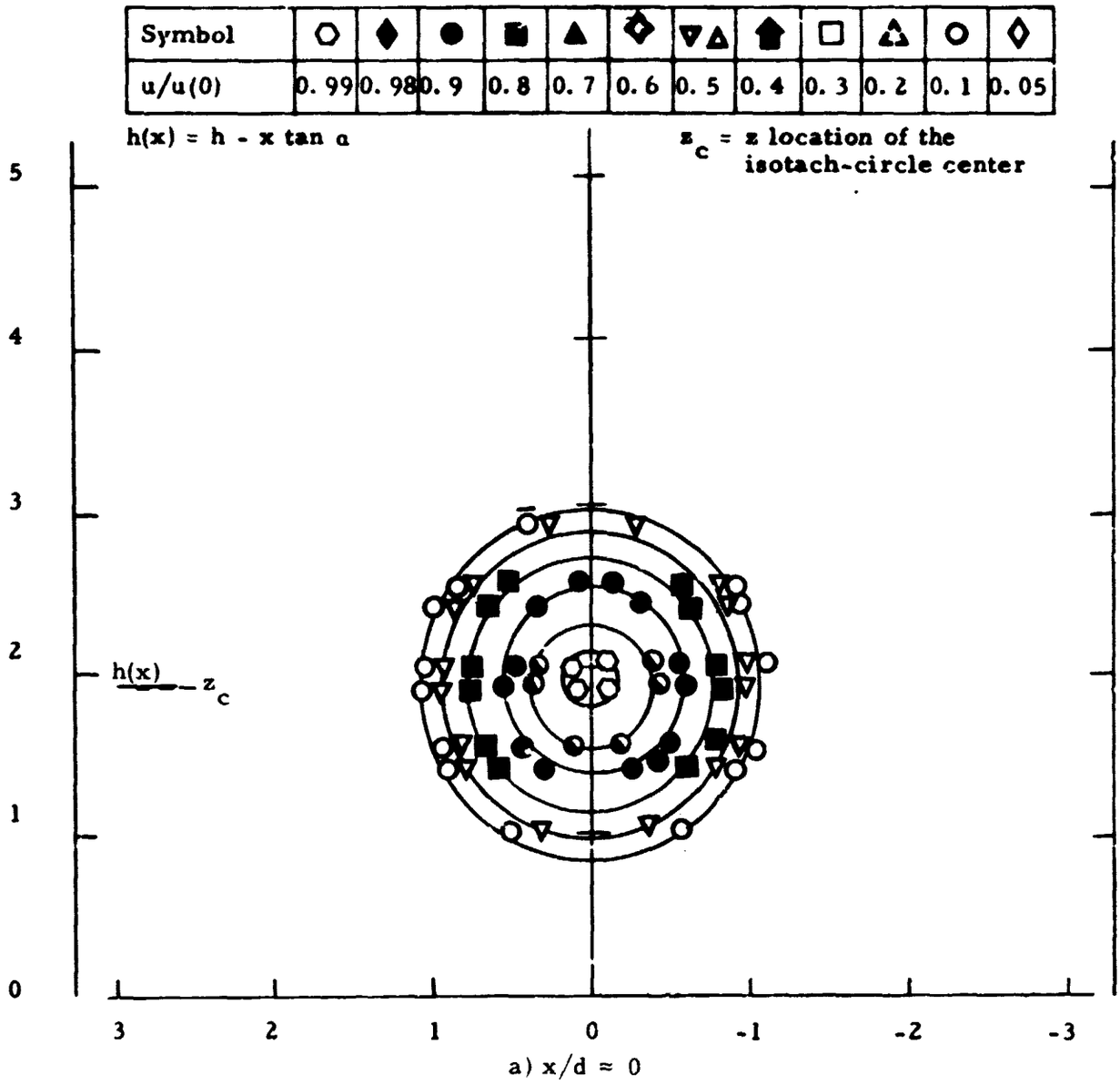

Figure 24. Isotach contours $\alpha = 15$, $h/d = 1$, fully developed.

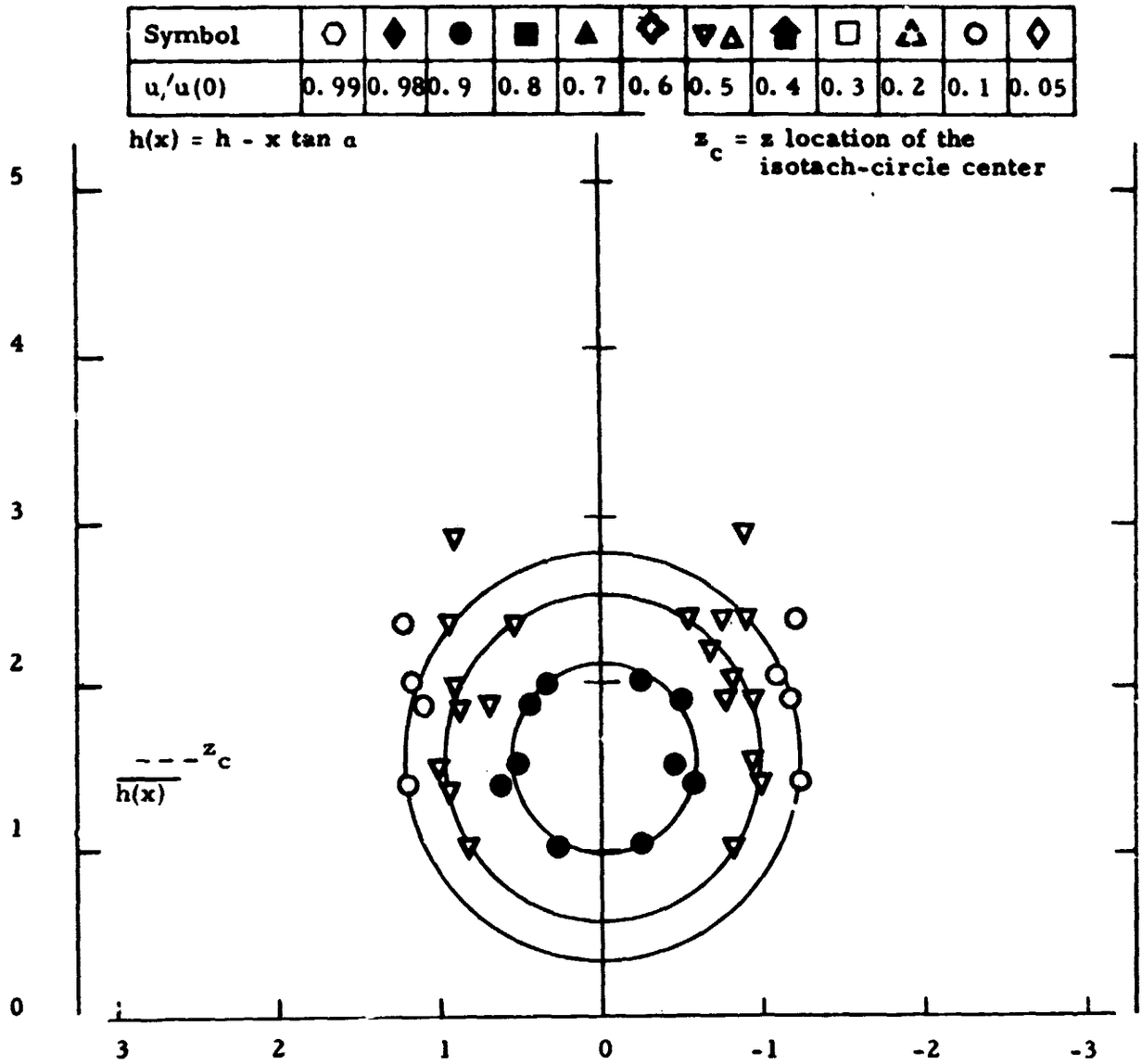
Symbol
u'/u(0)
0.99
0.98
0.9
0.8
0.7
0.6
0.5
0.4
0.3
0.2
0.1
0.05
h(x) = h - x tan α
z_c = z location of the isotach-circle center
z_c / h(x)
5
4
3
2
1
0
3
2
1
0
-1
-2
-3

b) x/d = 1

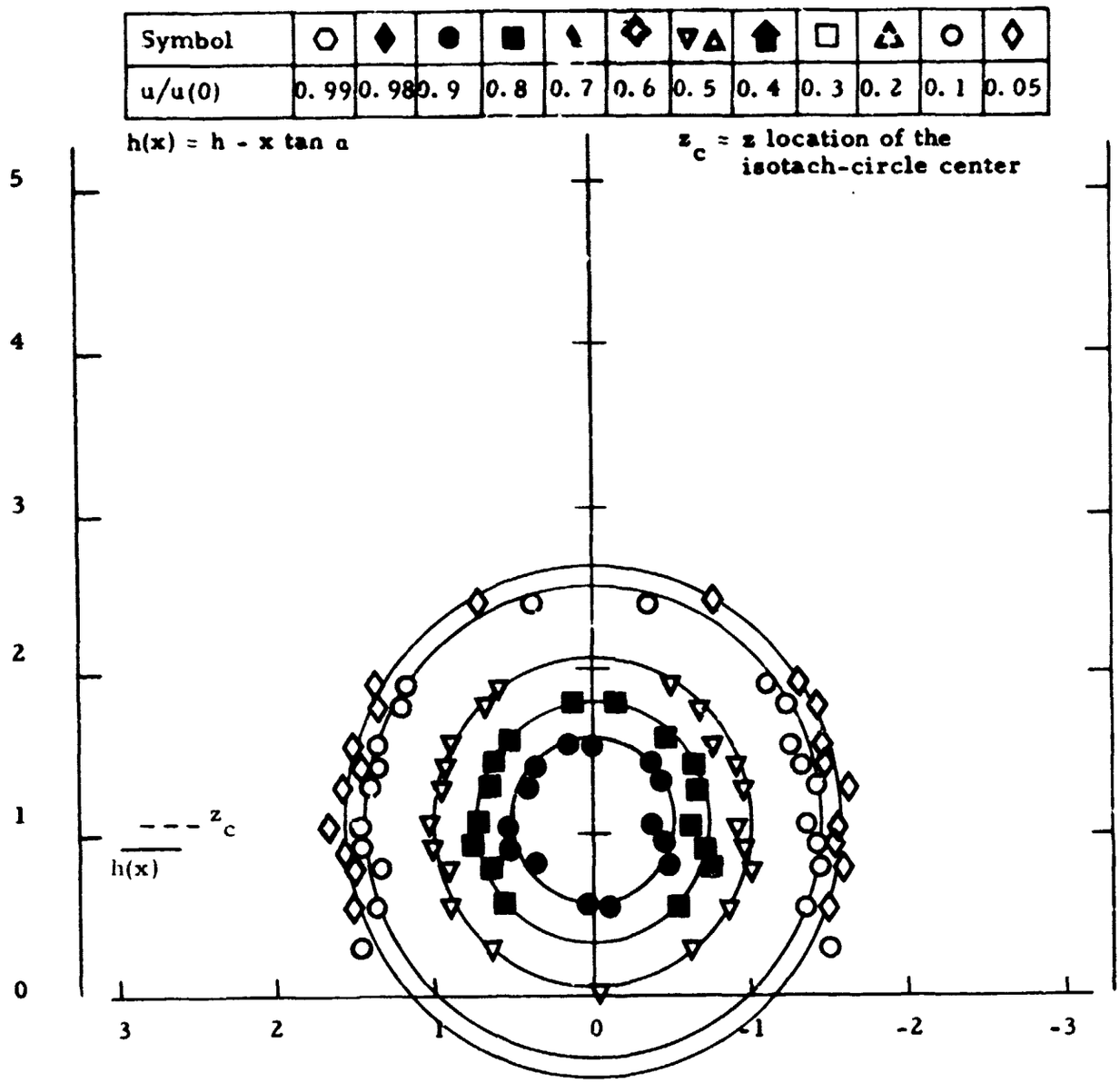
Symbol
u/u(0)
0.99
0.98
0.9
0.8
0.7
0.6
0.5
0.4
0.3
0.2
0.1
0.05
h(x) = h - x tan α
z_c = z location of the isotach-circle center
z_c
h(x)
5
4
3
2
1
0
3
2
1
0
-1
-2
-3

c) x/d = 2

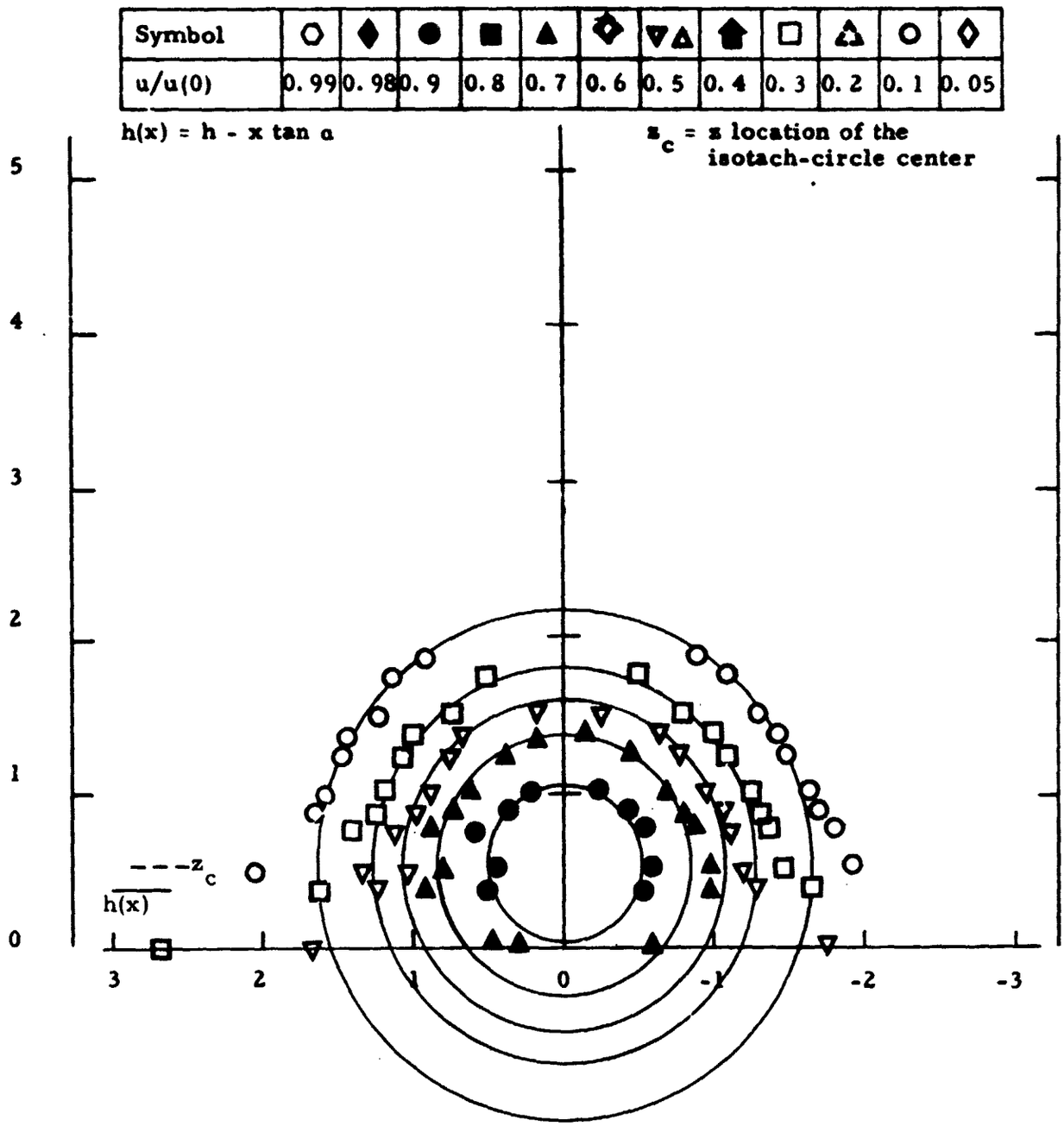
Symbol
u/u(0)
0.99
0.98
0.9
0.8
0.7
0.6
0.5
0.4
0.3
0.2
0.1
0.05
h(x) = h - x tan α
z_c = z location of the isotach-circle center
z_c
h(x)
5
4
3
2
1
0
3
2
1
0
-1
-2
-3

d) x/d = 3

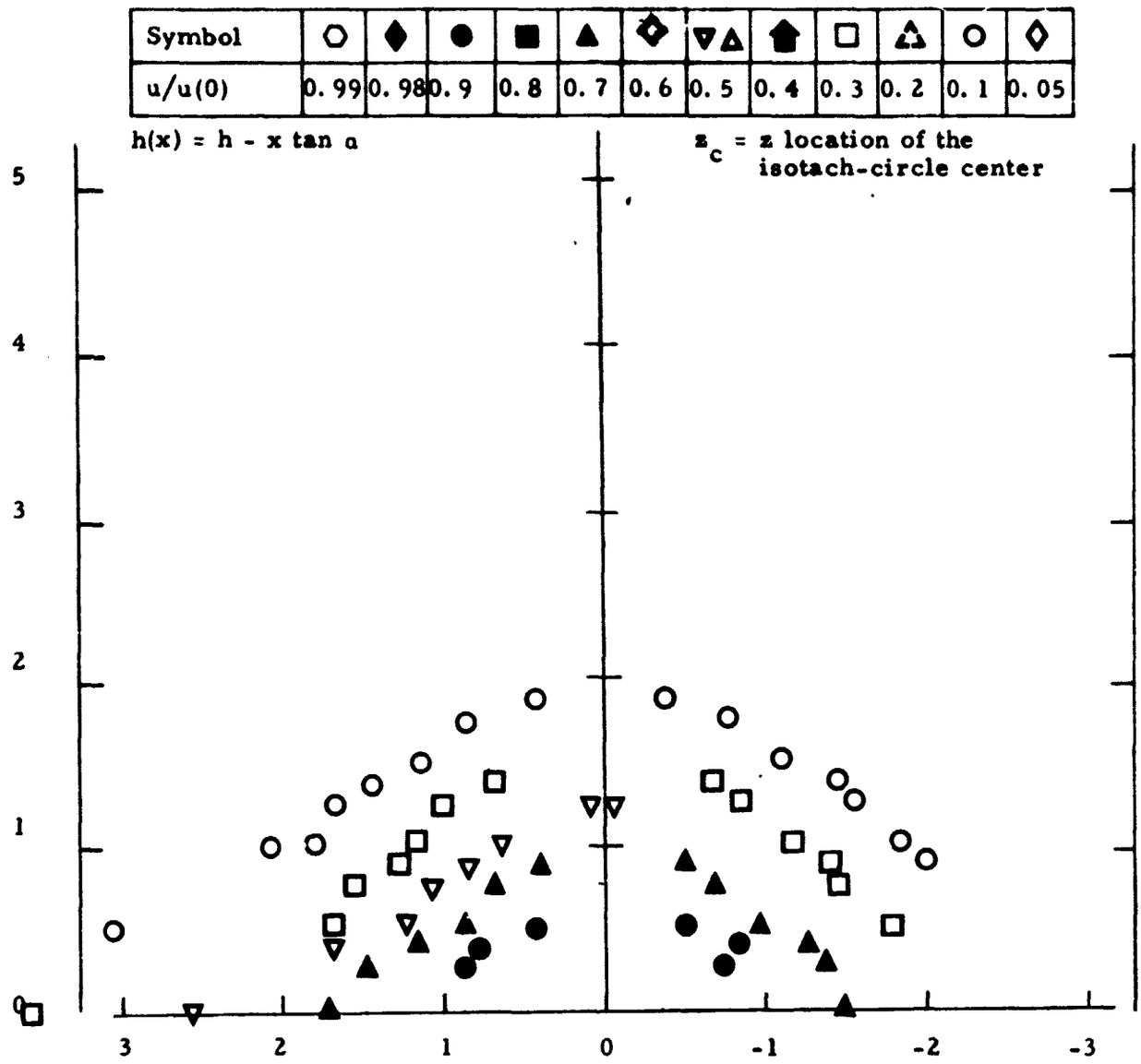
Symbol
u/u(0)
0.99
0.98
0.9
0.8
0.7
0.6
0.5
0.4
0.3
0.2
0.1
0.05
h(x) = h - x tan α
z_c = z location of the isotach-circle center
5
4
3
2
1
0
3
2
1
0
-1
-2
-3

e) x/d = 4

Symbol	○	◆	●	■	▲	◆	▽△	⬟	□	△	○	◇
u/u(0)	0.99	0.98	0.9	0.8	0.7	0.6	0.5	0.4	0.3	0.2	0.1	0.05

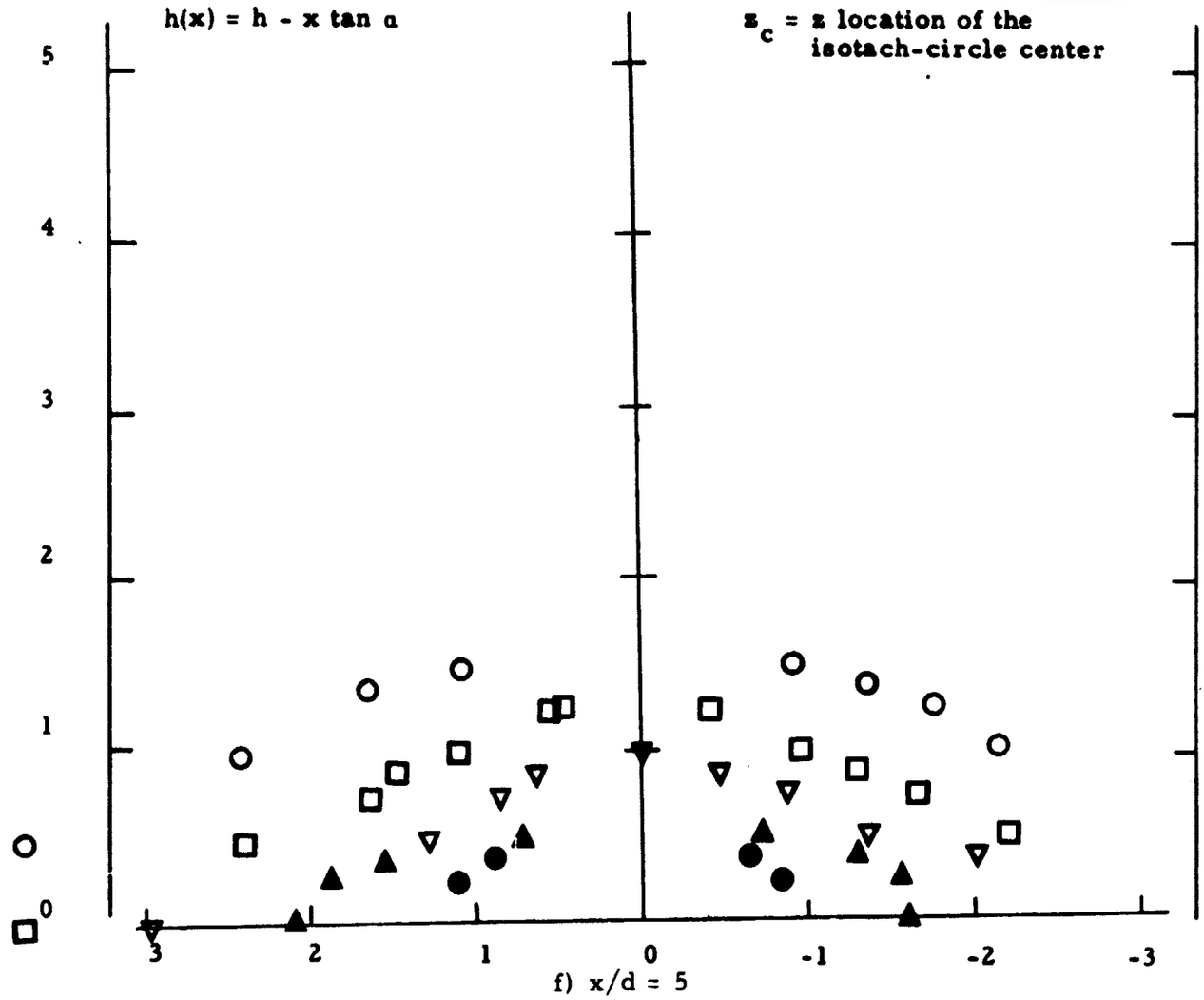

f) x/d = 5

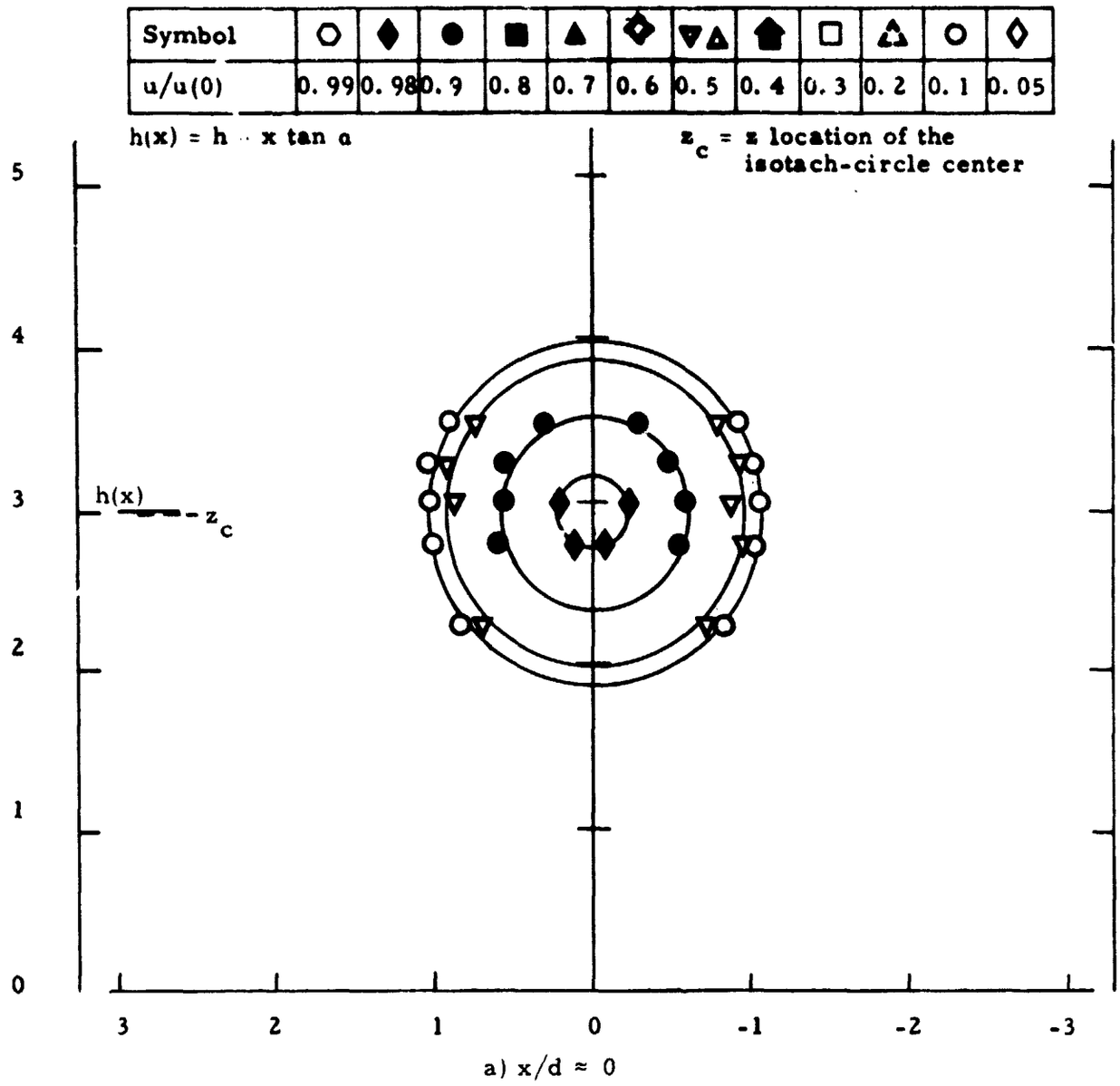

Figure 25. Isotach contours $\alpha = 15$, $h/d = 1.5$, fully developed.

Symbol	○	◆	●	■	▲	◆	▽△	⬟	□	△	○	◇
u/u(0)	0.99	0.98	0.9	0.8	0.7	0.6	0.5	0.4	0.3	0.2	0.1	0.05

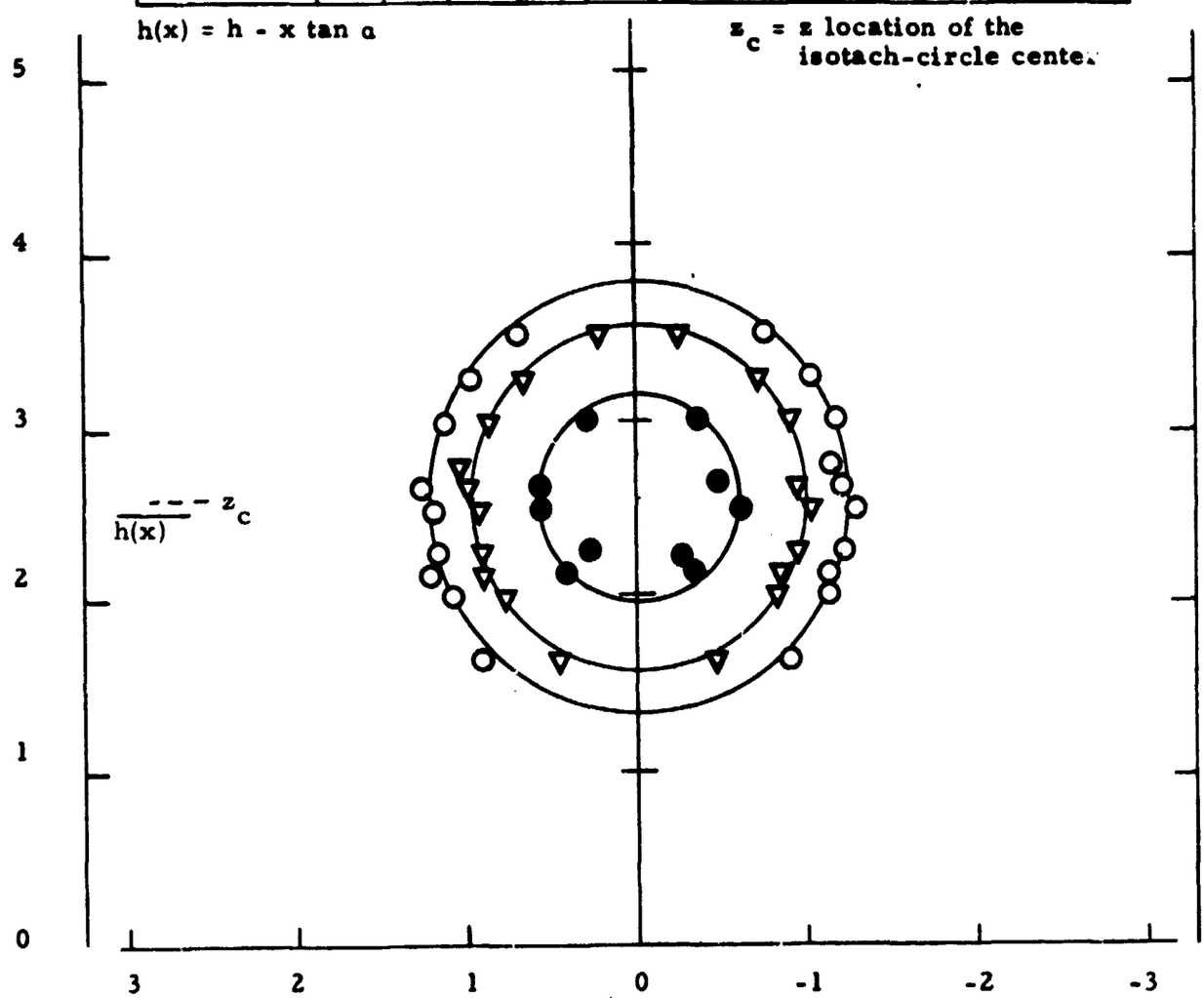

b) x/d = 1

Symbol	○	◆	●	■	▲	◇	▽△	⬟	□	△	○	◇
u/u(0)	0.99	0.98	0.9	0.8	0.7	0.6	0.5	0.4	0.3	0.2	0.1	0.05

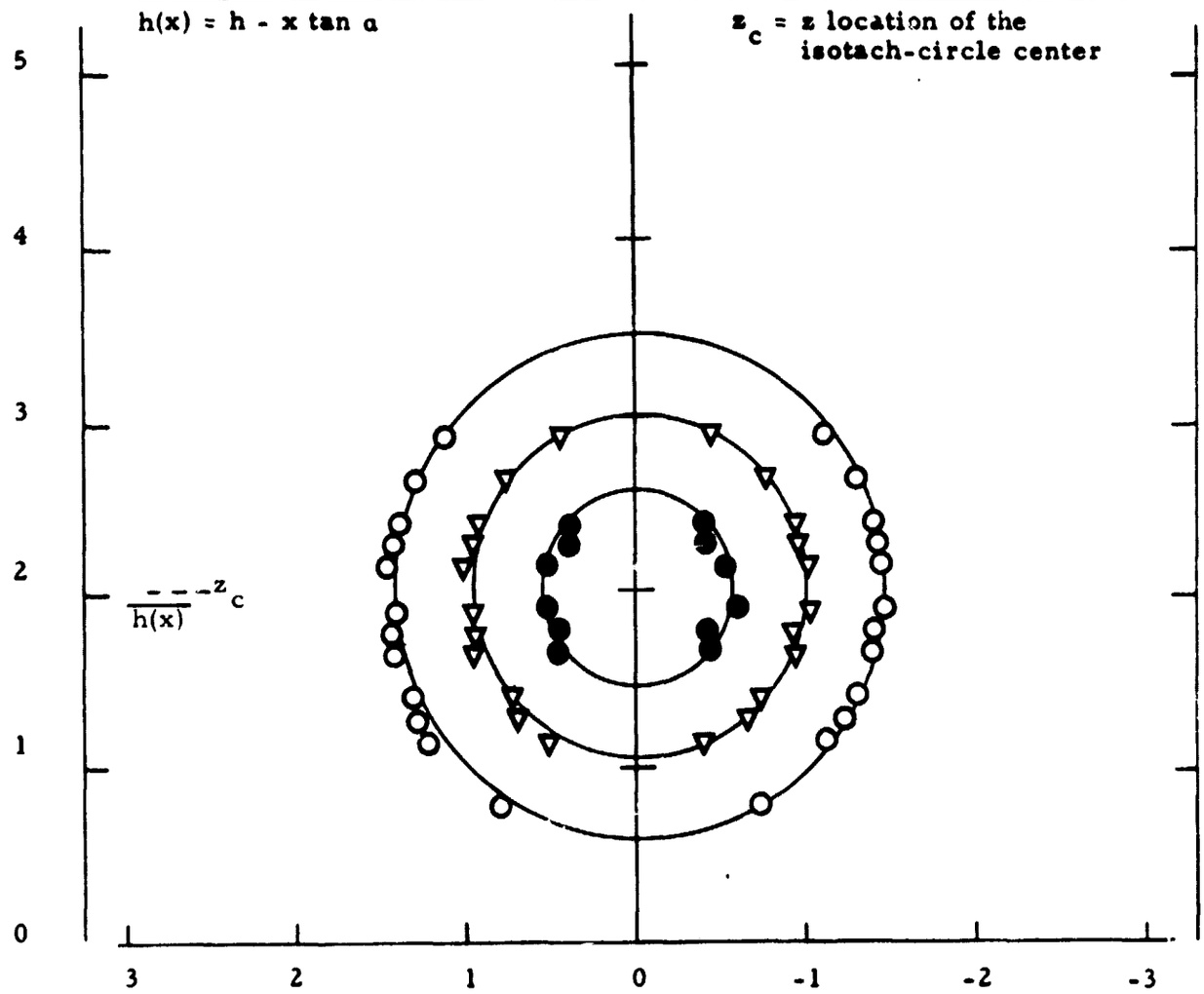

c) x/d = 2

Symbol	○	◆	●	■	▲	◆	▼▲	⬟	□	△	○	◇
u/u(0)	0.99	0.98	0.9	0.8	0.7	0.6	0.5	0.4	0.3	0.2	0.1	0.05

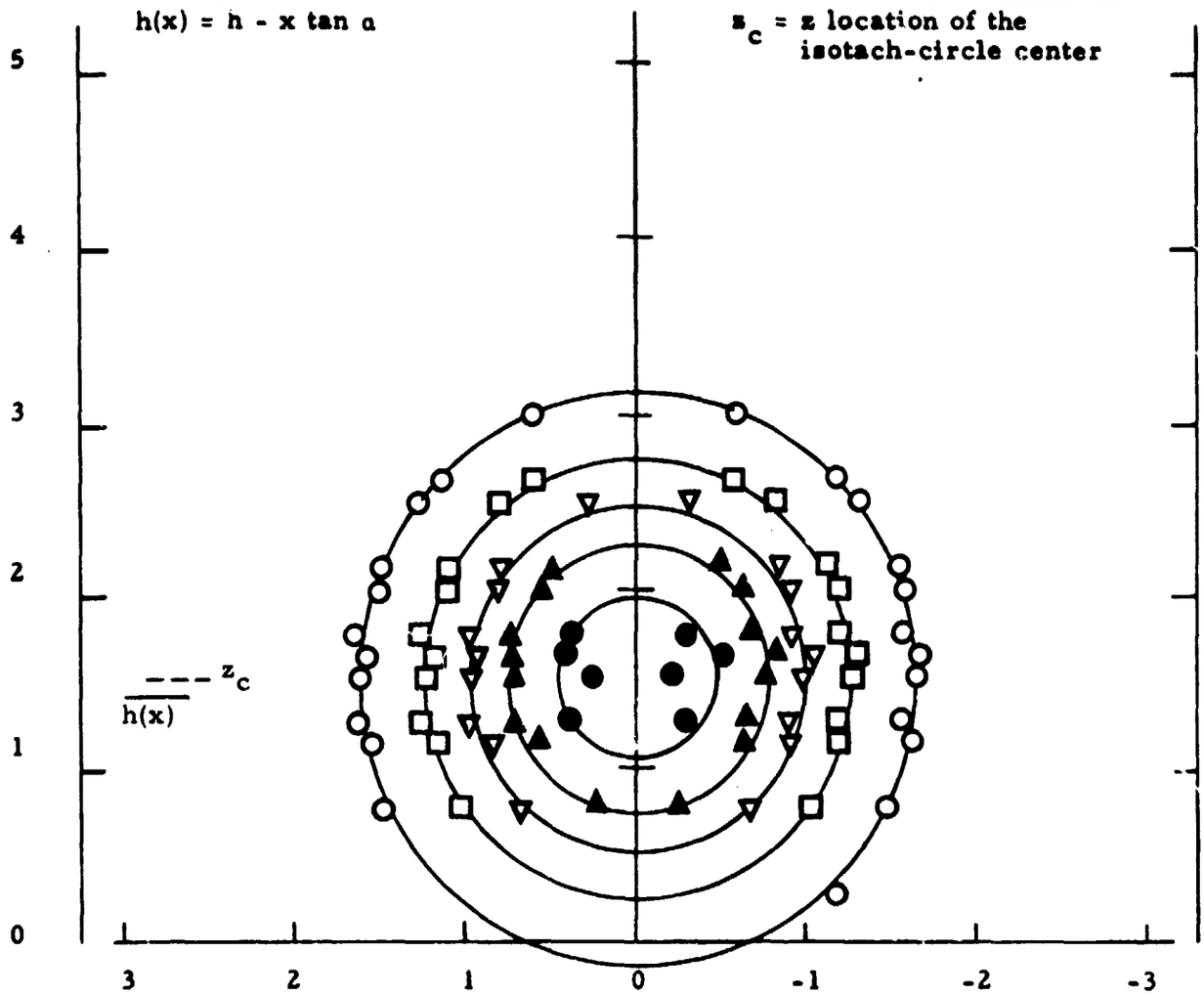

d) x/d = 3

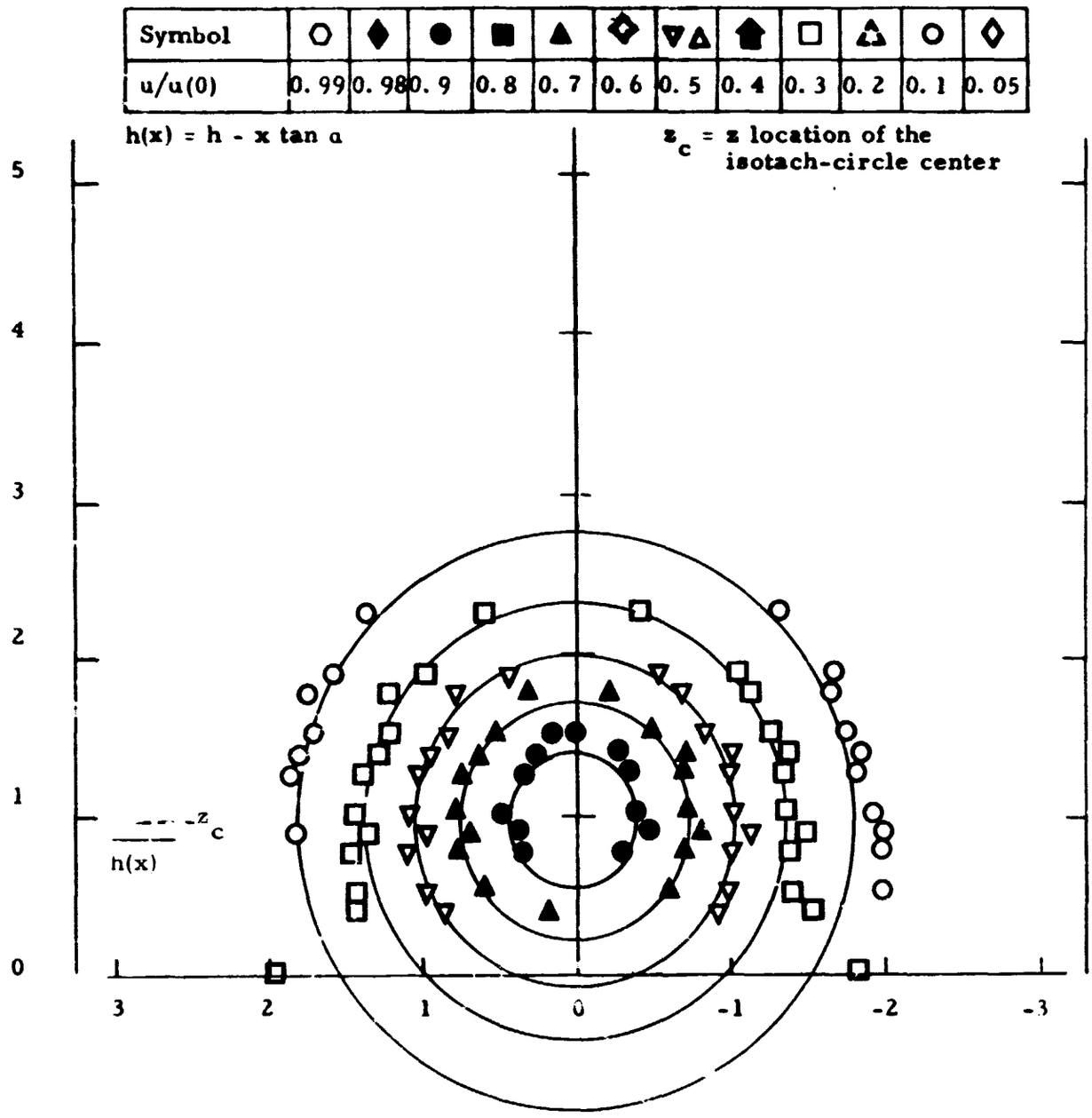
Symbol
u/u(0)
0.99
0.98
0.9
0.8
0.7
0.6
0.5
0.4
0.3
0.2
0.1
0.05
h(x) = h - x tan α
z_c = z location of the isotach-circle center
z_c
h(x)
5
4
3
2
1
0
3
2
1
0
-1
-2
-3

e) x/d = 4

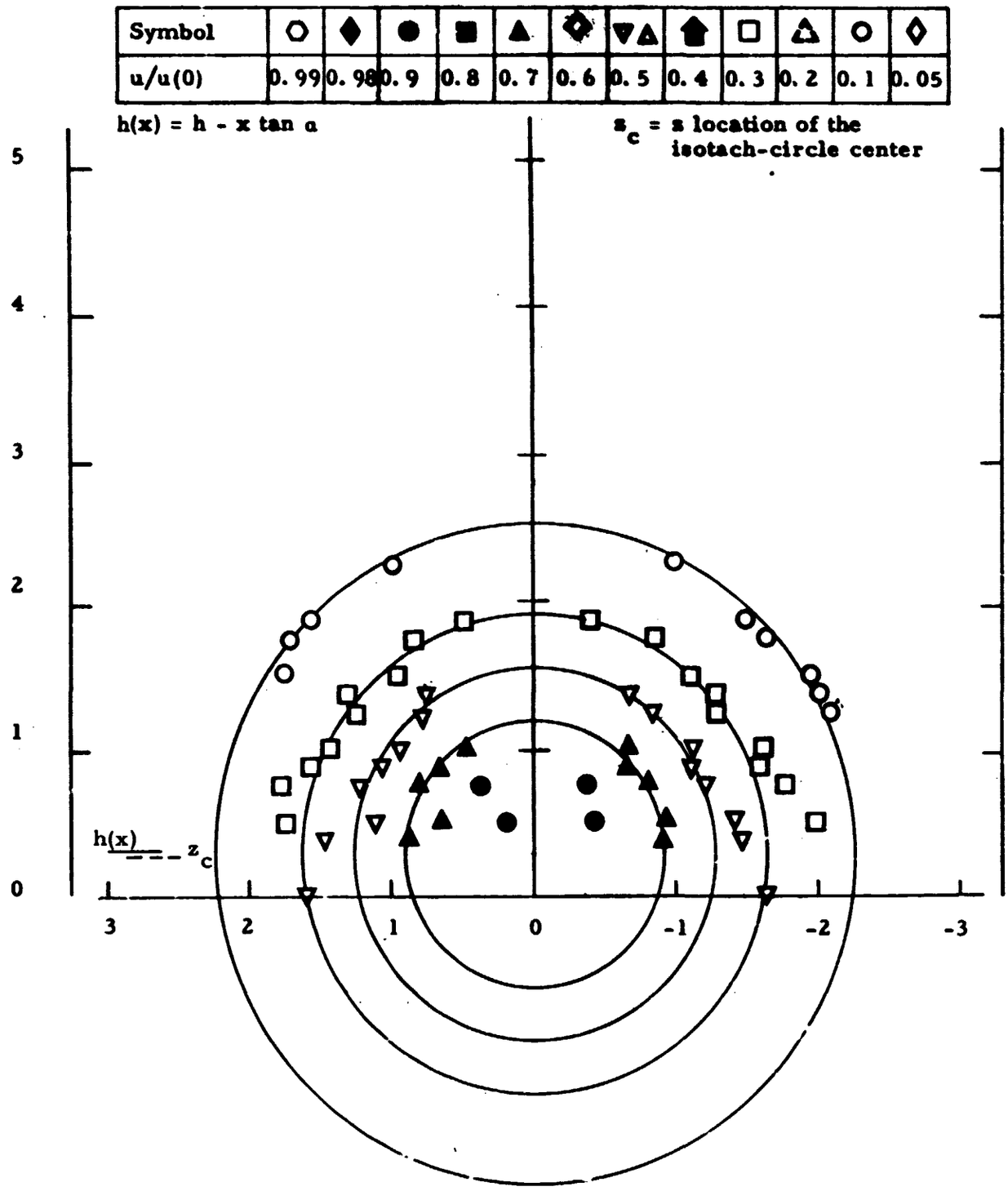
Symbol
u/u(0)
0.99
0.98
0.9
0.8
0.7
0.6
0.5
0.4
0.3
0.2
0.1
0.05
h(x) = h - x tan α
z_c = z location of the isotach-circle center
h(x)
z_c
5
4
3
2
1
0
3
2
1
0
-1
-2
-3

i) x/d = 5

APPENDIX E. Corrections to the Center of Momentum z_m Analysis, Section 4.5.2 of [1]

Following equation 30, the expression $\vec{v}_e = -\hat{n}\, Q_e$ results in

$$(\vec{v}_e \cdot \hat{k})\,(\vec{v}_e \cdot \hat{n}) = +Q_e^2\, \hat{n} \cdot \hat{k} \qquad \text{(A. 1)}$$

and hence equation (31) should be (the c following the equation number denotes "corrected")

$$\frac{F_p(x)}{J_o} = \frac{1}{J(0)} \int_{A_p} p\,dA = \frac{J_z}{J(0)}(x) + \sin\alpha + \frac{1}{2J(0)} \int_{A_c} \rho\, Q_e^2\, \hat{k} \cdot \hat{n}\, dA \qquad \text{(31c)}$$

The effect of the low pressure in the entrainment region was omitted from the moment-of-momentum equation (32). Including this term results in the following expression for the negative y-component equation evaluated with r measured from the center of the exit nozzle

$$\int_{A_p} p\, x\, dA = (h - z_m)J_x + xJ_z - \int_{A_e} \rho\,(\vec{r} \times \vec{v}_e) \cdot \hat{j}\,(\vec{v}_e \cdot \hat{n})\, dA - \int_{A_e} p(\vec{r} \times \hat{n}) \cdot \hat{j}\, dA \qquad \text{(32c)}$$

The remark that "the entrainment integral is zero except for the plane x = 0" is incorrect. Consequently, this term must be included in equation 33. The integrand of the entrainment integral may be written as

$$\rho\,[(\vec{r} \times \vec{v}_e) \cdot \hat{j}]\,[(\vec{v}_e \cdot \hat{n})] = \rho\,[-(z\,\hat{n} \cdot \hat{i} - x\,\hat{n} \cdot \hat{k})Q_e]\,[-Q_e]$$

$$= \rho\,[z\,\hat{n} \cdot \hat{i} - x\,\hat{n} \cdot \hat{k}]\,Q_e^2 \qquad \text{(A. 2)}$$

and combined with the integrand of the pressure integral over the entrainment area as shown by the following. The integrand of the pressure integral is

$$p_e(\vec{r} \times \hat{n}) \cdot \hat{j} = p_e[z\,\hat{n} \cdot \hat{i} - x\,\hat{n} \cdot \hat{k}]$$

or, using (29) (i.e., $(p_e)_g = -\rho Q_e^2/2$)

$$p(\vec{r} \times \hat{n}) \cdot \hat{j} = -\rho \frac{Q_e^2}{2} [z\,\hat{n} \cdot \hat{i} - x\,\hat{n} \cdot \hat{k}]$$

and combining this with the integrand of the other entrainment integral of (32c) results in

$$-\frac{1}{2} \int_{A_e} \rho Q_e^2 \, [z\,\hat{n} \cdot \hat{i} - x\,\hat{n} \cdot \hat{k}] \, dA \qquad \text{(A. 3)}$$

The corrected form for equation (33) can now be developed

$$\frac{z_m}{d} = \frac{h}{d} + \frac{x}{d} \frac{J_z}{J(0)\cos\alpha} - \frac{1}{J(0)\cos\alpha} \int_{A_p} p \frac{x}{d} \, dA - \frac{1}{2J(0)\cos\alpha} \int_{A_e} \rho Q_e^2 [z\,\hat{n} \cdot \hat{i} - x\,\hat{n} \cdot \hat{k}] \, dA$$

$$= \frac{h}{d} + \frac{x}{d} \frac{F_p}{J(0)\cos\alpha} - \frac{x}{d} \tan\alpha - \frac{x/d}{2J(0)\cos\alpha} \int_{A_e} \rho Q_e^2 \, \hat{k} \cdot \hat{n} \, dA$$

$$- \frac{1}{J(0)\cos\alpha} \int_{A_p} \frac{x}{d} p \, dA - \frac{1}{2J(0)\cos\alpha} \int \rho Q_e^2 (z\,\hat{n} \cdot \hat{i} - x\,\hat{n} \cdot \hat{k}) \, dA$$

$$= \frac{h}{d} + \frac{x}{d} \frac{F_p}{J(0)\cos\alpha} - \frac{x}{d} \tan\alpha - \frac{1}{J(0)\cos\alpha} \int_{A_p} \frac{x}{d} p \, dA$$

$$- \frac{1}{2J(0)\cos\alpha} \left\{ \int_{A_e} \rho Q_e^2 \left(\frac{z}{d} \hat{n} \cdot \hat{i} - \frac{x}{d} \hat{n} \cdot \hat{k} \right) dA + \frac{x}{d} \int_{A_e} \rho Q_e^2 \, k \cdot n \, dA \right\}$$

(33c)

Reasonable approximations can be made to this moment-of-momentum equation. Specifically, in the region where the jet is curving because of the plate presence, the term $z\,\hat{n} \cdot \hat{i}$ can be considered small with respect to the term $x\,\hat{n} \cdot \hat{k}$. Consequently, the bracketed term in the above equation can be approximated as

$$\frac{1}{2J(0)\cos\alpha} \left\{ -\int_{A_e} \rho Q_e^2 \left(\frac{z}{d} \hat{n} \cdot \hat{i} - \frac{x}{d} \hat{n} \cdot \hat{k} \right) dA + \frac{x}{d} \int_{A_e} \rho Q_e^2 \, \hat{k} \cdot \hat{n} \, dA \right\}$$

$$\cong \frac{1}{2J(0)\cos\alpha} \left\{ -\int_{A_e} \rho Q_e^2 \frac{x}{d} \hat{n} \cdot \hat{k} \, dA + \frac{x}{d} \int \rho Q_e^2 \, \hat{n} \cdot \hat{k} \, dA \right\}$$

$$\cong \frac{1}{2J(0)\cos\alpha} \frac{x}{2d} \int_{A_e} \rho Q_e^2 \hat{n} \cdot \hat{k} \, dA \qquad \text{(A. 7)}$$

A further simplification is possible on the basis of the numerical magnitude of this term with respect to z_m/d. The jet will be deflected upward in such a manner that the z_m/d values will be of the order 0.25 or greater. (See the calculations of the First Annual Report [1] which, although in error, are of the correct order of magnitude.) The ratio of the entrainment velocity at the edge of the jet to the jet exit velocity can be evaluated from the mass flux evaluations of the First Annual Report [1]. In order to estimate the order of magnitude of the entrainment integral term we use the result for the value of $d[\mathring{M}/(K\lambda)^{1/2}\rho u(o) A_o]/dx$ from Figure 34 of the earlier report. The values are

$$\frac{d}{dx}[\mathring{M}/(k\lambda)^{1/2}\rho u(o) A_o] = 0.171 \text{ fully developed nozzle} \qquad \text{(A. 4)}$$

$$\frac{d}{dx}[\mathring{M}/(k\lambda)^{1/2} \rho u(o) A_o] = 0.134 \text{ uniform nozzle} \qquad \text{(A. 5)}$$

where k and λ are coefficients to correct the momentum flux and to allow u(o) to be used as a normalizing velocity respectively, see [1]. The value of k can be considered to be unity. The velocity magnitude Q_e can be related to the $\mathring{M}$ values by the relationship

$$\rho \, 2\pi R \, Q_e = \frac{d}{dx} \mathring{M} \qquad \text{(A. 6)}$$

where R is the radius at which Q_e is evaluated. Since the ratio $\frac{1}{2J(0)\cos\alpha} \int \rho Q_e^2 \hat{n} \cdot \hat{k} \, dA$ is desired it is only important to accurately model Q_e where the product $\hat{n} \cdot \hat{k}$ is appreciable. This is fortunate since the isotachs of the First Annual Report indicate that the upper portion of the jet is unaffected by the jet-plate interaction except for a sufficiently large combination of α and x/d and even then the upper portion of the jet tends to retain a circular appearance. Also, since the control volume is a semi circular arc above the plate and since the entrainment in the bottom of the jet enters the lateral sides where $\hat{n} \cdot \hat{k} = 0$ it is only necessary to accurately model the upper portion. The magnitude of Q_e can then be evaluated from (A.6) as (note that the linear $d\mathring{M}/dx$

implies $dQ_e/dx = 0$)

$$\left[\frac{Q_e^2}{\lambda u(o)^2}\right] = \left[\frac{d}{dx/d}\ \dot{M}/\rho\lambda^{1/2}u(o)\ A_o\right]^2 \left[\frac{A_o}{2\pi\ Rd}\right]^2$$

$$= (0.17)^2 \left[\frac{d}{8R}\right]^2 \qquad \text{(A. 8)}$$

Recognizing that $(d/2R) \lesssim 1$, the magnitude of the term in equation (A. 7) can be estimated as

$$\frac{1}{2J(0)\cos\alpha}\ \frac{x}{2d} \int_{A_e} \rho Q_e^2\ \hat{n} \cdot \hat{k}\ dA \cong \left[\frac{Q_e^2}{\lambda u(o)^2}\right] \frac{1}{2A_o\cos\alpha}\left(\frac{x}{2d}\right)(0.7)\ \pi Rx$$

$$= \left(\frac{0.17}{4}\right)\left(\frac{1}{\cos\alpha}\right)(0.7)\left(\frac{R}{d}\right)\left(\frac{x}{d}\right)^2$$

$$\cong (x/d)^2\ \times\ 10^{-3} \qquad \text{(A. 9)}$$

where (0. 7) is considered to be the average value of $\hat{n} \cdot \hat{k}$ and the combination of the numerical values is rounded to 10^{-3}.

These considerations show that the entrainment effects are small for the x/d $(0 \leq x/d \leq 5)$ domain of interest. Hence, the integral representing the entrainment effects can safely be neglected for the purposes of computing $z_m(x)$ and the quantities which depend upon it.

APPENDIX C. Mass, Momentum, and Energy Flux Values

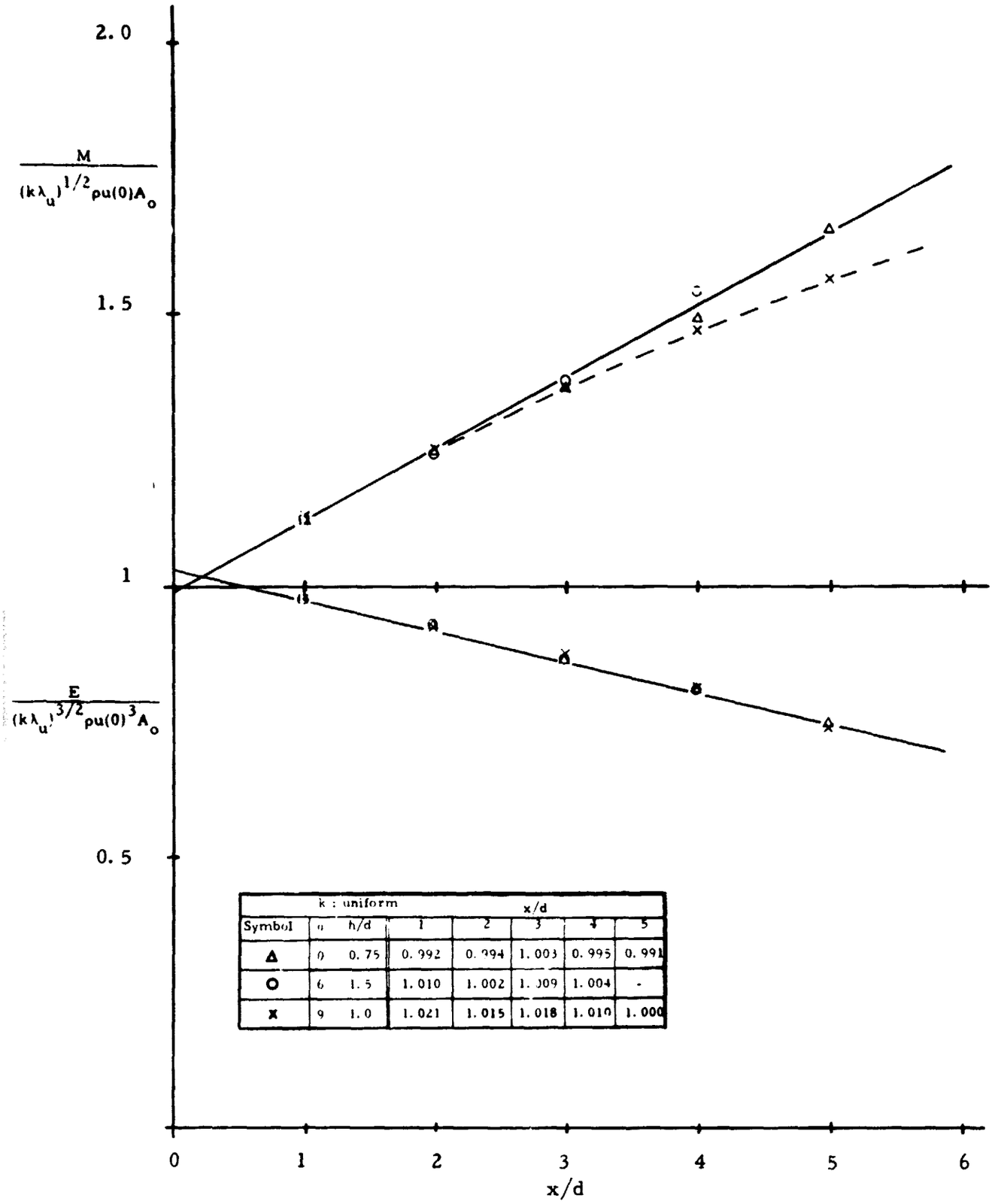

k : uniform			x/d				
Symbol	α	h/d	1	2	3	4	5
△	0	0.75	0.992	0.994	1.003	0.995	0.991
○	6	1.5	1.010	1.002	1.009	1.004	-
×	9	1.0	1.021	1.015	1.018	1.010	1.000

Figure 30. Normalized mass and energy flux values, uniform, $0 \leq |k - 1| \leq 0.03$

PRECEDING PAGE BLANK NOT FILMED

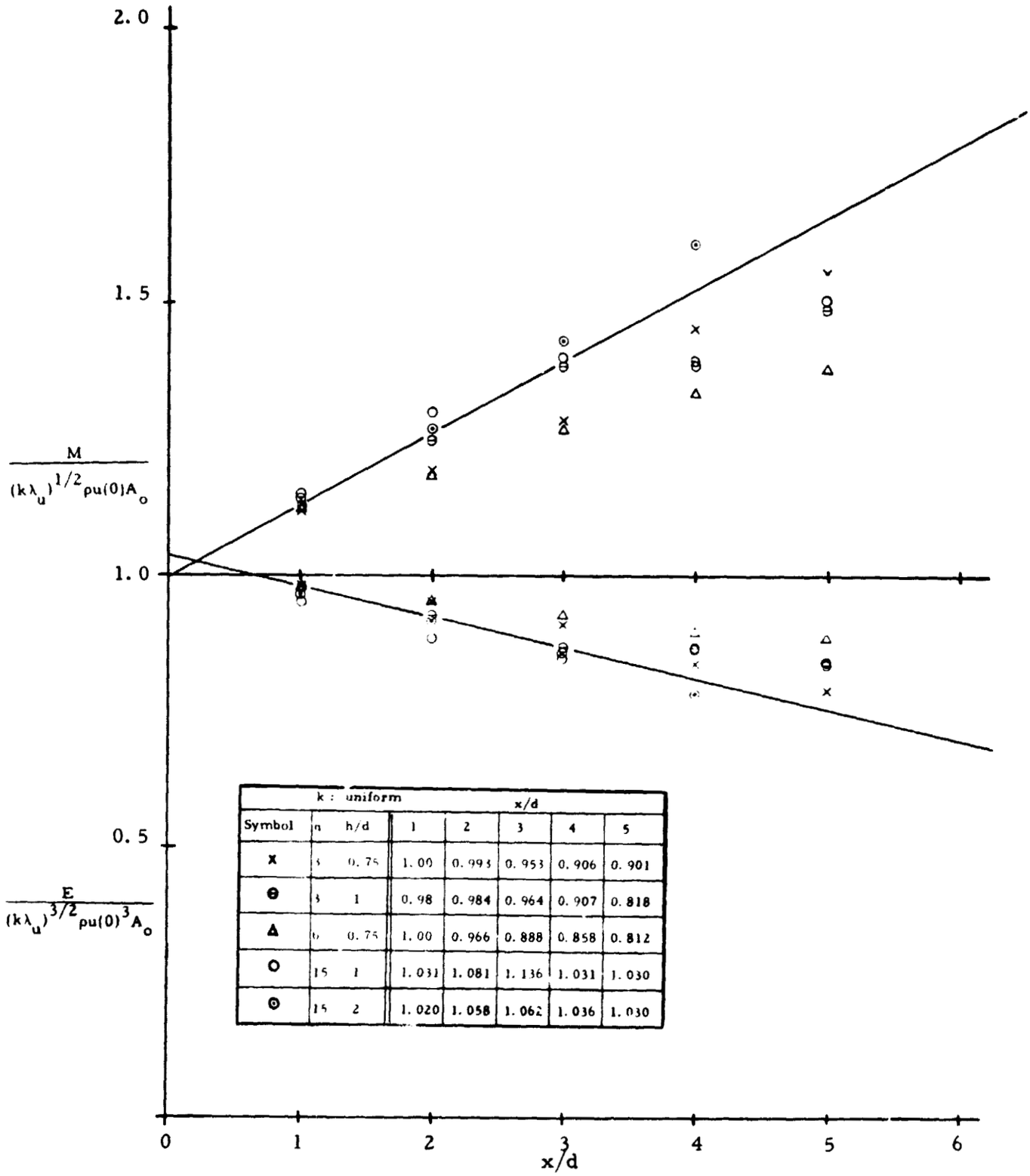

k : uniform			x/d				
Symbol	n	h/d	1	2	3	4	5
×	3	0.75	1.00	0.995	0.953	0.906	0.901
⊖	3	1	0.98	0.984	0.964	0.907	0.818
△	6	0.75	1.00	0.966	0.888	0.858	0.812
○	15	1	1.031	1.081	1.136	1.031	1.030
⊙	15	2	1.020	1.058	1.062	1.036	1.030

Figure 31. Normalized mass and energy flux values, uniform, $|k - 1| > 0.03$.

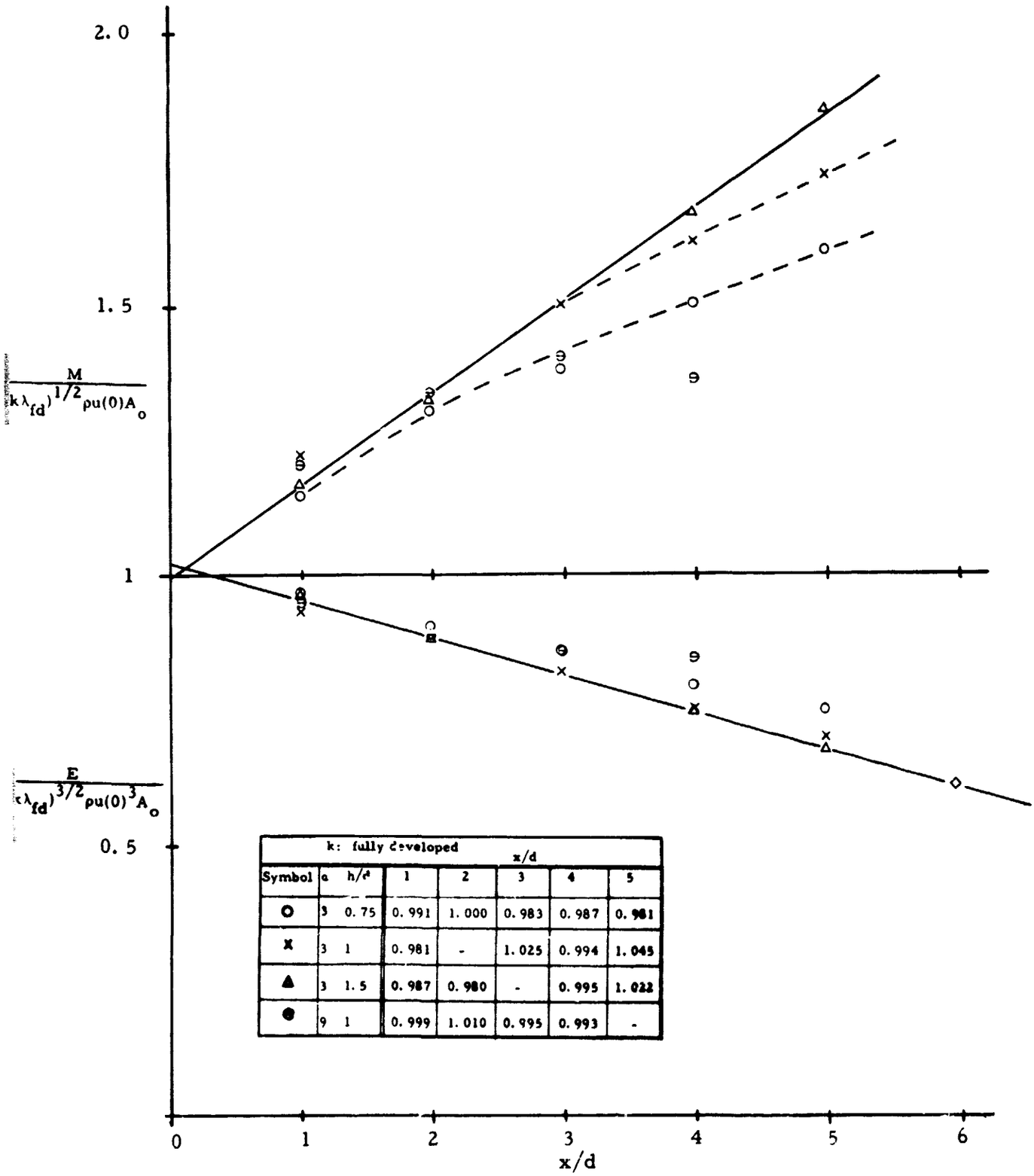

k: fully developed			x/d				
Symbol	α	h/d	1	2	3	4	5
○	3	0.75	0.991	1.000	0.983	0.987	0.981
×	3	1	0.981	-	1.025	0.994	1.045
▲	3	1.5	0.987	0.980	-	0.995	1.022
●	9	1	0.999	1.010	0.995	0.993	-

Figure 32. Normalized mass and energy flux values, fully developed, $0 \leq |k - 1| \leq 0.03$.

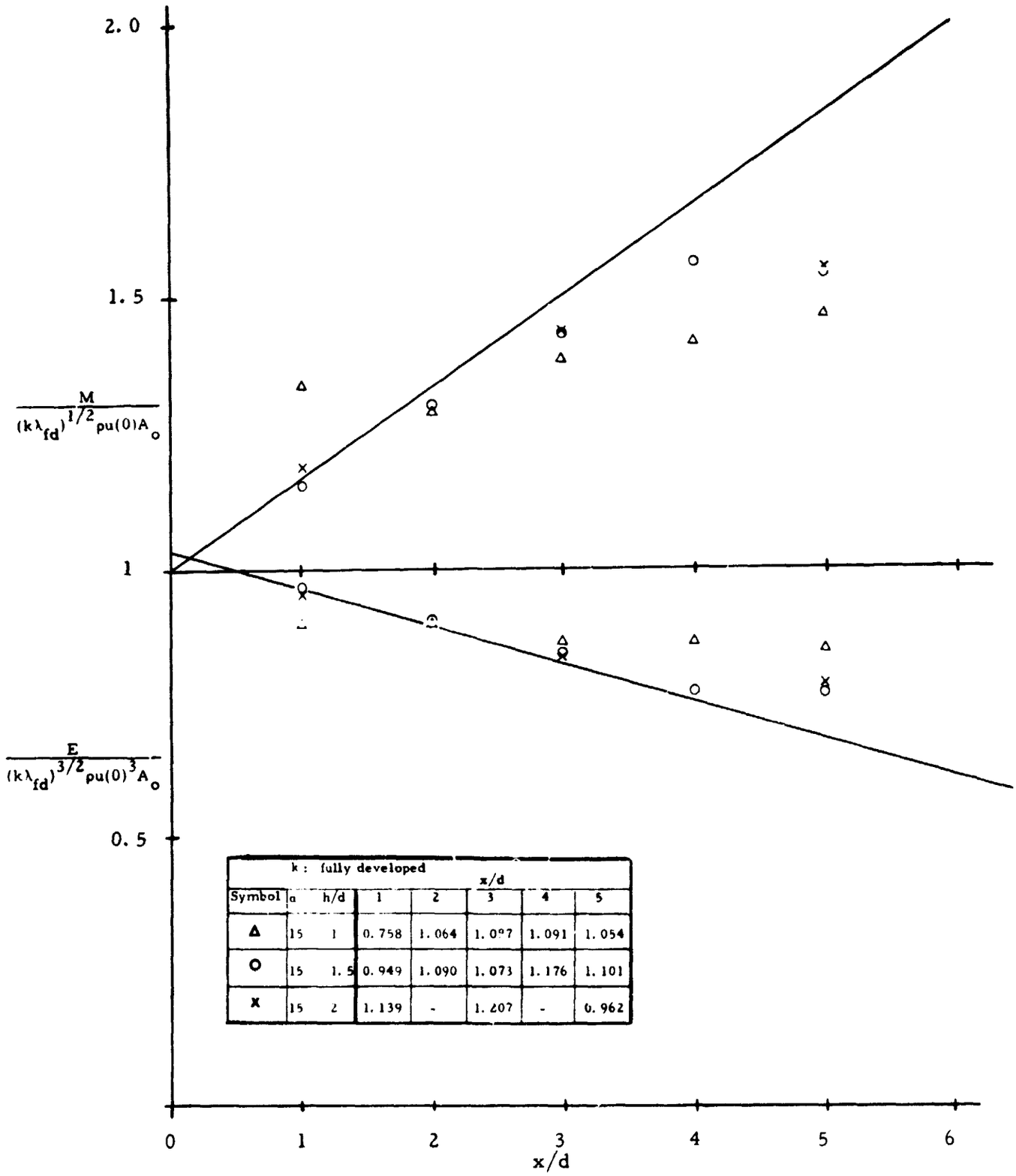

k : fully developed			x/d				
Symbol	a	h/d	1	2	3	4	5
△	15	1	0.758	1.064	1.0°7	1.091	1.054
○	15	1.5	0.949	1.090	1.073	1.176	1.101
×	15	2	1.139	-	1.207	-	0.962

Figure 33. Normalized mass and energy flux values, fully developed, $|k - 1| > 0.03$.

Comment: The data of Hill [19], obtained with a porous cylinder, indicate that the slope of the mass flux curve is not constant in this region. The relative accuracy of the porous cylinder versus the integration of the velocity readings is indeterminate since they are influenced by different errors. The slope values of [19] are

x/d	1	2	4.25	5.5	7.1	10
a_1	0.11	0.19	0.24	0.27	0.3	~0.32 ↓ asymptotic value

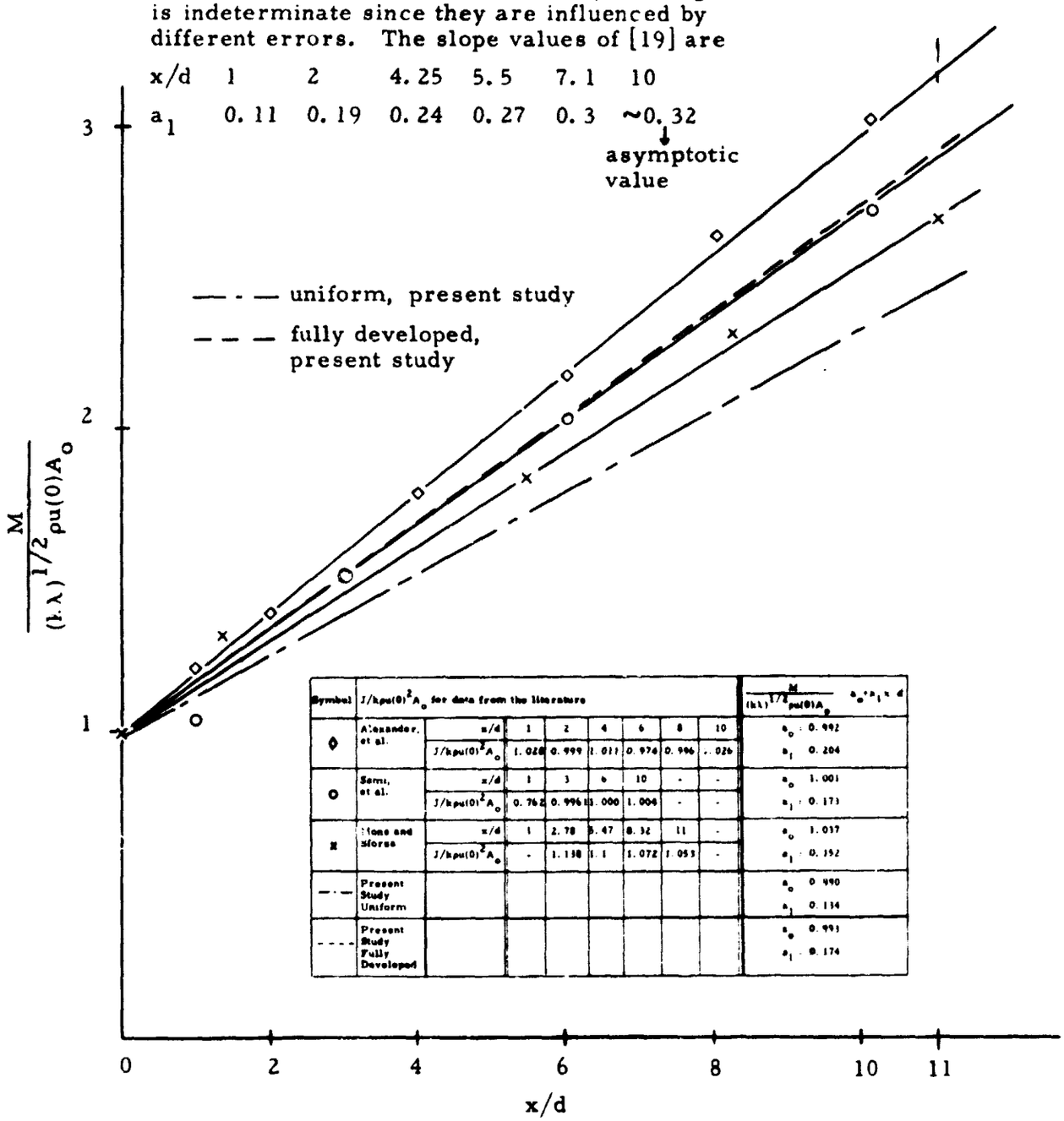

Symbol	$J/k\rho u(0)^2 A_o$ for data from the literature								$\frac{M}{(k\lambda)^{1/2}\rho u(0)A_o}$ $a_o + a_1 x/d$
◊	Alexander, et al.	x/d	1	2	4	6	8	10	a_o : 0.992
		$J/k\rho u(0)^2 A_o$	1.028	0.999	1.011	0.974	0.996	1.026	a_1 0.204
○	Sami, et al.	x/d	1	3	6	10	-	-	a_o 1.001
		$J/k\rho u(0)^2 A_o$	0.762	0.996	1.000	1.004	-	-	a_1 : 0.173
x	Stone and Morse	x/d	1	2.78	5.47	8.32	11	-	a_o 1.037
		$J/k\rho u(0)^2 A_o$	-	1.138	1.1	1.072	1.053	-	a_1 : 0.152
—·—	Present Study Uniform								a_o 0.990
									a_1 0.134
- - - -	Present Study Fully Developed								a_o 0.993
									a_1 : 0.174

Figure 1. Normalized mass flux values as evaluated from references [12], [14], and [21] (Data for Crow and Champagne [29] not not shown, $a_1 = 0.136$ for $0 \le x/d \le 2$; $a_1 = 0.292$ for $x/d > 6$.)

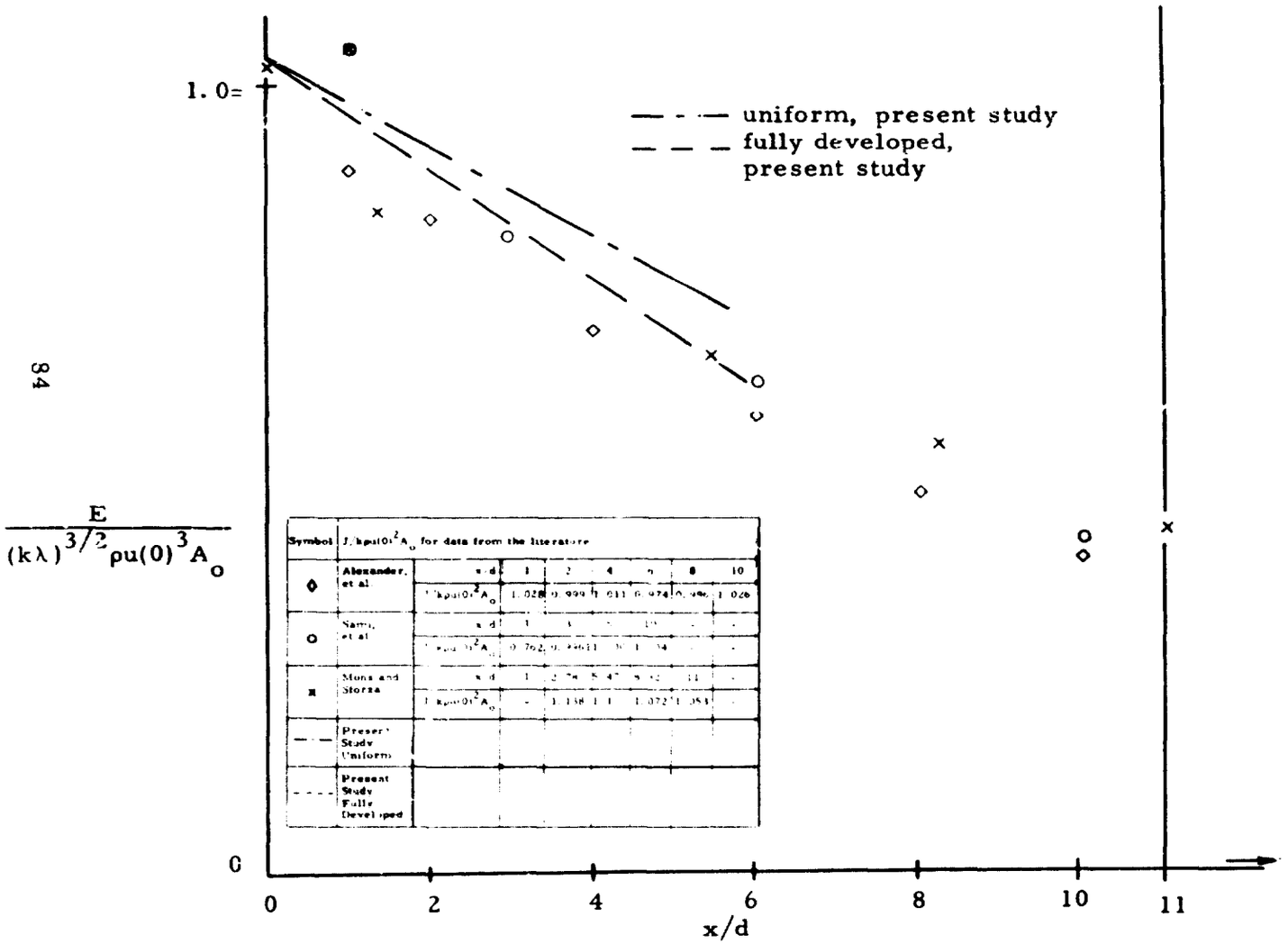

Symbol	$\int k\rho u(0)^2 A_o$ for data from the literature							
◇	Alexander, et al	x/d	1	2	4	6	8	10
		$\int k\rho u(0)^2 A_o$	1.028	0.999	0.911	0.974	[illegible]	1.026
○	Sami, et al	x/d	1	[illegible]	[illegible]	[illegible]	[illegible]	-
		$\int k\rho u(0)^2 A_o$	0.762	[illegible]	[illegible]	1.34	[illegible]	-
×	Mons and Storza	x/d	1	2.74	5.47	[illegible]	11	-
		$\int k\rho u(0)^2 A_o$	-	1.138	1.1	1.072	1.051	-
— —	Present Study Uniform							
- - - -	Present Study Fully Developed							

Figure 35. Normalized energy flux values as evaluated from references [12], [14] and [21].

APPENDIX D. Normalized J_z Values to Demonstrate the Effective Extent of the Interaction Region

Z-COMPONENT MOMENTUM/SIN(ALPHA)

	15.000			- 0.99999		- 0.99999
	12.000				- 1.00000	
ALPHA	9.000				- 0.99999	
	6.000					
	3.000					
x/d = 1	0.000					
		0.50000	0.75000	1.00000	1.50000	2.00000
					H/D	

Z-COMPONENT MOMENTUM/SIN(ALPHA)

	15.000			- 0.80419		- 1.00529
	12.000				- 1.00951	
ALPHA	9.000			- 0.99999	- 1.00192	
	6.000				- 0.99999	
	3.000					
x/d = 2	0.000					
		0.50000	0.75000	1.00000	1.50000	2.00000
					H/D	

Z-COMPONENT MOMENTUM/SIN(ALPHA)

	15.000			- 0.39684		- 1.01222
	12.000				- 1.00922	
ALPHA	9.000			- 0.86540	- 1.00471	
	6.000		- 0.99999	- 0.99999	- 0.99938	
	3.000		- 1.00000	- 1.00000		
x/d = 3	0.000		0.00000	0.00000		
		0.50000	0.75000	1.00000	1.50000	2.00000
					H/D	

Z-COMPONENT MOMENTUM/SIN(ALPHA)

	15.000			- 0.10517		
	12.000				- 0.92929	
ALPHA	9.000			- 0.61194	- 1.00707	
	6.000		- 0.60765	- 0. 9245	- 0.99814	
	3.000		- 0.74821	- 0.96427		
x/d = 4	0.000		0.00000	0.00000		
		0.50000	0.75000	.00000	1.50000	2.00000
					H/D	

Z-COMPONENT MOMENTUM/SIN(ALPHA)

	15.000					
	12.000				- 0.68396	
ALPHA	9.000				- 0.94577	
	6.000		- 0.38323	- 1.23213	- 1.00061	
	3.000		- 0.50039	- 0.87497		
x/d = 5	0.000		0.00000	0.00000		
		0.50000	0.75000	1.00000	1.50000	2.00000
					H/D	

Z-COMPONENT MOMENTUM/SIN(ALPHA)

C·2

	15.000					
	12.000					
ALPHA	9.000					
	6.000			- 1.41309	- 0.97193	
	3.000			- 0.73271		
x/d = 6	0.000		0.00000			
		0.50000	0.75000	1.00000	1.50000	2.00000
					H/D	

Table 1.a. Normalized J_z values to show the effective development length for the uniform nozzle exit condition ($J_z/J(0) \sin \alpha$).

PRECEDING PAGE BLANK NOT FILMED

```
Z-COMPONENT MOMENTUM/SIN(ALPHA)
            15.000
            12.000
ALPHA        9.000
             6.000          - 0.99999 - 0.99999
             3.000- 1.00000 - 1.00000
x/d = 1      0.000            0.00000

                   0.50000   0.75000   1.00000   1.50000   2.00000
                                                  H/D

Z-COMPONENT MOMENTUM/SIN(ALPHA)
            15.000                                          - 0.99999
            12.000                                - 0.99999 - 1.00000
ALPHA        9.000                     - 0.99999 - 0.99999 - 1.00000
             6.000          - 0.94906 - 1.14371 - 0.99999
             3.000- 0.78155 - 1.06855 - 0.99999
x/d = 2      0.000            0.00000

                   0.50000   0.75000   1.00000   1.50000   2.00000
                                                  H/D

Z-COMPONENT MOMENTUM/SIN(ALPHA)
            15.000                                          - 1.00657
            12.000                                - 1.01113 - 1.00790
ALPHA        9.000                     - 0.87519 - 1.01432 - 1.01000
             6.000          - 0.75791 - 1.13051 - 1.02154
             3.000- 0.59022 - 0.99070 - 1.07225
x/d = 3      0.000            0.00000   0.00000

                   0.50000   0.75000   1.00000   1.50000   2.00000
                                                  H/D

Z-COMPONENT MOMENTUM/SIN(ALPHA)
            15.000                                          - 1.00085
            12.000                                - 0.94033 - 1.01273
ALPHA        9.000                     - 0.62151 - 1.00971 - 1.01775
             6.000          - 0.55041 - 0.99402 - 1.03662
             3.000- 0.39153 - 0.84778 - 1.06332
x/d = 4      0.000            0.00000   0.00000

                   0.50000   0.75000   1.00000   1.50000   2.00000
                                                  H/D

Z-COMPONENT MOMENTUM/SIN(ALPHA)
            15.000                                          - 0.87263
            12.000                                - 0.72149 - 0.99729
ALPHA        9.000                     - 0.37006 - 0.92051 - 1.02847
             6.000          - 0.34967 - 0.78143 - 1.03995
             3.000- 0.18936 - 0.67969 - 0.97979
x/d = 5      0.000            0.00000   0.00000

                   0.50000   0.75000   1.00000   1.50000   2.00000
                                                  H/D

Z-COMPONENT MOMENTUM/SIN(ALPHA)
            15.000                                          - 0.59647
            12.000                                - 0.46072 - 0.88841
ALPHA        9.000                     - 0.15981 - 0.73887 - 1.01775
             6.000          - 0.17319 - 0.55339 - 0.99001
             3.000  0.00816 - 0.50772 - 0.83373
x/d = 6      0.000            0.00000   0.00000

                   0.50000   0.75000   1.00000   1.50000   2.00000
                                                  H/D
```

Table 1.b. Normalized J_z values to show the effective development length for the fully developed nozzle exit condition ($J_z/J(0)\sin\alpha$).

Table 1. Radius r as a function of x/d to define the 0.1 isotach (u (x, r) / u (o) = 0.1) for the fully developed and uniform nozzle exit conditions. (The data shown are from those cases for which the measured x-component momentum flux was constant to within ± 3%.)

Fully Developed

a	h/d	x/d=1	2	3	4	5
3	0.75	1.25	1.41	1.61	1.82	2.07
3	1	1.21	--	1.62	--	2.01
3	1.5	1.25	1.43	--	1.85	2.0
9	1	1.26	--	1.61	--	--
12	1	1.21	1.40	1.63	--	--
15	1	1.20	1.38	1.62	--	--
15	1.5	1.22	1.42	1.63	1.83	--
15	2	1.28	--	1.72	--	--
Average		1.23	1.41	1.63	1.83	2.02

Uniform

0	0.75	0.9	1.03	1.13	1.25	1.40
0	1	0.94	1.05	1.20	1.32	--
3	0.75	0.9	1.01	1.11	1.26	1.40
3	1	0.9	1.0	1.12	1.25	1.38
6	1.5	0.91	1.03	1.17	1.30	--
9	1	0.92	1.03	1.16	1.30	--
15	1	0.93	1.02	--	--	--
Average	--	0.91	1.02	1.15	1.28	1.39

Table 2. Summary of percent widths, distance to maximum pressure and isobar which aligns with free isotach intersection.

		Width of 0.1 free isotach intersection contour as a percentage of the zero isobar width recorded at the x-location of the maximum pressure		x/d distance from x=o to p max		p_{agree} $\lambda \rho u(0)^2 \sin \alpha$ all x 10^{-2}		x/d distance from x=0 to 0.1 free isotach intersection	
α	h/d	u	fd	u	fd	u	fd	u	fd
3	0.5625	--	74	--	0.7	--	0.57	--	0.321
	0.667	--	80	--	2.3	--	0.31	--	1.003
	0.75	0.75	80	4.5	2.9	0.35	0.266	1.663	1.544
	1	0.68	78	5.9	5.7	0.38	0.266	3.543	3.176
6	0.75	0.69	76	1.9	2.1	0.36	0.30	1.16	1.18
	1	0.75	71	4.7	4.2	0.29	0.30	2.5	2.324
	1.5	0.64	68	6.4	7	0.20	0.22	5.178	4.737
9	1	0.64	71	3.2	3.3	0.38	0.27	1.91	1.81
	1.5	0.65	70	5.7	6.2	0.25	0.22	3.715	3.979
	2	--	66	--	7.5	--	0.18	--	5.619
12	1	--	--	--	--	--	--	--	--
	1.5	0.58	65	5	5.1	0.28	0.224	3.202	3.029
	2	--	65	--	7.2	--	0.22	--	4.59
15	1	0.46	--	2	--	1.0	--	1.247	--
	1.5	--	--	--	--	--	--	--	--
	2	--	61	--	6	--	0.24	4.06	3.855
30	2	0.3	--	3.4	--	0.65	--	1.978	--
	3	0.36	--	5.2	--	0.61	--	3.429	--
60	2	0.25	--	1.9	--	0.92	--	0.37	--

Table 4. Data from the Stagnation Point Investigation. Uniform Exit Condition $v_p(\frac{x}{d}, 0, 0) = \left\{\frac{2}{\rho}[p(x,0,0) - p_{atm}]\right\}^{1/2}$. $v_w(\frac{x}{d}, 0, \frac{z}{d})$ recorded from the hot-wire anenometer. $\Delta\frac{z}{d}$ of traverse and $\Delta\frac{x}{d}$ to align v_p and v_w are indicated $\Delta\frac{x}{d} = \Delta\frac{z}{d}(\tan\alpha + \beta)^{-1}$.

α = 3 degrees, h/d = 1; $\Delta\frac{z}{d} = 0.0328$, $\Delta\frac{x}{d} = 0.249$				α = 9 degrees, h/d = 1; $\Delta\frac{z}{d} = 0.0395$, $\Delta\frac{x}{d} = 0.164$				α = 15 degrees, h/d = 1; $\Delta\frac{z}{d} = 0.0308$, $\Delta\frac{x}{d} = 0.0871$			
$\frac{x}{d}$	v_p(fps)	$\frac{x}{d}$	v_w(fps)	$\frac{x}{d}$	v_p(fps)	$\frac{x}{d}$	v_w(fps)	$\frac{x}{d}$	v_p(fps)	$\frac{x}{d}$	v_w(fps)
2.291	0.000	2.166	8.106	0.875	7.393	0.958	2.421	0.000	3.031	0.000	0.728
2.458	0.000	2.333	10.267	1.041	3.201	1.125	1.956	0.166	2.279	0.166	1.760
2.625	0.000	2.500	12.149	1.208	3.201	1.291	2.528	0.333	3.160	0.333	1.905
2.791	0.000	2.666	14.374	1.374	0.001	1.458	5.184	0.500	3.284	0.500	1.841
2.958	0.000	2.833	16.430	1.541	1.848	1.624	7.270	0.666	2.279	0.666	1.664
3.124	0.000	2.999	18.488	1.708	4.802	1.791	10.428	0.833	3.845	0.833	0.606
3.291	0.000	3.166	20.618	1.874	10.496	1.958	14.903	0.999	3.322	0.999	4.838
3.458	0.000	3.333	22.374	2.041	13.862	2.124	19.776	1.166	13.290	1.166	10.633
3.624	0.000	3.499	24.077	2.208	17.534	2.291	24.703	1.333	24.829	1.333	19.937
3.791	0.000	3.666	26.123	2.374	20.056	2.458	30.275	1.499	34.430	1.499	30.459
3.958	0.000	3.833	28.288	2.541	22.656	2.624	34.888	1.666	40.723	1.666	40.350
4.124	0.000	3.999	29.605	2.708	24.711	2.791	39.815	1.833	44.385	1.833	50.807
4.291	0.000	4.166	31.387	2.874	25.577	2.958	43.902	1.999	46.185	1.999	63.566
4.458	0.000	4.333	32.986	3.041	26.528	3.124	47.981	2.166	45.769	2.166	81.836
4.624	0.000	4.499	35.254	3.208	27.352	3.291	51.562	2.333	45.031	2.333	93.062
4.791	0.000	4.666	36.443	3.374	27.305	3.458	54.864	2.499	43.768	2.499	97.307
4.958	0.000	4.833	38.389	3.541	27.321	3.624	58.891	2.666	42.056	2.666	100.325
5.124	0.000	4.999	39.859	3.708	26.816	3.791	60.690	2.833	40.283	2.833	103.503
5.291	0.000	5.166	41.628	3.874	26.302	3.958	62.490	2.999	38.768	2.999	104.968
5.458	0.000	5.333	42.329	4.041	26.188	4.124	64.608	3.166	36.255	3.166	108.305
5.624	0.000	5.499	44.399	4.208	25.893	4.291	66.757	3.333	35.725	3.333	109.831
5.791	0.000	5.666	46.283	4.374	25.037	4.458	67.454	3.499	34.663	3.499	110.896
5.958	0.000	5.833	48.111	4.541	25.003	4.624	68.610	3.666	33.275	3.666	111.201
6.124	0.000	5.999	50.033	4.708	24.187	4.791	70.441	3.833	32.631	3.833	111.751
6.458	0.000	6.333	50.960	5.041	23.048	5.124	71.489	4.166	30.380	4.166	111.474
6.791	0.000	6.666	52.007	5.374	21.927	5.458	73.076	4.499	29.559	4.499	111.481
7.124	0.000	6.999	52.883	5.708	20.890	5.791	74.197	4.833	28.685	4.833	111.242
7.458	0.000	7.333	54.158	6.041	21.475	6.124	74.837	5.166	27.382	5.166	111.224
7.791	0.000	7.666	54.311	6.374	19.992	6.458	75.387	5.499	27.320	5.499	110.310
8.124	0.000	7.999	55.447	6.708	19.341	6.791	75.374	5.833	25.420	5.833	109.738
8.458	0.000	8.333	55.611	7.041	18.713	7.124	75.130	6.166	23.184	6.166	108.238

PRECEDING PAGE BLANK NOT FILMED

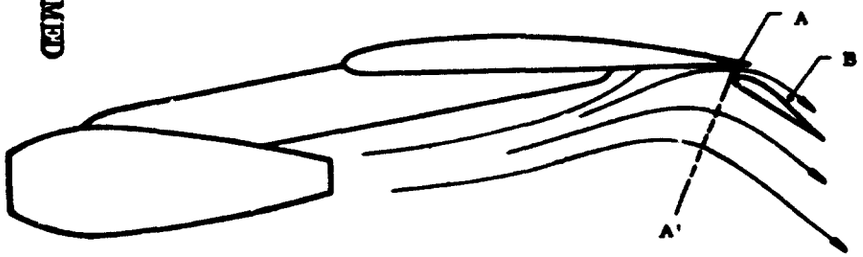

Figure 1a. Externally blown flap STOL aircraft configuration.

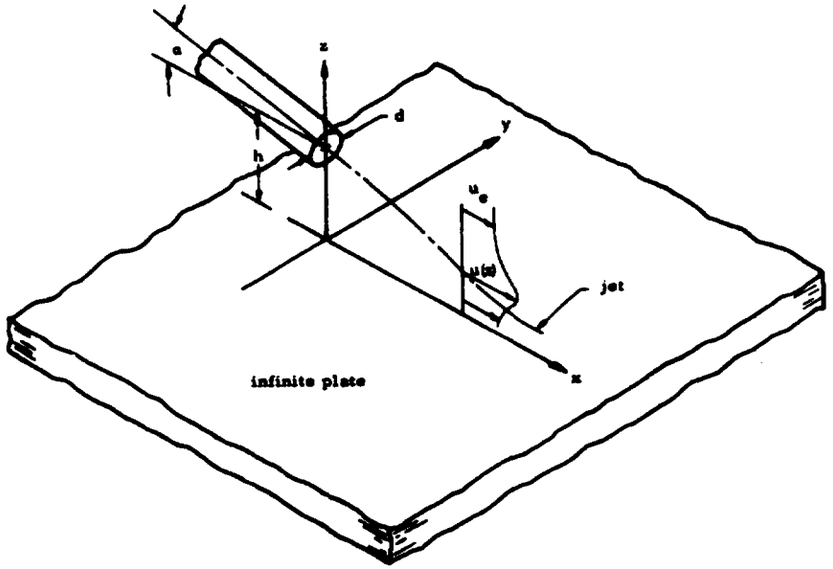

Figure 1b. The round-jet/plane-wall flow field, coordinate system and nomenclature.

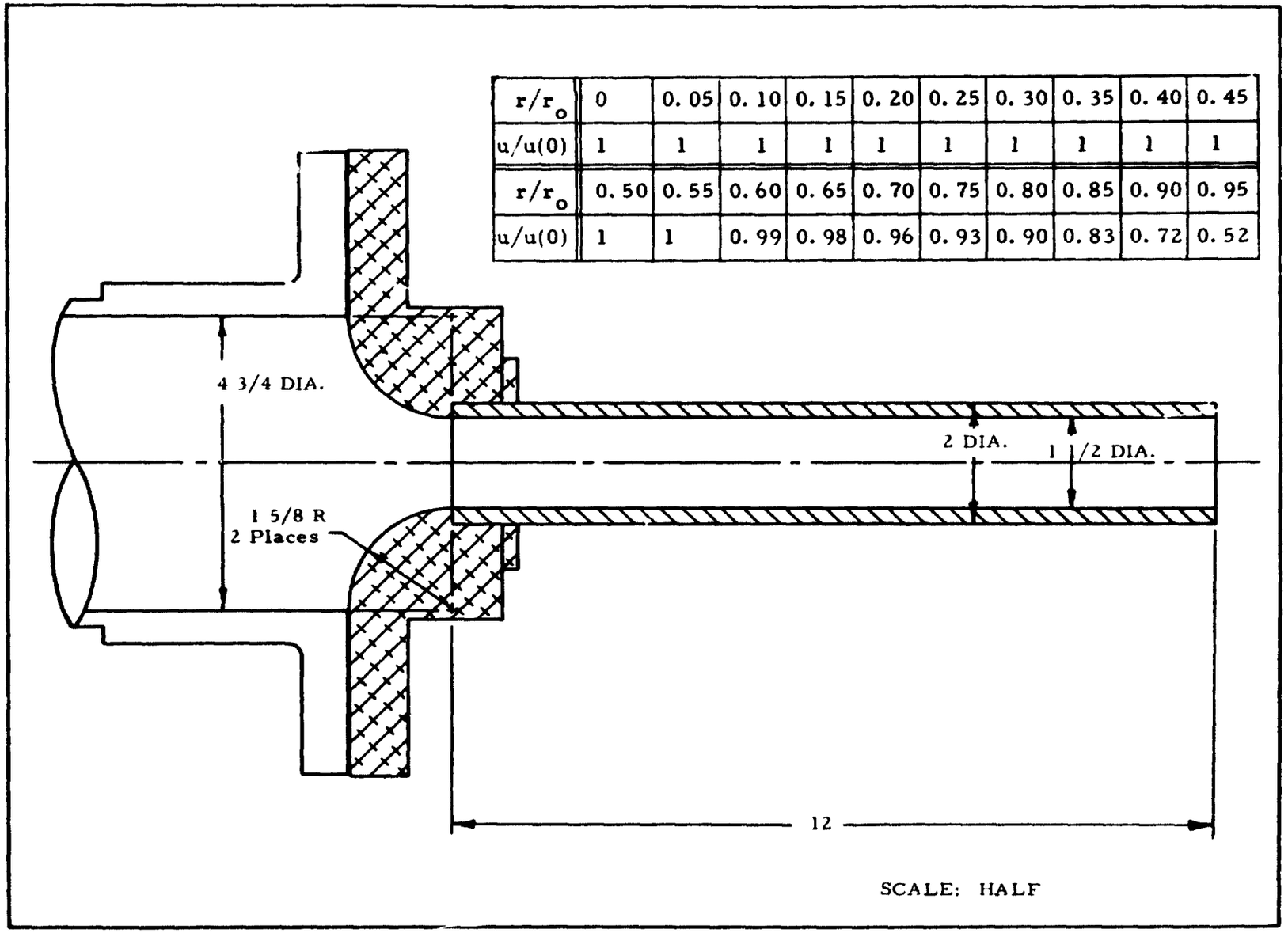

r/r_o	0	0.05	0.10	0.15	0.20	0.25	0.30	0.35	0.40	0.45
$u/u(0)$	1	1	1	1	1	1	1	1	1	1
r/r_o	0.50	0.55	0.60	0.65	0.70	0.75	0.80	0.85	0.90	0.95
$u/u(0)$	1	1	0.99	0.98	0.96	0.93	0.90	0.83	0.72	0.52

Figure 2. Detail of uniform flow nozzle.

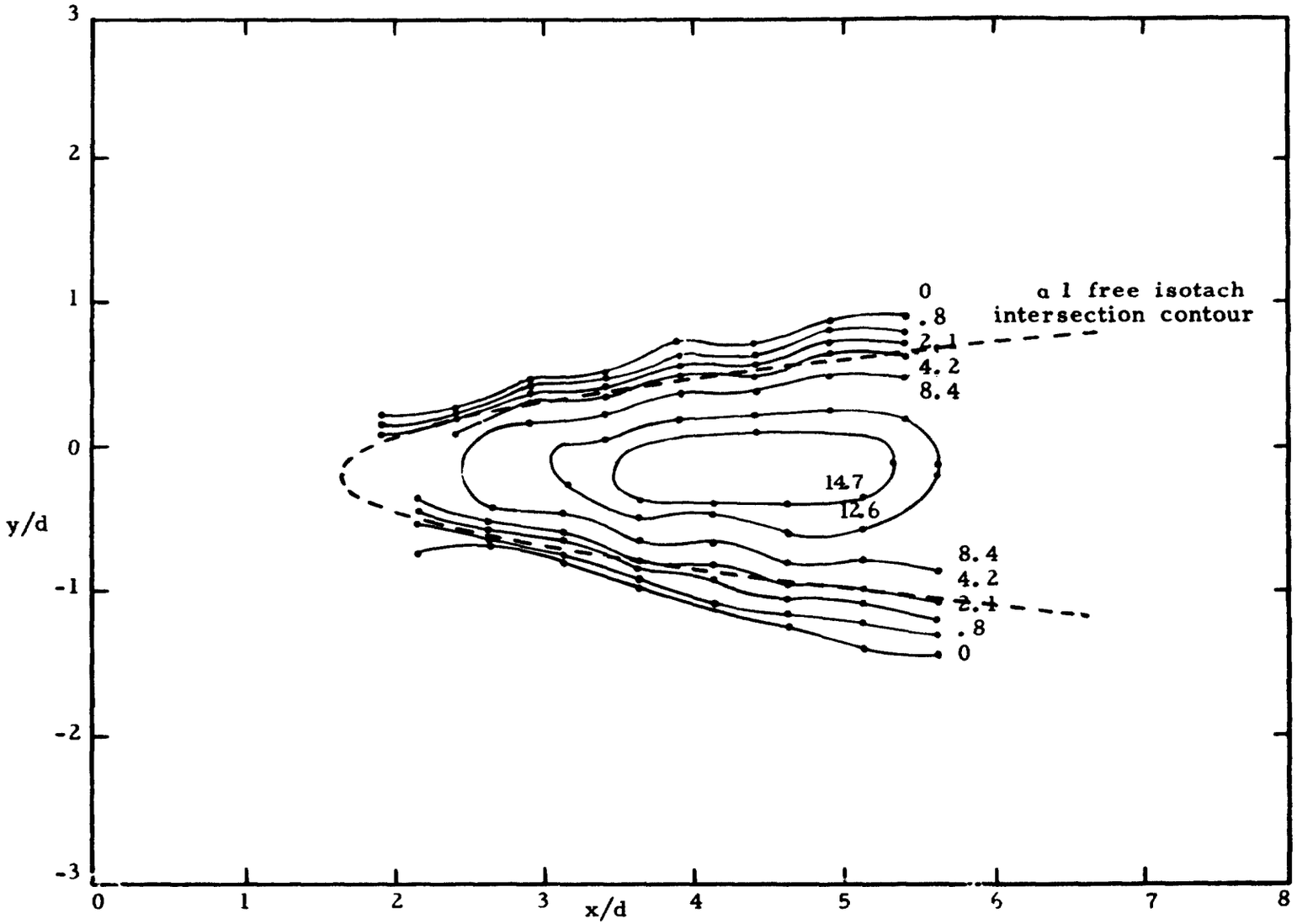

Figure 3. Isobar plot values shown are $p(x, y, 0)/\rho \lambda u(0)^2 \sin \alpha \times 10^2$ for the conditions 3, 0.75, u.

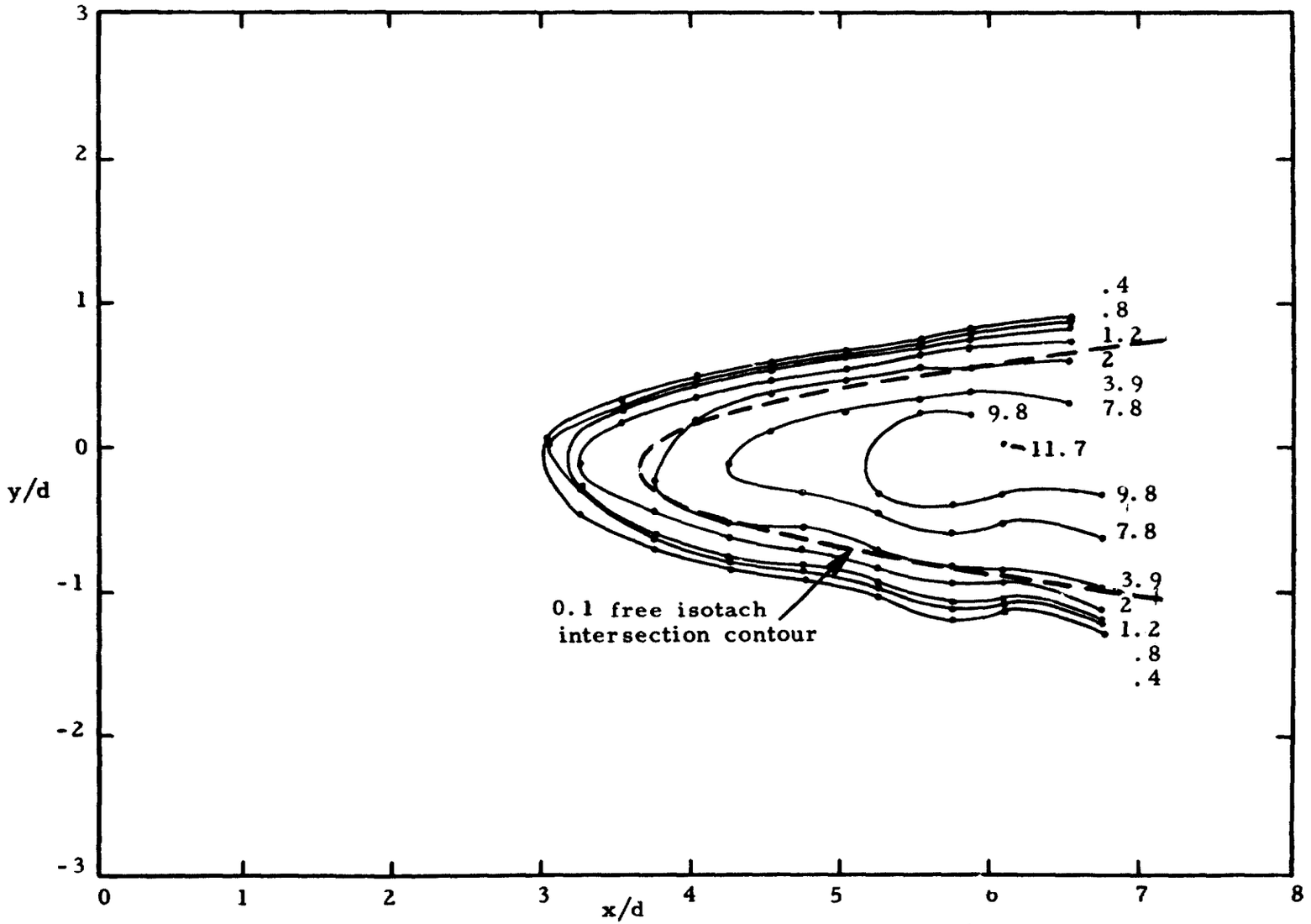

Figure 4. Isobar plot values shown are $p(x, y, 0)/\rho \lambda u(0)^2 \sin \alpha \times 10^2$ for the conditions 3, 1, u.

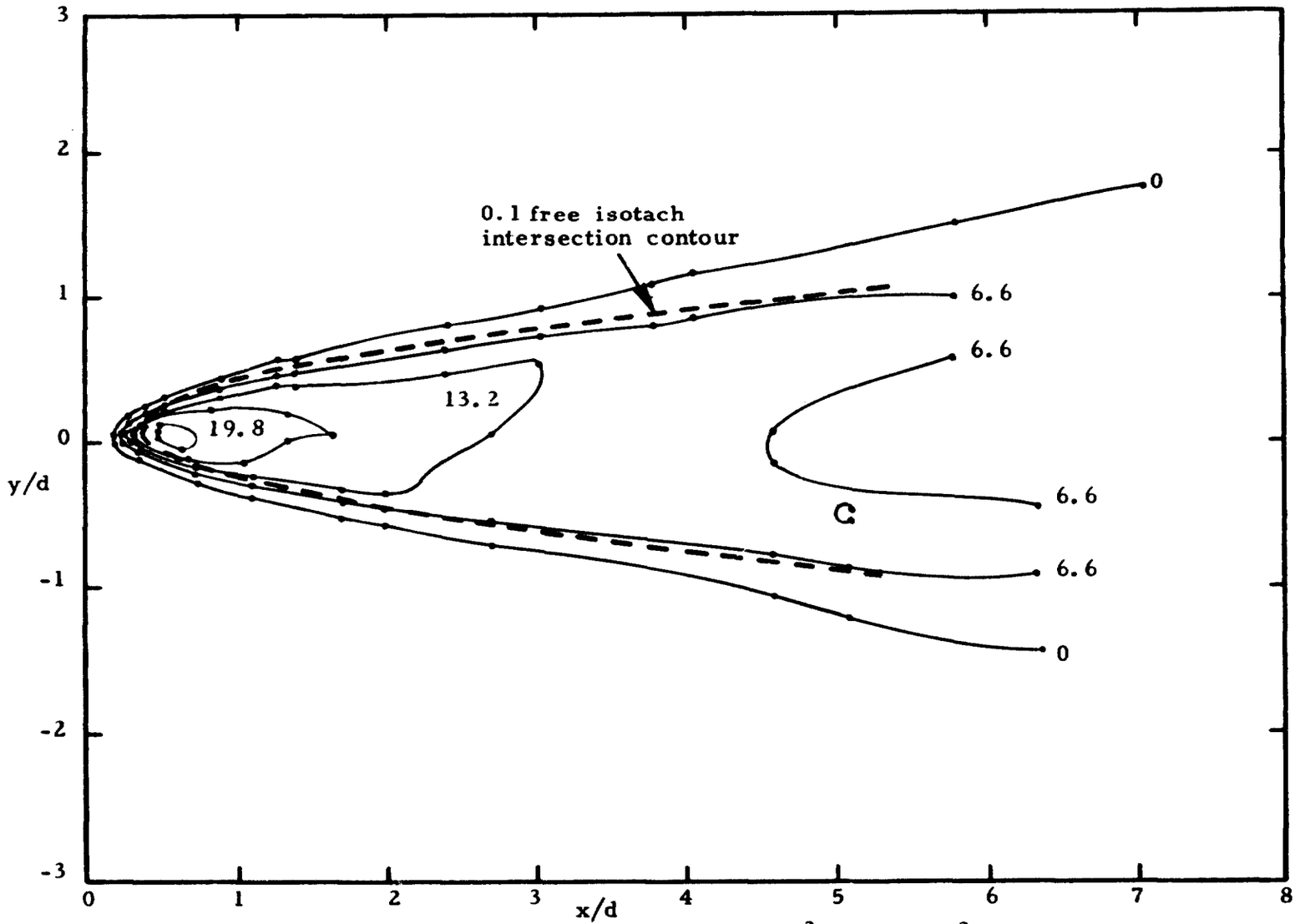

Figure 5. Isobar plot values shown are $p(x, y, 0)/\rho \lambda u(0)^2 \sin \alpha \times 10^2$ for the conditions 3, 0.5626, fd.

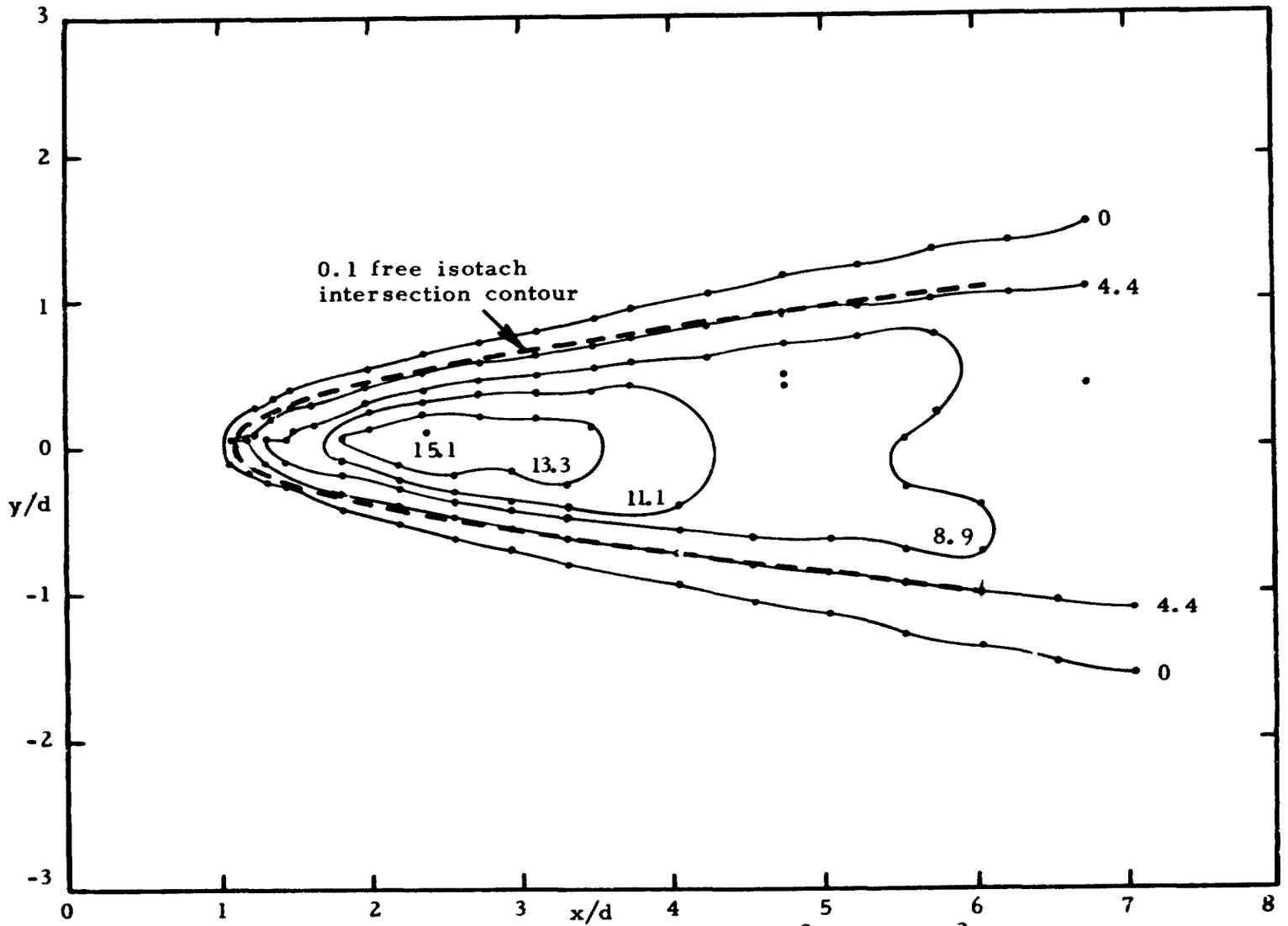

Figure 6. Isobar plot values shown are $p(x, y, 0)/\rho \lambda u(0)^2 \sin \alpha \times 10^2$ for the conditions 3, 0.667, fd.

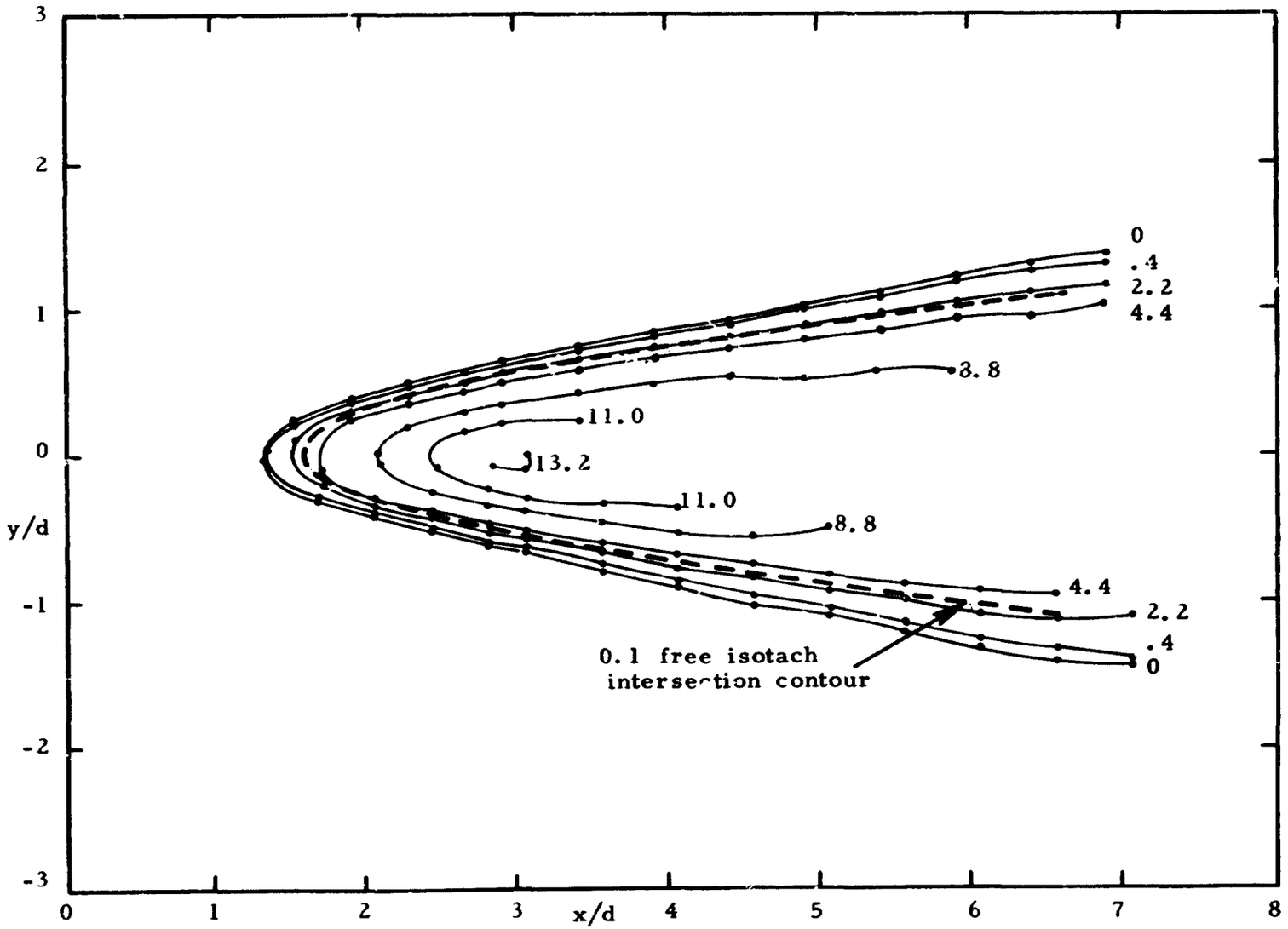

Figure 7. Isobar plot values shown are $p(x, y, 0)/\rho \lambda u(0)^2 \sin \alpha \times 10^2$ for the conditions 3, 0.75, fd.

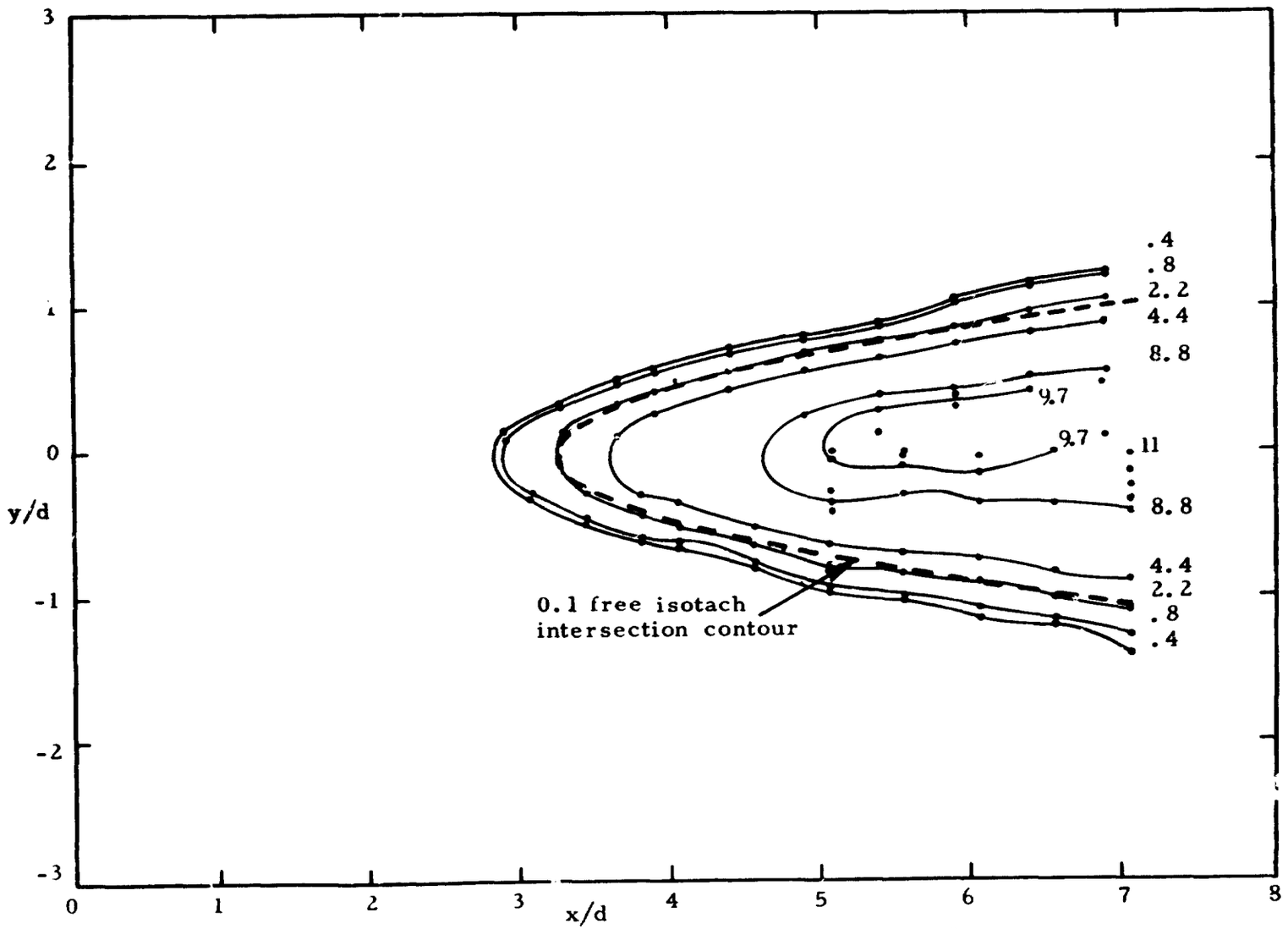

Figure 8. Isobar plot values shown are $p(x, y, 0)/\rho \lambda u(0)^2 \sin \alpha \times 10^2$ for the conditions 3, 1, fd.

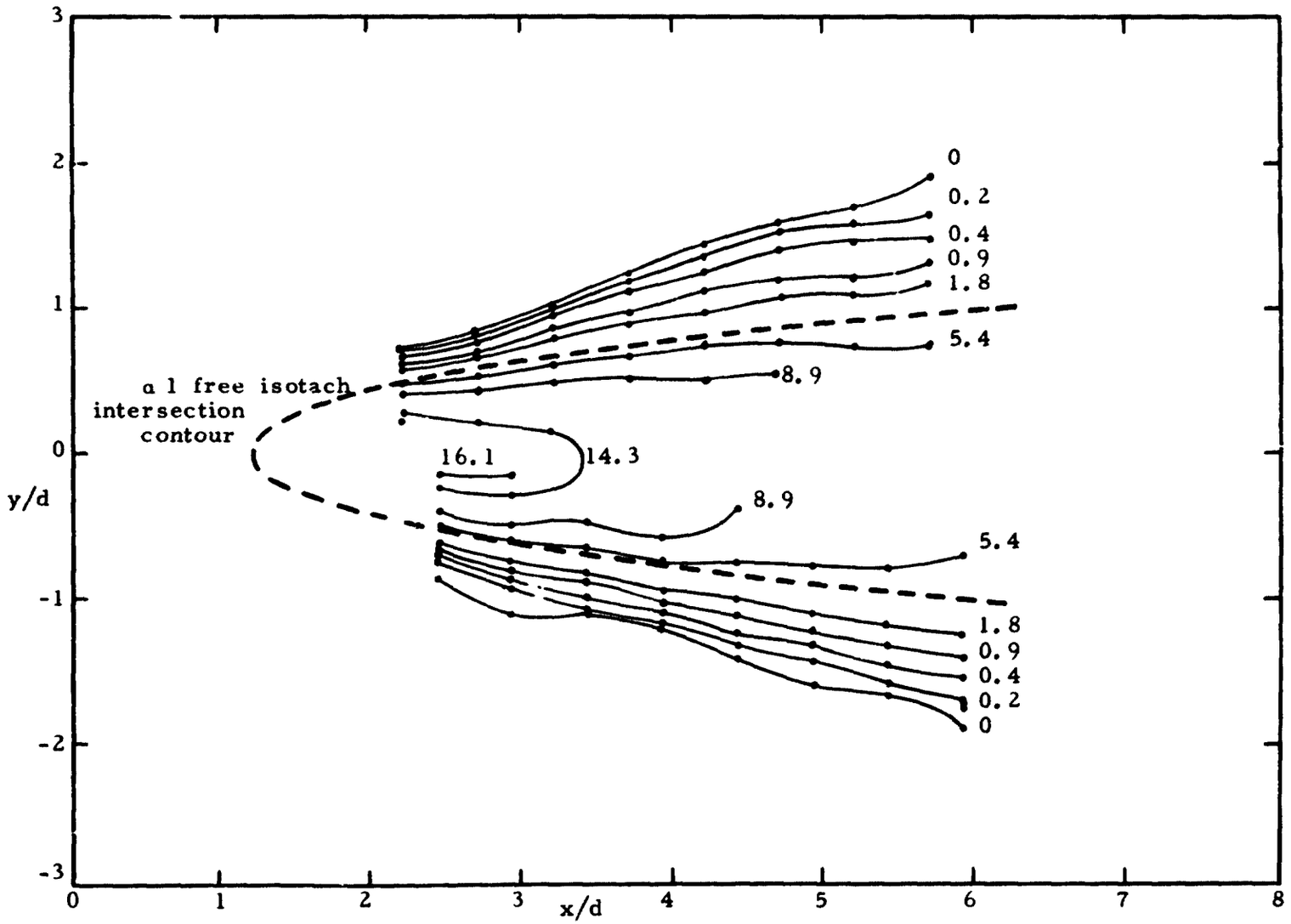

Figure 9. Isobar plot values shown are $p(x, y, 0)/\rho \lambda u(0)^2 \sin \alpha \times 10^2$ for the conditions 6, 0.75, u.

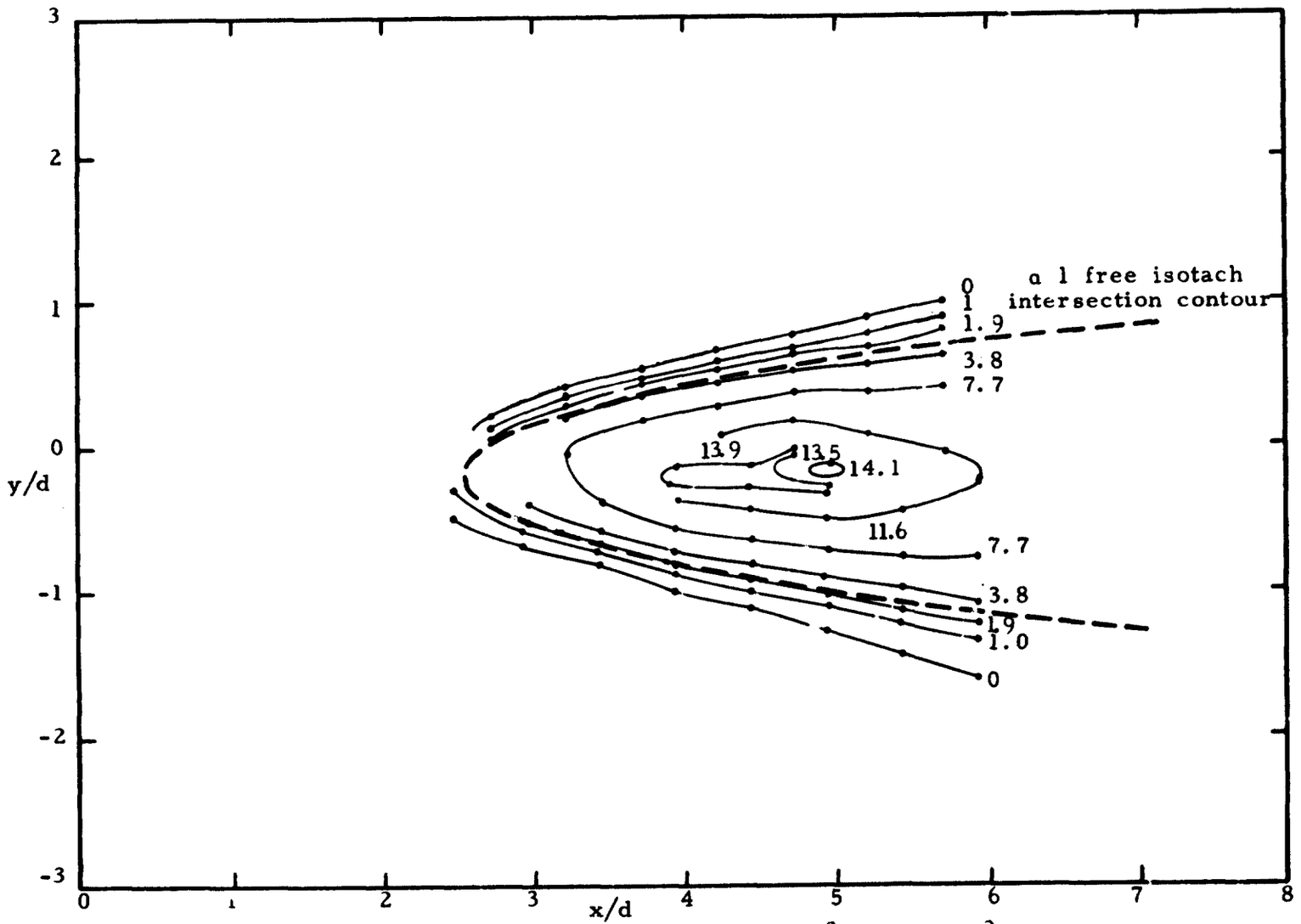

Figure 10. Isobar plot values shown are $p(x, y, 0)/\rho \lambda u(0)^2 \sin \alpha \times 10^2$ for the conditions 6, 1, u.

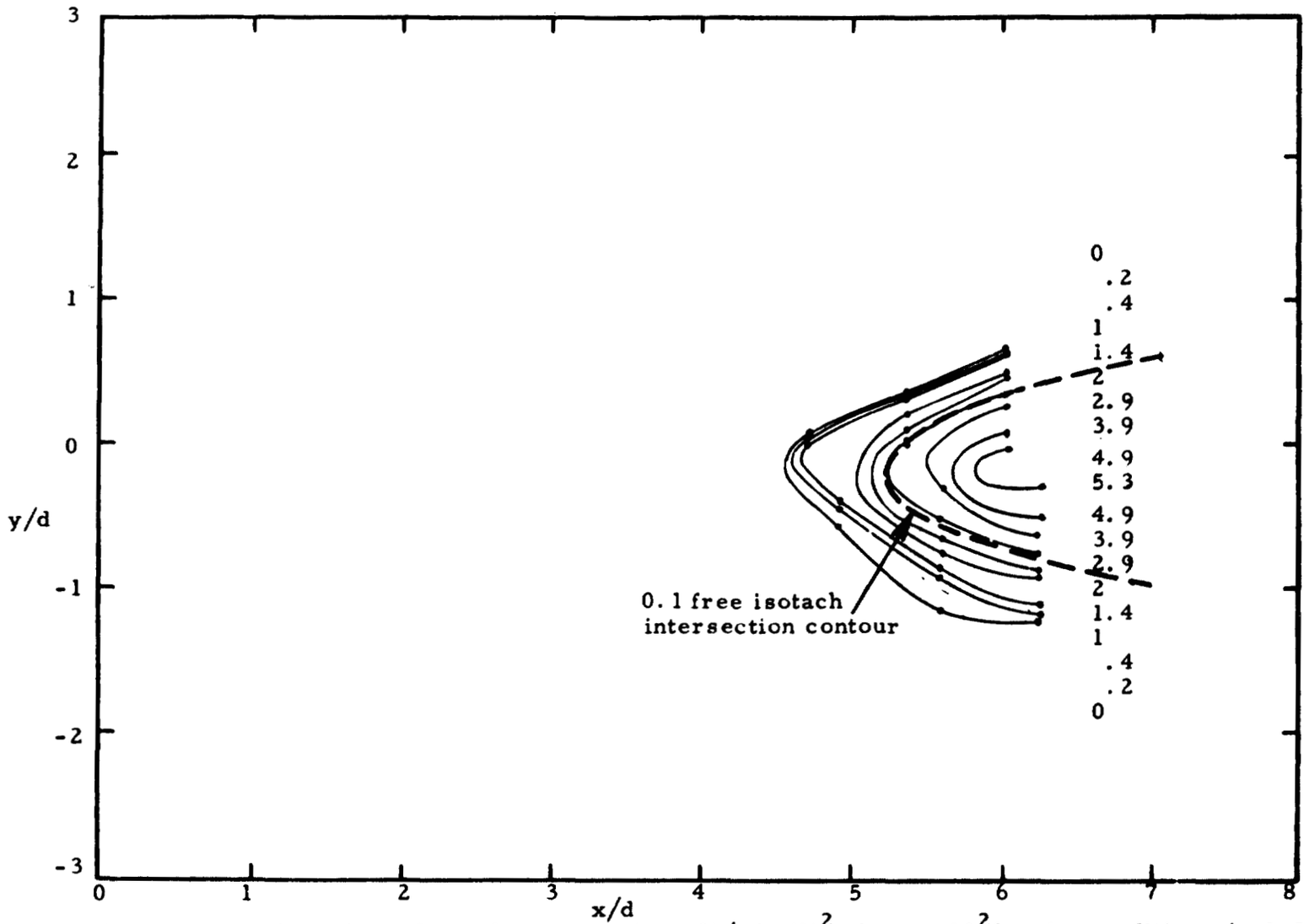

Figure 11. Isobar plot values shown are $p(x, y, 0)/\rho \lambda u(0)^2 \sin \alpha \times 10^2$ for the conditions 6, 1.5, u.

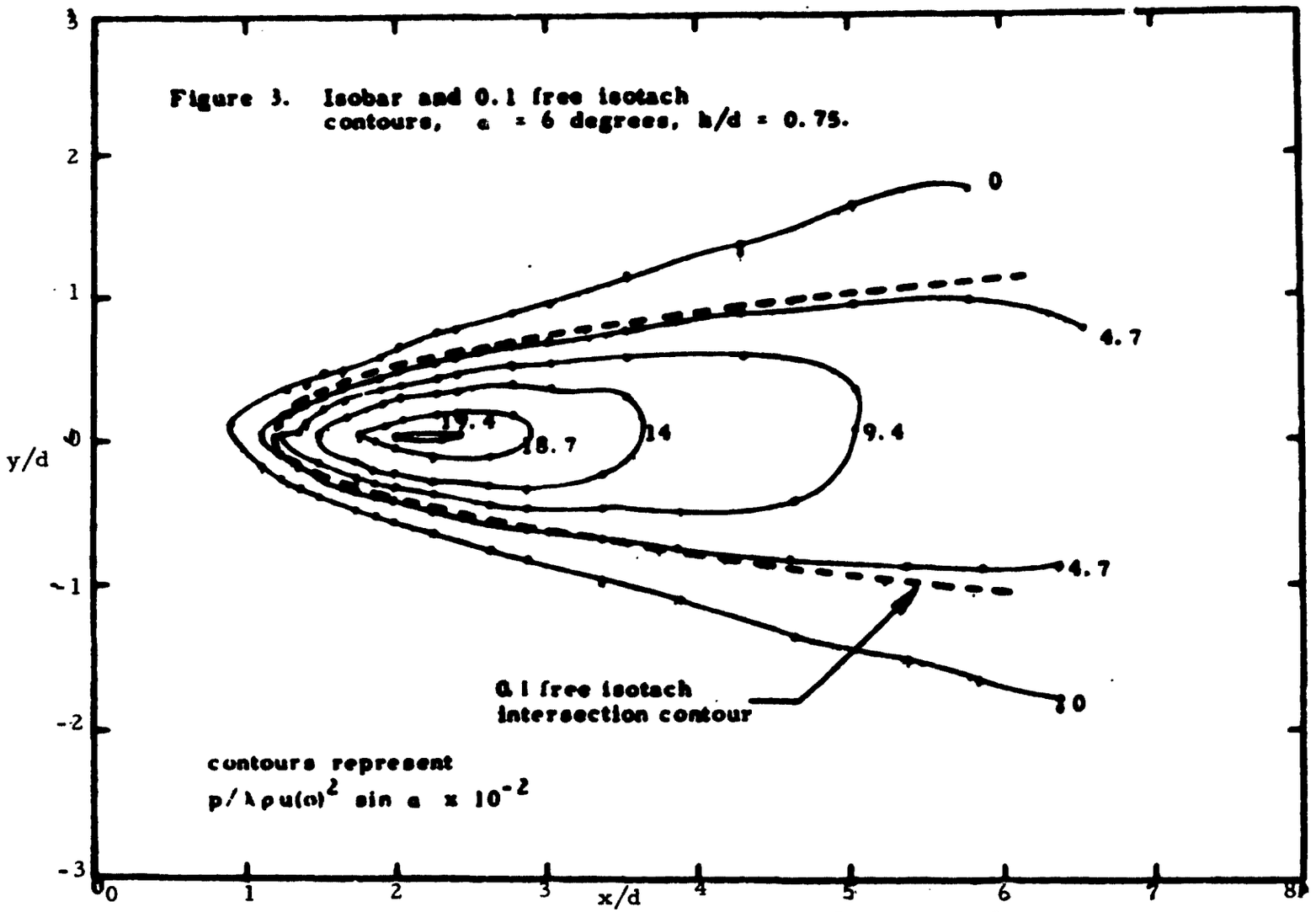

Figure 12. Isobar plot values shown are $p(x, y, 0)/\rho \lambda u(0)^2 \sin \alpha \times 10^2$ for the conditions 6, 0.75, fd.

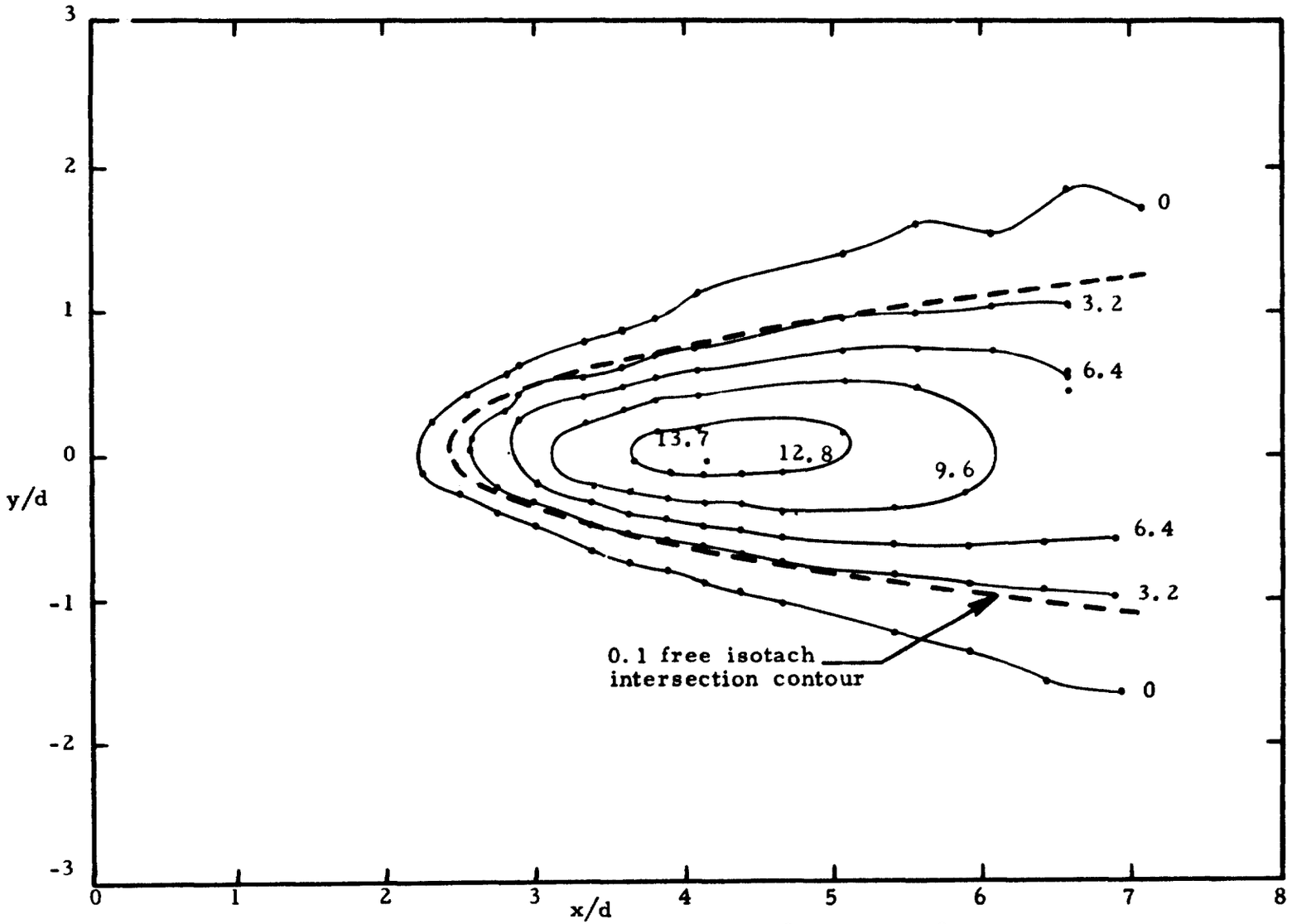

Figure 13. Isobar plot values shown are $p(x, y, 0)/\rho \lambda u(0)^2 \sin \alpha \times 10^2$ for the conditions 6, 1, fd.

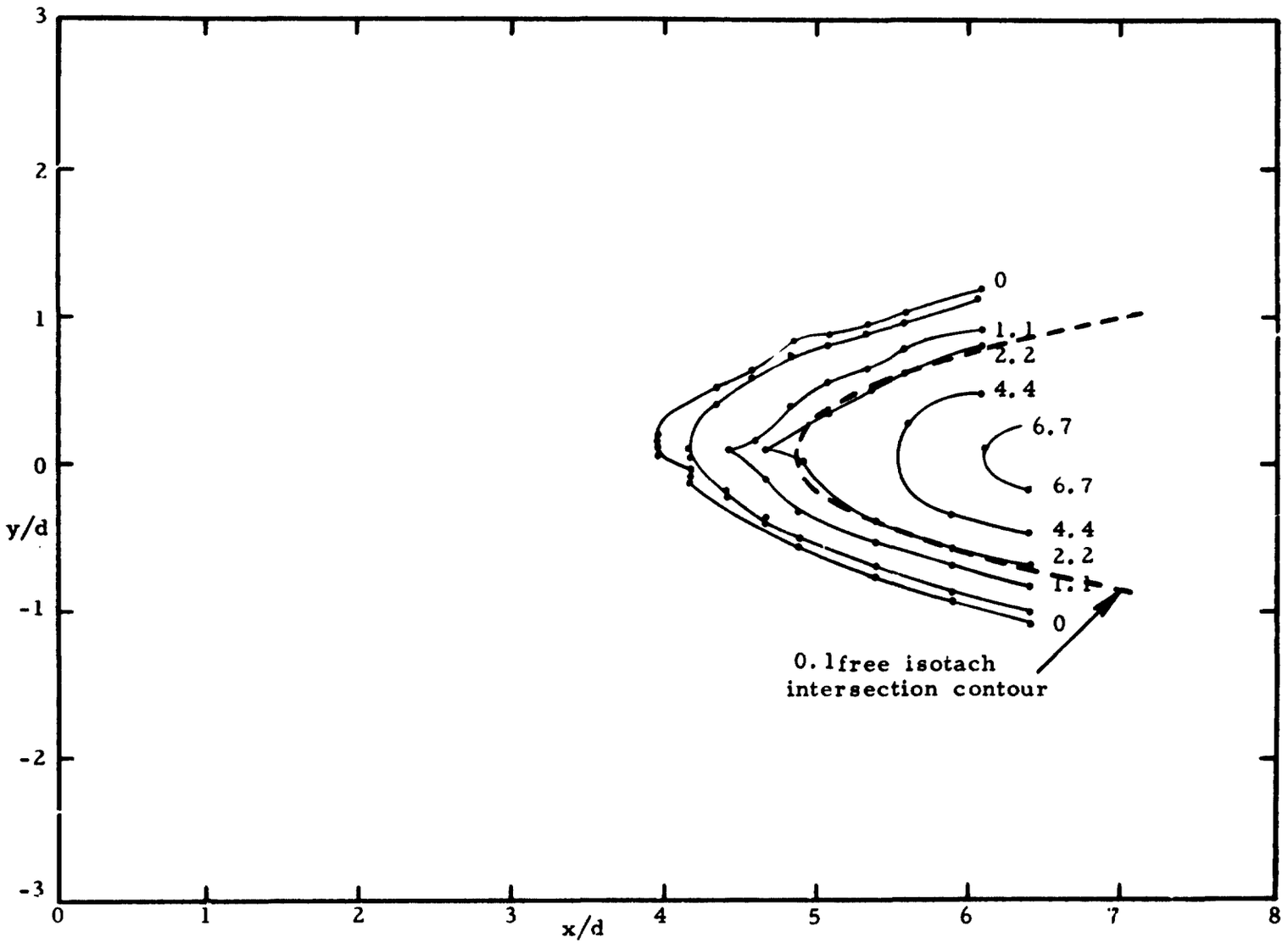

Figure 14. Isobar plot values shown are $p(x, y, 0)/\rho \lambda u(0)^2 \sin \alpha \times 10^2$ for the conditions 6, 1.5, fd.

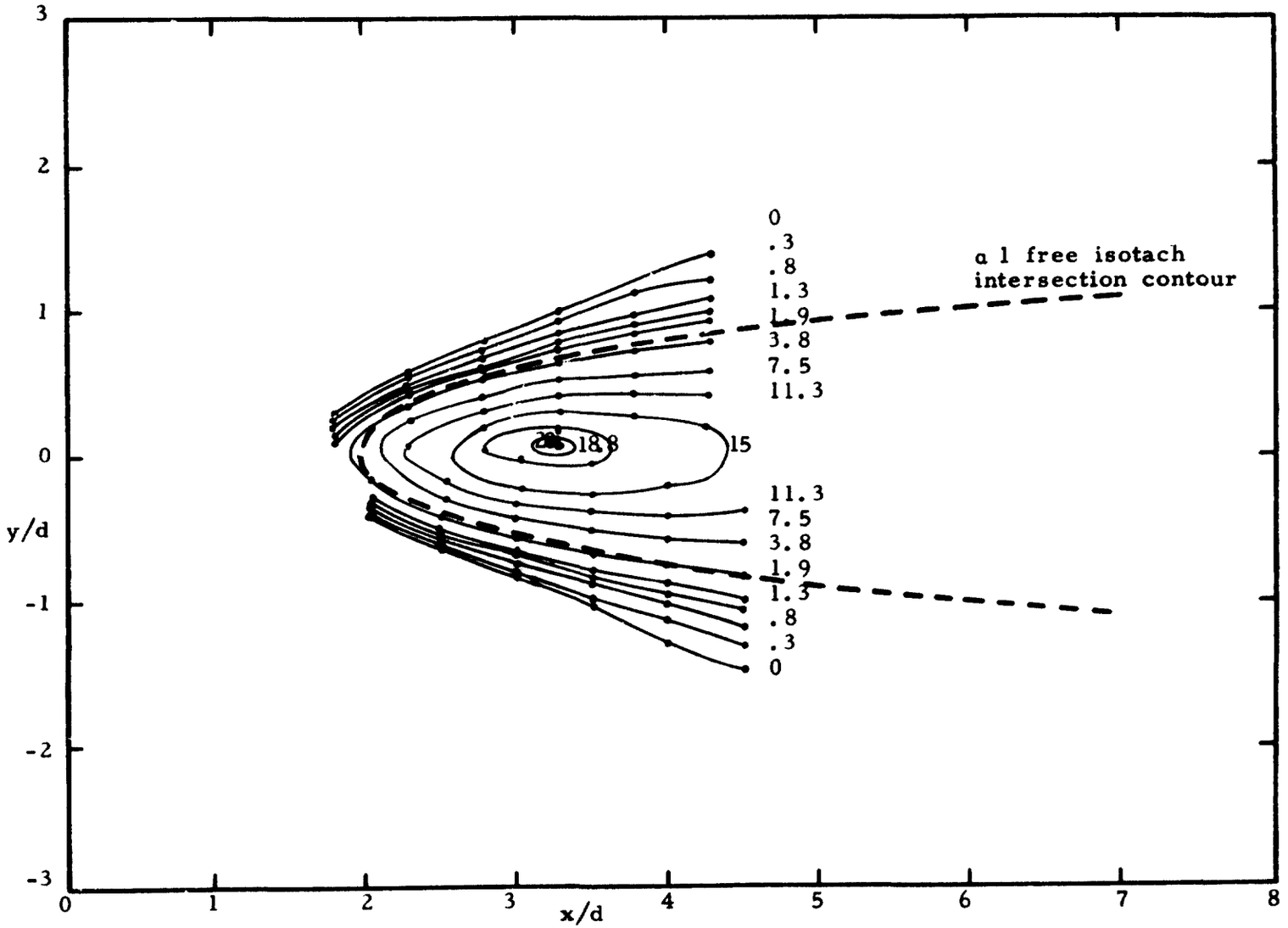

Figure 15. Isobar plot values shown are $p(x, y, 0)/\rho \lambda u(0)^2 \sin \alpha \times 10^2$ for the conditions 9, 1, u.

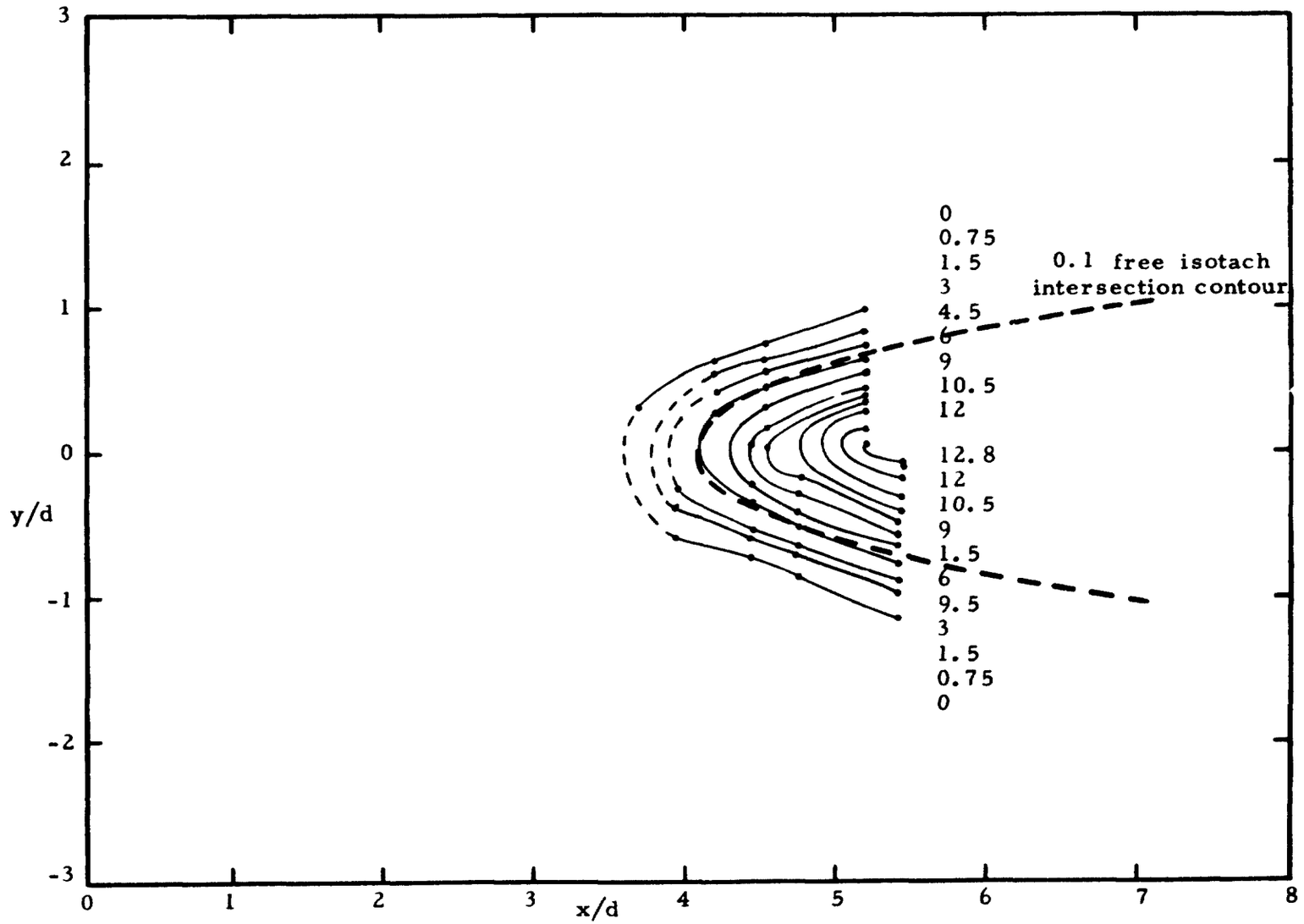

Figure 16. Isobar plot values shown are $p(x, y, 0)/\rho \lambda u(0)^2 \sin \alpha \times 10^2$ for the conditions 9, 1.5, u.

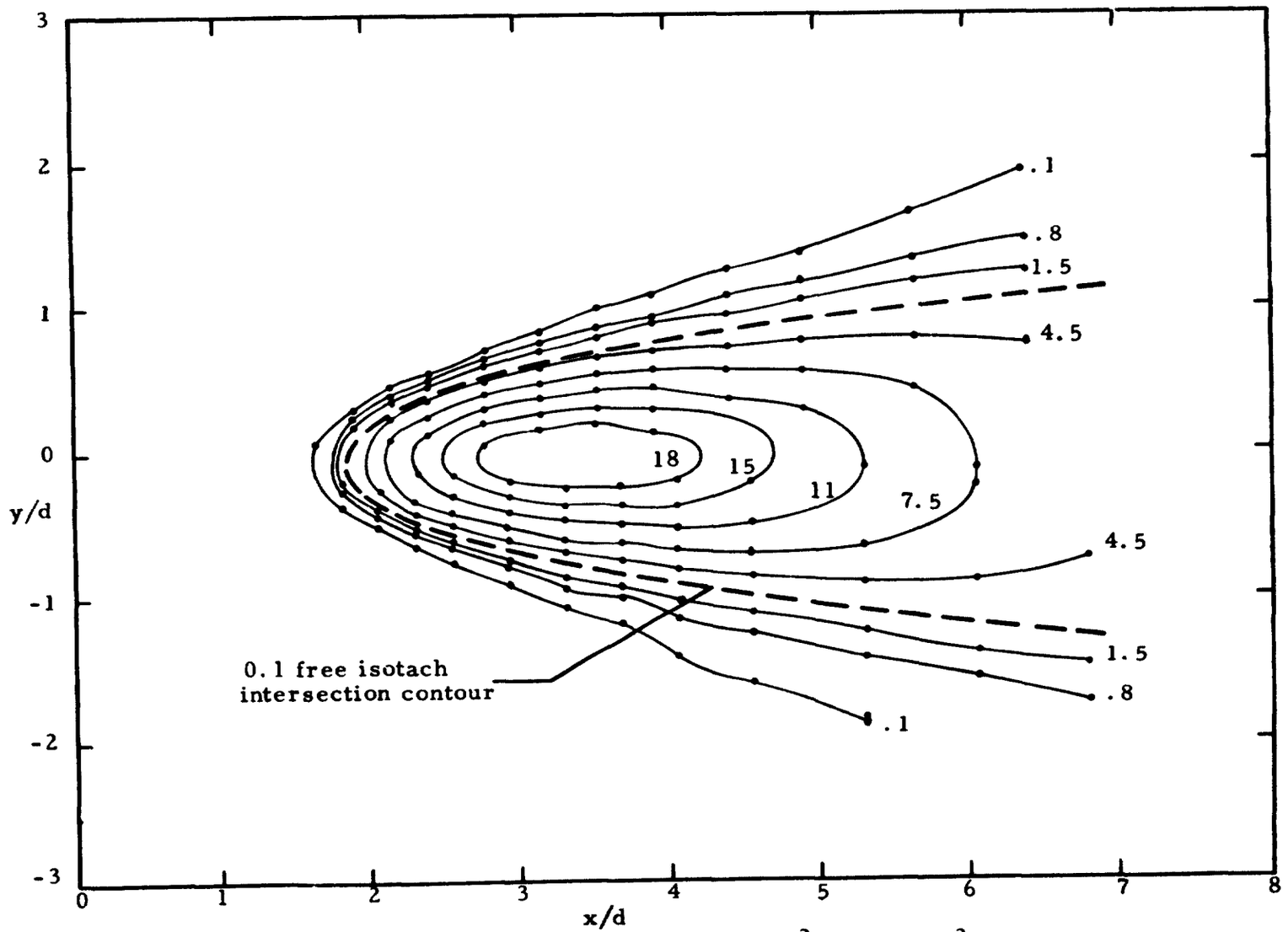

Figure 17. Isobar plot values shown are $p(x, y, 0)/\rho \lambda u(0)^2 \sin \alpha \times 10^2$ for the conditions 9, 1, fd.

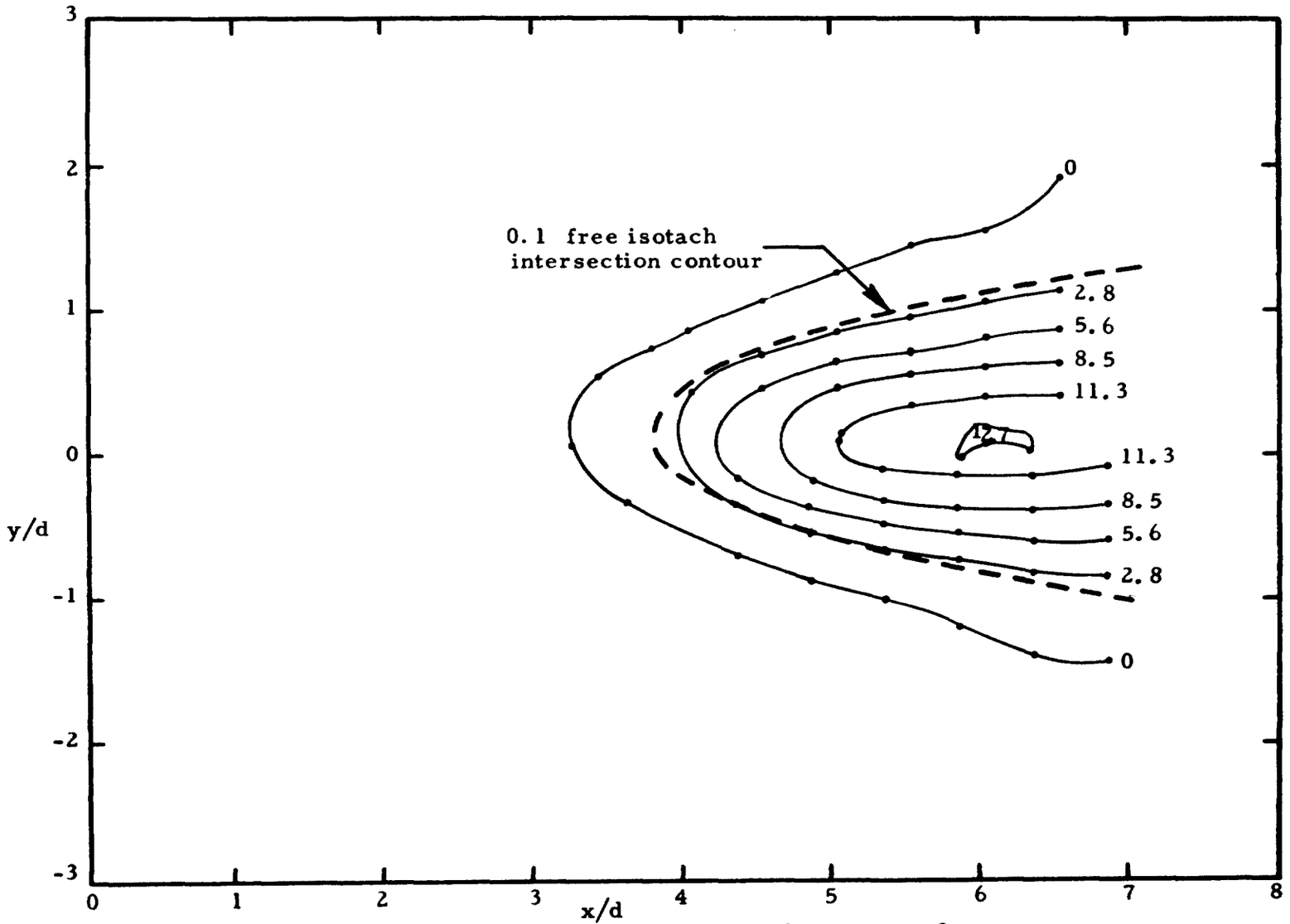

Figure 18. Isobar plot values shown are $p(x, y, 0)/\rho \lambda u(0)^2 \sin \alpha \times 10^2$ for the conditions 9, 1.5, fd.

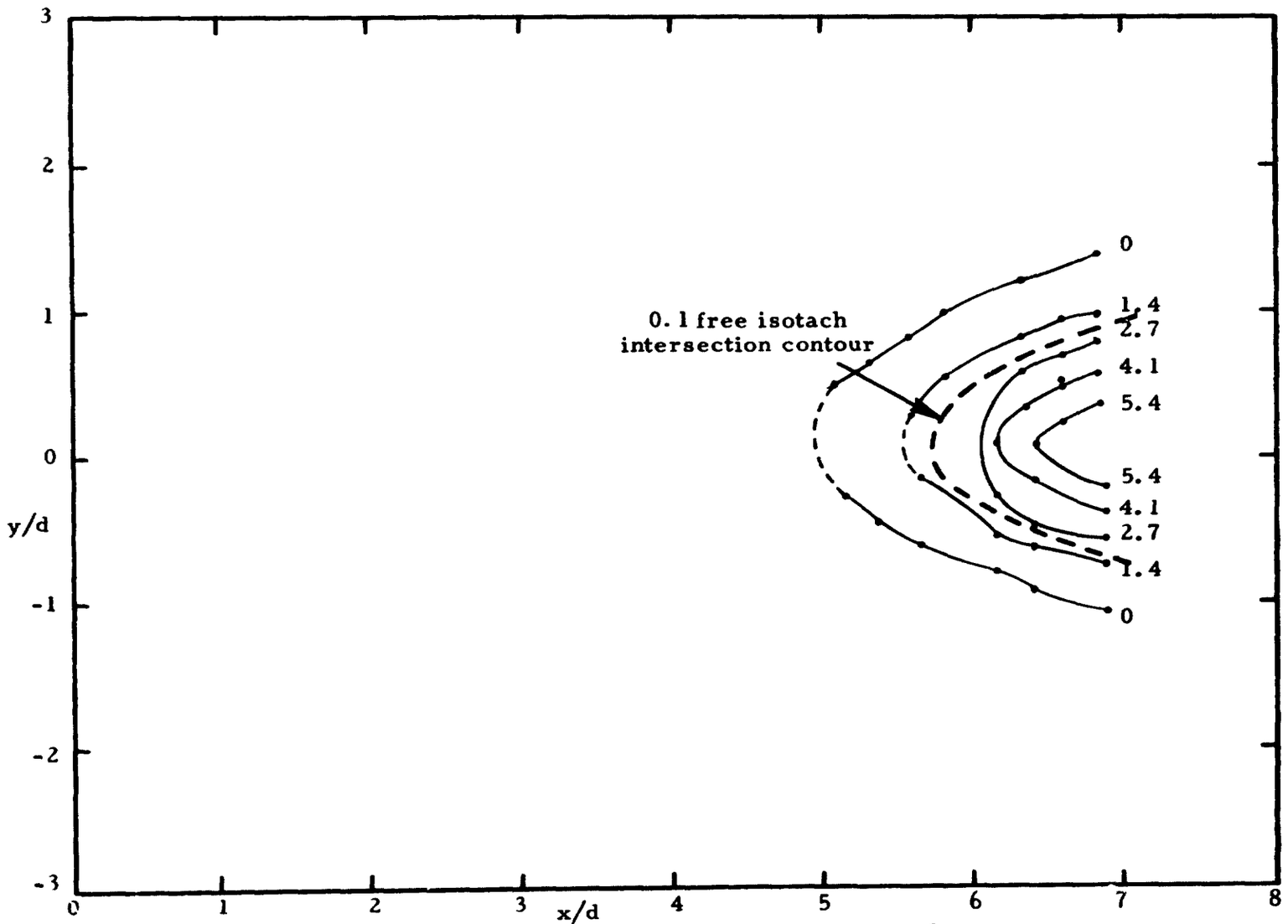

Figure 19. Isobar plot values shown are $p(x, y, 0)/\rho \lambda u(0)^2 \sin \alpha \times 10^2$ for the conditions 9, 2, fd.

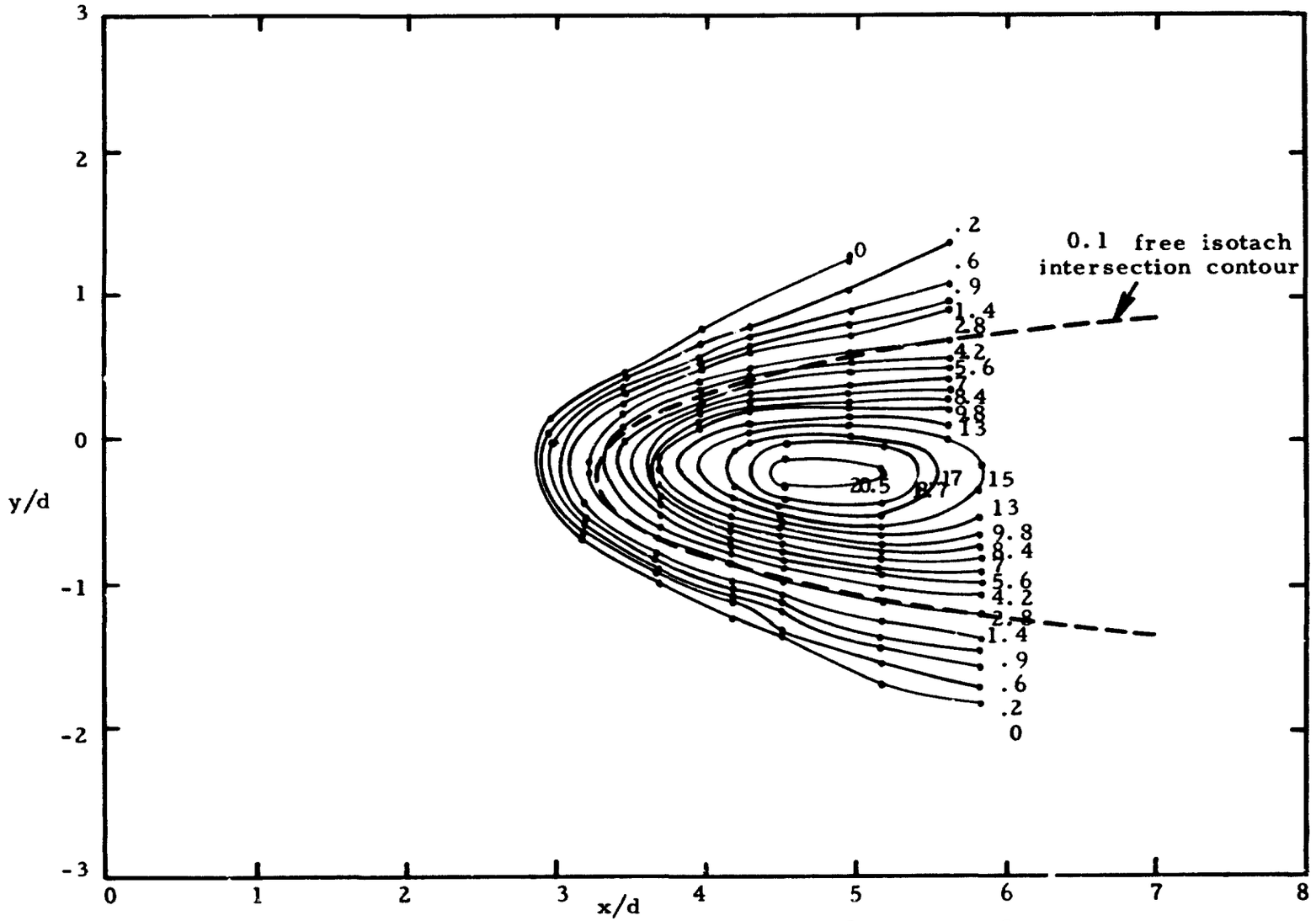

Figure 20. Isobar plot values shown are $p(x, y, 0)/\rho \lambda u(0)^2 \sin \alpha \times 10^2$ for the conditions 12, 1.5, u.

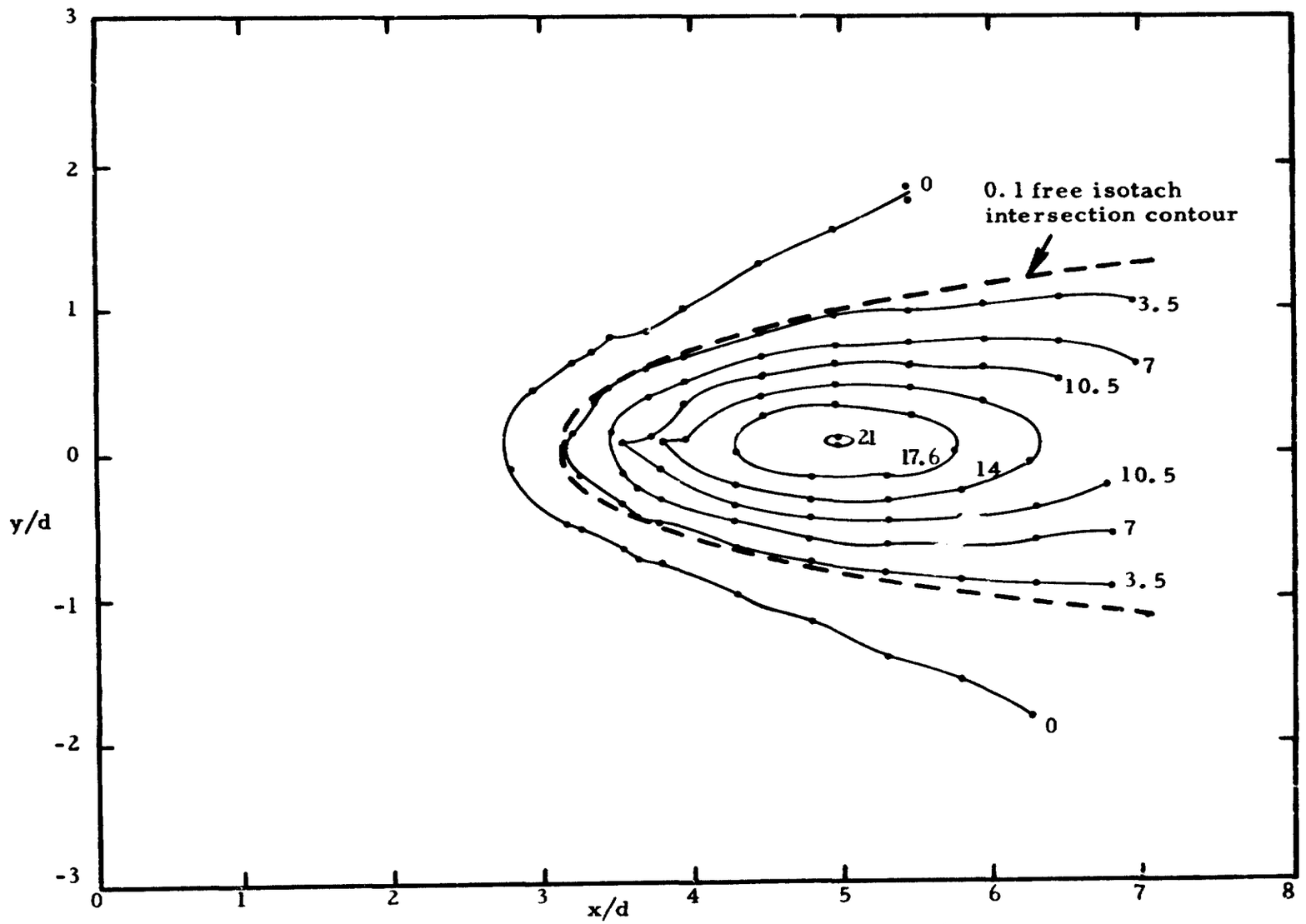

Figure 21. Isobar plot values shown are $p(x, y, 0)/\rho \lambda u(0)^2 \sin \alpha \times 10^2$ for the conditions 12, 1.5, fd.

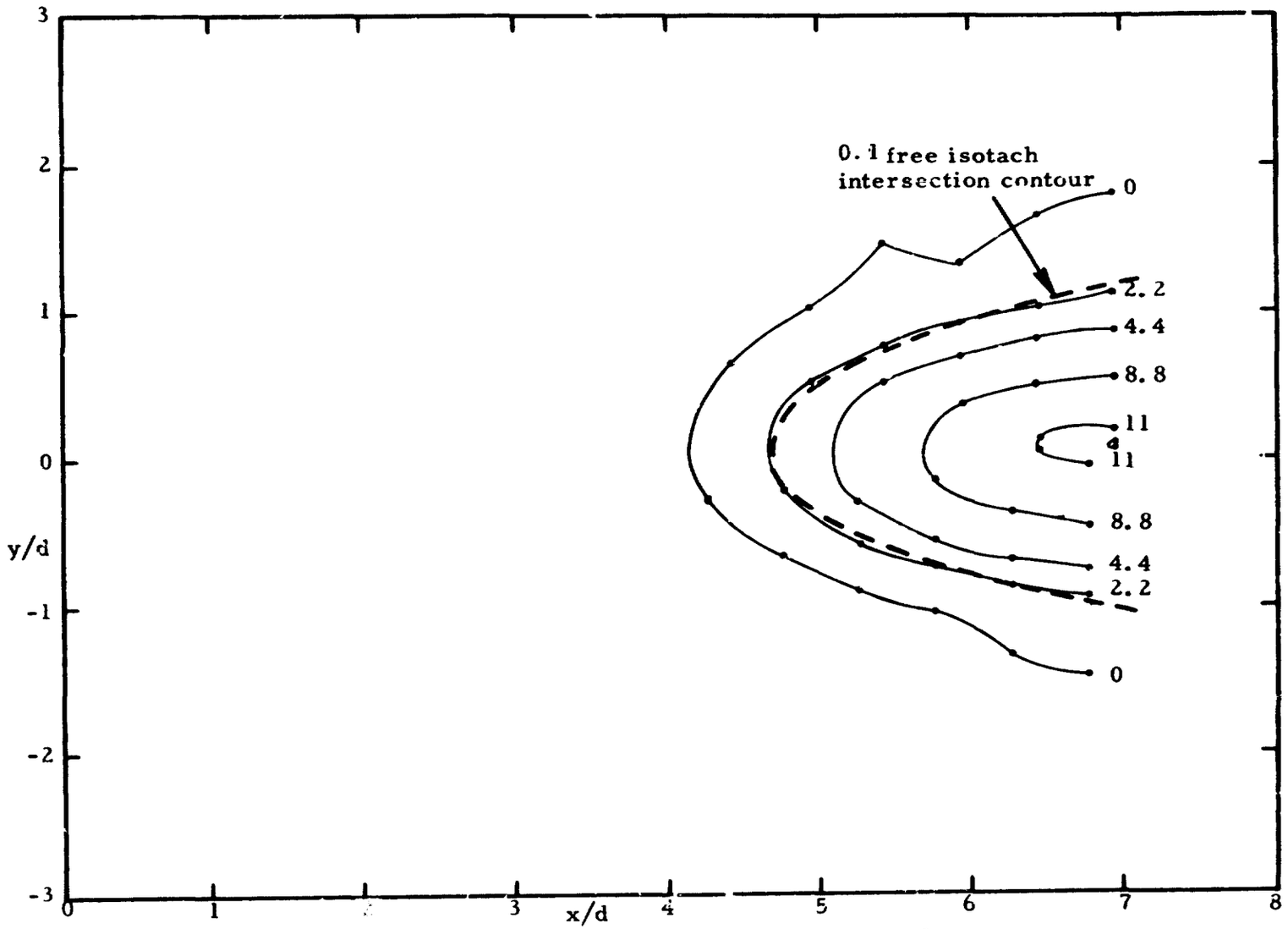

Figure 22. Isobar plot values shown are $p(x, y, 0)/\rho \lambda u(0)^2 \sin \alpha \times 10^2$ for the conditions 12, 2, fd.

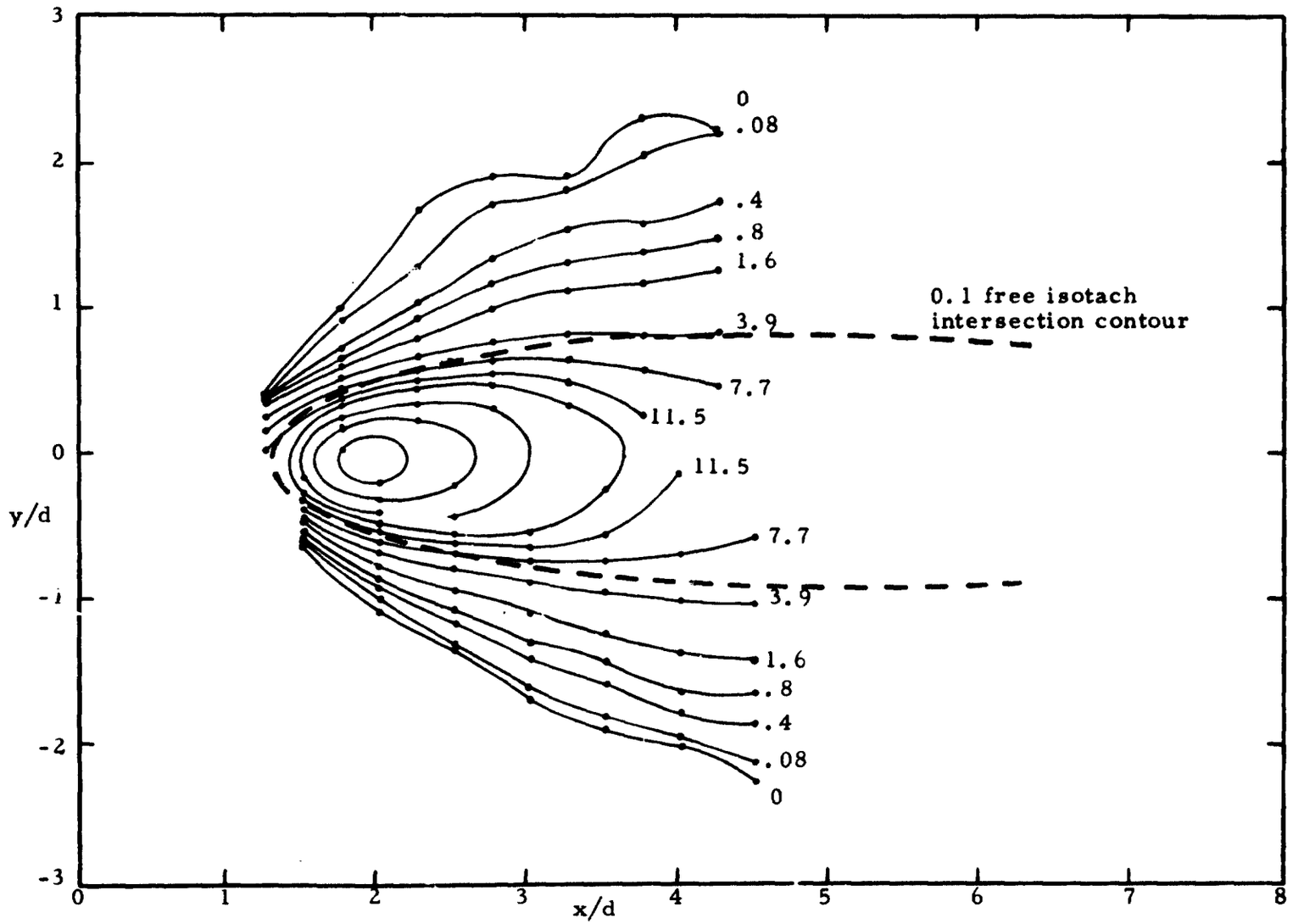

Figure 23. Isobar plot values shown are $p(x, y, 0)/\rho \lambda u(0)^2 \sin \alpha \times 10^2$ for the conditions 15, 1, u.

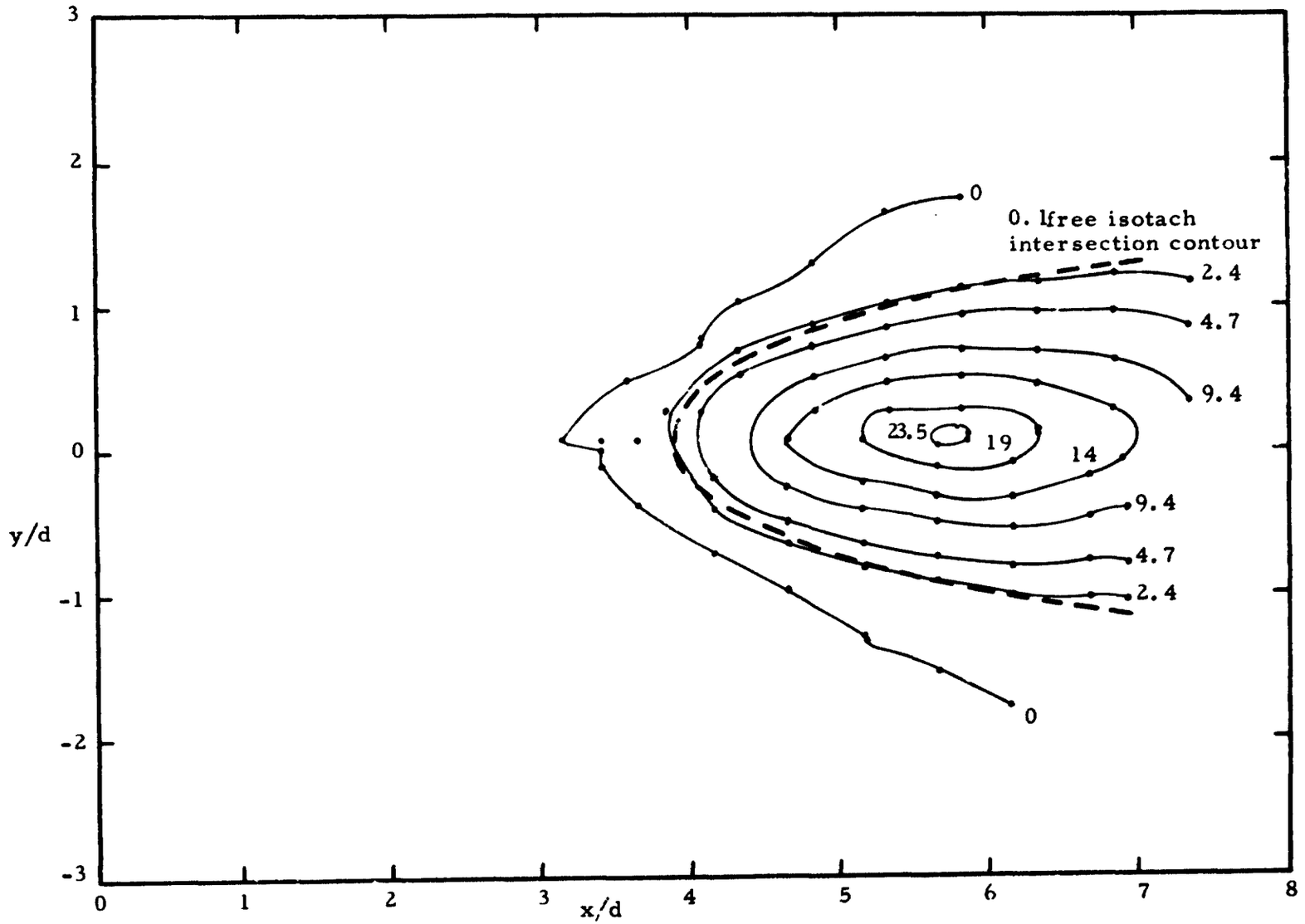

Figure 24. Isobar plot values shown are $p(x, y, 0)/\rho \lambda u(0)^2 \sin \alpha \times 10^2$ for the conditions 15, 2, fd.

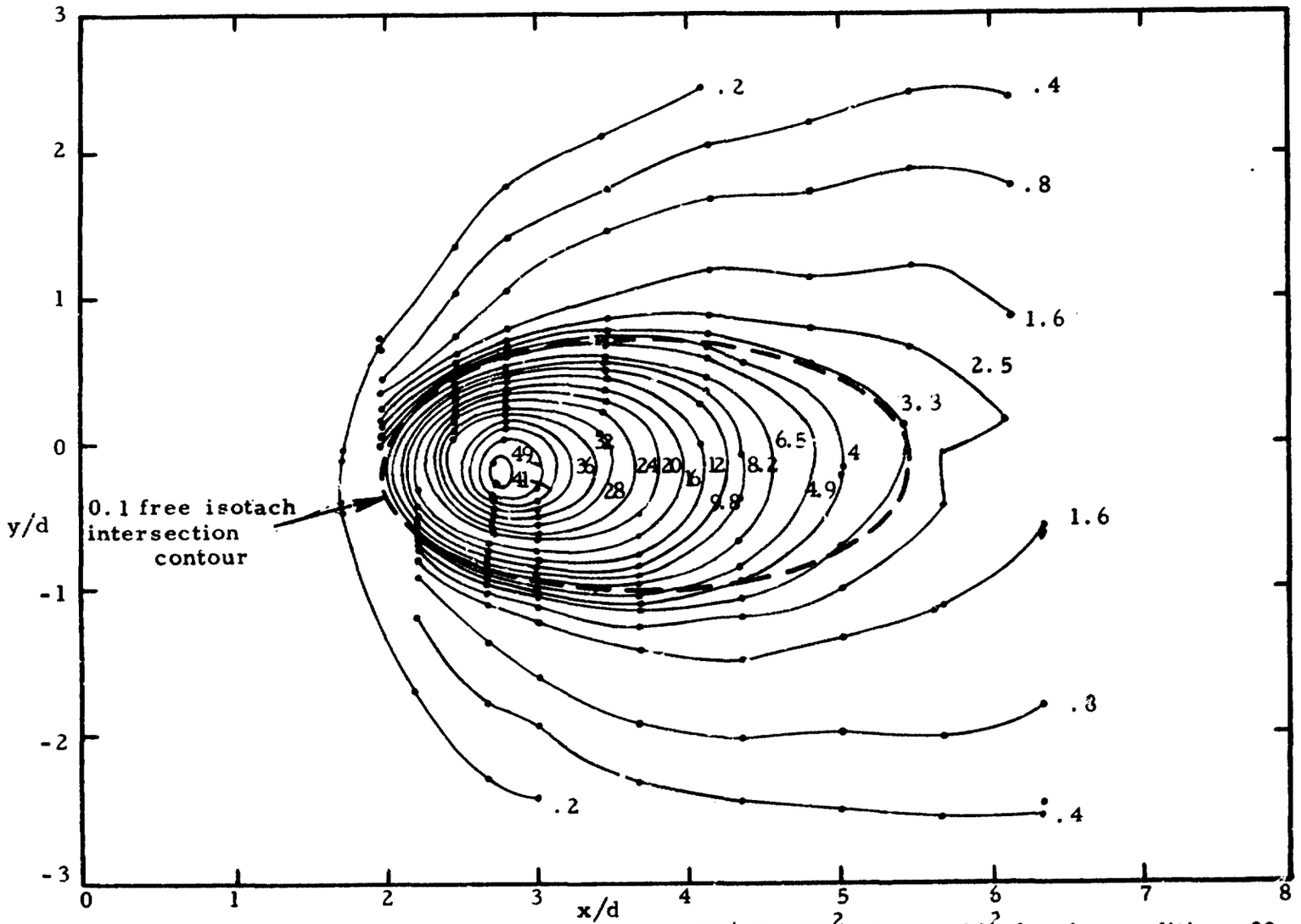

Figure 25. Isobar plot values shown are $p(x, y, 0)/\rho \lambda u(0)^2 \sin \alpha \times 10^2$ for the conditions 30, 2, u.

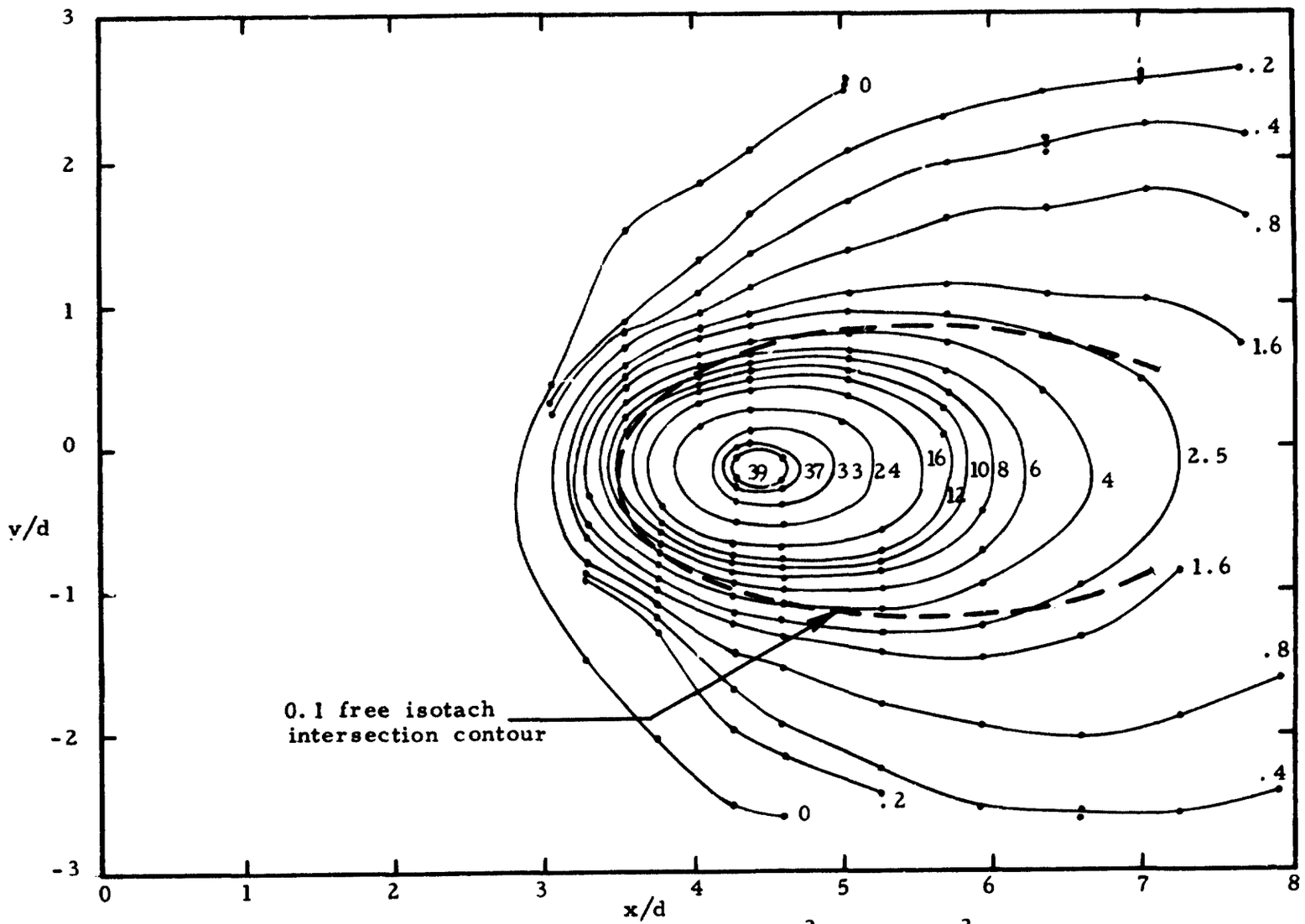

Figure 26. Isobar plot values shown are $p(x, y, 0)/\rho \lambda u(0)^2 \sin \alpha \times 10^2$ for the conditions 30, 3, u.

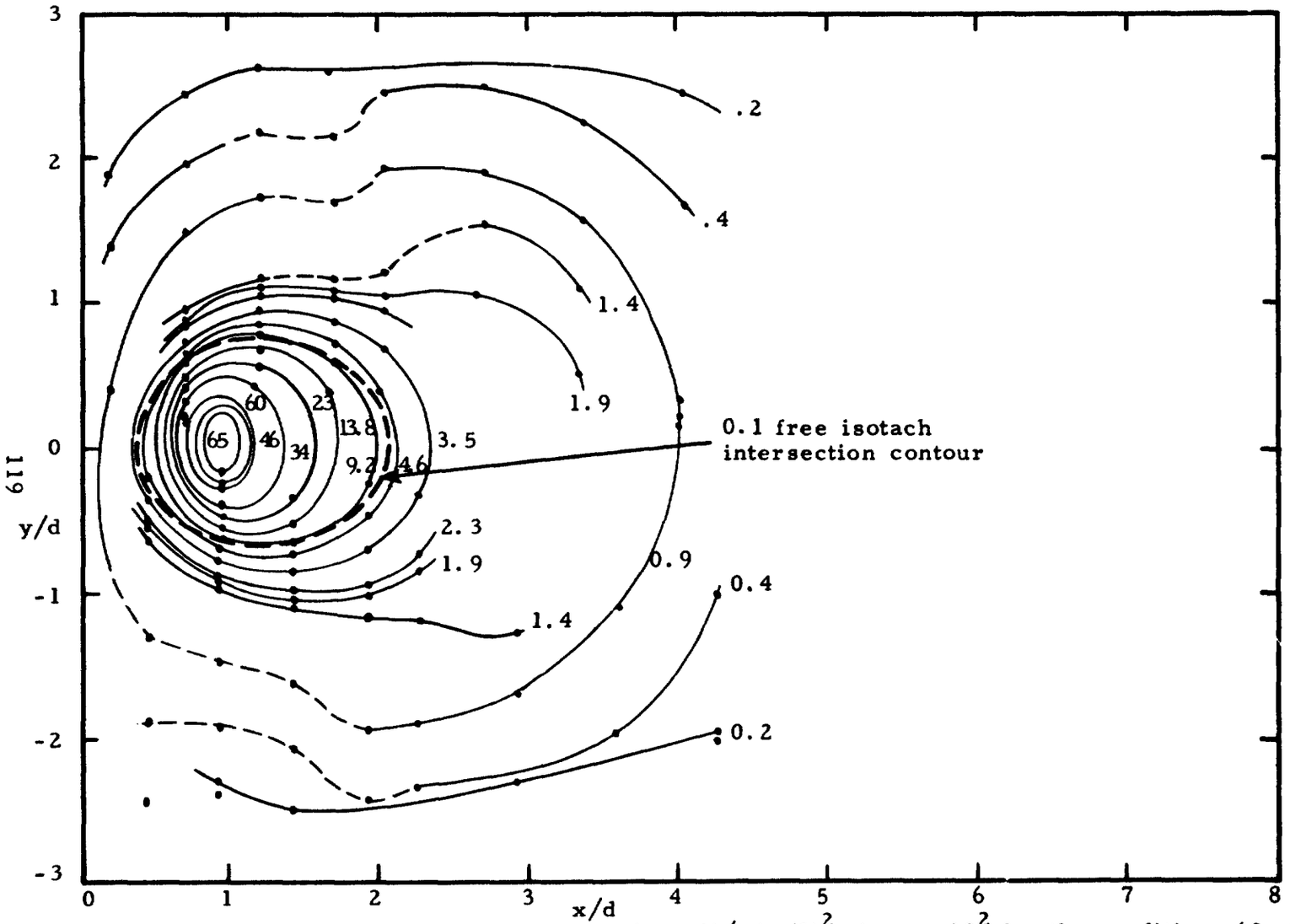

Figure 27. Isobar plot values shown are $p(x, y, 0)/\rho \lambda u(0)^2 \sin \alpha \times 10^2$ for the conditions 60, 2, u.

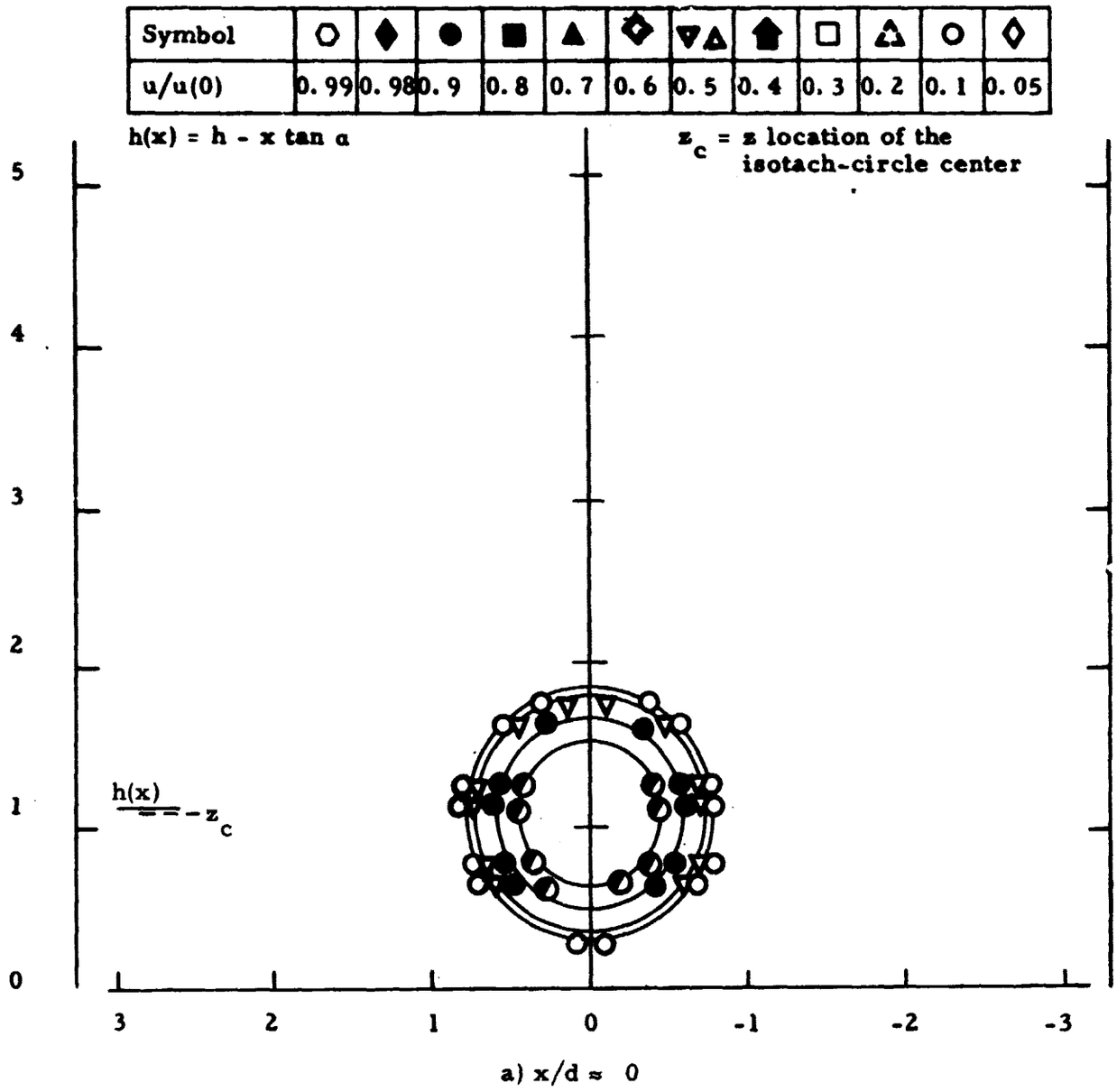

Figure 28. Isotach contours $\alpha = 3$, $h/d = 0.75$, uniform.

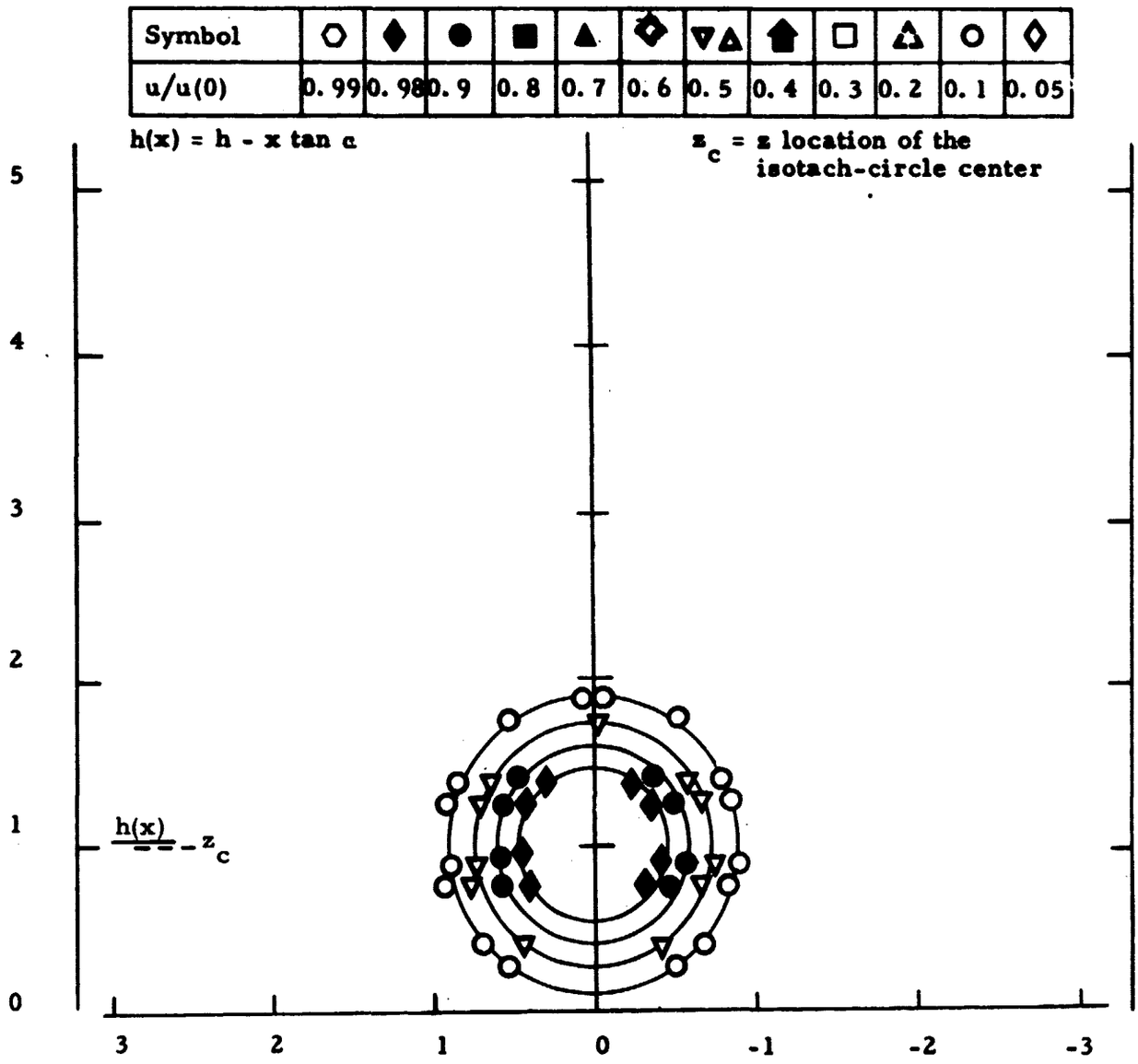
Symbol
u/u(0)
0.99
0.98
0.9
0.8
0.7
0.6
0.5
0.4
0.3
0.2
0.1
0.05
h(x) = h - x tan α
z_c = z location of the isotach-circle center
h(x) - z_c
5
4
3
2
1
0
3
2
1
0
-1
-2
-3

b) x/d = 1

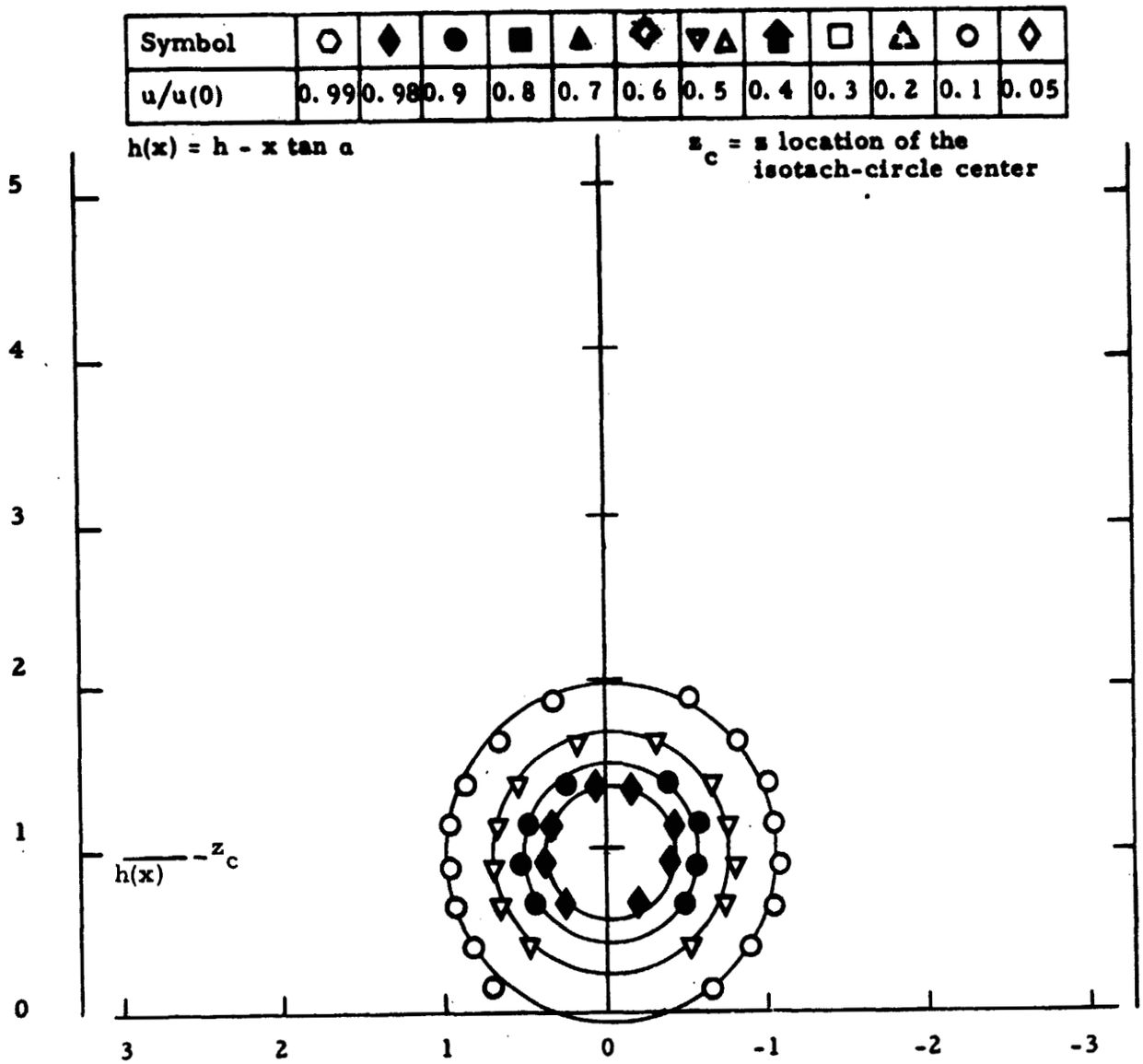
Symbol
u/u(0)
0.99
0.98
0.9
0.8
0.7
0.6
0.5
0.4
0.3
0.2
0.1
0.05
h(x) = h - x tan α
z_c = z location of the isotach-circle center
$\frac{z_c}{h(x)}$
5
4
3
2
1
0
3
2
1
0
-1
-2
-3

c) x/d = 2

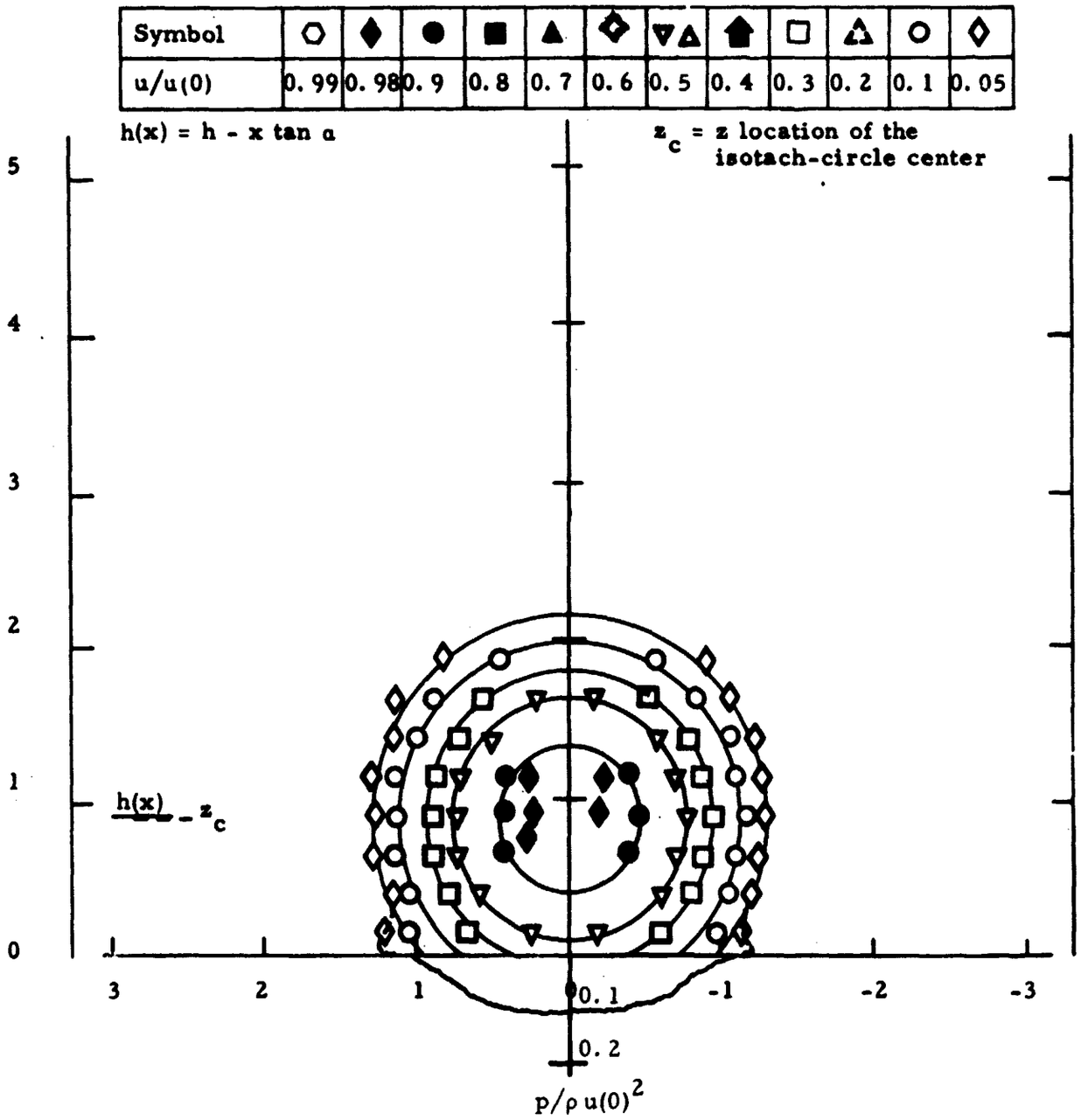
Symbol
u/u(0)
0.99
0.98
0.9
0.8
0.7
0.6
0.5
0.4
0.3
0.2
0.1
0.05
h(x) = h - x tan α
z_c = z location of the isotach-circle center
h(x)/d - z_c
5
4
3
2
1
0
3
2
1
0.1
-1
-2
-3
0.2
p/ρ u(0)^2

d) x/d = 3

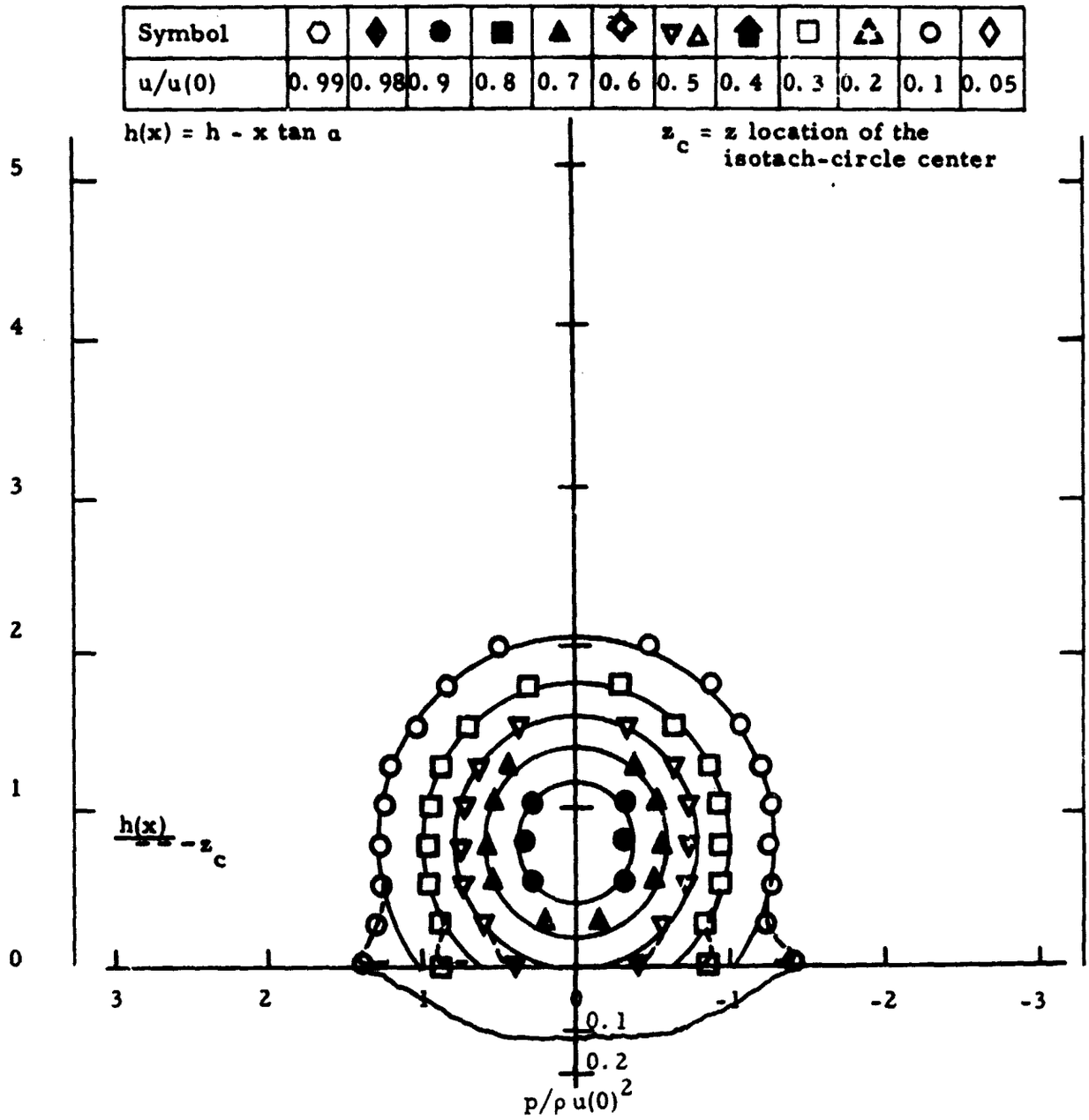
Symbol
u/u(0)
0.99
0.98
0.9
0.8
0.7
0.6
0.5
0.4
0.3
0.2
0.1
0.05
h(x) = h - x tan α
z_c = z location of the isotach-circle center
h(x) - z_c
5
4
3
2
1
0
3
2
1
0
-1
-2
-3
0.1
0.2
p/ρ u(0)^2

e) x/d = 4

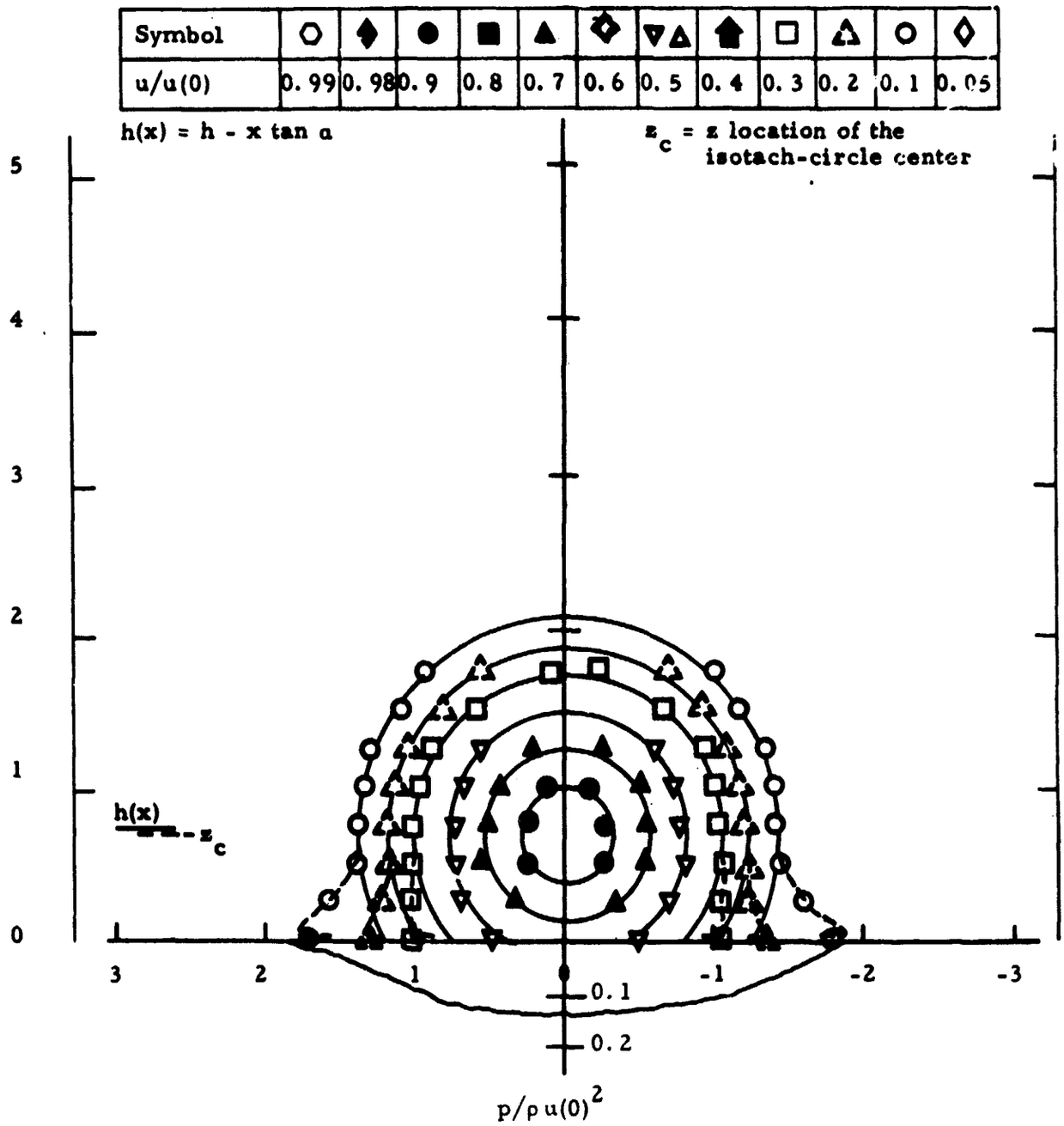
Symbol
u/u(0)
0.99
0.98
0.9
0.8
0.7
0.6
0.5
0.4
0.3
0.2
0.1
0.05
h(x) = h - x tan α
z_c = z location of the isotach-circle center
h(x)
z_c
5
4
3
2
1
0
3
2
1
-1
-2
-3
0.1
0.2
$p/\rho u(0)^2$

f) x/d = 5

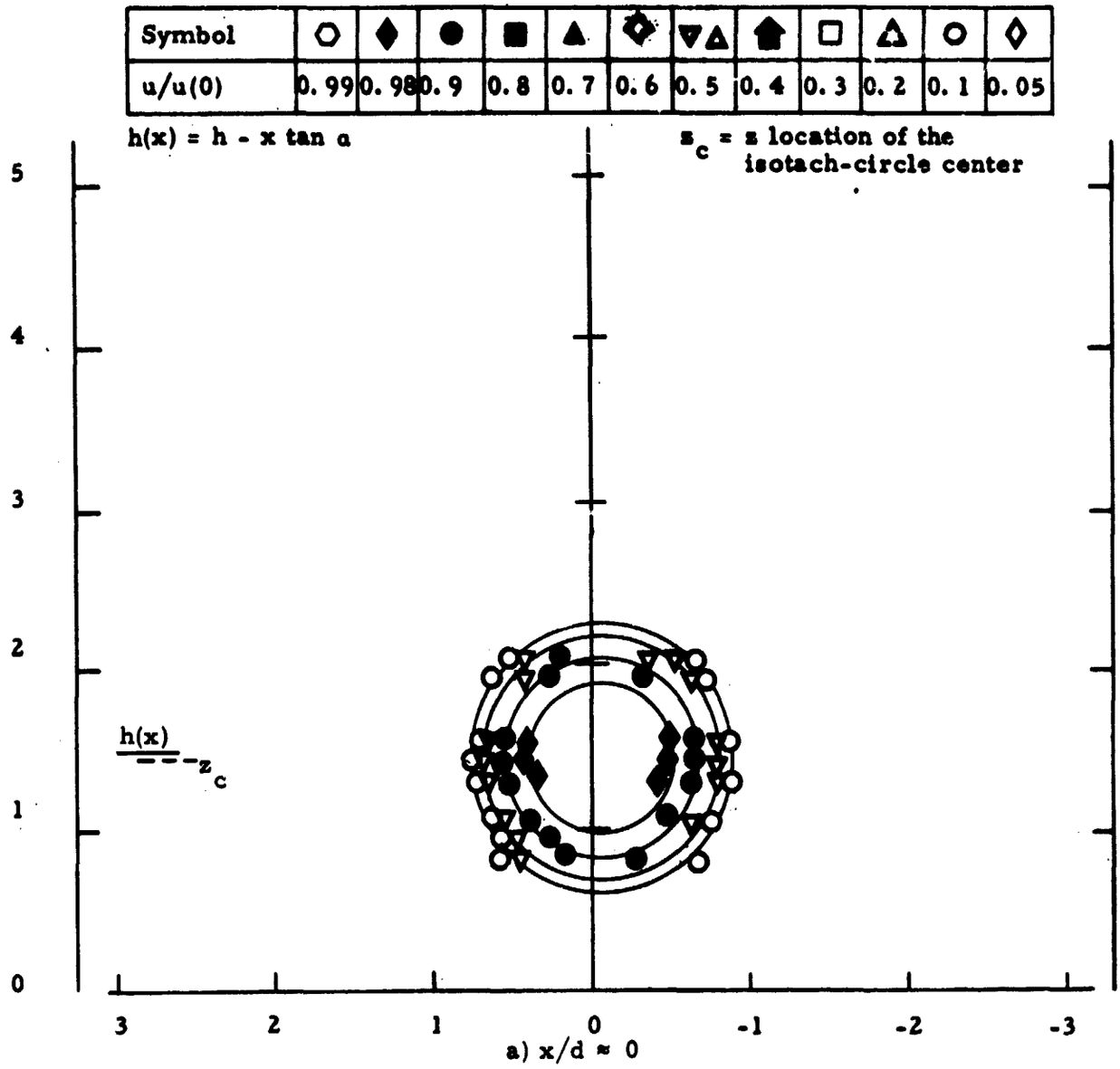

Figure 29. Isotach contours α = 9, h/d = 1, uniform.

Symbol	○	♦	●	■	▲	◆	▽△	⬟	□	△	○	◇
u/u(0)	0.99	0.98	0.9	0.8	0.7	0.6	0.5	0.4	0.3	0.2	0.1	0.05

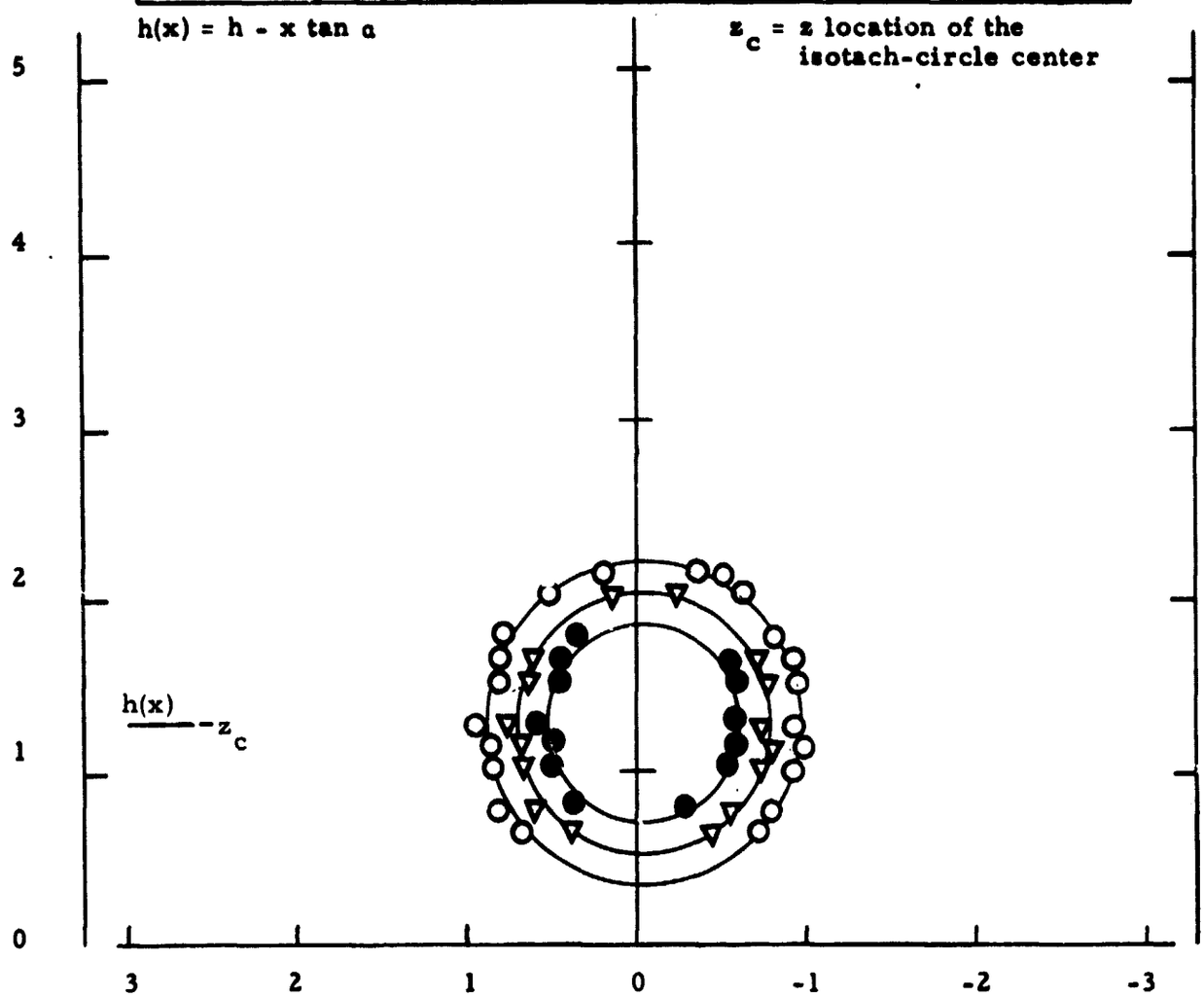

b) x/d = 1

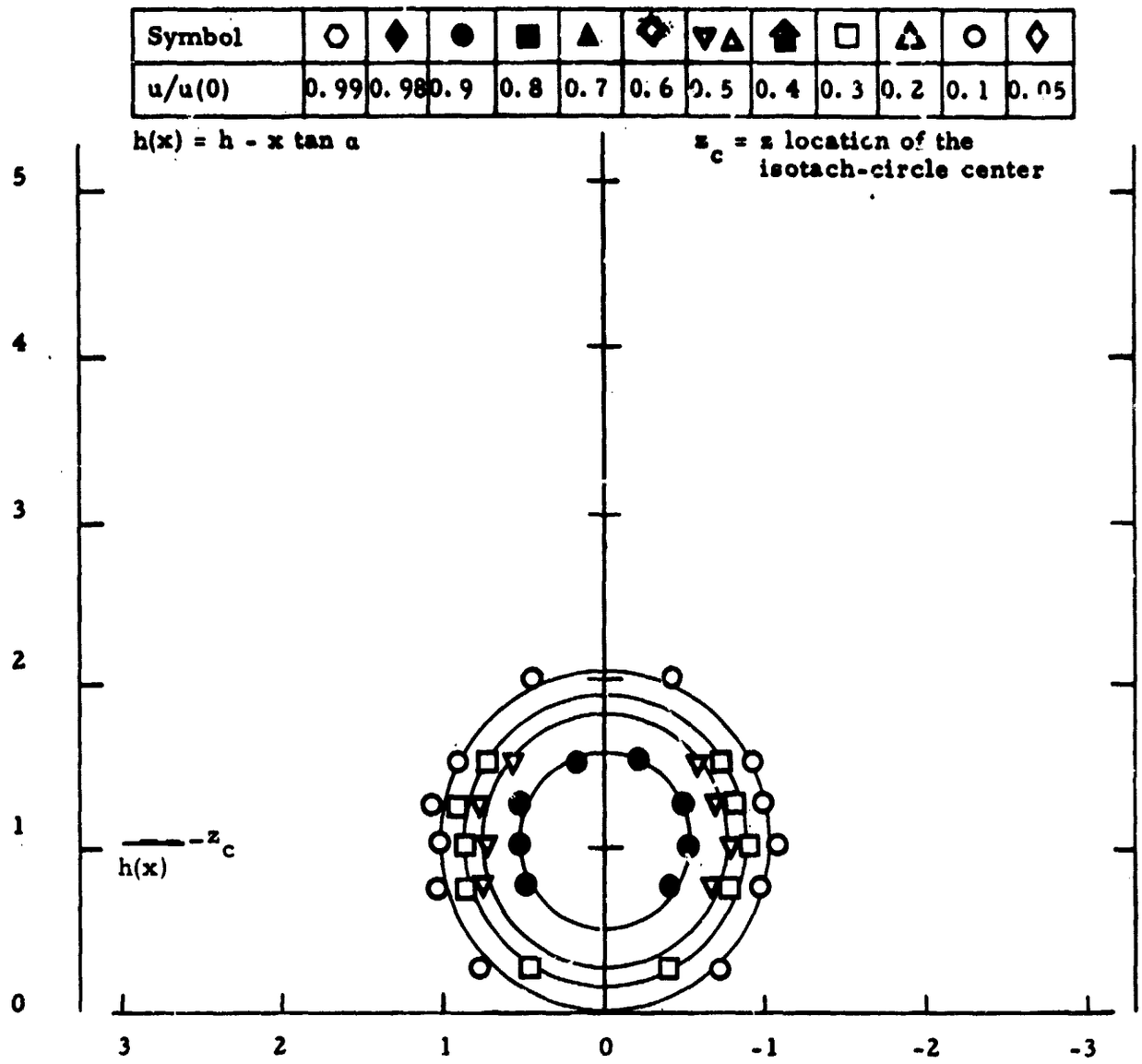
Symbol
u/u(0)
0.99
0.98
0.9
0.8
0.7
0.6
0.5
0.4
0.3
0.2
0.1
0.05
h(x) = h - x tan α
z_c = z location of the isotach-circle center
$-z_c$
h(x)
5
4
3
2
1
0
3
2
1
0
-1
-2
-3

c) x/d = 2

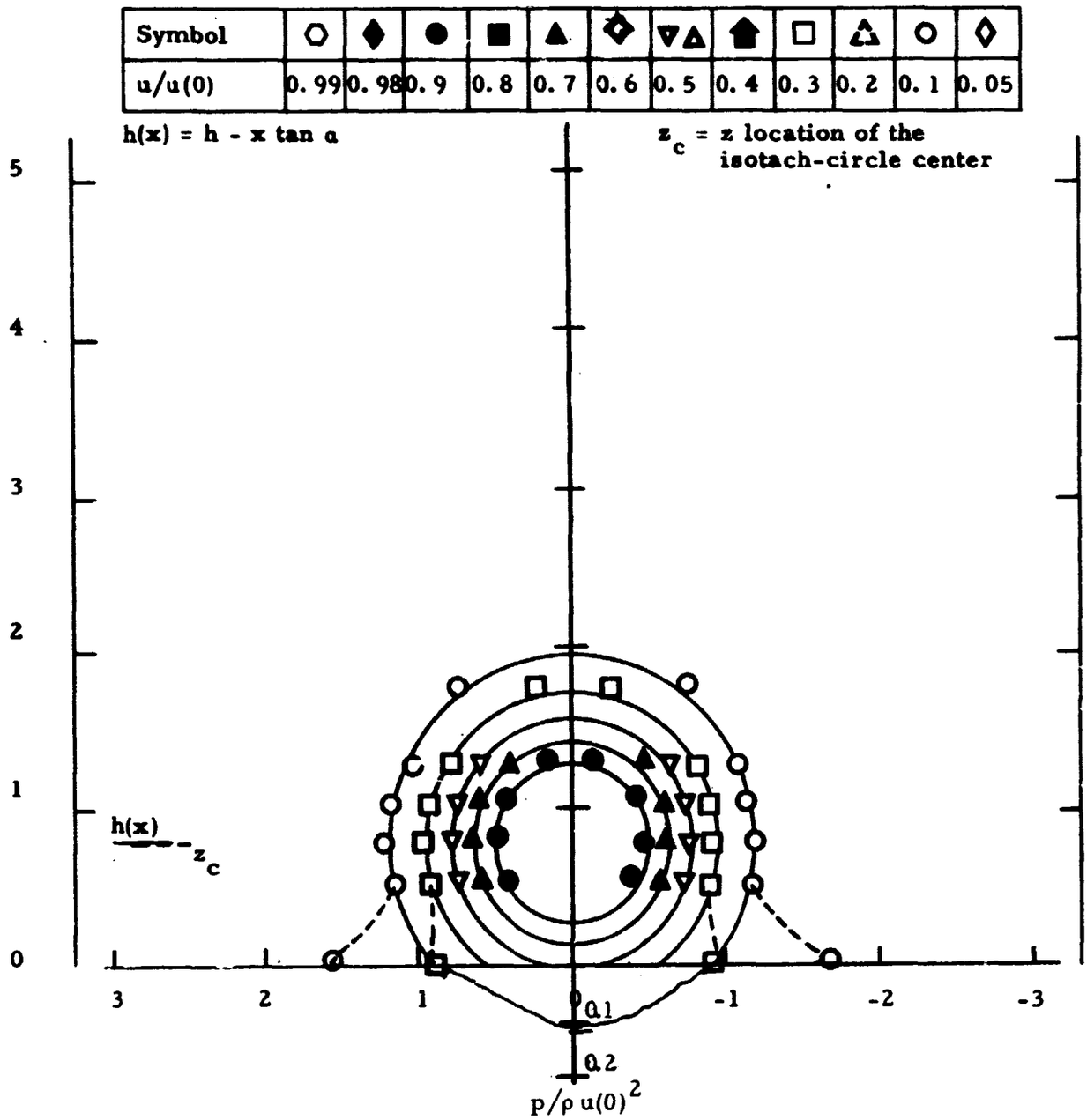
Symbol
u/u(0)
0.99
0.98
0.9
0.8
0.7
0.6
0.5
0.4
0.3
0.2
0.1
0.05
h(x) = h - x tan α
z_c = z location of the isotach-circle center
h(x) - z_c
5
4
3
2
1
0
3
2
1
0
-1
-2
-3
0.1
0.2
p/ρ u(0)^2

d) x/d = 3

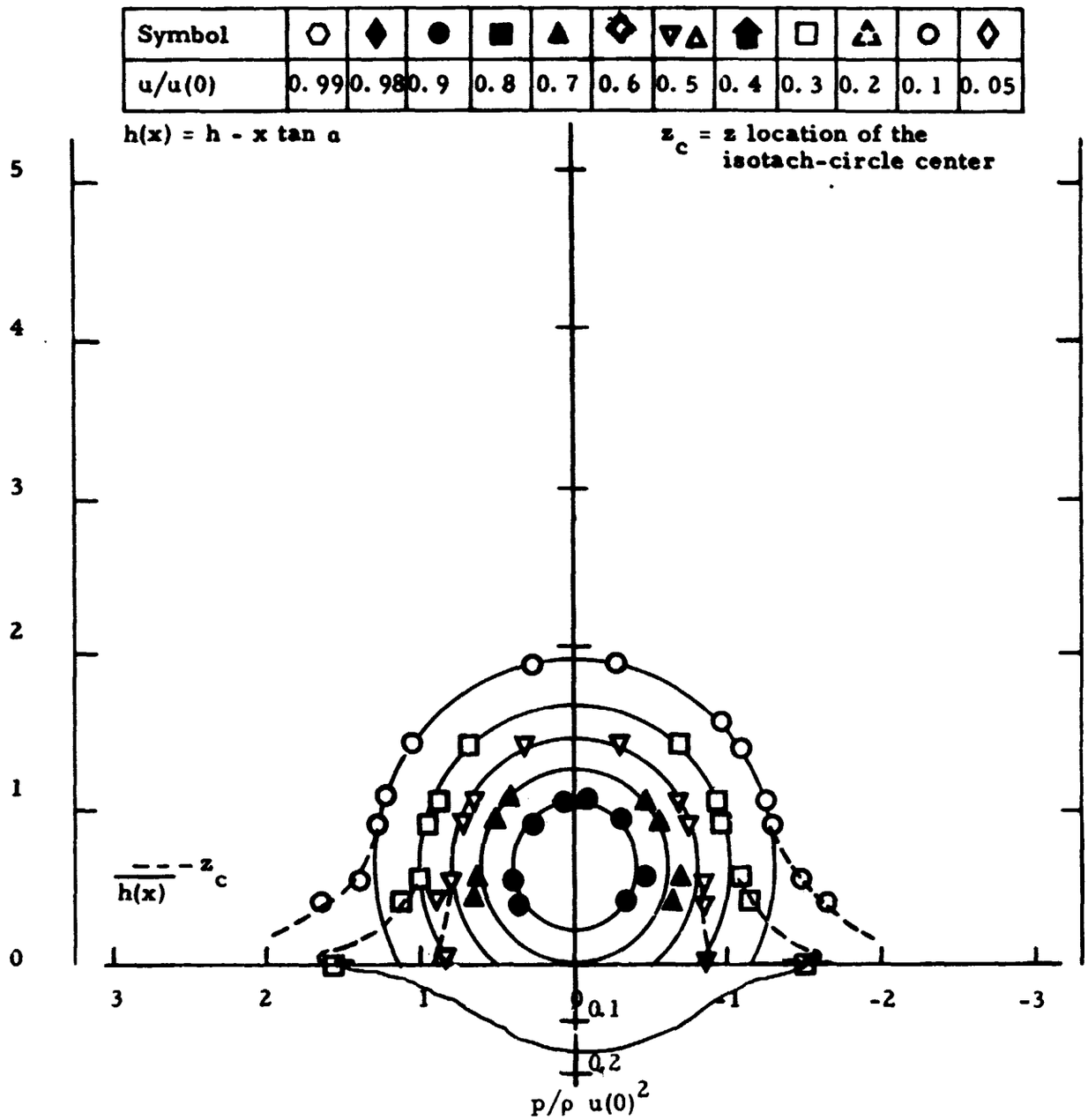
Symbol
u/u(0)
0.99
0.98
0.9
0.8
0.7
0.6
0.5
0.4
0.3
0.2
0.1
0.05
h(x) = h - x tan α
z_c = z location of the isotach-circle center
z_c / h(x)
5
4
3
2
1
0
3
2
1
0
-1
-2
-3
0.1
0.2
p/ρ u(0)^2

e) x/d = 4

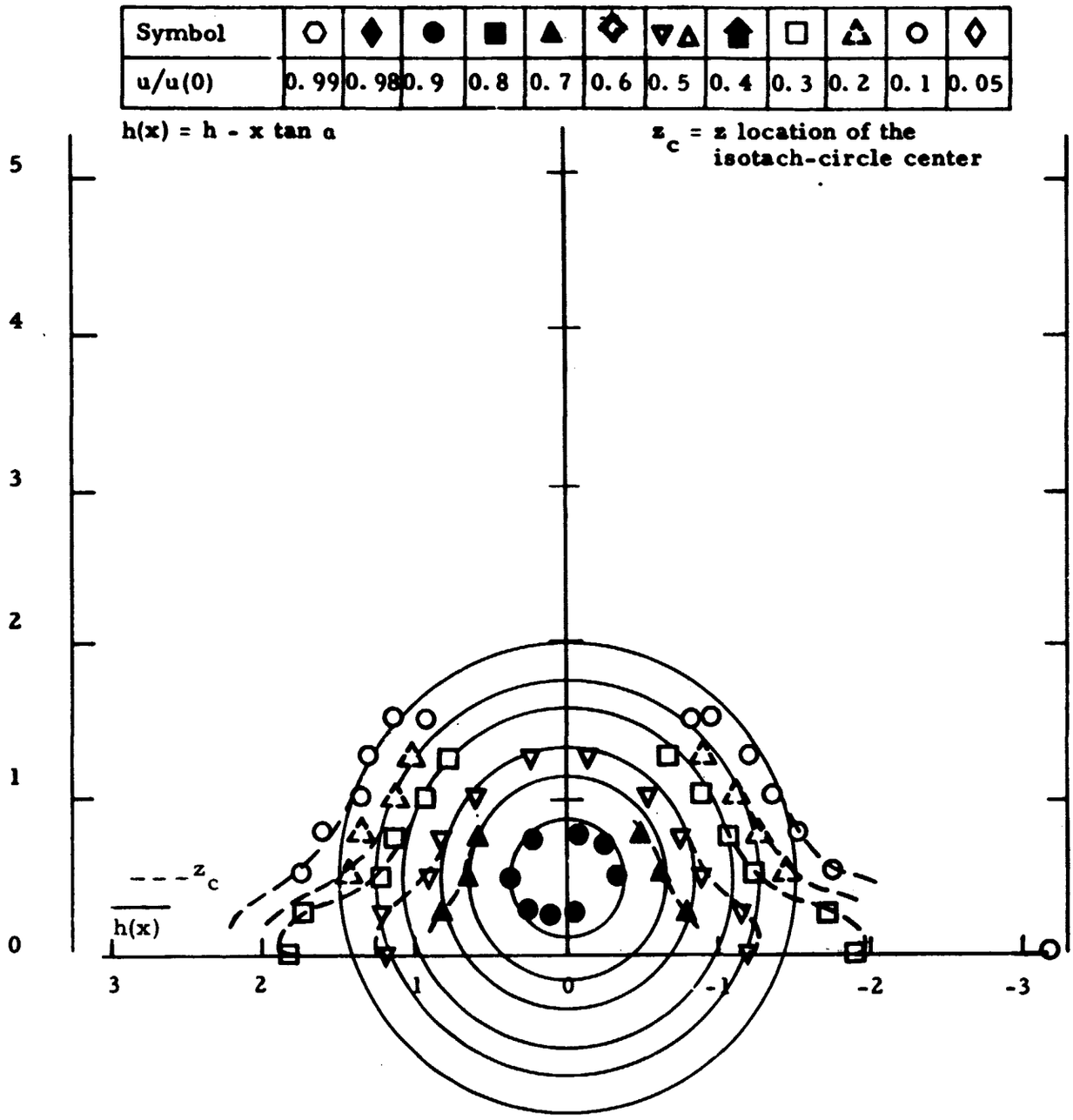
Symbol
u/u(0)
0.99
0.98
0.9
0.8
0.7
0.6
0.5
0.4
0.3
0.2
0.1
0.05
h(x) = h - x tan α
z_c = z location of the isotach-circle center
z_c
h(x)
5
4
3
2
1
0
3
2
1
0
-1
-2
-3

f) x/d = 5

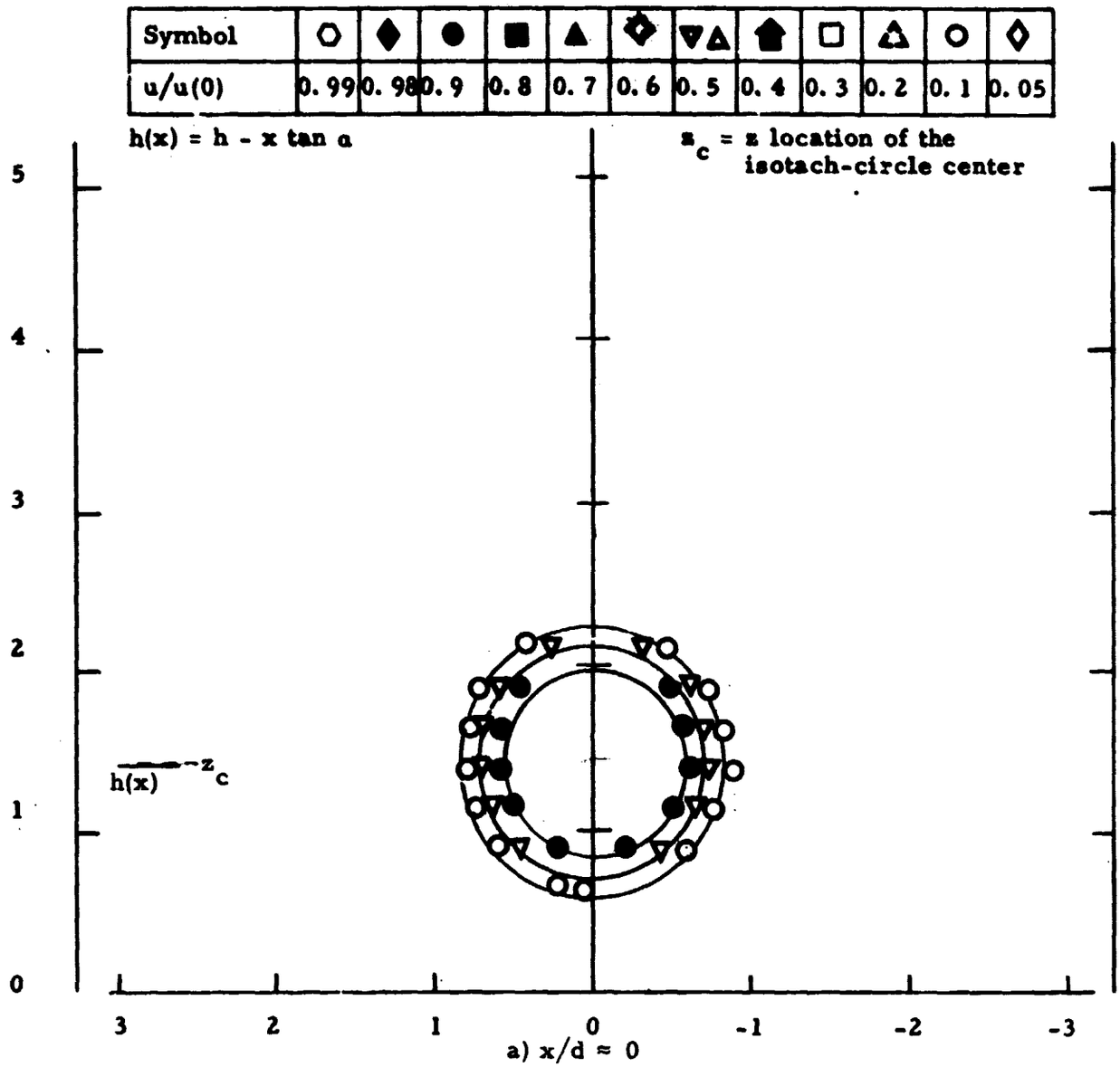

Figure 30. Isotach contours α = 15, h/d = 1, uniform.

Symbol	○	◆	●	■	▲	◆	▽△	⬟	□	△	○	◇
u/u(0)	0.99	0.98	0.9	0.8	0.7	0.6	0.5	0.4	0.3	0.2	0.1	0.05

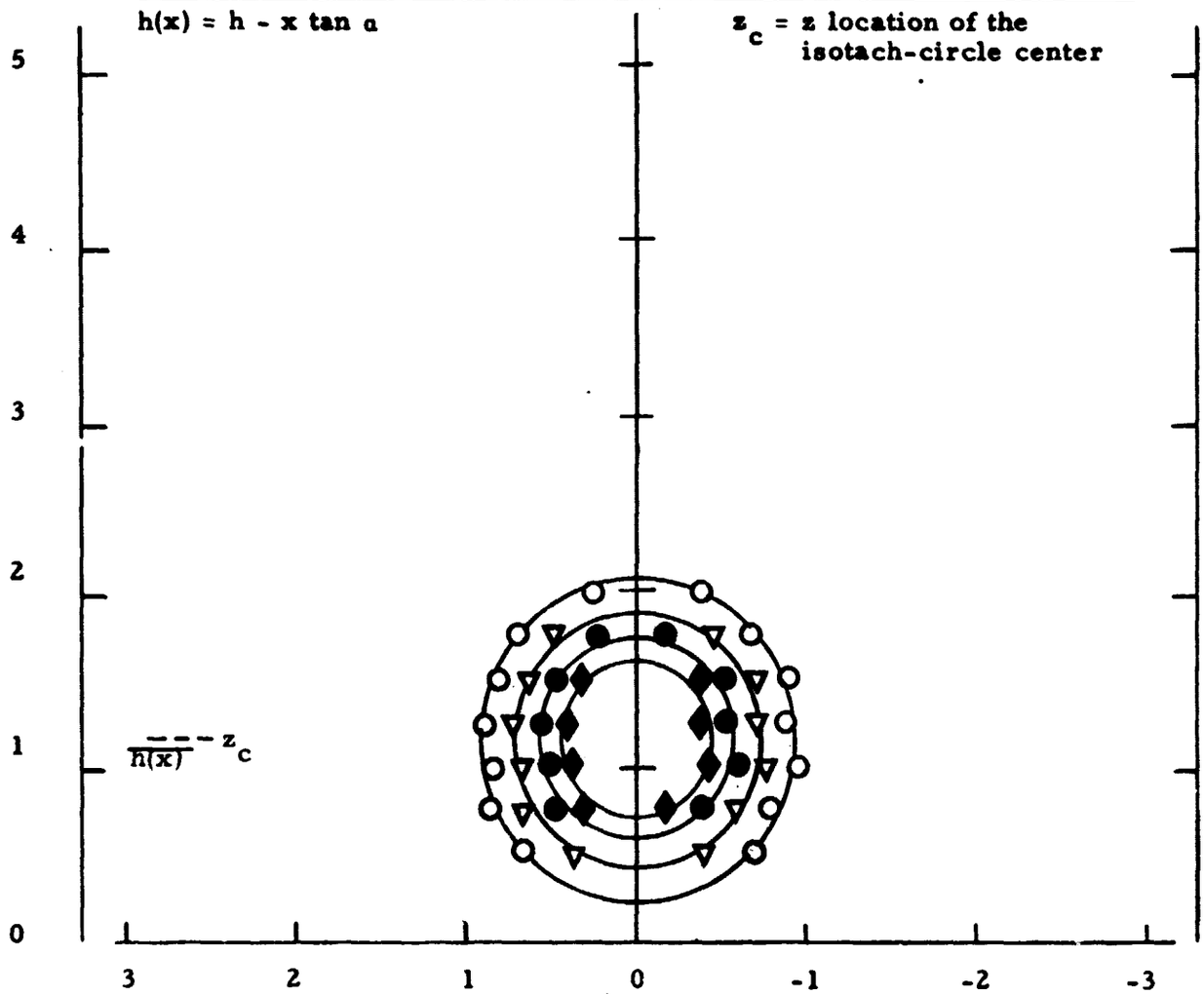

b) x/d = 1

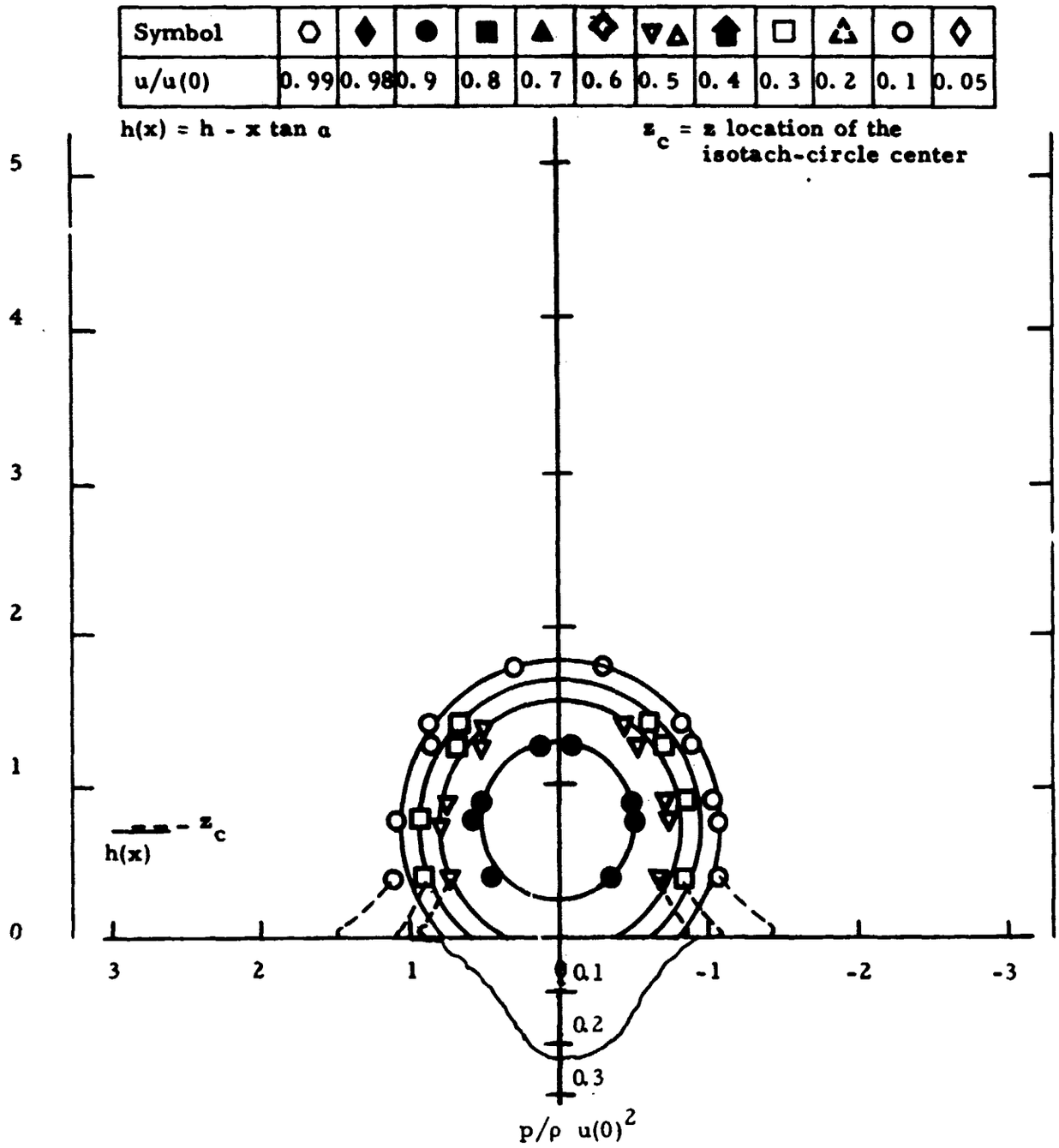
Symbol
u/u(0)
0.99
0.98
0.9
0.8
0.7
0.6
0.5
0.4
0.3
0.2
0.1
0.05
h(x) = h - x tan α
z_c = z location of the isotach-circle center
z_c
h(x)
5
4
3
2
1
0
3
2
1
0.1
-1
-2
-3
0.2
0.3
p/ρ u(0)^2

c) x/d = 2

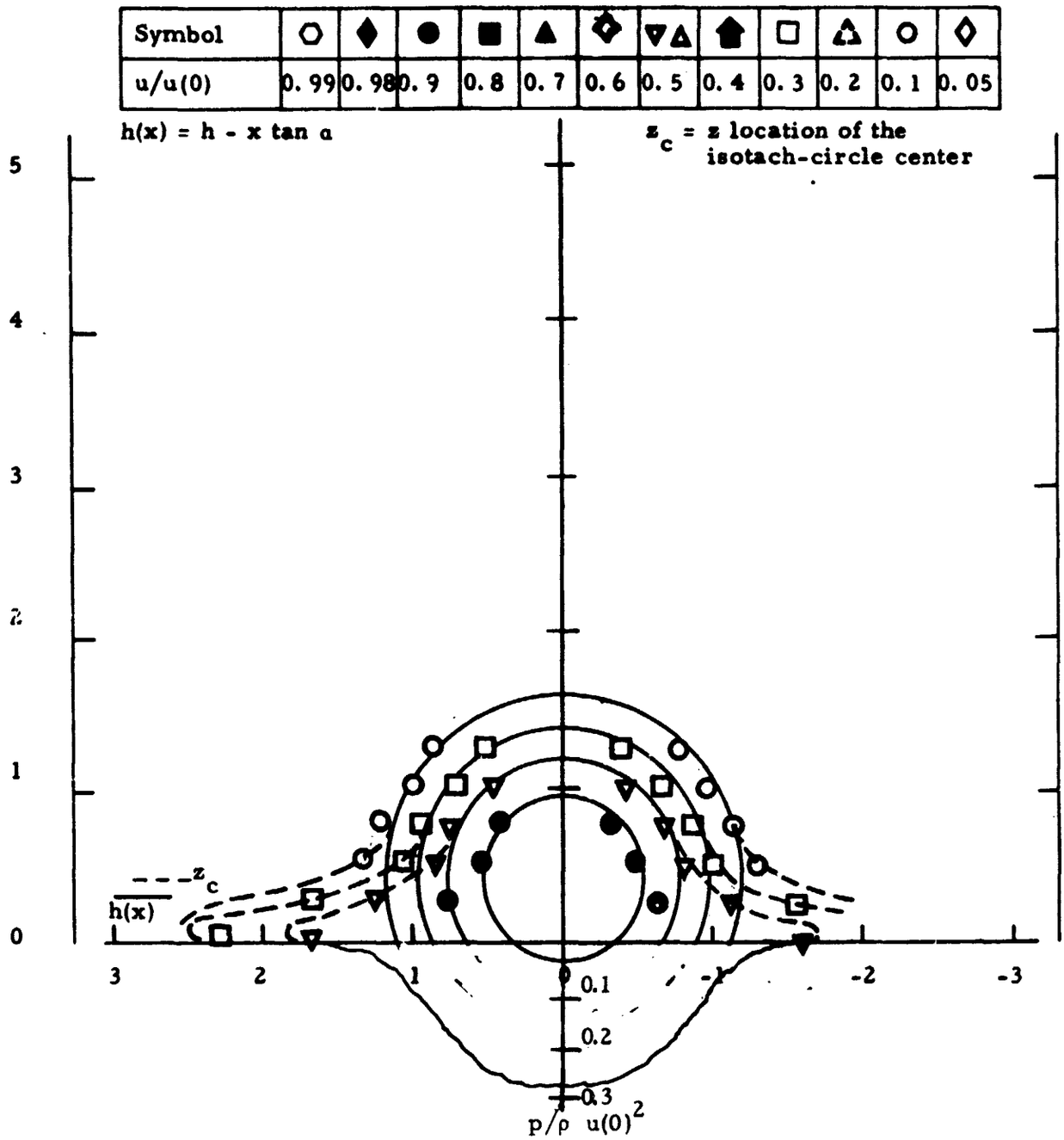
Symbol
u/u(0)
0.99
0.98
0.9
0.8
0.7
0.6
0.5
0.4
0.3
0.2
0.1
0.05
h(x) = h - x tan α
z_c = z location of the isotach-circle center
z_c
h(x)
5
4
3
2
1
0
3
2
1
0
-1
-2
-3
0.1
0.2
0.3
p/ρ u(0)^2

d) x/d = 3

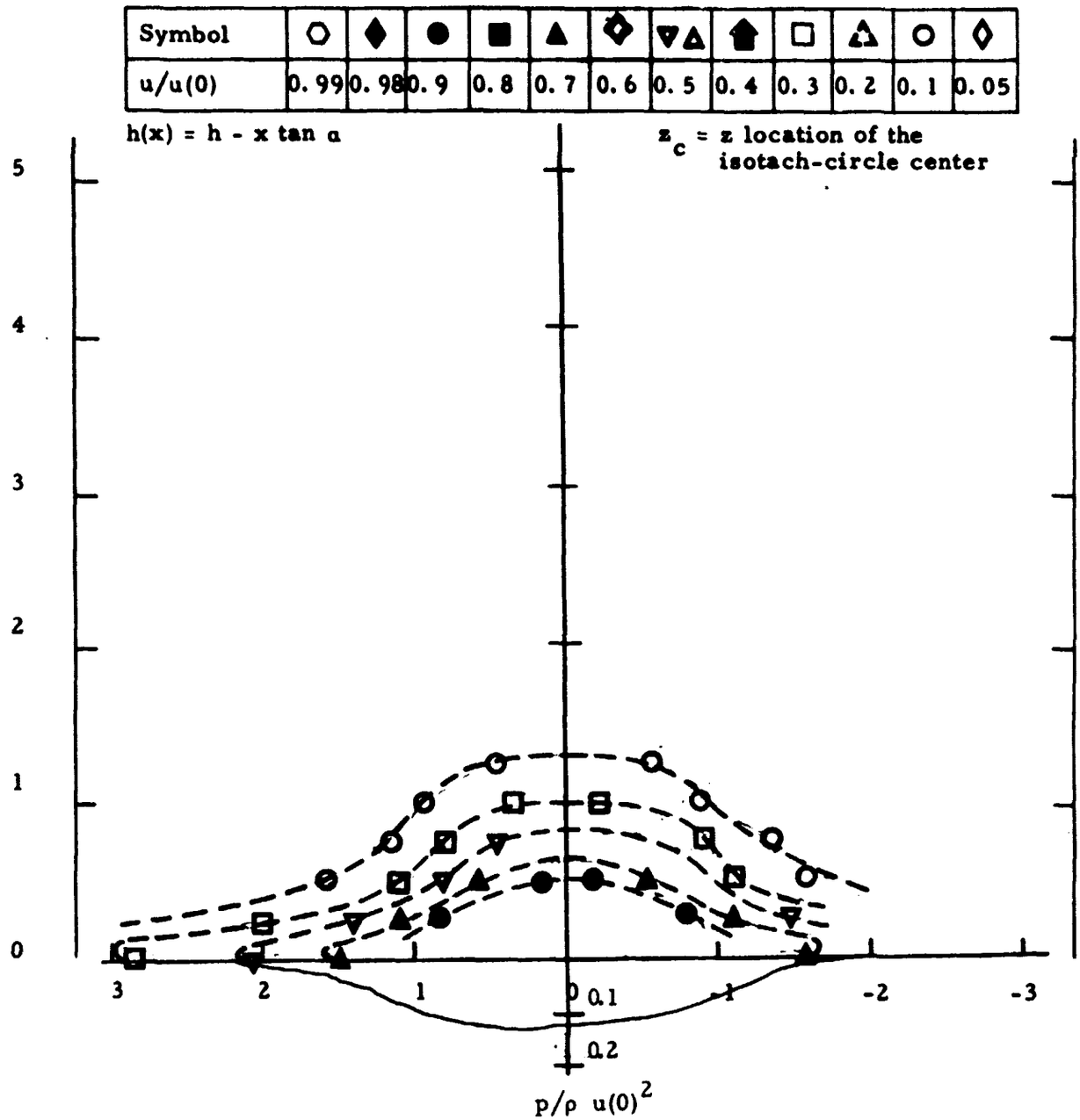
Symbol
u/u(0)
0.99
0.98
0.9
0.8
0.7
0.6
0.5
0.4
0.3
0.2
0.1
0.05
h(x) = h - x tan α
z_c = z location of the isotach-circle center
5
4
3
2
1
0
3
2
1
0
-1
-2
-3
0.1
0.2
p/ρ u(0)^2

e) x/d = 4

Symbol	○	◆	●	■	▲	◇	▼▲	⬟	□	△	○	◇
u/u(0)	0.99	0.98	0.9	0.8	0.7	0.6	0.5	0.4	0.3	0.2	0.1	0.05

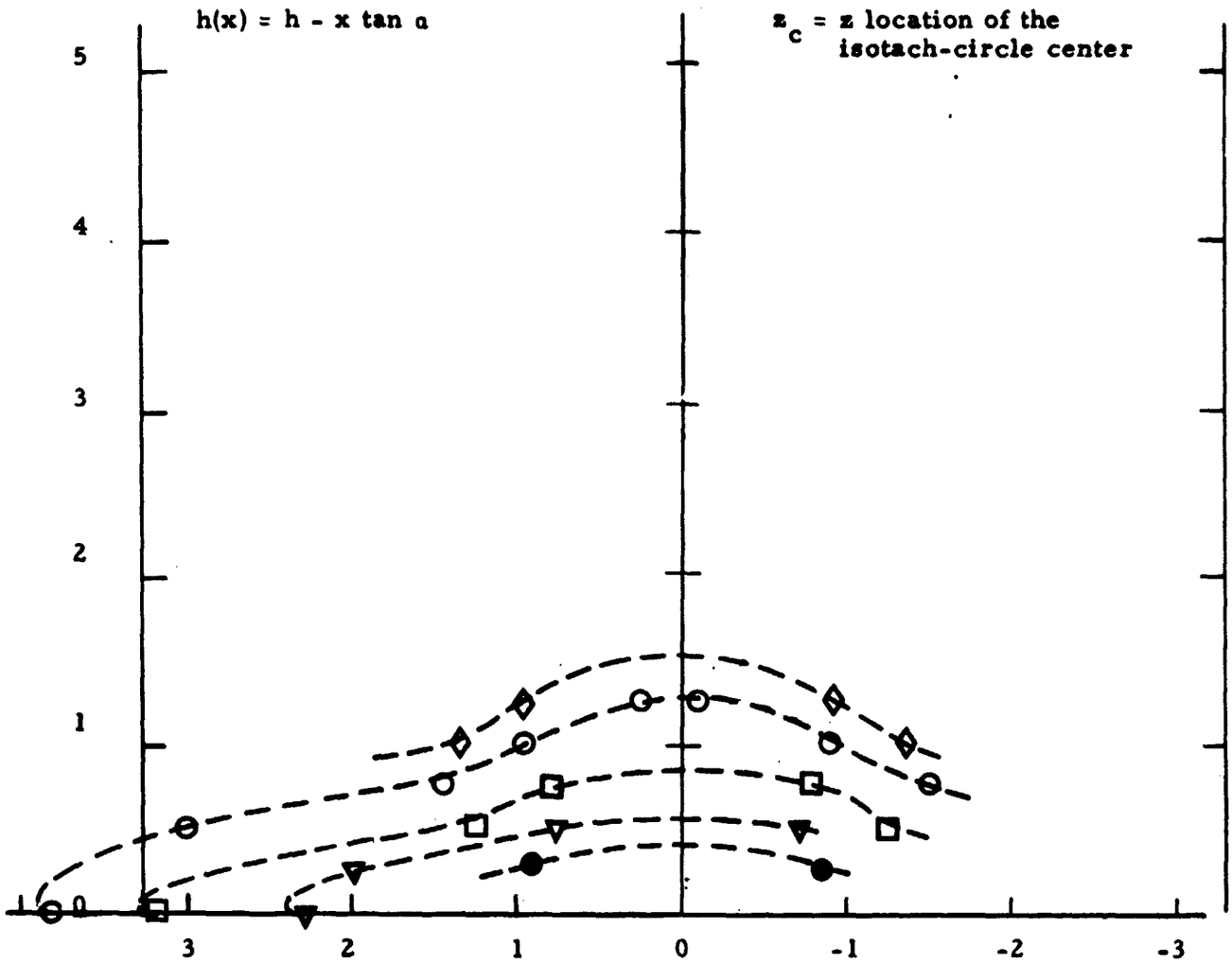

f) x/d = 5

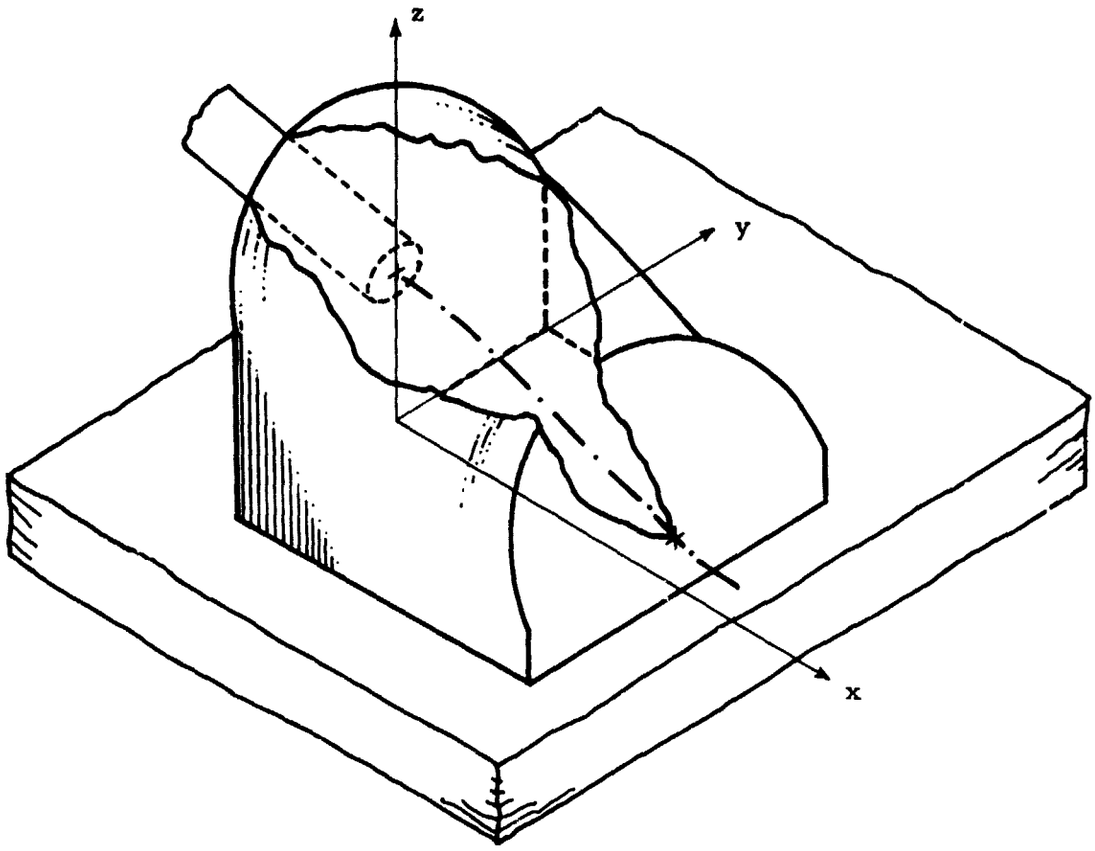

TOP

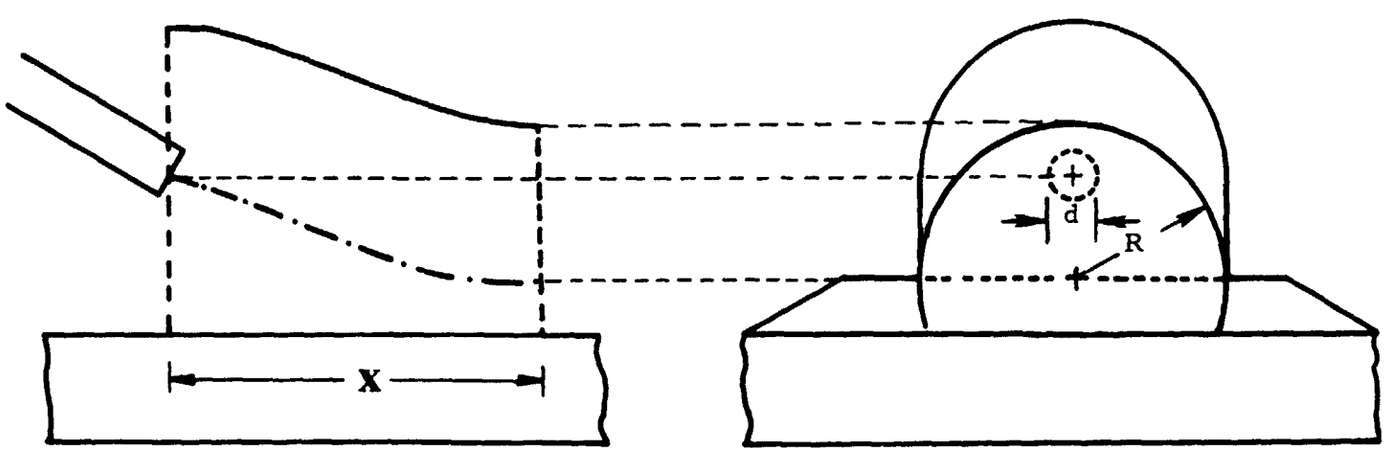

SIDE **FRONT**

Figure 31. Control volume for the analysis of the round-jet/plane-wall flow field.

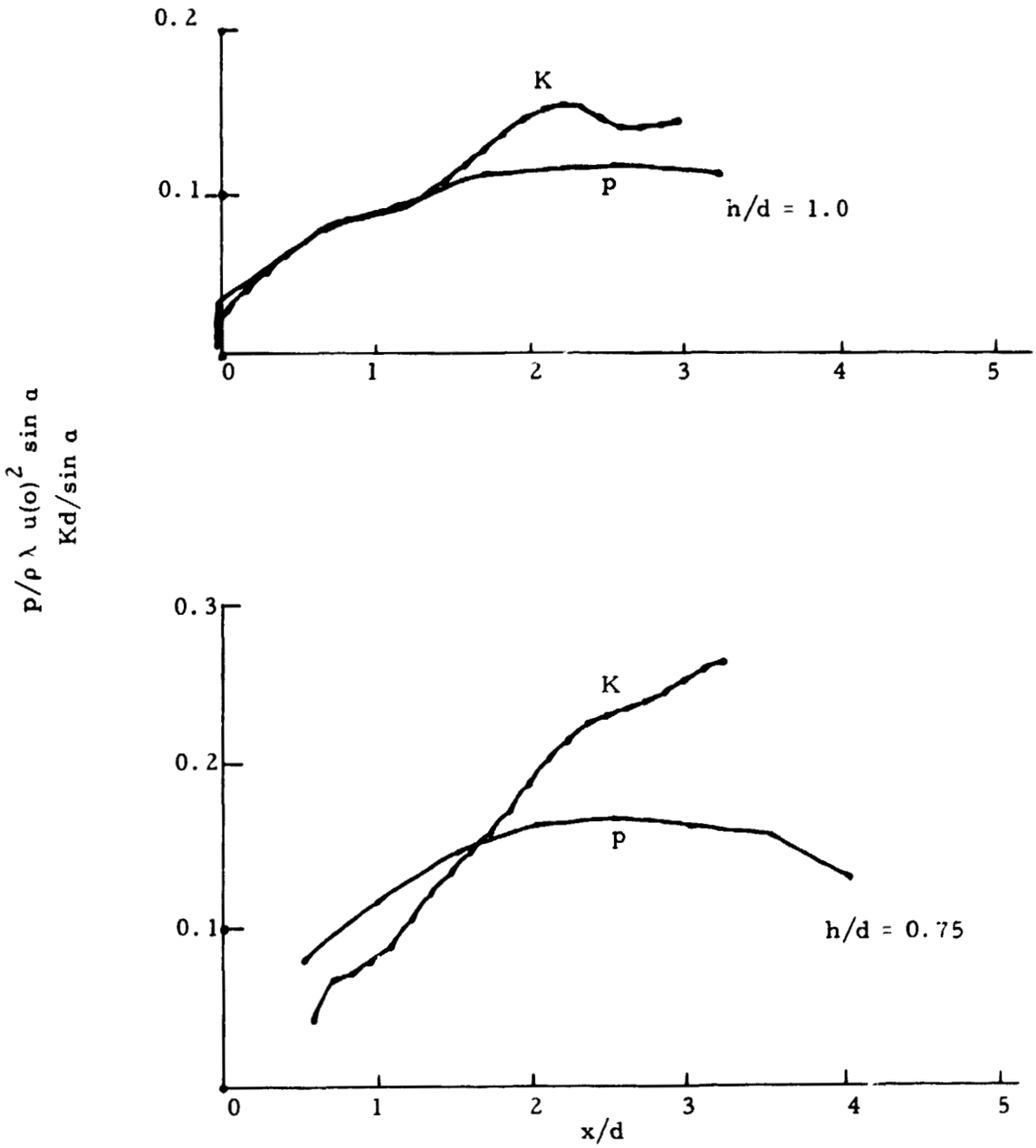

Figure 32. Normalized centerline pressure $p/\rho \lambda u(o)^2 \sin \alpha$ and the normalized curvature of the jet's momentum flux centerline $Kd/\sin\alpha$. The x/d origin for each h/d value represents the intersection point of the 0.1 free isotach. α = 3 degrees uniform exit condition

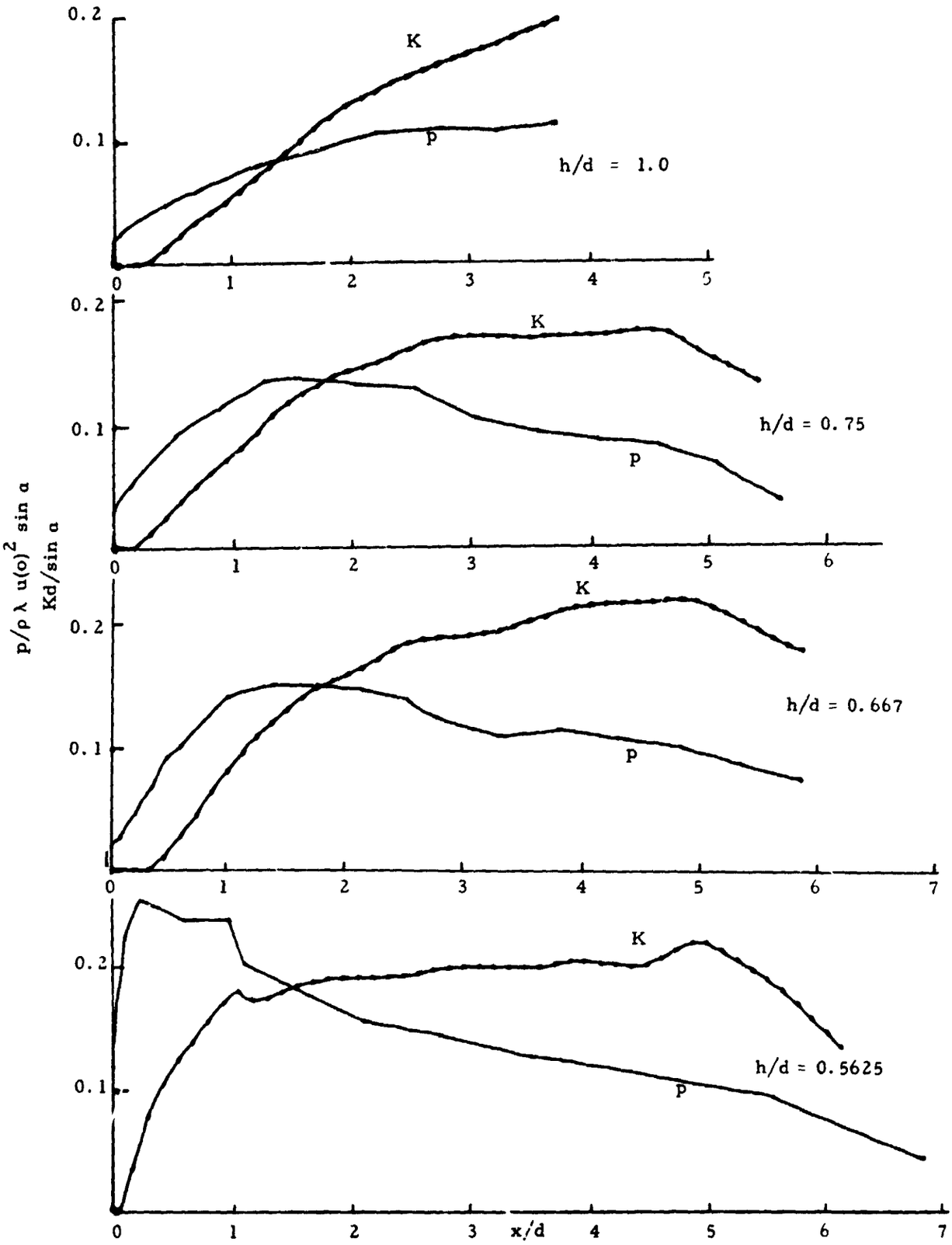

Figure 33. Normalized centerline pressure $p/\rho \lambda u(o)^2 \sin \alpha$ and the normalized curvature of the jet's momentum flux centerline $Kd/\sin\alpha$. The $x/d = 0$ origin for each h/d value represents the intersection point of the 0.1 free isotach.
α = 3 degrees fully developed exit condition

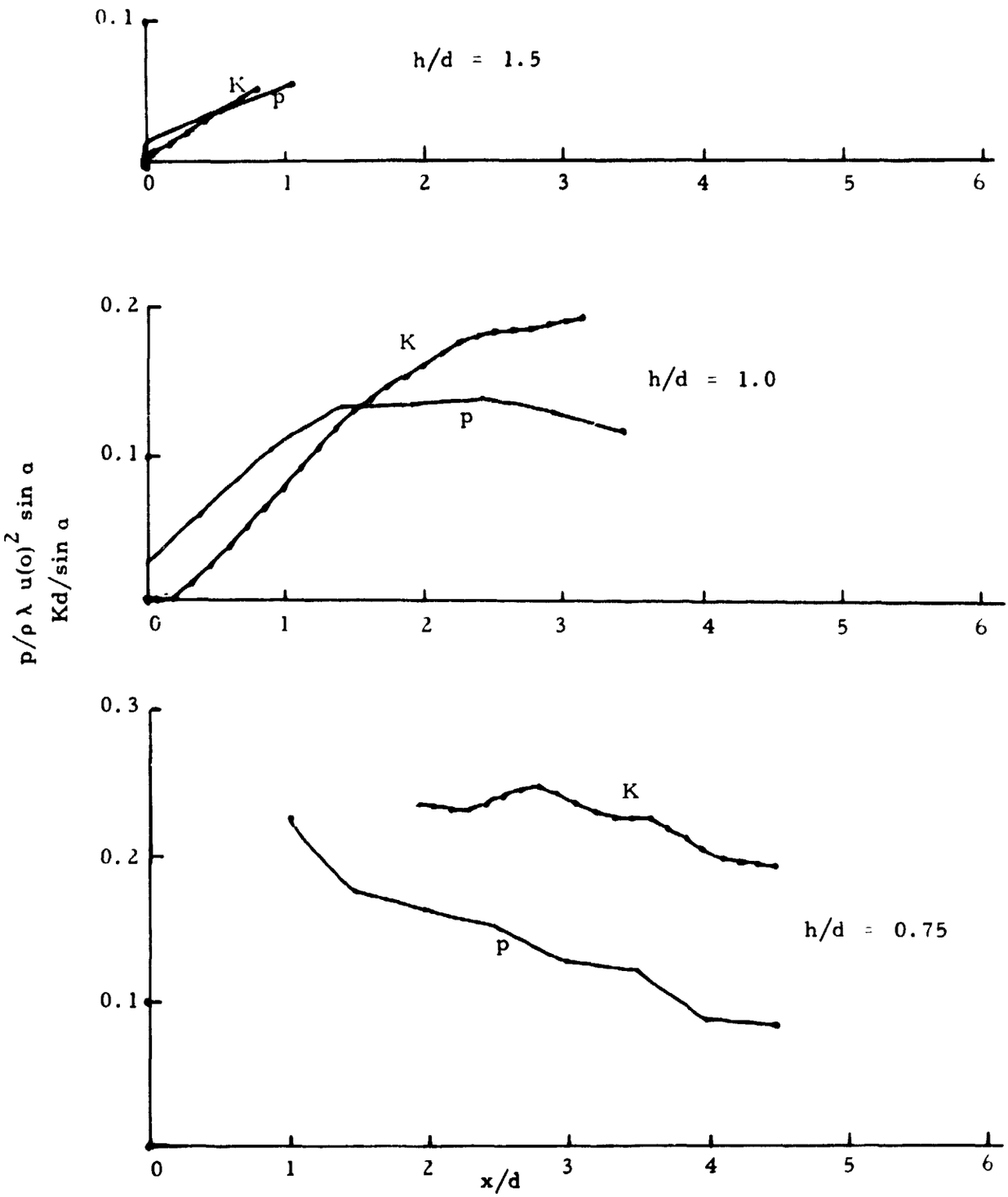

Figure 34. Normalized centerline pressure $p/\rho \lambda u(o)^2 \sin \alpha$ and the normalized curvature of the jet's momentum flux centerline $Kd/\sin \alpha$. The $x/d = 0$ origin for each h/d value represents the intersection point of the 0.1 free isotach.
$\alpha = 6$ degrees uniform exit condition

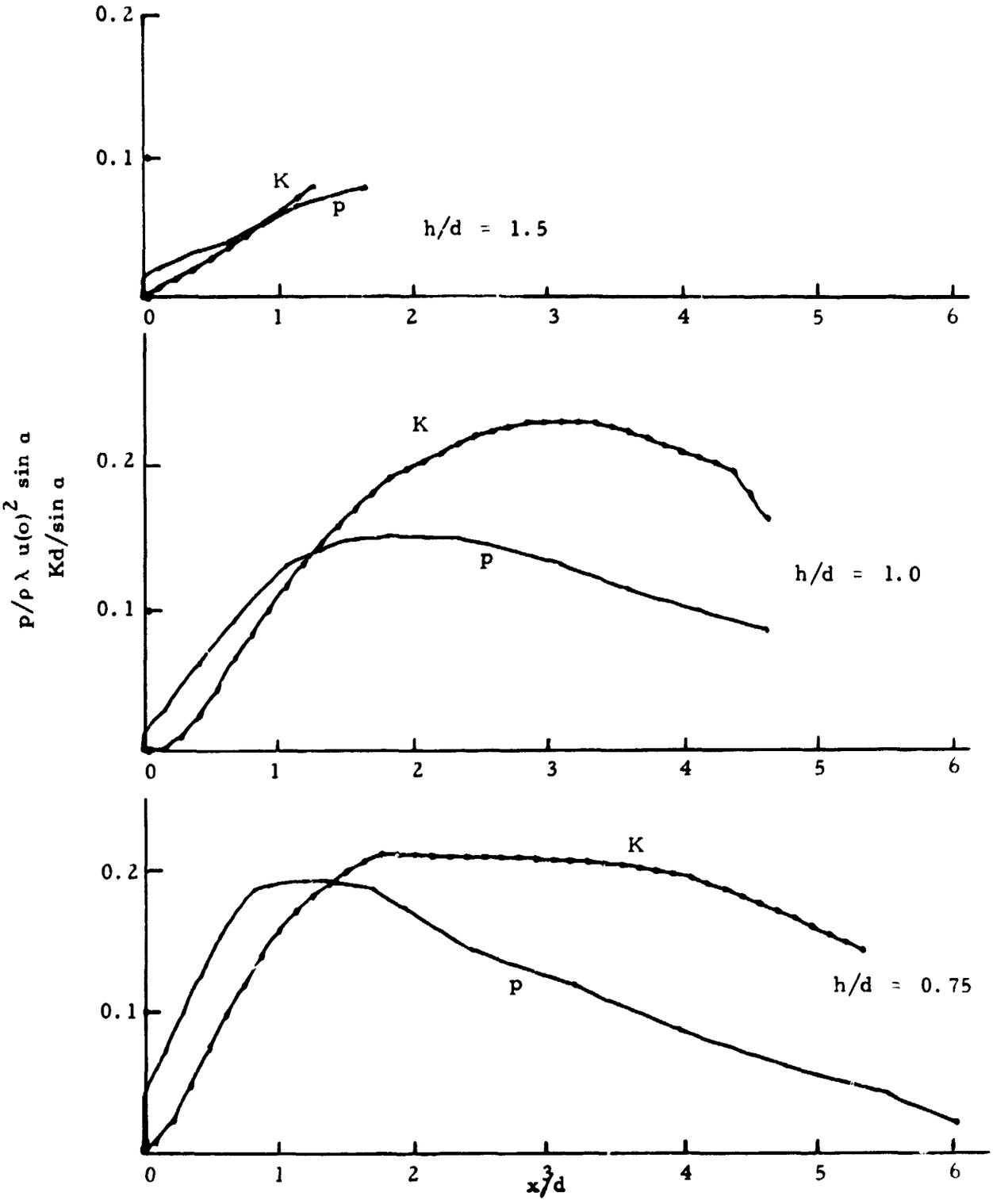

Figure 35 . Normalized centerline pressure $p/\rho \lambda u(o)^2 \sin \alpha$ and the normalized curvature of the jet's momentum flux centerline $Kd/\sin \alpha$. The $x/d = 0$ origin for each h/d value represents the intersection point of the 0.1 free isotach.
$\alpha = 6$ degrees fully developed exit condition

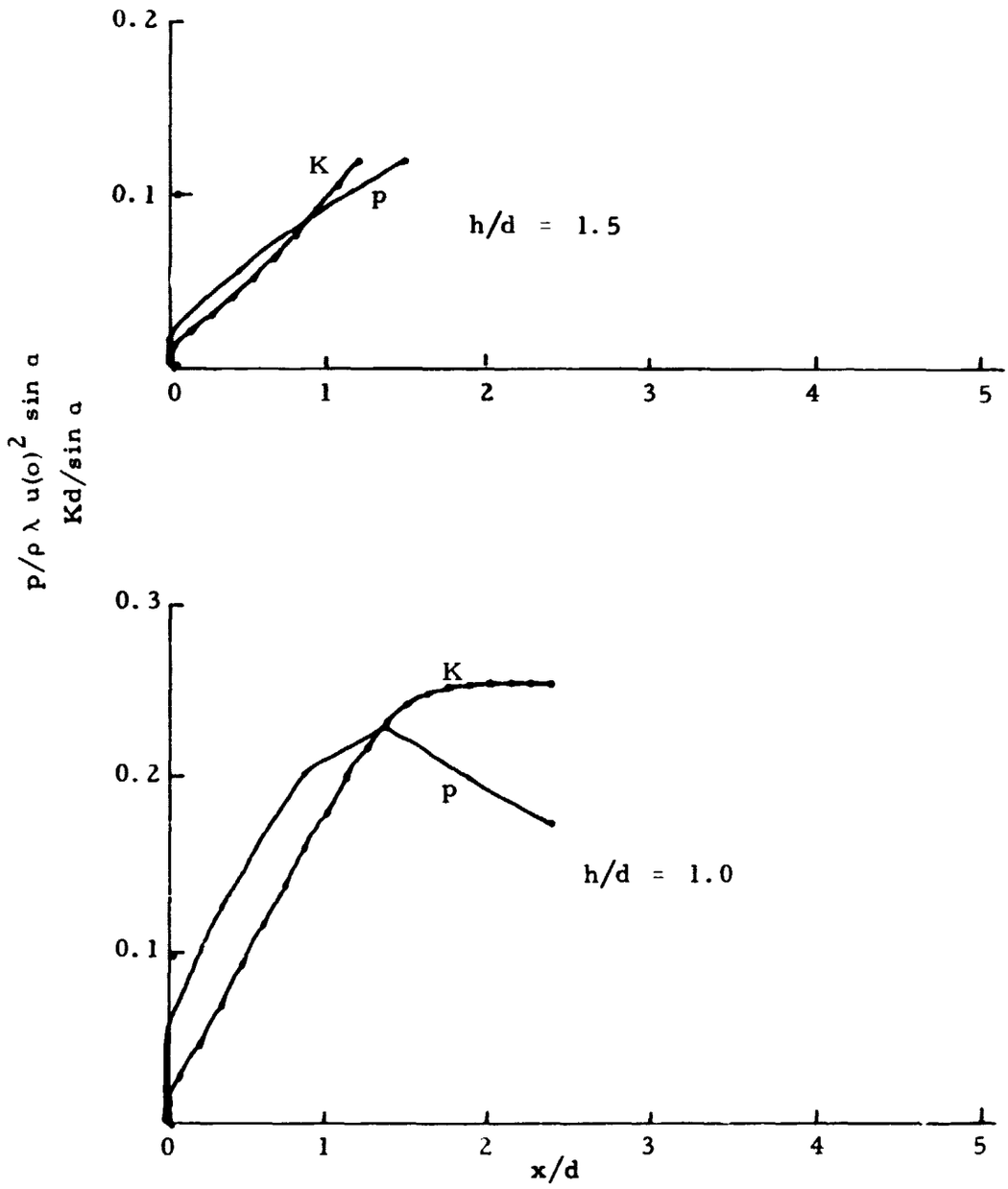

Figure 36. Normalized centerline pressure $p/\rho \lambda u(o)^2 \sin \alpha$ and the normalized curvature of the jet's momentum flux centerline $Kd/\sin \alpha$. The $x/d = 0$ origin for each h/d value represents the intersection point of the 0.1 free isotach. $\alpha = 9$ degrees uniform exit condition

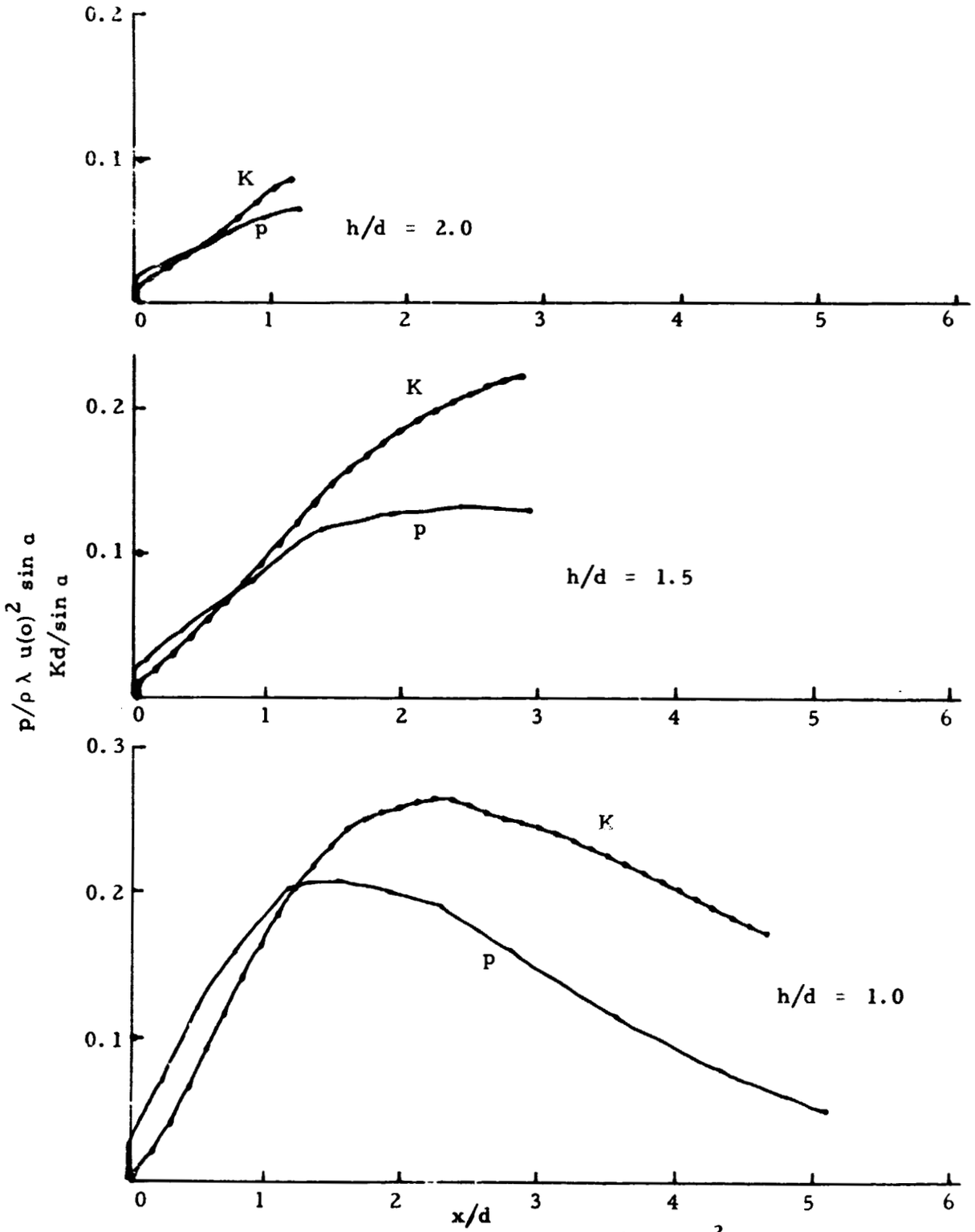

Figure 37. Normalized centerline pressure $p/\rho \lambda u(o)^2 \sin \alpha$ and the normalized curvature of the jet's momentum flux centerline $Kd/\sin \alpha$. The $x/d = 0$ origin for each h/d value represents the intersection point of the 0.1 free isotach.
α = 9 degrees fully developed exit condition

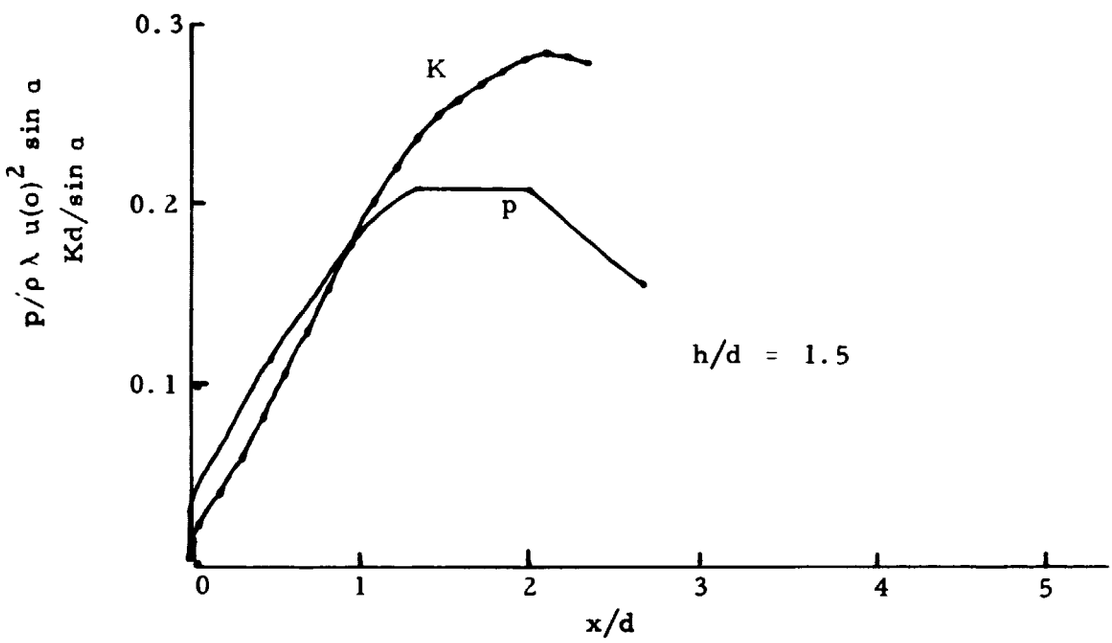

Figure 38. Normalized centerline pressure $p/\rho \lambda u(o)^2 \sin \alpha$ and the normalized curvature of the jet's momentum flux centerline $Kd/\sin \alpha$. The $x/d = 0$ origin for each h/d value represents the intersection point of the o.1 free isotach.
α = 12 degrees uniform exit condition

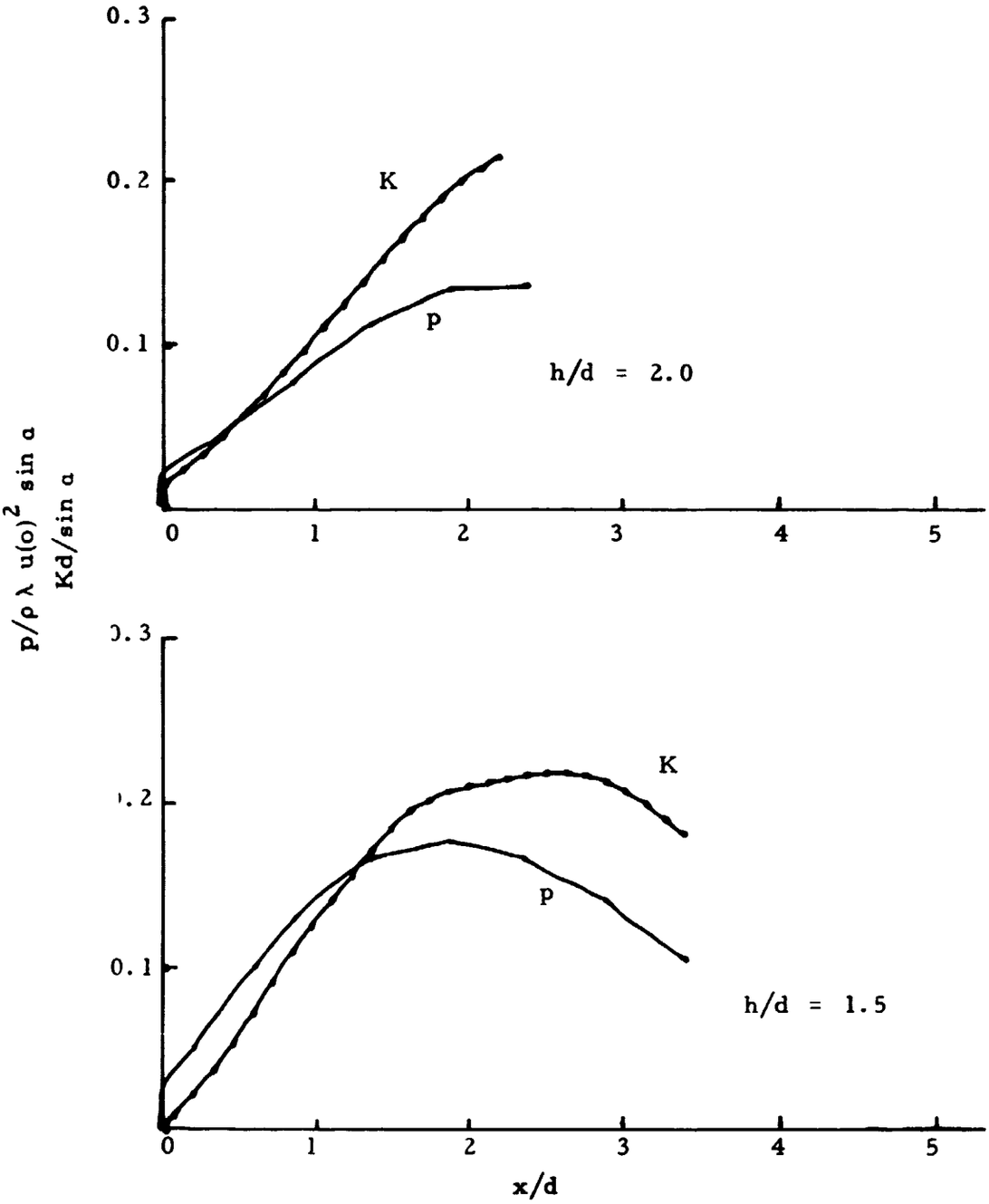

Figure 39. Normalized centerline pressure $p/\rho \lambda u(o)^2 \sin \alpha$ and the normalized curvature of the jet's momentum flux centerline $Kd/\sin \alpha$. The $x/d = 0$ origin for each h/d value represents the intersection point of the 0.1 free isotach. α = 12 degrees fully developed exit condition

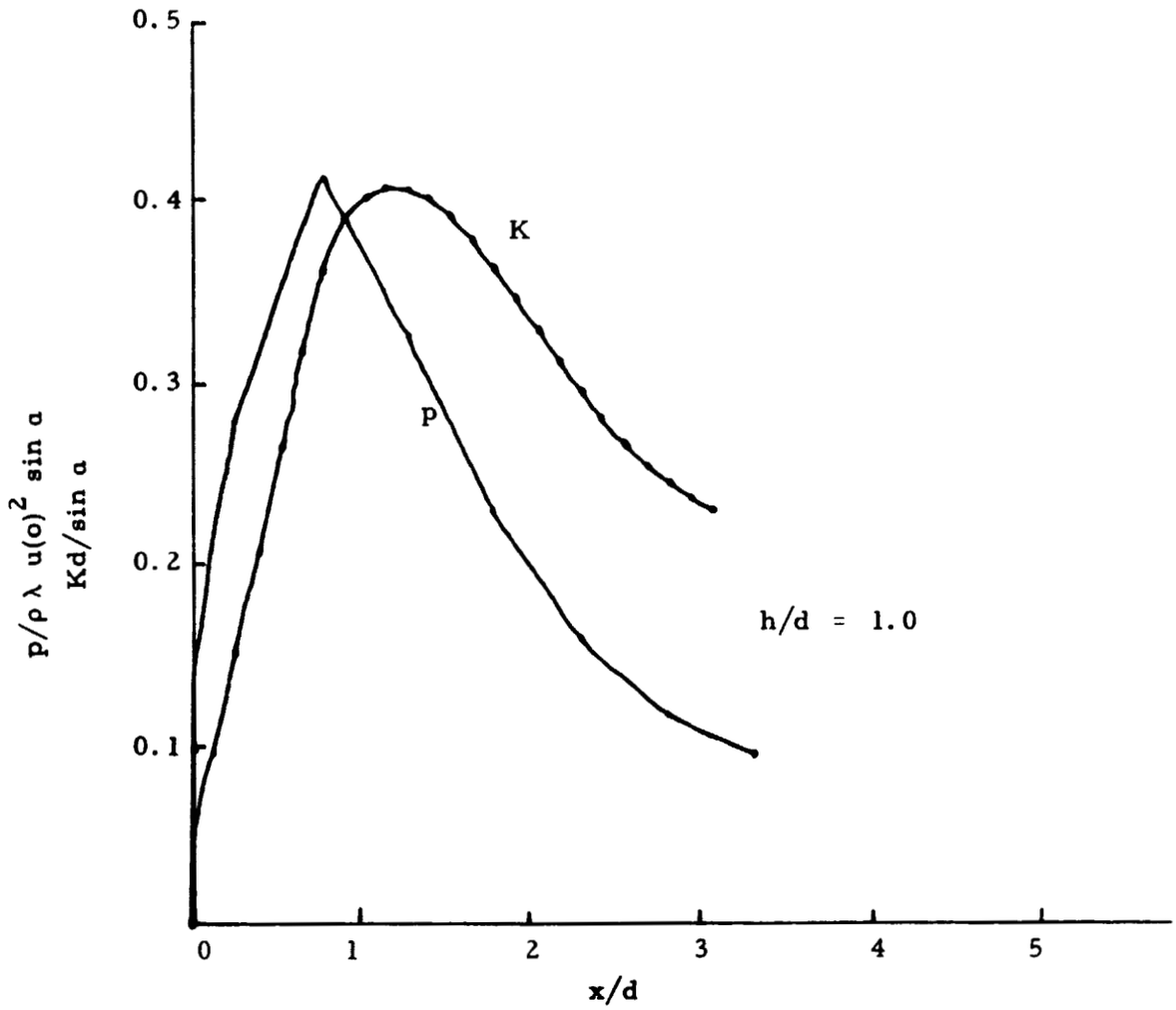

Figure 40. Normalized centerline pressure $p/\rho \lambda u(o)^2 \sin \alpha$ and the normalized curvature of the jet's momentum flux centerline $Kd/\sin \alpha$. The $x/d = 0$ origin for each h/d value represents the intersection point of the 0.1 free isotach.
α = 15 degrees uniform exit condition

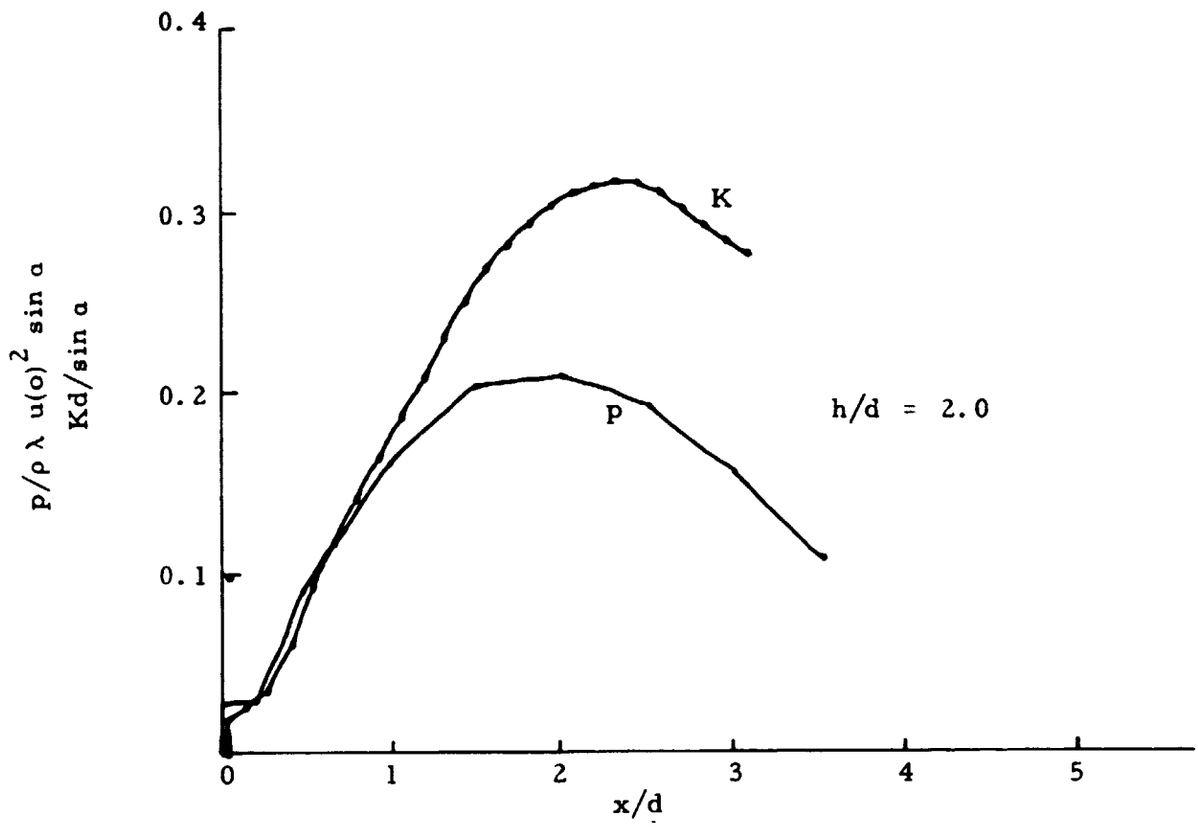

Figure 41. Normalized centerline pressure $p/\rho\lambda\, u(o)^2 \sin\alpha$ and the normalized curvature of the jet's momentum flux centerline $Kd/\sin\alpha$. The $x/d = 0$ origin for each h/d value represents the intersection point of the 0.1 free isotac
α = 15 degrees fully developed exit condition

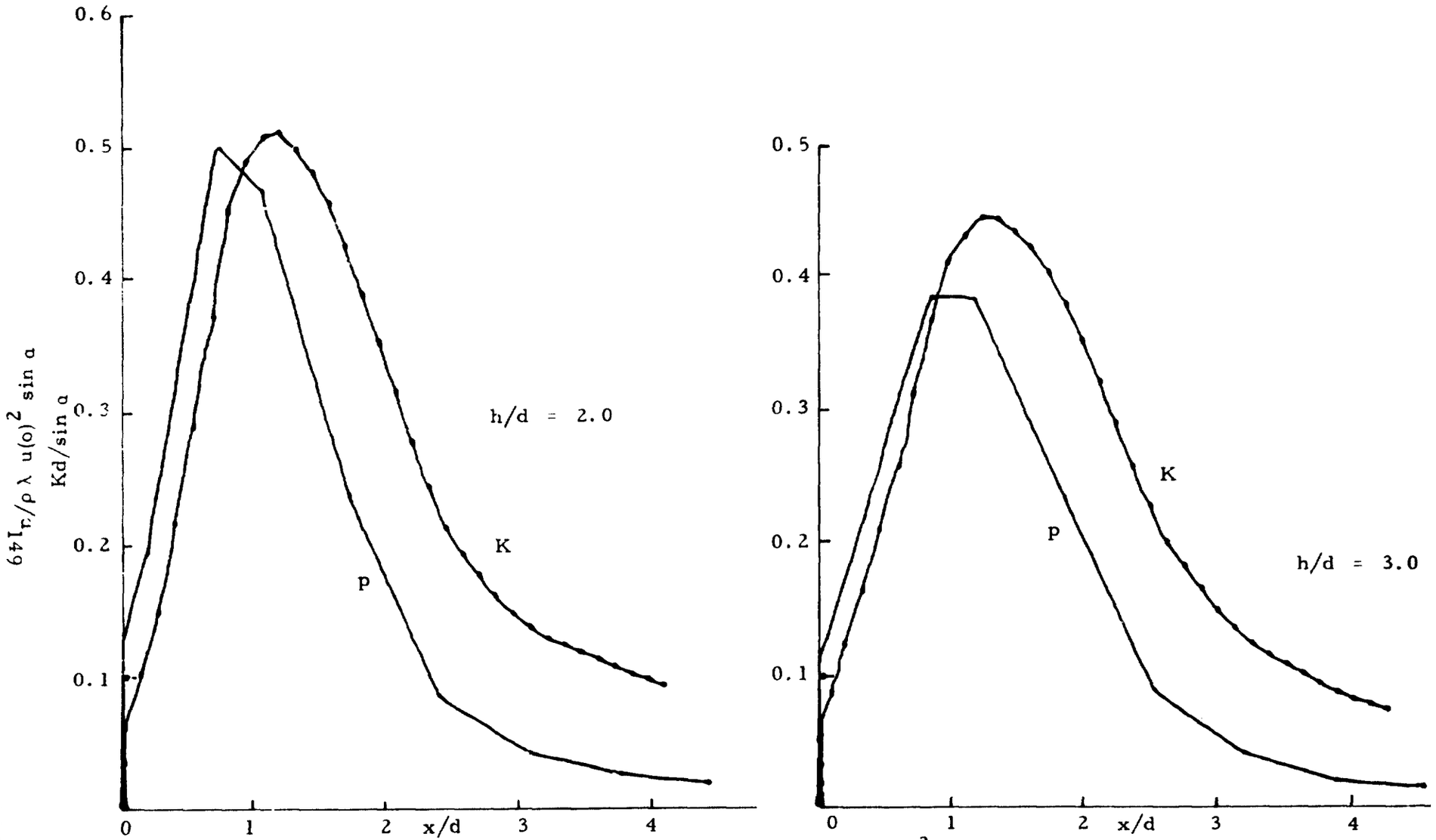

Figure 42. Normalized centerline pressure $p/\rho\lambda u(o)^2 \sin\alpha$ and the normalized curvature of the jet's momentum flux centerline $Kd/\sin\alpha$. The x/d = 0 origin for each h/d value represents the intersection point of the 0.1 free isotach.

α = 30 degrees uniform exit condition

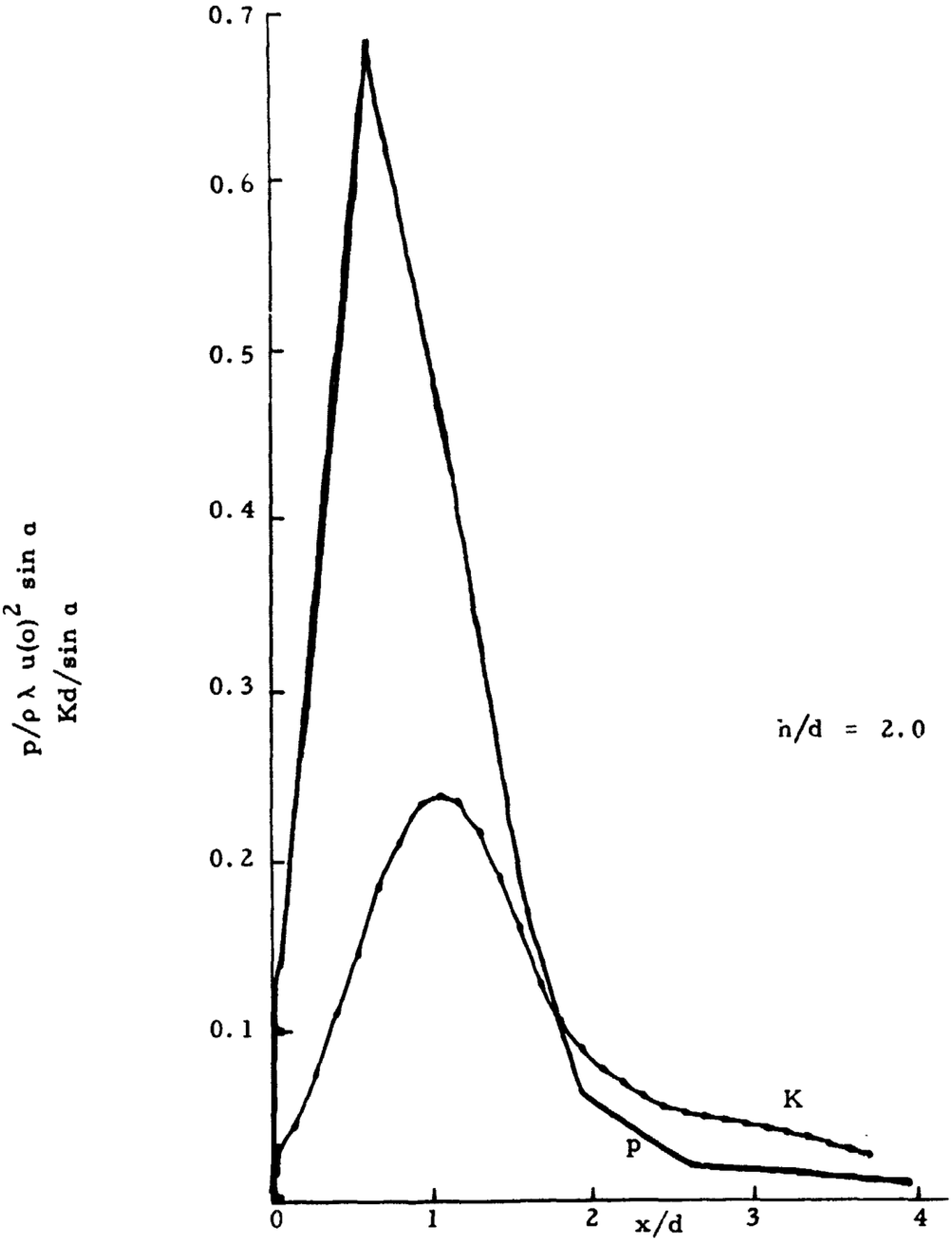

Figure 43. Normalized centerline pressure $p/\rho \lambda u(o)^2 \sin \alpha$ and the normalized curvature of the jet's momentum flux centerline $Kd/\sin \alpha$. The $x/d = 0$ origin for each h/d value represents the intersection point of the 0.1 free isotach.
α = 60 degrees uniform exit condition

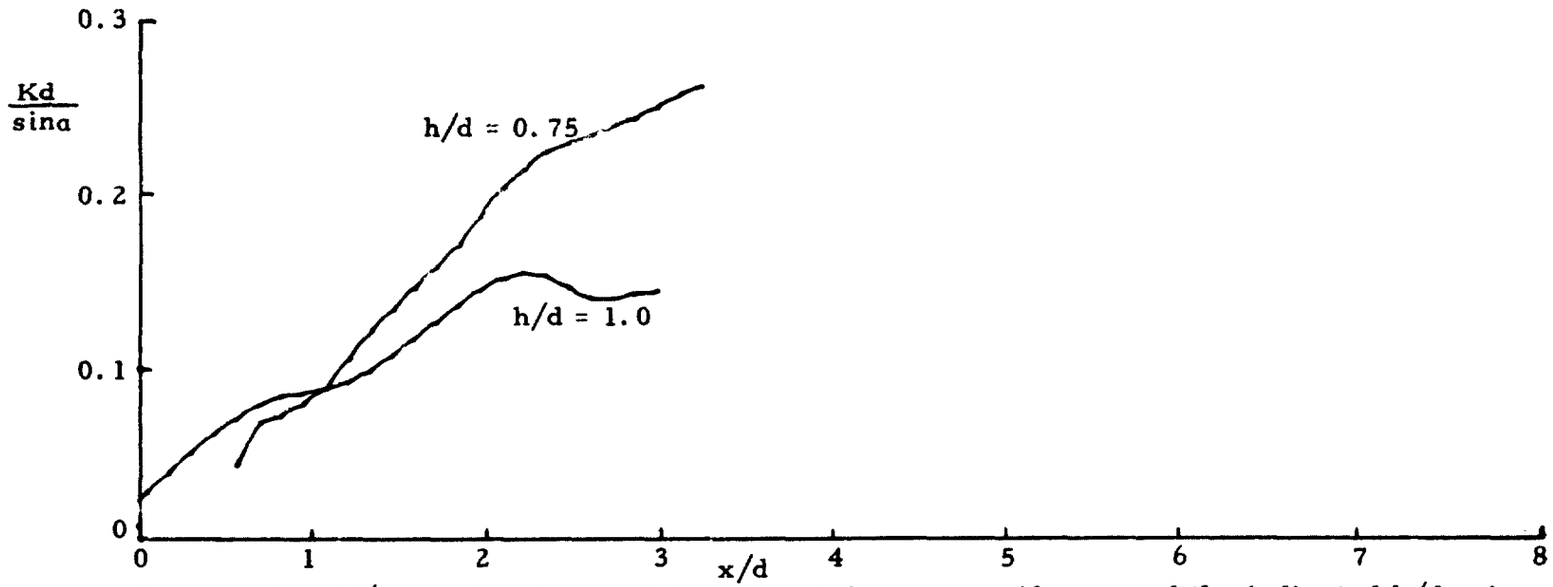

Figure 44. Kd/sin α for the conditions α = 3 degrees, uniform, and the indicated h/d values. The abscissa of the separate curves has been shifted such that the intersection of the 0.1 free isotach occurs at the origin.

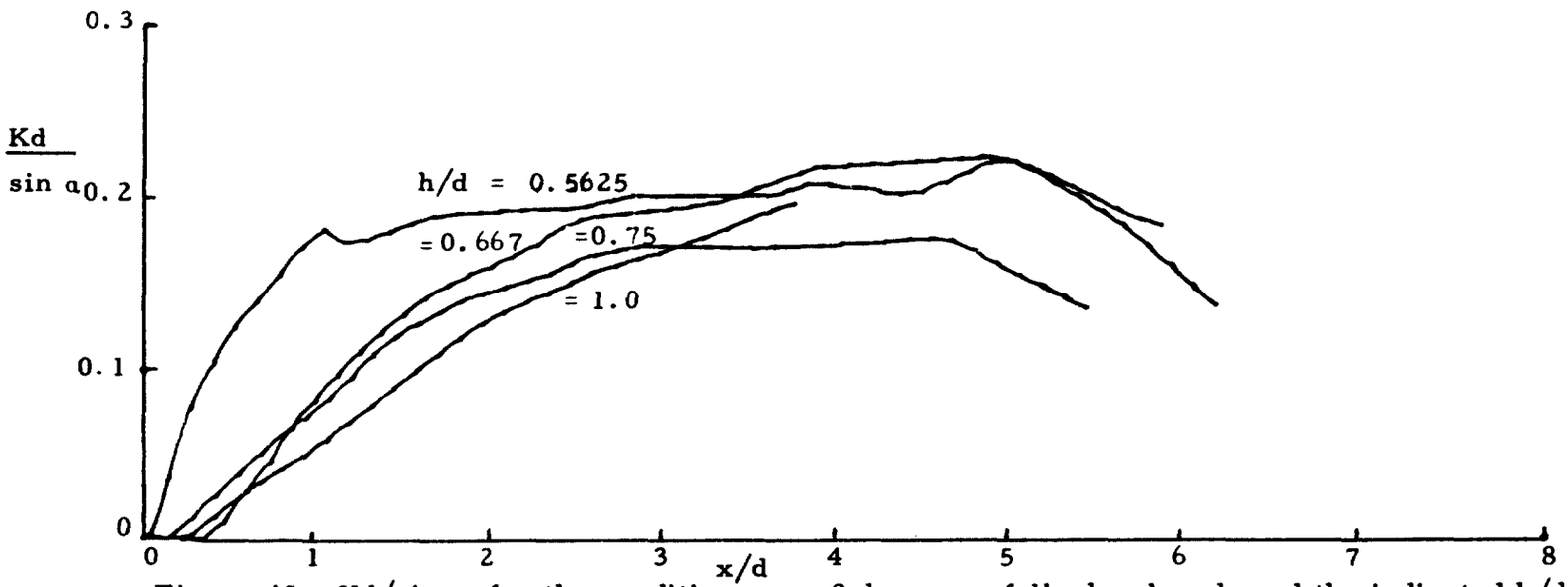

Figure 45. Kd/sin α for the conditions α = 3 degrees, fully developed, and the indicated h/d values. The abscissa of the separate curves has been shifted such that the intersection of the 0.1 free isotach occurs at the origin.

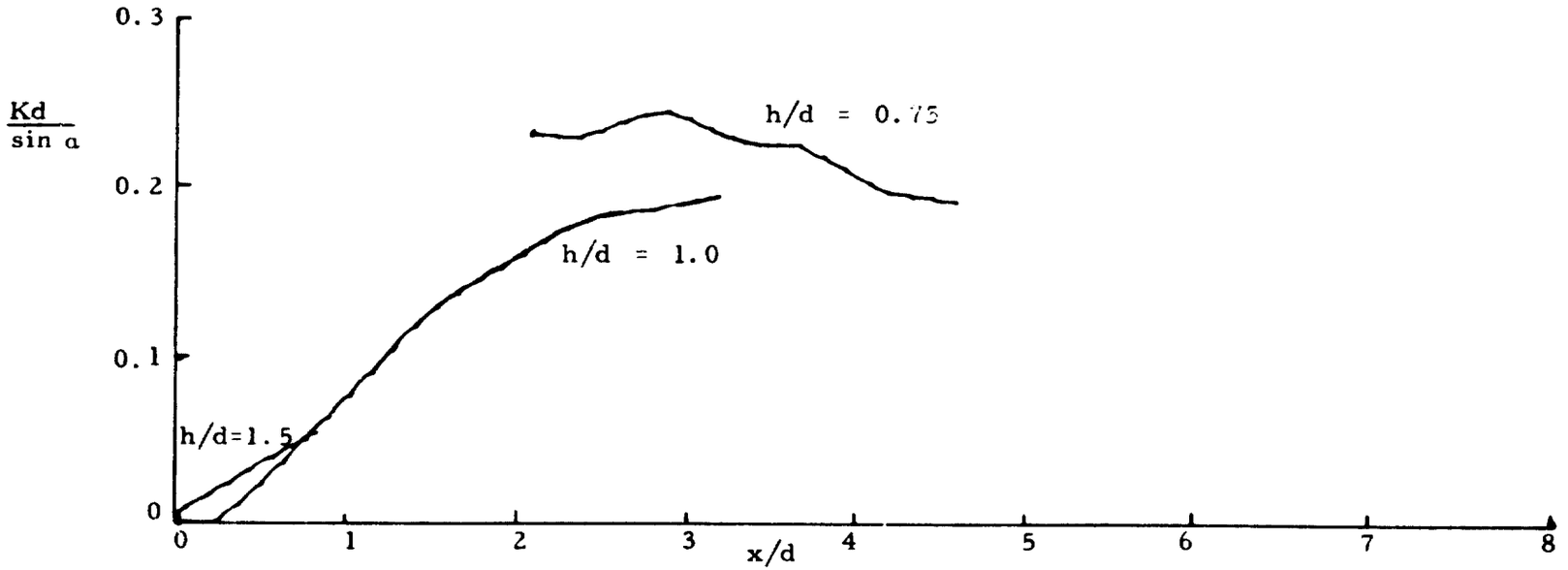

Figure 46. Kd/sin α for the conditions α = 3 degrees, fully developed, and the indicated h/d values. The abscissa of the separate curves has been shifted such that the intersection of the 0.1 free isotach occurs at the origin.

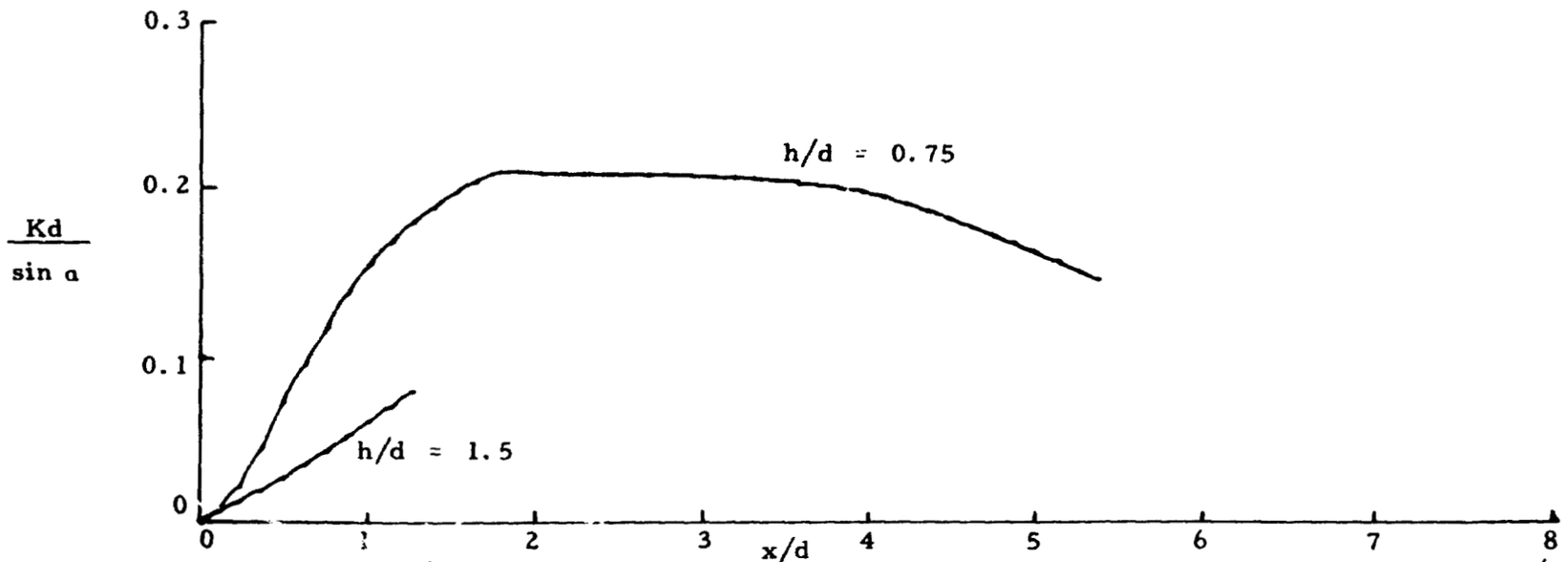

Figure 47. Kd/sin α for the conditions α = 6 degrees, fully developed, and the indicated h/d values. The abscissa of the separate curves has been shifted such that the intersection of the 0.1 free isotach occurs at the origin.

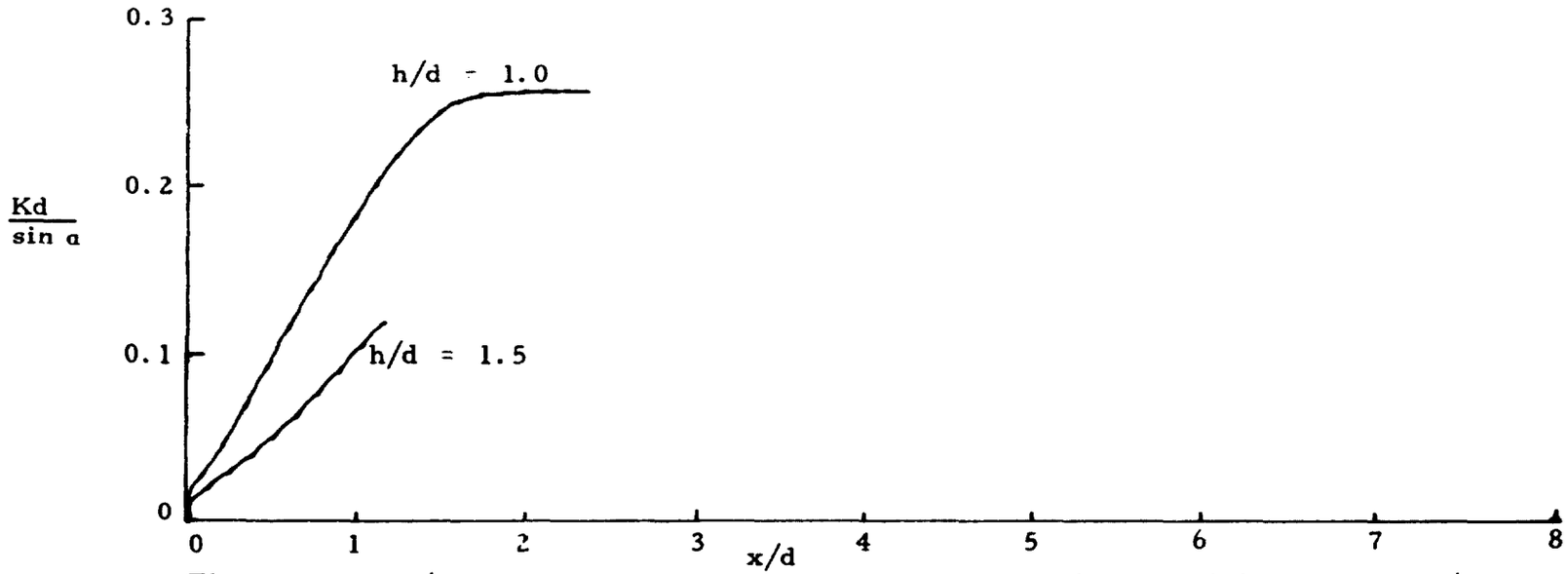

Figure 48. Kd/sin α for the conditions α = 9 degrees, uniform, and the indicated h/d values. The abscissa of the separate curves has been shifted such that the intersection of the 0.1 free isotach occurs at the origin.

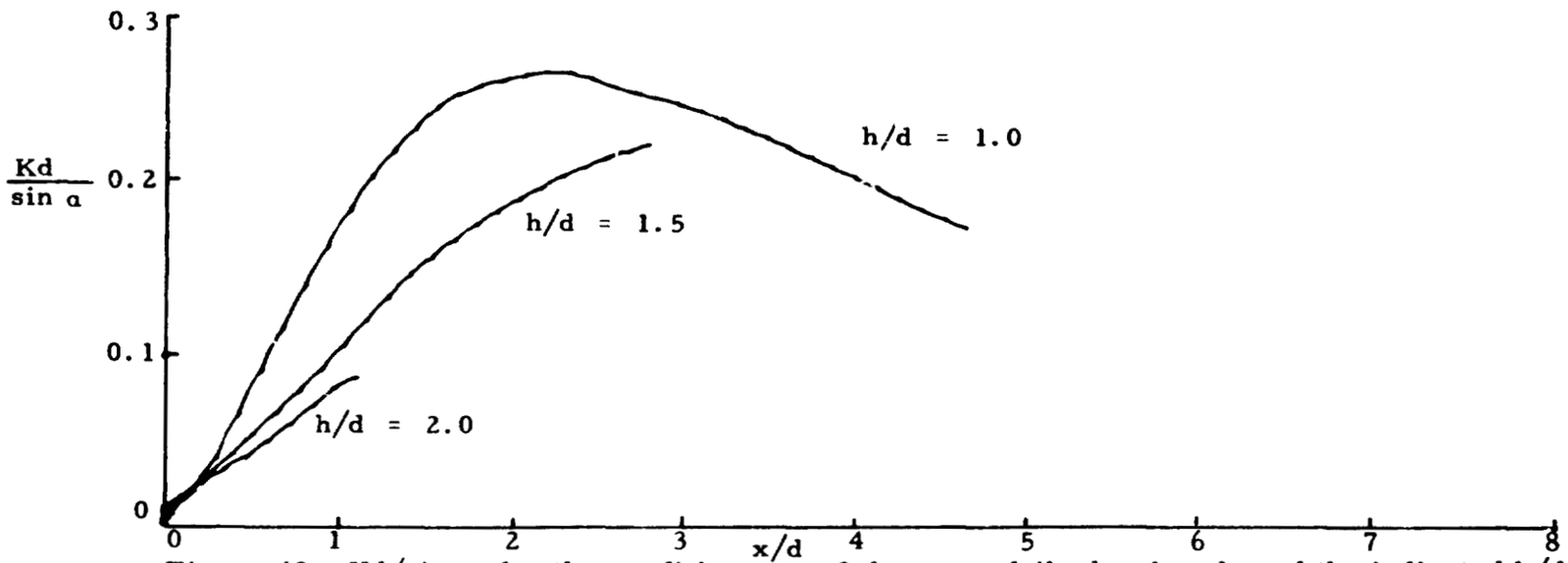

Figure 49. Kd/sin α for the conditions α = 9 degrees, fully developed, and the indicated h/d values. The abscissa of the separate curves has been shifted such that the intersection of the 0.1 free isotach occurs at the origin.

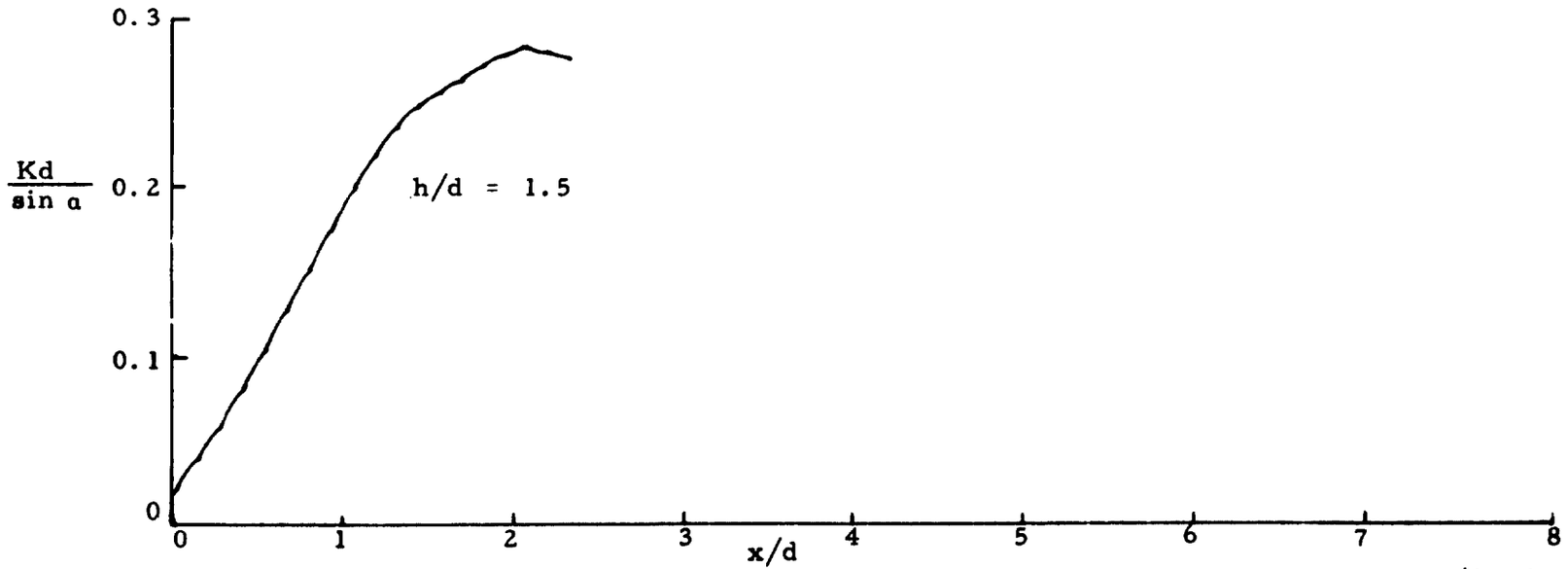

Figure 50. Kd/sin α for the conditions α = 12 degrees, uniform, and the indicated h/d values. The abscissa of the separate curves has been shifted such that the intersection of the 0.1 free isotach occurs at the origin.

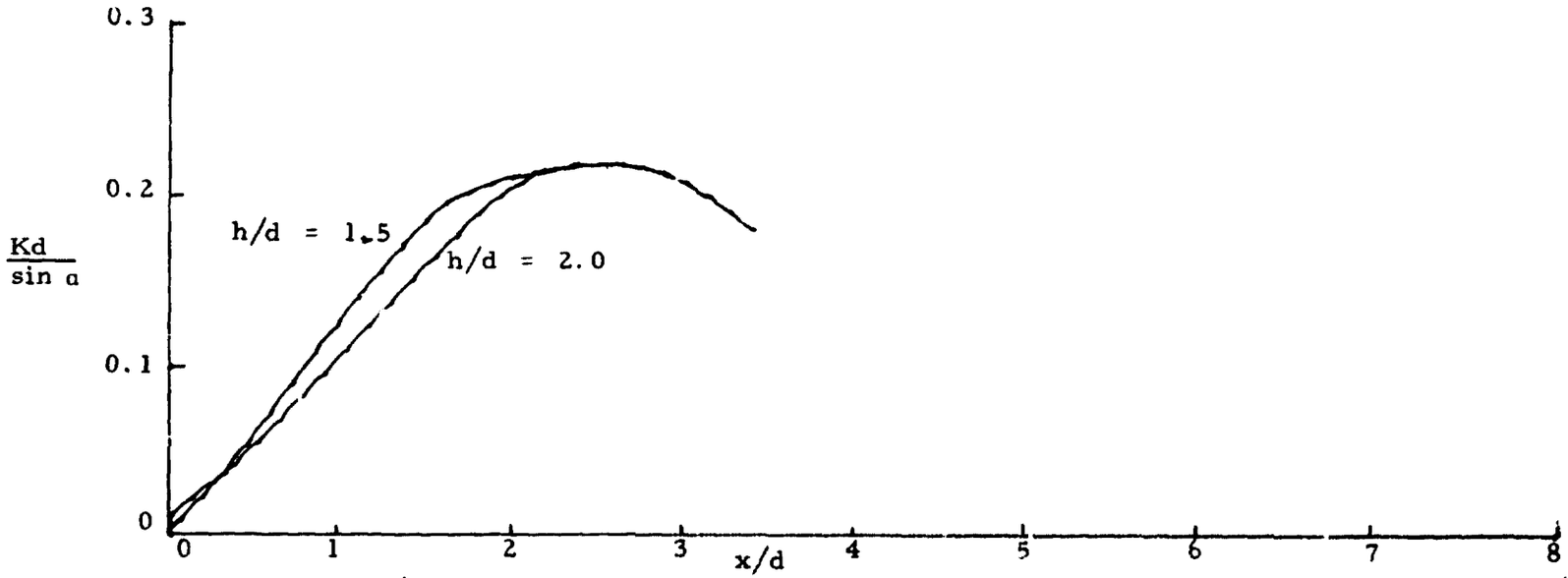

Figure 51. Kd/sin α for the conditions α = 12 degrees, fully developed, and the indicated h/d values. The abscissa of the separate curves has been shifted such that the intersection of the 0.1 free isotach occurs at the origin.

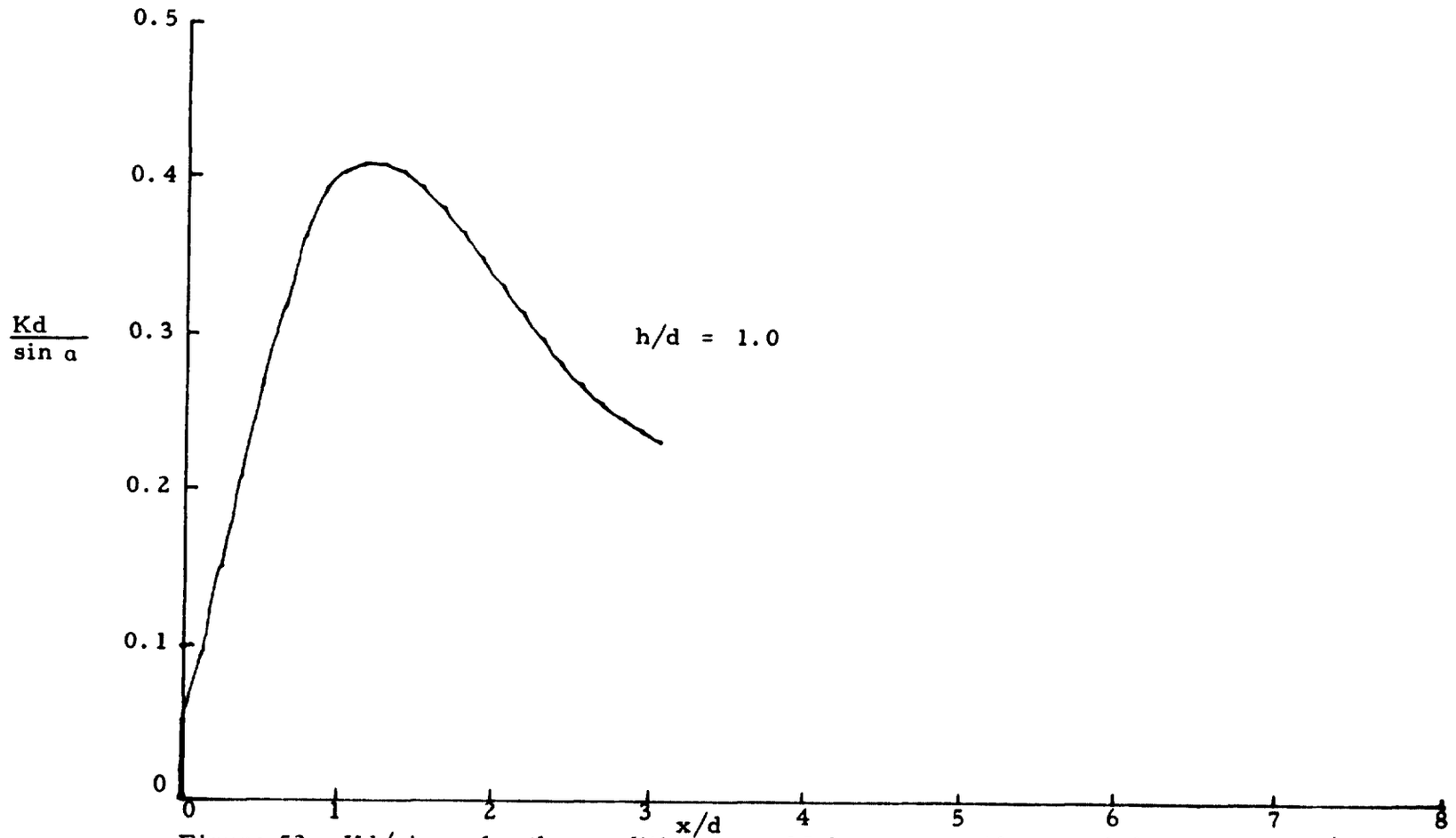

Figure 52. Kd/sin α for the conditions α = 15 degrees, uniform, and the indicated h/d values. The abscissa of the separate curves has been shifted such that the intersection of the 0.1 free isotach occurs at the origin.

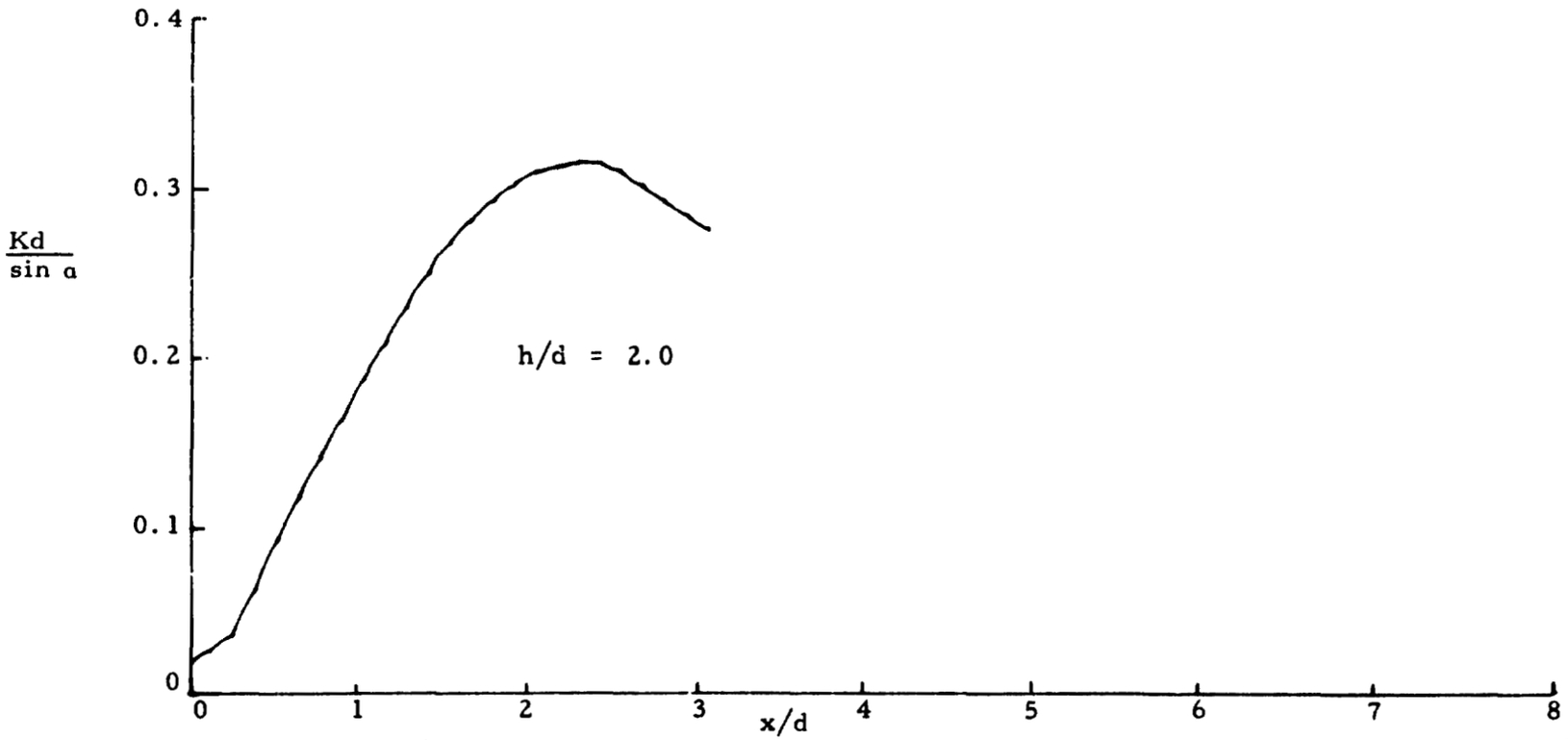

Figure 53. Kd/sin α for the conditions α = 15 degrees, fully developed, and the indicated h/d values. The abscissa of the separate curves has been shifted such that the intersection of the 0.1 f isotach occurs at the origin.

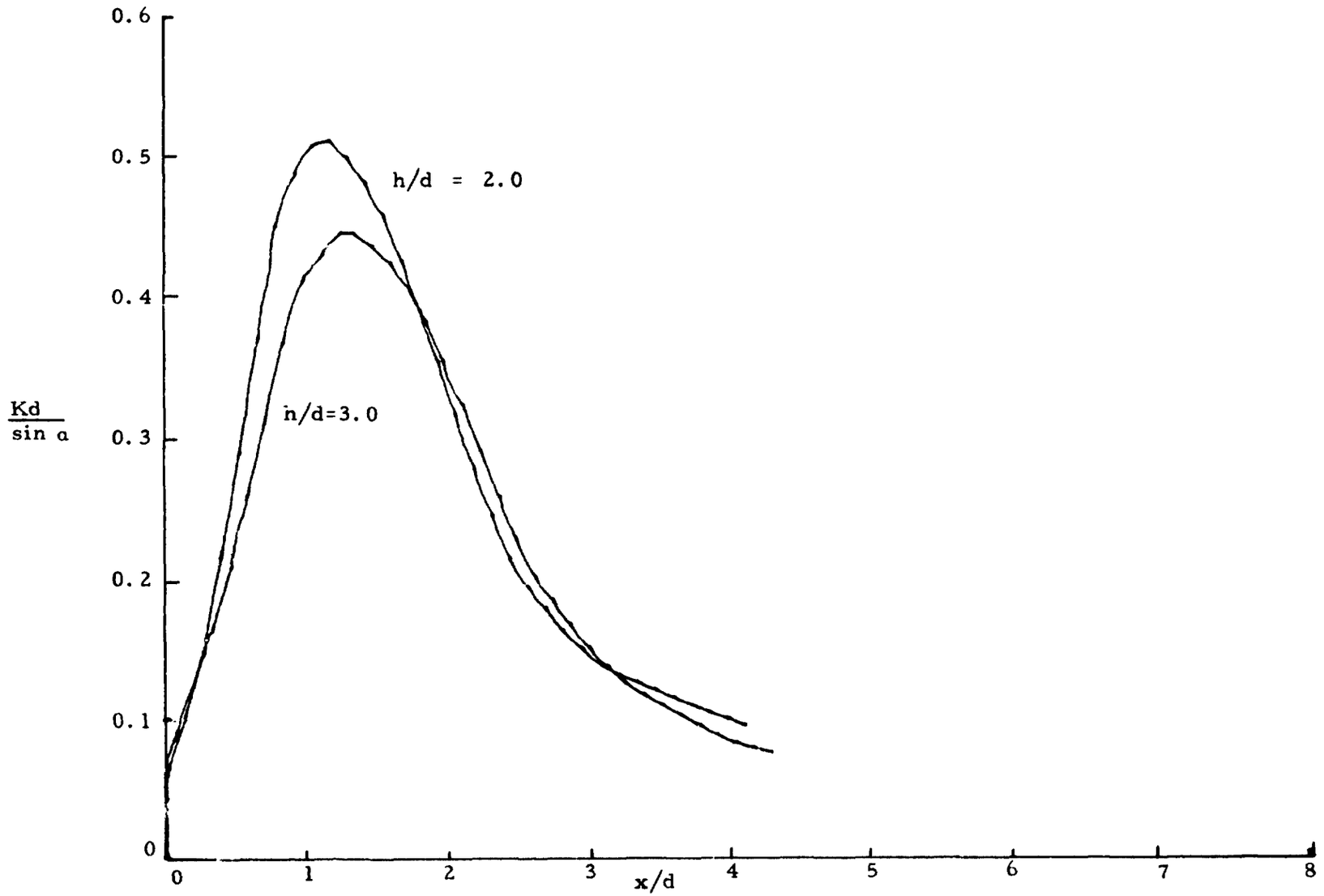

Figure 54. Kd/sin α for the conditions α = 30 degrees, uniform, and the indicated h/d values. The abscissa of the separate curves has been shifted such that the intersection of the 0.1 free isotach occurs at the origin.

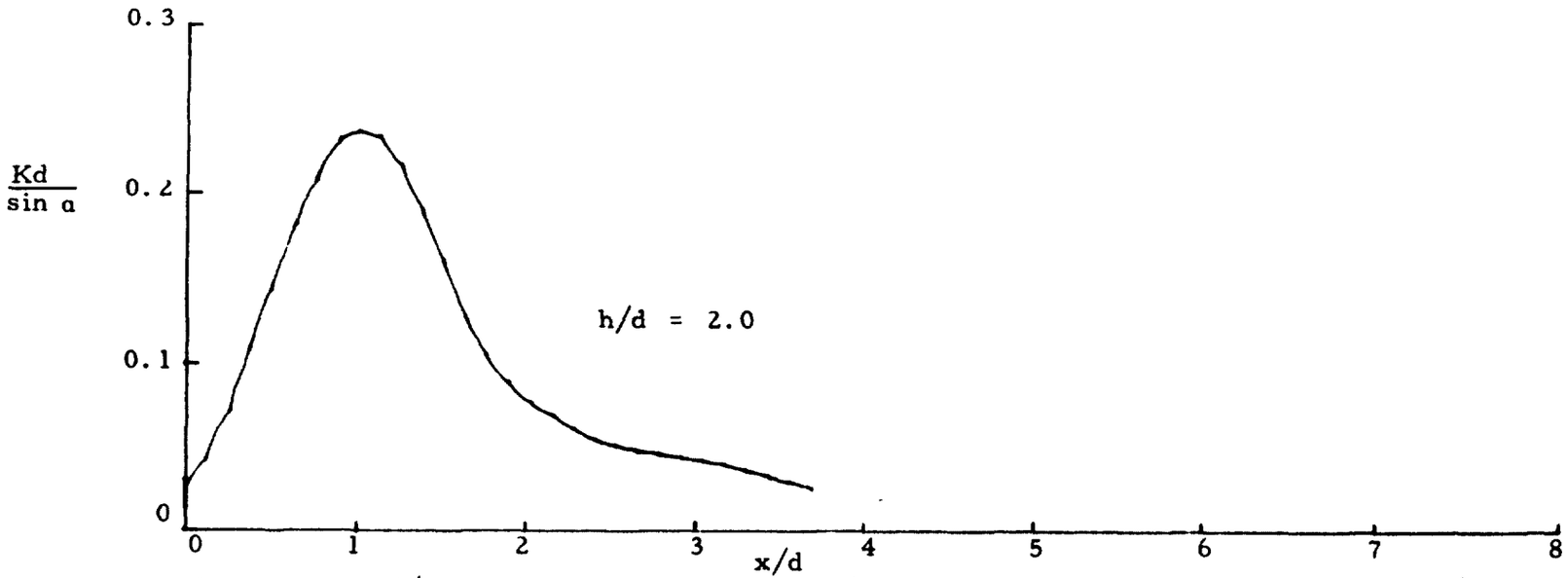

Figure 55. Kd/sin α for the conditions α = 60 degrees, uniform, and the indicated h/d values. The abscissa of the separate curves has been shifted such that the intersection of the 0.1 free isotach occurs at the origin.

Axisymmetric region, azimuthal vorticity of the approaching jet flow.

Buffer region, Streamwise vorticity production from reorientation of the azimuthal vorticity field $(\omega_\theta \, \partial u/\partial\theta)$.

Near wall region, streamwise vorticity from flux at wall $(\nu \, \partial \omega_x/\partial z)$ and vortex stretching $(\omega_y \, \partial u/\partial y)$.

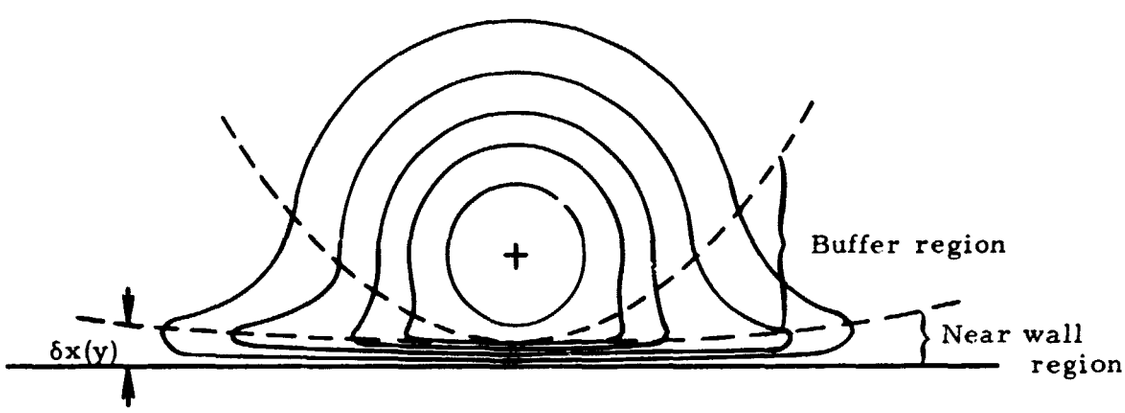

Figure 56. Schematic representation of general isotach distribution showing the axisymmetric region in the undisturbed flow, the buffer region and the near wall region.

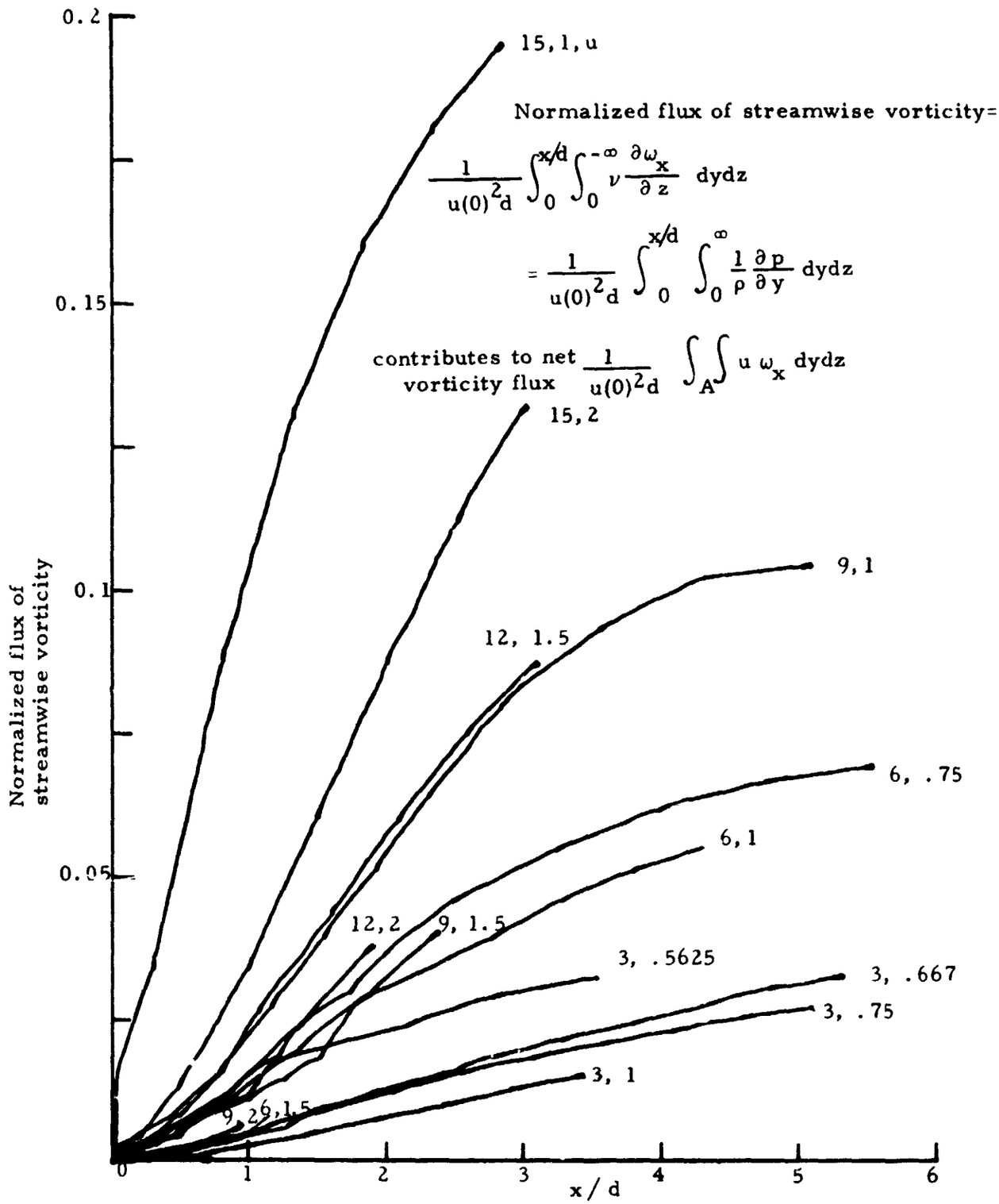

Figure 57a. Flux of streamwise vorticity into the flow as a result of the surface pressure distribution, fully developed cases (α degrees, h/d). Note, 15, 1, u is for the uniform exit condition.

NOTE: Abscissa for data shifted such that 0.1 free isotach aligns with the position x/d = 0.

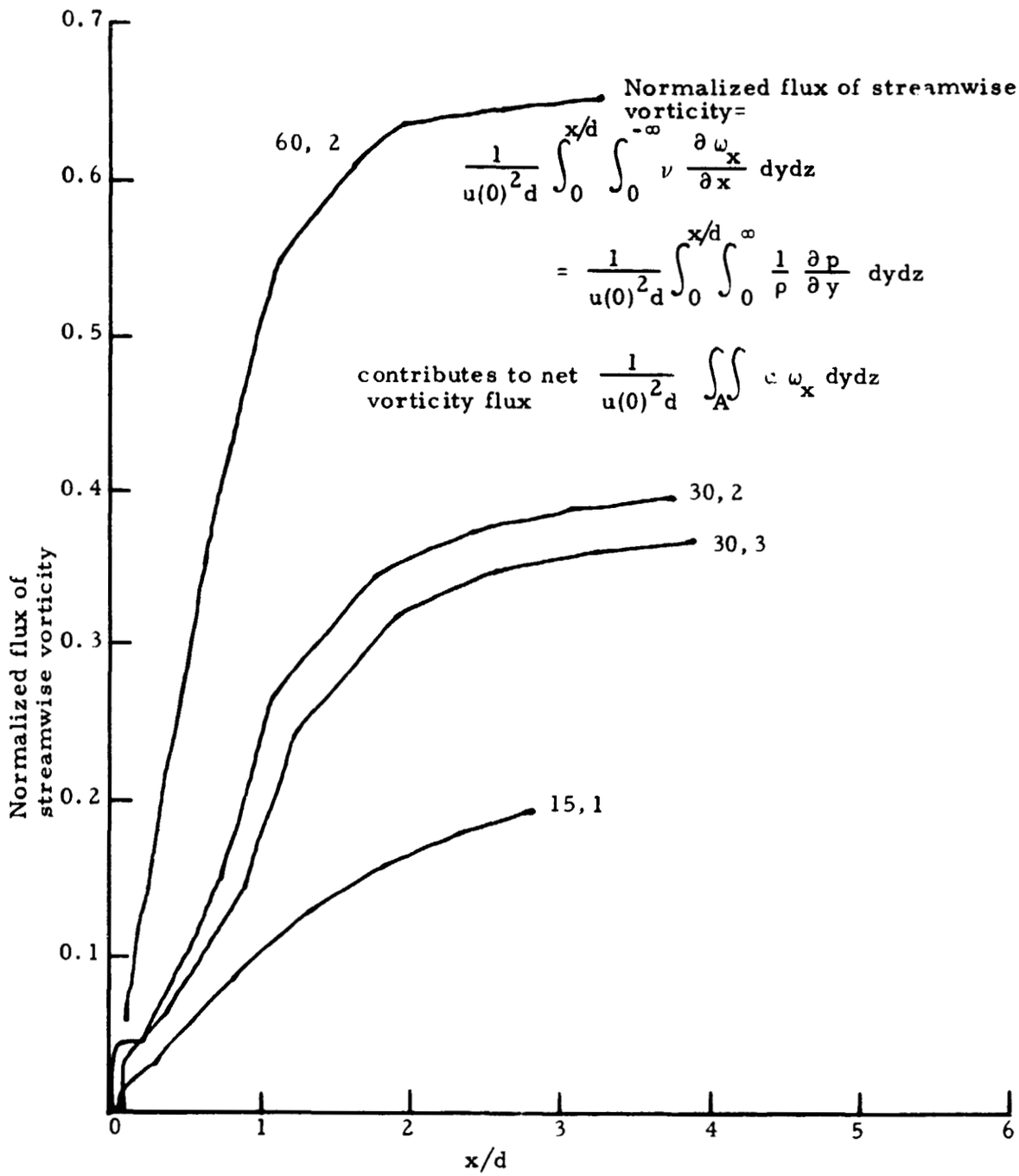

Figure 57 b. Flux of streamwise vorticity into the flow as a result of the surface pressure distribution, fully developed cases (α degrees, h/d).

NOTE: Abscissa for data shifted such that 0.1 free isotach aligns with the position x/d = 0.

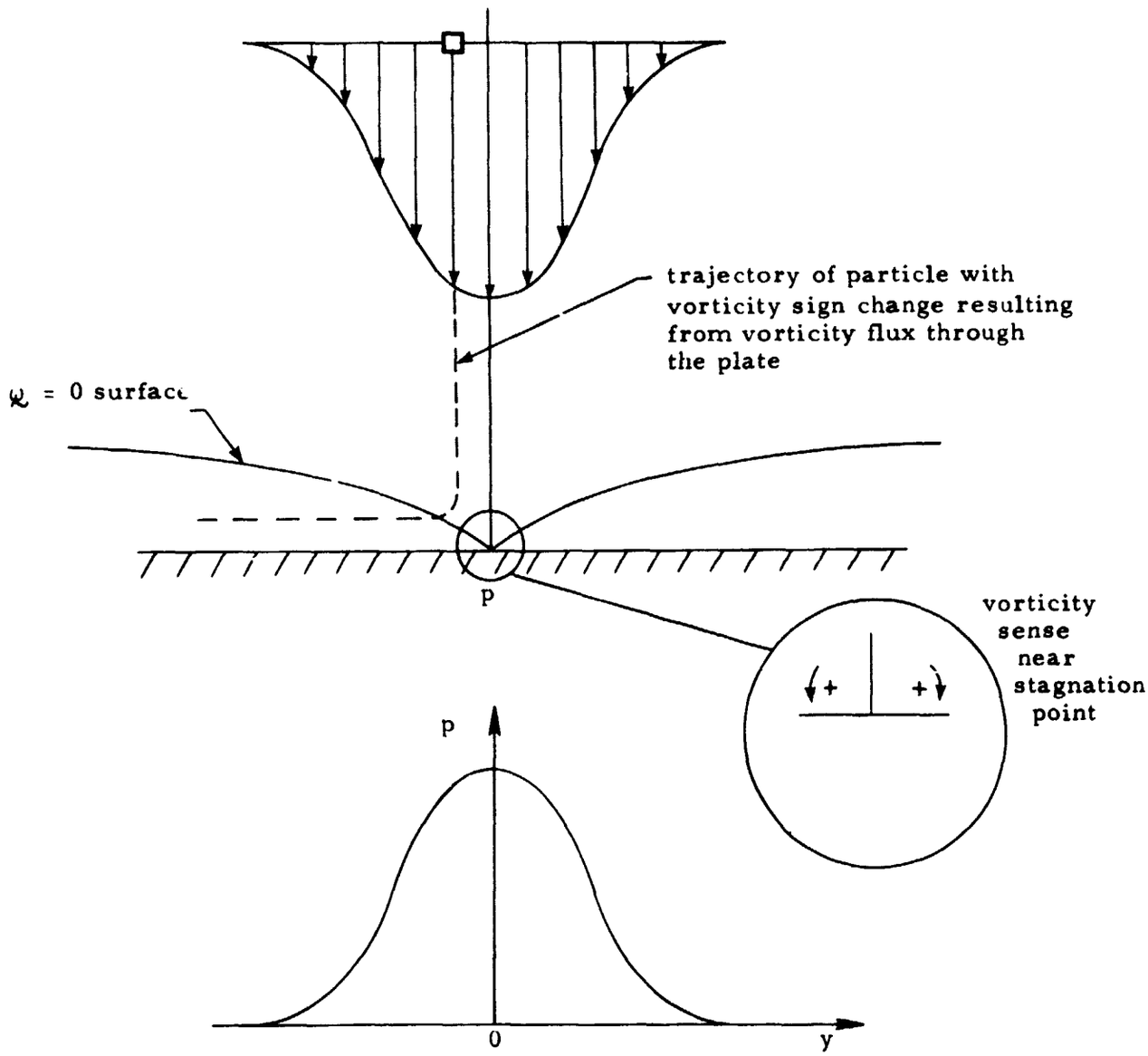

Figure 58. Vorticity, pressure relationships for normal jet impingement.

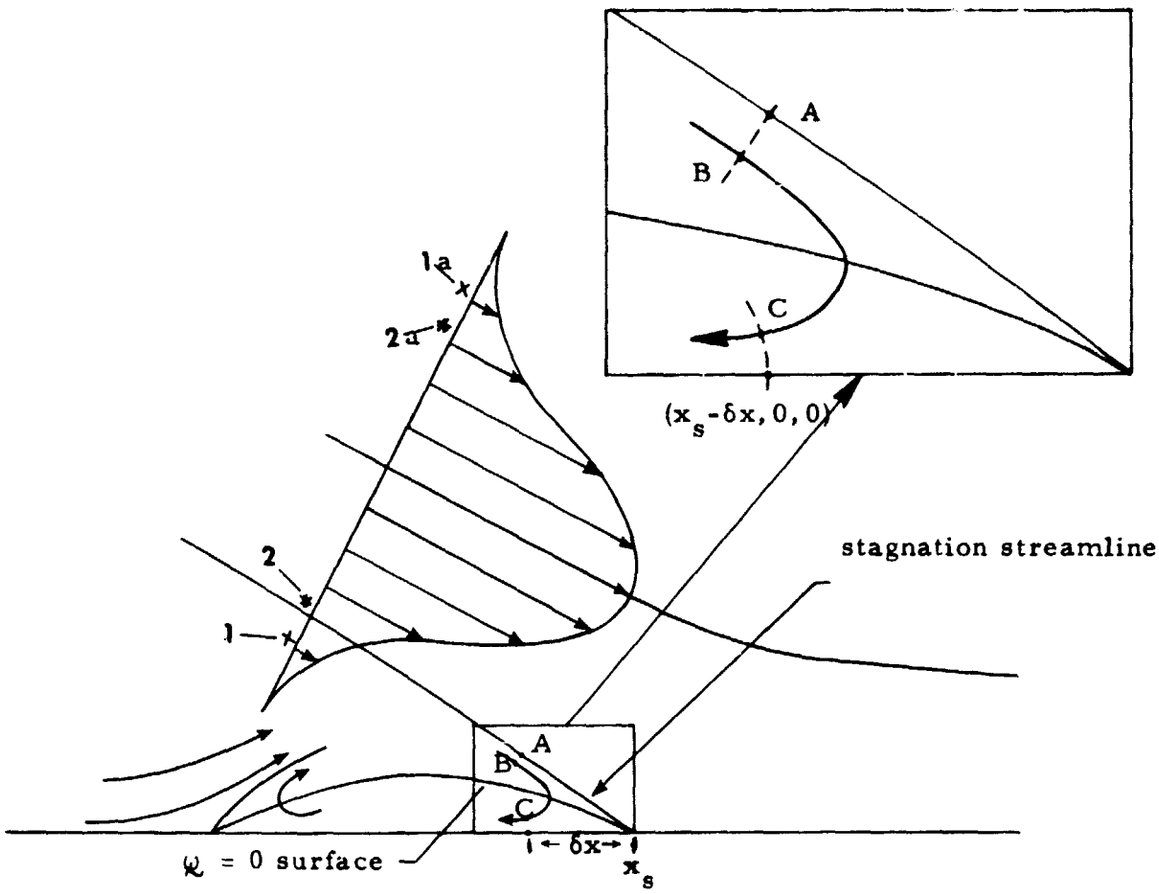

Figure 59. Physical characteristics of oblique jet impingement.

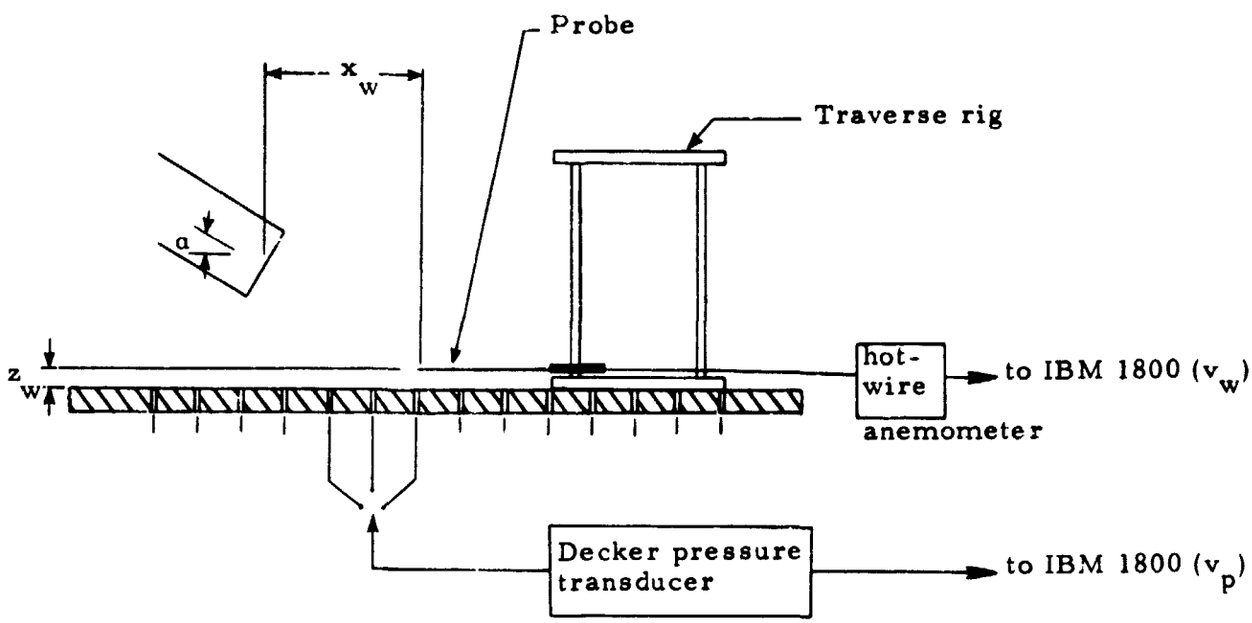

Note: For the comparison of the hot-wire and pressure data, v_w was shifted in x by an amount $v_w(x, z) = v_w(x+\Delta x, 0)$ where $\Delta x = z_w/\tan \alpha + \beta$.

Figure 60. Experimental technique for the acquisition of the velocity and surface static pressure data.

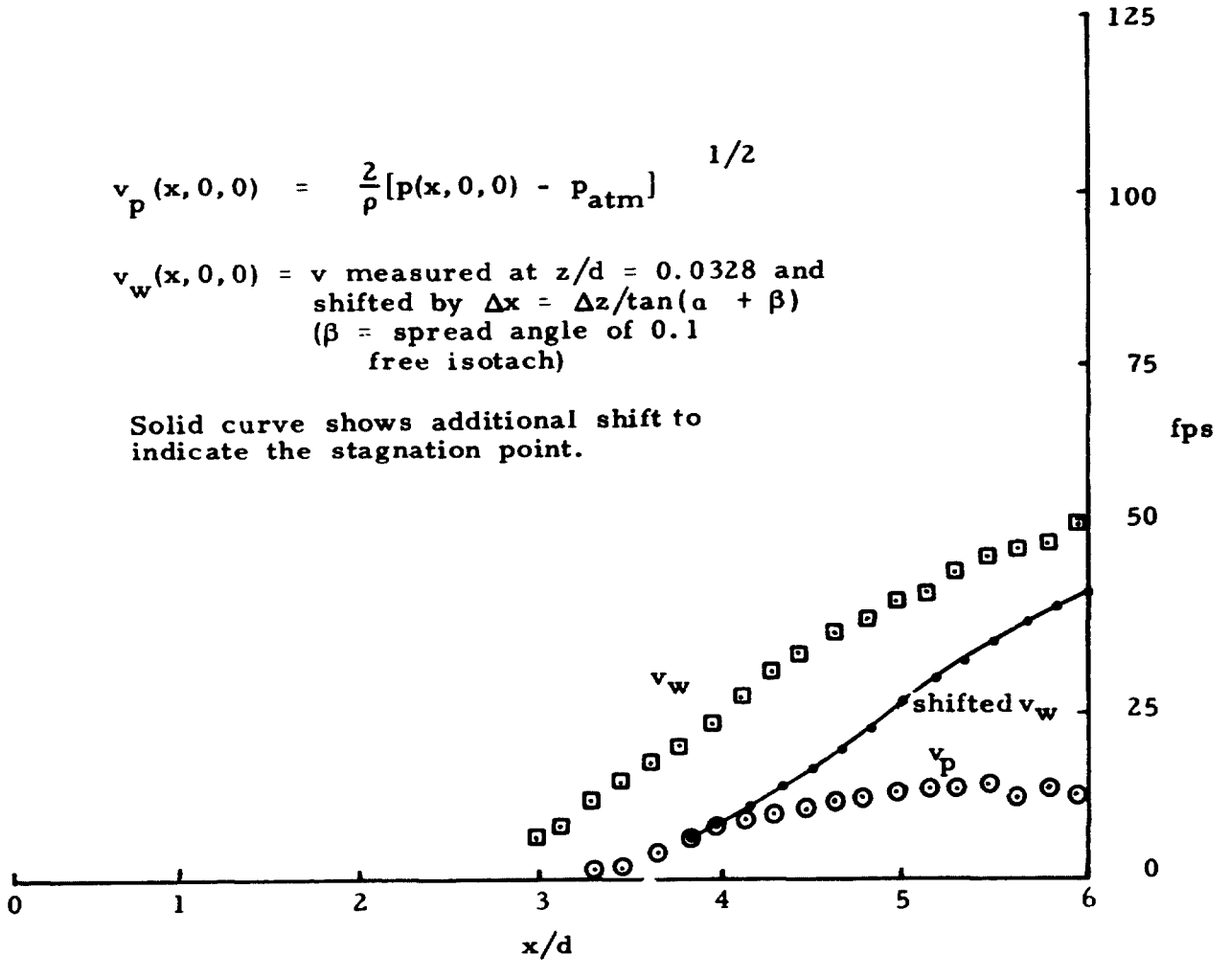

Figure 61. Measured, v_w, and equivalent stagnation streamline velocities (as inferred from the surface pressure), v_p, to determine the stagnation point for the conditions α = 3 degrees, h/d = 1, uniform.

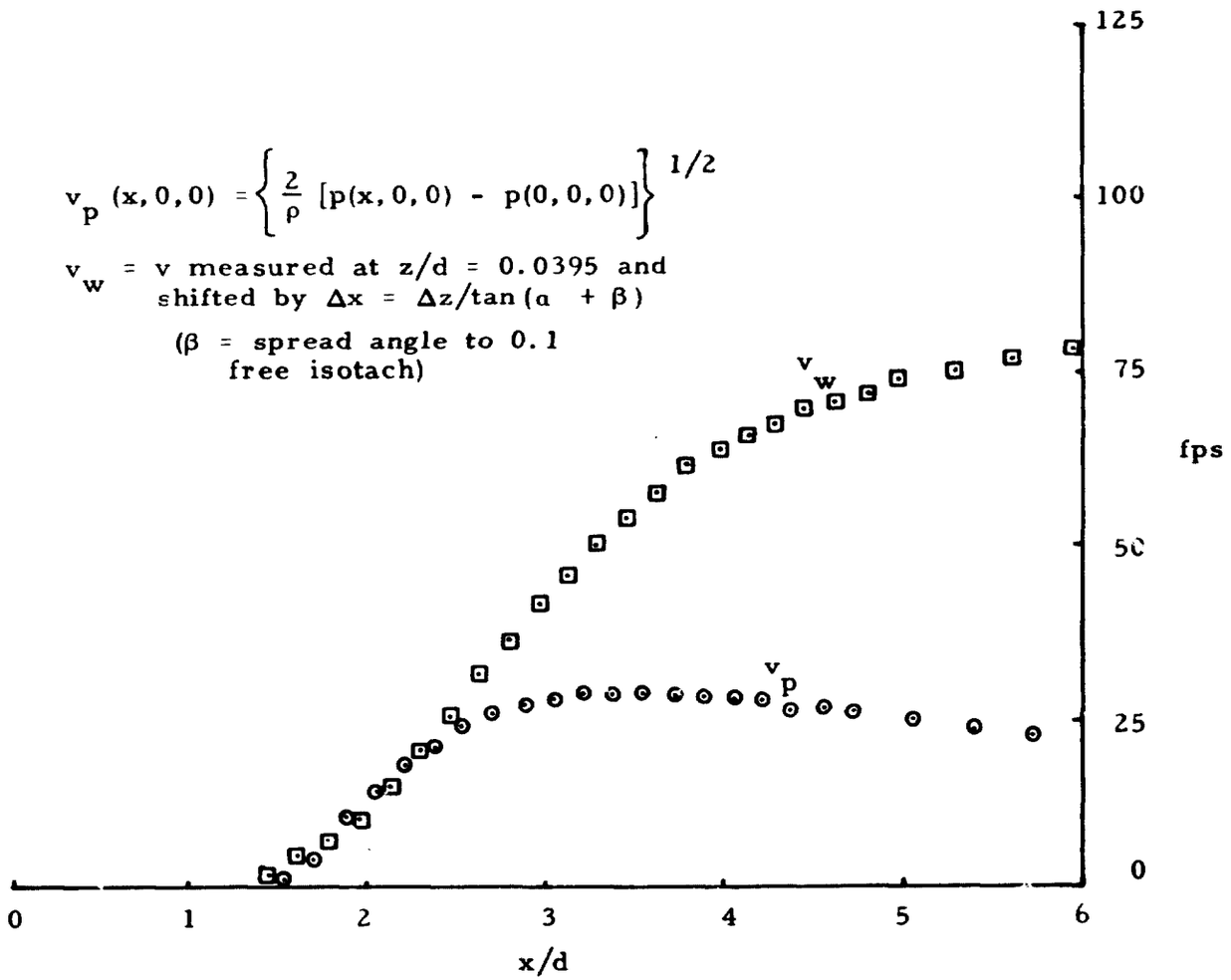

Figure 62. Measured, v_w, and equivalent stagnation streamline velocities (as inferred from the surface pressure), v_p, to determine the stagnation point for the conditions α = 9 degrees, h/d = 1, uniform.

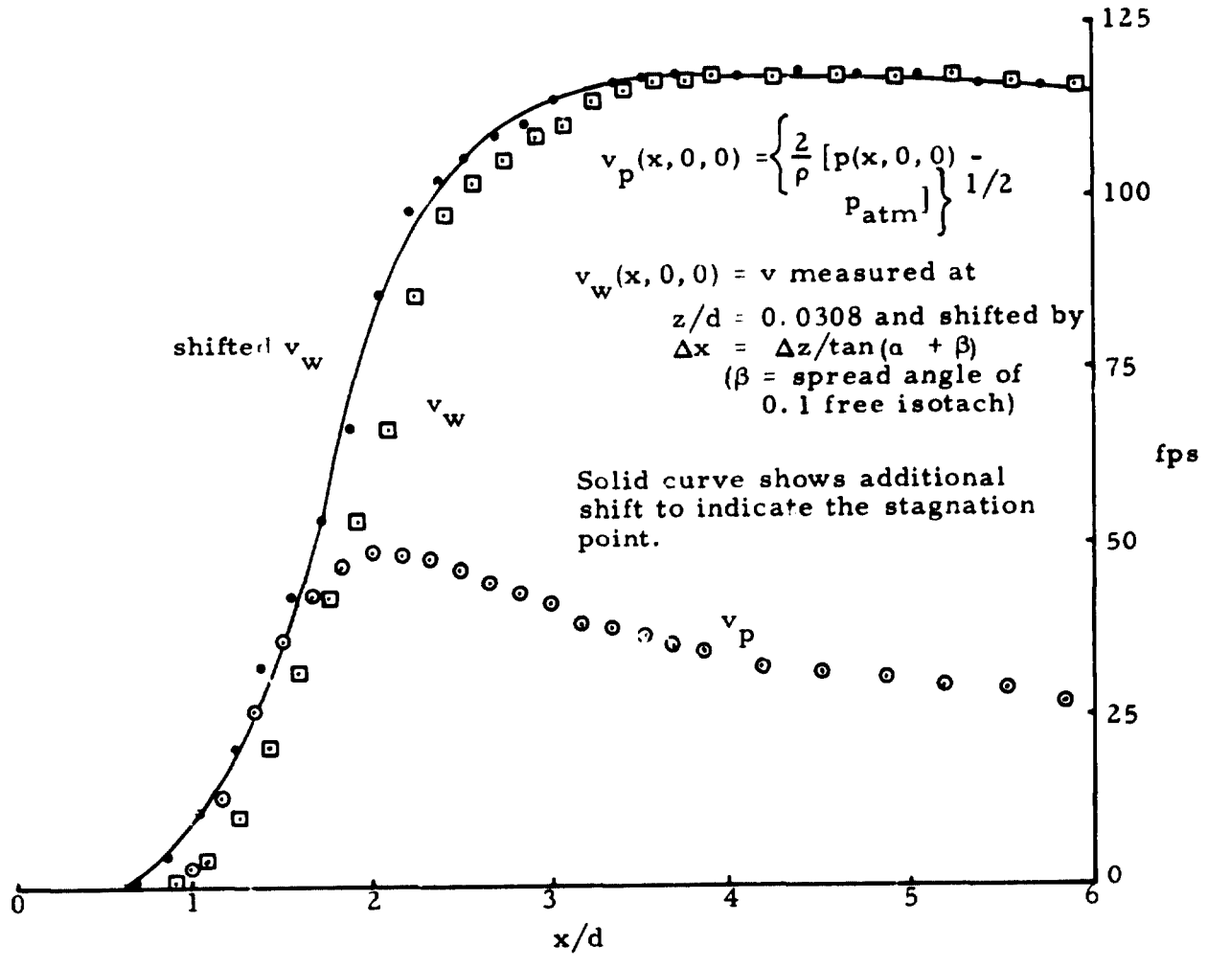

Figure 63. Measured, v_w, and equivalent stagnation streamline velocities (as inferred from the surface pressure), v_p, to determine the stagnation point for the conditions α = 15 degrees, h/d = 1, uniform.

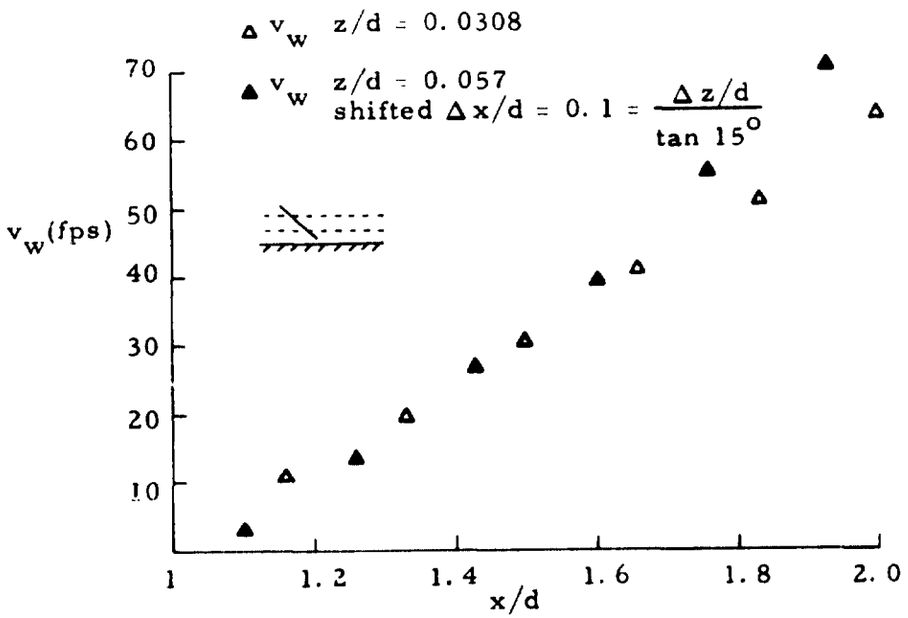

Figure 64. Comparison of v_w for two z values, α = 15 degrees, h/d = 1, uniform.